Czech Technical University in Prague

Faculty of Mechanical Engineering

Department of Physics

Doctoral thesis

Thermophysical properties of refrigerants: experiment and simulations

Ing. Martin Doubek

Doctoral Study Program: Mechanical Engineering

Study Field: Mathematical and Physical Engineering

Thesis supervisor: Doc. Ing. Václav Vacek, CSc.

Dissertation thesis for obtaining the academic title of "Doctor" abbreviated to "Ph.D."

Prague December 2018

Disclaimer

Prohlašuji, že jsem tuto disertační práci vypracoval samostatně pod vedením vedoucího práce a na zařízení, které bylo realizováno z grantových prostředků Ústavu fyziky Fakulty strojní ČVUT v Praze a je majetkem ústavu. Při vypracování své doktorské práce jsem použil literaturu uvedenou v seznamu na konci této práce. Nemám závažný důvod proti užití tohoto školního díla ve smyslu § 60 zákona č. 121/2000 Sb., o právu autorském, o právech souvisejících s právem autorským a o změně některých zákonů (autorský zákon)

V Praze dne: ....

Martin Doubek

Abstract

This PhD thesis focuses on thermodynamics of pure refrigerants and refrigerants mixtures including mixtures of unlike fluids. The vapour-liquid equilibrium of these mixtures is studied along with speed of sound in both phases. The thesis consists of two parts: the first part is dedicated to design of a high accuracy speed of sound measurement apparatus which is used to obtain unique thermodynamic data. The second part deals with prediction models in form of equations of state. The research is driven by ongoing development of new refrigerant blends for commercial applications and by future needs of the cooling and monitoring systems for particle detectors at CERN.

The prediction of thermodynamic properties of fluid mixtures, especially mixtures of unlike fluids (natural refrigerants + fluorocarbons) is a challenging task. Currently only complex contribution methods can provide reasonable accuracy for new blends where no experimental data exists. This work presents newly developed correlations for prediction of binary interaction coefficient for SAFT-BACK model which has never been used for such mixtures. Three SAFT models are scrutinized in terms of prediction of vapour liquid equilibrium and speed of sound using extensive data sets for natural refrigerants, fluorocarbons and their mixtures. The combination of the SAFT-BACK model with developed correlations creates prediction model for new refrigerant blends that uses only few fitting parameters.

Abstrakt

Předkládaná doktorská práce je studií termodynamických vlastností čistých chladiv a směsí chladiv včetně směsí nestejnorodých látek. Podrobně je studována rovnováha kapalina-pára a rychlost zvuku v obou fázích těchto směsí. První část práce se zabývá návrhem zařízení pro velmi přesné měření rychlosti zvuku, které je použito pro získání unikátních termodynamických dat. Druhá část je věnována výpočtům rychlosti zvuku a rovnováhy kapalina-pára čistých látek i směsí pomocí stavových rovnic. Hlavní motivací pro tento výzkum je současný vývoj nových směsí chladiv v komerčním sektoru a potřeby chladicích a monitorovacích systémů částicových detektorů v CERN v Ženevě.

Výpočty vlastností směsí různorodých látek (přírodní chladiva + fluorovaná chladiva) jsou náročný úkol. Složité kontribuční modely jsou v současné době jedinou volbou pro přesné výpočty směsí, ke kterým neexistují experimentální data. V rámci předkládané práce jsou vyvinuty nové korelace pro odhad binárních interakčních koeficientů pro model SAFT-BACK, který pro podobné směsi ještě nikdy nebyl použit. Tři SAFT modely jsou důkladně testovány na experimentálních datech rovnováhy kapalina-pára a rychlosti zvuku v obou fázích přírodních chladiv, fluorovaných chladiv a jejich směsí. Výsledkem spojení modelu SAFT-BACK s nově vyvinutými korelacemi je predikční model pro výpočty nových směsí chladiv, který vyžaduje jen malý počet parametrů.

Acknowledgements

I wish to express my deepest gratitude to my family for all the support that made it possible for me to pursue the doctoral degree.

Contents

Nomenclature

Subscripts

a	Acoustic
c	Critical
LJ	Lennard Jones
m	Mixture
p	At constant pressure
RA	Rackett
r	Reduced
S	At constant entropy
T	At constant temperature
v	At constant volume

Superscripts

$'$	Liquid phase
$''$	Vapor phase
0	Ideal gas contribution or reference state
$calc$	Calculated
exp	Experimental
HC	Hard chain
id	Ideal
p	Perturbation term
r	Residual part
ref	Reference

Lower Case

$\overline{a}$	Cubic equation parameter	$[Pa.kmol^{-2}.m^6]$
a	Helmholtz energy	$[J]$
a_i	Einstein coefficient	$[K]$
$\overline{b}$	Cubic equation parameter	$[m^3.kmol^{-1}]$
$\overline{c}$	Volume shift	$[m^3.mol^{-1}]$
c	Molar heat capacity	$[J.mol^{-1}.K^{-1}]$

d	Segment diameter	$[m]$
f	Frequency	$[Hz]$
$\tilde{g}$	Imaginary part of resonance frequency	$[Hz]$
g	Radial distribution function	$[-]$
h	Thermal accomodation coefficient	$[-]$
k	Thermal conductivity (chapter 3)	$[W.m^{-2}.K^{-1}]$
k_B	Boltzmann constant	$[J.K^{-1}]$
k_{ij}	Pair interaction coefficient	$[-]$
l_a	Accomodation length	$[m]$
m	Average length of chains	$[-]$
n	Number of components in a mixture	$[-]$
p	Pressure	$[Pa]$
r	Radius	$[m]$
t	time	$[s]$
t_{time}	Ultrasound time of flight (chapter 4)	$[s]$
u	Pair potential energy	$[J]$
u_A	Uncertainity type A (chapter 4)	$[various]$
u_B	Uncertainity type B (chapter 4)	$[various]$
v	Molar volume	$[m^3.mol^{-1}]$
w	Speed of sound	$[m.s^{-1}]$
x	Mole fraction	$[1]$

Greek Letters

α	Dimensionless Helmholtz Energy	$[1]$
α	Helmholtz energy	$[1]$
$\overline{\alpha}$	Cubic equation alpha function	$[-]$
α_s	Attenuation (chapter 3)	$[1.m^{-1}]$
β	Adiabatic compressibility	$[1.Pa^{-1}]$
δ	Reduced density	$[1]$
ϵ	Interaction strength	$[J]$
ϵ^{AB}	Association energy parameter	$[Pa.m^3]$
η	Packing fraction	$[1]$
γ	Heat capacity ratio	$[1]$
κ	Scaling factor	$[-]$
κ^{AB}	Association volume	$[m^3.mol^{-1}]$

λ	Wave length	$[m]$
μ	Chemical potental	$[J/particle]$
μ	Dynamic viscosity	$[Pa.s]$
ν	Eigenvalue of resonance modes	$[-]$
$\hat{\omega}$	Complex angular frequency	$[Hz]$
ω	Accentric factor	$[-]$
ϕ	Attenuation coefficient (chapter 3)	$[-]$
ρ	Molar density	$[mol.m^{-3}]$
σ	Molecule diameter	[Å]
$\hat{\tau}$	Relaxation time	$[s]$
τ	Inverse reduced temperature	[1]
τ_{RC}	Time constant	$[s]$
φ	Energy loss coefficient (chapter 3)	$[-]$
φ	Fugacity	$[Pa]$
ζ	Dimensionless speed of sound	[1]
Upper Case		
B	Second virial coefficient	$[m^{-3}.mol^{-1}]$
C	Third virial coefficient	$[m^{-6}.mol^{-2}]$
D	Distance	$[m]$
D_p	Thickness	$[m]$
D_t	Thermal diffusivity	$[m^2.s^{-1}]$
I	Wave intensity (chapter 3)	$[W.m^{-2}]$
L	Length	$[m]$
M	Molar mass	$[kg.mol^{-1}]$
N	Frequency constants of piezo crystals (chapter 3)	$[Hz.m]$
N	Number of particles/molecules	$[-]$
Q	Charge	$[C]$
Q_f	Resonance quality factor	[1]
R	Reflection coefficient (chapter 3)	$[-]$
R	Universal gas constant	$[J.mol^{-1}.K^{-1}]$
S	Entropy	$[J.K^{-1}]$
T	Temperature	$[K]$
T_p	Transmission coefficient (chapter 3)	$[-]$
U	Expanded uncertainity (chapter 4)	$[various]$

U	Voltage	$[V]$
Z	Acustic impedance (chapter 3)	$[Pa.s.m^{-3}]$
Z	Compressibility factor	[1]

Publications

I am author or co-author of folllowing publications that present results described in this thesis and that can be found in the references:

1. M. Doubek and V. Vacek, Speed of Sound Data in Pure Refrigerants R-116 and R-218 and Their Mixtures: Experiment and Modeling, Journal of Chemical & Engineering Data, 2016, 61(12), pp. 4046-4056

2. M. Doubek, V. Vacek, G. Hallewell and B. Pearson, Speed-of-sound based sensors for environmental monitoring, IEEE SENSORS, Orlando FL, 2016, pp. 1-3

3. M. Doubek, M. Haubner, V. Vacek, M. Battistin, G. Hallewell, S. Katunin, D. Robinson, Measurement of heat transfer coefficient in two phase flows of radiation-resistant zeotropic C_2F_6/C_3F_8 blends, International Journal of Heat and Mass Transfer, 2017, 113, pp. 246-256

4. M. Alhroob, M. Battistin, S. Berry, ... M. Doubek et al., Custom ultrasonic instrumentation for flow measurement and real-time binary gas analysis in the CERN ATLAS experiment, Journal of Instrumentation, 2017, 12, C01091, ISSN 1748-0221

5. M. Alhroob, M. Battistin, S. Berry, ... M. Doubek et al., Custom real-time ultrasonic instrumentation for simultaneous mixture and flow analysis of binary gases in the CERN ATLAS experiment, Nuclear Instruments and Methods in Physics Research Section A: Accelerators, Spectrometers, Detectors and Associated Equipment, 2017, 845(11), pp. 273-277

6. M. Battistin, S. Berry, A. Bitadtze, ... M. Doubek et al., The thermosiphon cooling system of the atlas experiment at the cern large hadron collider. International Journal of Chemical Reactor Engineering, 2015, ISSN (Online) 1542-6580, ISSN (Print) 2194-5748

7. R. Bates, M. Battistin, S. Berry, ... M. Doubek et al., The cooling capabilities of C_2F_6 / C_3F_8 saturated fluorocarbon blends for the atlas silicon tracker. Journal of Instrumentation, 2015, 10(03), P03027

8. M. Alhroob, R. Bates M. Battistin, ... M. Doubek et al., Development of a custom on-line ultrasonic vapour analyser and flow meter for the atlas inner detector, with application to cherenkov and gaseous charged particle detectors, Journal of Instrumentation, 2015, 10(03):C03045

9. M. Doubek, M. Haubner, D: Houška et al. Experimental investigation and modelling of flow boiling heat transfer of C_3F_8/C_2F_6 blends, In: Proceedings of the 13th International Conference on Heat Transfer, Fluid Mechanics and Thermodynamics 2017. Pretoria: University of Pretoria, pp. 355-364.

10. M. Doubek and V. Vacek, Experimental study of refrigerants and their mixtures, Paper and Poster presentation, Proceedings of 13th International Conference on Properties and Phase Equilibria for Products and Process Design, 22–26 May 2016, Granja – Portugal.

11. M. Doubek and V. Vacek, Thermodynamic properties of fluorocarbons: Simulations and experiment. In proceedings of the 24th IIR International Congress of Refrigeration, number ID:340, 2015, Yokohama, Japan, ISBN : 9782362150128

1 Introduction

All refrigerants were pure fluids in the past (R-11, R-22, carbon dioxide) but blends have been slowly introduced along the way. Either to replace phased-out pure refrigerants that were no longer allowed due to their high environmental impact (high Global Warming Potential GWP or Ozone Depletion Potential ODP). Or to provide certain performance characteristics that could not be achieved with pure fluids. In either case, the composition of refrigerant blends is carefully formulated to meet complex requirements on evaporation and condensation temperatures, energy efficiency, miscibility with oils, low environmental impact and many others.

Modern refrigerant blends are often mixtures of very different components (natural refrigerant, hydrofluorocarbons HFCs, hydrofluoroolefins HFOs etc.) in order to provide desired properties, namely the low environmental impact. Modelling is always used before any experimental testing to formulate new blends or to study effect of changes in composition on behaviour and cooling performance. Unfortunately, modelling of such complex mixtures is a difficult task. Accurate models of the pure fluids coupled with appropriate mixing rules are required along with large and accurate experimental data sets that are needed for model fitting and model evaluations.

Apart from the fact that the speed of sound is needed to obtain the ideal gas heat capacity of the refrigerants and that it plays important role during the development of the thermodynamic models, it can be also used for fluid analysis. Relatively simple and inexpensive yet accurate instruments for speed of sound measurement coupled with appropriate model can be used for online monitoring of blend composition. Such blend analysis is useful in an experimental circuit during blend development and testing but it can be also employed to monitor blend composition during cooling plant operation since the composition can change in time due to leaks and/or wrong filling procedures.

1.1 Refrigerant blends

Zeotropic mixtures have different composition of vapour phase and liquid phase, Figure 1.1. The zeotropic behaviour is called fractionation in the refrigeration industry. It is most pronounced when components of highly different volatilities are combined in a blend. For simplicity, let's consider a binary zeotropic blend. The more volatile component, in other words the component with higher vapour pressure, will be prevalent in the gas phase at a vapour-liquid equilibrium. The vapour phase of the equilibrium state will have therefore different composition than the liquid. The difference in composition will be higher for components with highly different volatilities (vapour pressures) as is shown in the Figure 1.1 where the blend B components have a higher difference in vapour pressures.

The fractionation of zeotropic blends has following consequences for cooling system design:

- The fractionation precludes the zeotropic blends from use in systems where a pool boiling occurs, for instance in flooded evaporators or in suction line heat exchangers;
- The boiling temperature is higher at the input of the evaporator and lower at the evaporator exit. This effect is called evaporator glide, and it is caused by the different volatility and thus different rate of boiling of the blend constituents.

There are also consequences for cooling system operation:

- Only liquid phase of zeotropic fluid must be used to fill a cooling circuit. Either cylinders with a dip tube must be used or the cylinder must be positioned upside down during the filling. This was not the case in the past when only pure fluids were used as refrigerants and therefore mistakes can happen especially when inexperienced personnel are working on such systems;
- If the cooling system develops a vapour leak (for instance from the liquid receiver or suction accumulator, Figure 1.2) the composition of the blend can change in time affecting the performance and efficiency.

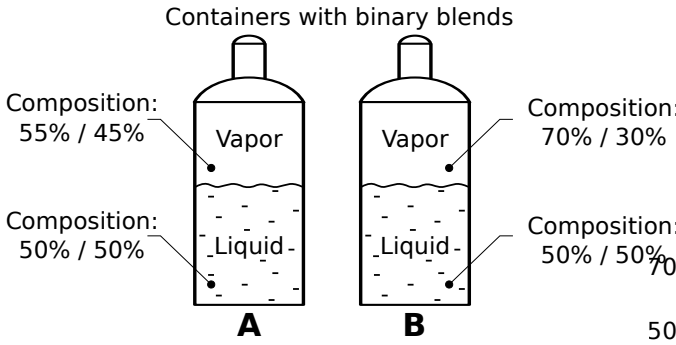

Figure 1.1: Illustration of fractionation of binary mixture

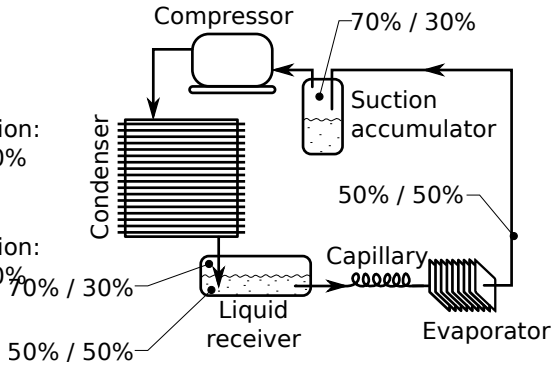

Figure 1.2: Illustration of fractionation in a two-phase cooling system

A typical example of strongly zeotropic mixtures are refrigerant blends designed to replace refrigerants with GWP above 2500 which will be banned by the F-gas Directive 517/2014 in commercial applications from year 2020. One of these fluids is the widely used nearly-azeotropic blend R-404a which is being replaced by more ecologic variants R-452a, R-448a or R-449a which are strongly zeotropic.

The R-404a is a nearly azeotropic blend of 52wt% R-143a, 44wt% R-125 and 4wt% R-134a. At equilibrium at 20°C the vapour composition is 51.6wt% R-143a, 45.8wt% R-125 and 2.6wt% R-134a which is very close to the liquid phase composition. Due to such small fractionation the R-404a can be charged in vapour state with only small change in R-134a concentration. The R-448a, for example, is a zeotropic blend of 26wt% R-32, 26wt% R-125, 21wt% R-134a, 7wt% R-1234ze and 20wt% R-1234yf. At equilibrium at 20°C the vapour phase composition is 35.0% R-32, 30.0% R-125, 13.5% R-134a, 0.04% R-1234ze and 17.3% R-1234yf. One can see that the new refrigerant is a complex mixture of different fluids with complicated behaviour.

One example of refrigerant blends currently under development is mixture of carbon dioxide (R-744) and small amount of ethane (R-170) or propane (R-290). An addition of natural refrigerant effectively lowers the evaporation temperature and the freezing point (carbon dioxide triple point is -56.6°C), [Nasruddin. & Alhamid, 2011] and [Alhamid *et al.*, 2013]. This would allow to use the blends for very low temperature refrigeration instead of flammable pure ethane or propane and to avoid extremely environmentally unfriendly R-23 which is still a common very low temperature refrigerant. Note that this binary blend is again a mixture of unlike fluids: inert carbon dioxide and hydrocarbon.

1.2 Importance of speed of sound in Thermodynamics

The speed of sound plays an important role in the thermodynamics, fluid mechanics and gas dynamics. It tells us how fast a mechanical perturbation propagates in a substance. The first recorded attempt to measure the speed of sound in air dates back to 1635 when Pierre Gassendi fired a cannon and recorded the time elapsed between the muzzle flash and the sound. His effort led to a number around 447 meters per second. In 1864 Henro Regnault, French scientist and photographer, carried out more scientific experiment where the human reaction time no longer played role. Henro used a recording device with a pen connected to a sound sensitive diaphragm, chronograph with rotating paper cylinder and electric trigger circuit. The result was speed of sound in air around 335 meters per second. In fact, Henro devised this experiment in his studies of specific heat (ratio of heat capacities) of gases and he eventually measured speed of sound in five other gases [Poncet & Dahlberg, 2011]. The speed of sound in water was measured in 1826 on Geneva Lake (Lac Léman) during the famous experiment where a bell suspended under water from a boat was struck with a hammer and a gunpowder was ignited at the same time providing a light signal for a second boat in a distance to start a stopwatch. When the bell sound was heard with an underwater hearing device on the second boat the elapsed time on stopwatch was noted down.

Isaac Newton derived equation for the speed of sound from a propagation of a pressure wave in his Principia. Unfortunately, he incorrectly assumed that sound propagation is a isothermic process. The compression and expansion of the air due to the propagating sound wave is too fast for any heat transfer to take place therefore it is adiabatic process. The speed of sound calculated by Newton differed from experiments by more than 20% [Ampel & Uzzle, 1993].

Valuable thermodynamic properties such as the ideal heat capacity can be derived from measurements of the speed of sound. In fact, the speed of sound measurements and molecular simulations are the only ways to obtain the ideal gas heat capacity of complex molecules. The ideal gas heat capacities of all refrigerants including nitrogen and carbon dioxide were obtained from speed of sound measurements.

Speed of sound data can be also used to obtain inter-molecular potential energy through virial equation of state. The acoustic virial equation is used to derive coefficients of classical virial equation and the ideal gas heat capacity ratio due to the fact that the speed of sound measurements can be carried out at extremely high accuracy (below 0.01%) unlike, for instance density or heat capacity measurements.

Since relatively complex manipulations are needed to obtain the speed of sound from equations of states the comparison of calculated speed of sound with precise measurements is often used as a benchmark in testing and development of new equations of state. Both heat capacities (c_p and c_v) and derivative of pressure ($\frac{\partial p}{\partial \rho}$) are needed in order to calculate the speed of sound which puts the equation of state to a tough test.

The experimental work in the field of speed of sound measurement is still very much alive and in the past 50 years new and highly precise methods have been developed and are widely used. It is the high accuracy and relative simplicity of speed of sound measurement that are driving the interest.

1.3 Uses of speed of sound in refrigeration

Analysis of fluid mixtures based on the speed of sound has a long history. In the 1913 the German chemist Fritz Haber invented a whistle that could be used to detect methane in mines [Stoltzenberg, 2004]. Lamps were used to detect presence of methane at that time since the lamp flame created a mild corona in presence of methane but this wasn't very safe detection method for obvious reasons. The Fritz's invention was taking advantage of the fact that the speed of sound is higher in methane than in air (343.3 vs $445.4\,m.s^{-1}$ at atmospheric pressure and $20°C$). Two whistles were first tuned with air to the same audible frequency so that when later a small amount of methane changed the pitch of one of the whistles, noticeable beats were

produced. Levels from 1% of methane in air were indicated [Wikipedia, 2015]. Unfortunately, the whistle wasn't robust enough to be used in the harsh environment of mines.

Obviously, the same principle could be used to detect other possible air contaminants. Some gasses have lower speed of sound than air, some higher (like the Methane or Helium) and some gases have only slightly different speed of sound in air and they are therefore very hard to detect (carbon monoxide for example). The speed of sound is tightly related with the molecular weight and density, very light or very heavy gases exhibit large differences in speed of sound when compared to air. Such differences allow for very sensitive detection. Figure 1.3 shows how some selected gases affects the speed of sound when mixed with air.

The same principle can be applied to liquids. The speed of sound in water solution has been studied extensively. For instance, the speed of sound in water-sucrose solution or water-methanol mixtures is shown in in Figure 1.4.

Many more advanced instruments have been developed for the determination of composition of binary mixtures since the "methane-whistle", the oldest known instruments were even using vacuum tubes. Nowadays, advanced speed of sound based analysers are commercially available both for gas and liquid phases.

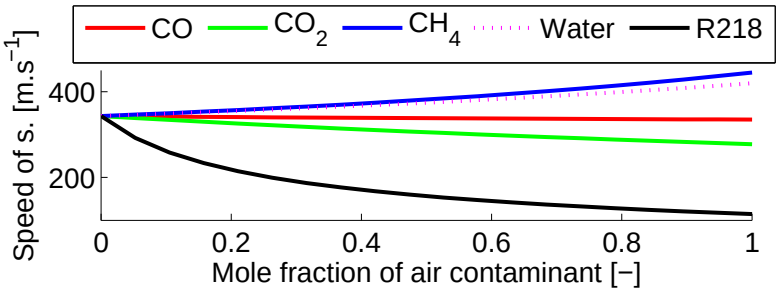

Figure 1.3: Illustration of impact of air contaminants on speed of sound

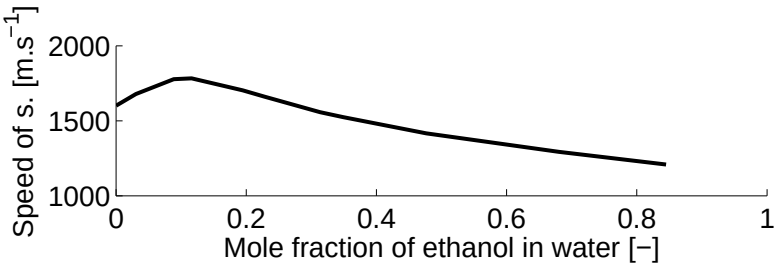

Figure 1.4: Speed of sound in water-methanol solution[Meister, 2015]

Possible uses for acoustic analysis in a typical refrigeration circuit are outlined in Figure 1.5. The speed of sound can be measured either in liquid or gas phase. The analyser number 1 in Figure 1.5 monitors the ambient air inside the cooling plant housing or in the room where the plant is installed to detect leak of a refrigerant from the system. The refrigerant sometimes leaks out of the system and sometimes air gets inside the system. This can happen during maintenance, through pneumatically controlled valves and pressure regulators that are driven by compressed air (dome loaded / piloted valves) or when the low pressure suction side of the system operates below atmospheric pressure. This is the case in various low temperature applications, for example with R-404a refrigerant and two stage reciprocal compressors. The air is then present in the cooling system as non-condensable gas that elevates the condenser pressure and reduces the system performance. These gases can be detected by the analyser number 2 at the top of the condenser. Some

portion of the air is dissolved in the refrigerant and it circulates with the refrigerant reducing the mass flow through capillaries or other throttling devices. The humidity that enters the system with the air can react with oil to form acid, fortunately this can be prevented by a filter-drier that can absorb water ingested in the system. The refrigerant blend composition monitoring can be provided by the analysers 3 and 4 that operates in liquid phase and vapour phase respectively. The number 3 can furthermore monitor the oil content in the refrigerant.

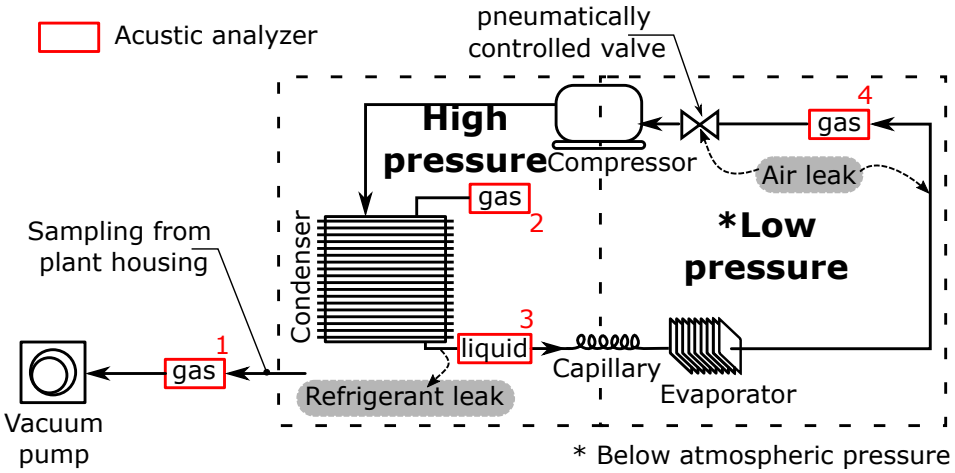

Figure 1.5: Internal and external leak detection

Any acoustic analyser can provide real time analysis of either liquid or gas phase if designed accordingly. Two main principles of speed-of-sound measurement can be employed: the resonance or time-of-flight method. In fact, the very common industrial ultrasonic flowmeters based on the ultrasound transition time measurement (time-of-flight technique) measure also the speed of sound. Unfortunately, unlike the value of the flow rate, the measured speed of sound is often unavailable to the user.

1.4 Refrigerant blends at CERN

The zeotropic mixtures of R-218 and R-116 are proposed as a replacement for pure R-218 that is currently in use as a refrigerant in the evaporative cooling of the inner detector that is part of the ATLAS experiment in the Large Hadron Collider at CERN [Bitadze, 2014]. The silicon particle detectors used in the ATLAS Inner Detector decay under the radiation exposure in the Large Hadron Collider. The gradual decay increases the electrical current passing through the detectors and consequently the dissipated heat. It turned out that the actual level of accumulated radiation damage is higher than what was originally predicted by models. Unfortunately, the damage will be increasing even faster when the Large Hadron Collider reaches higher luminosity[1]. Addition of certain amount of R-116 (up to 30%) into the currently used R-218 refrigerant would allow to keep the silicon particle detectors at lower temperatures almost without any modifications to the cooling plant. The lower temperature would provide increased safety margins from thermal runaways effectively extending the detectors lifespan.

[1]Collider luminosity is defined as the number of events detected (collisions) per area, see https://en.wikipedia.org/wiki/Luminosity_(scattering_theory)

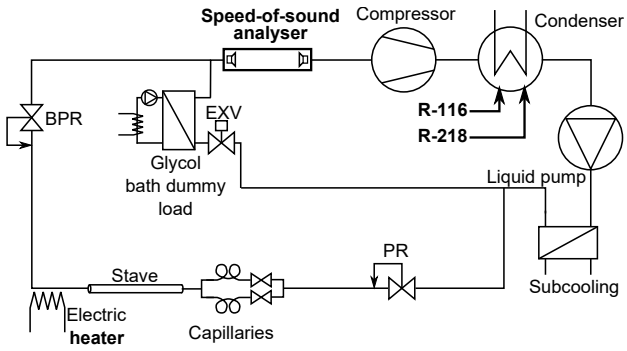

Figure 1.6: Experimental cooling plant for tests of refrigerant blends at CERN

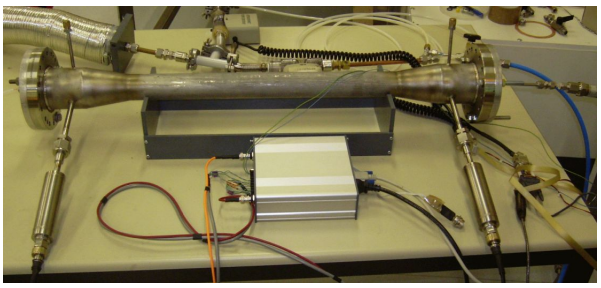

Figure 1.7: Testing and calibration of axial flowmeter/analyser

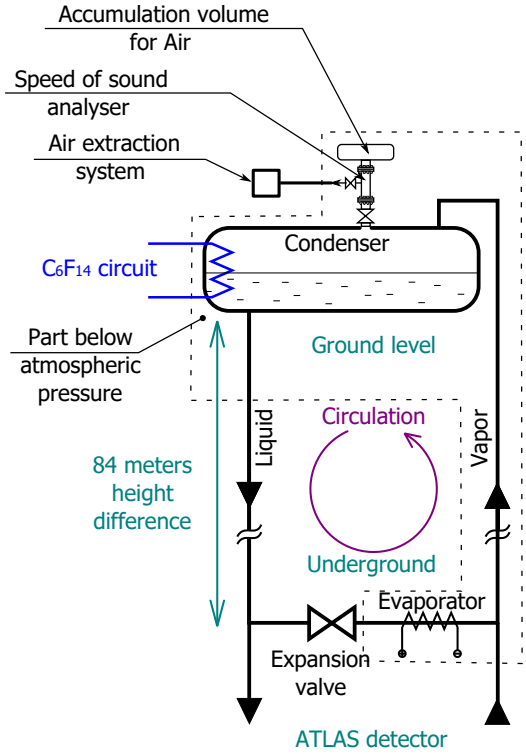

Figure 1.8: The Thermosiphon cooling circuit for ATLAS detector at CERN

The R-116+R-218 blends are strongly zeotropic and therefore thermodynamic models have to be used to predict the composition of the saturated phases and the glide (temperature change) during isobaric evaporation. A small experimental cooling plant (Figure 1.6) equipped with a speed-of-sound based gas analyser (Figure 1.7) was constructed as a proof-of-concept for the blends R-116+R-218. Various evaluations of the blends performance including the evaporator temperature profile and heat transfer measurements have been carried out. The online composition analysis provided by the speed-of-sound analyser proved to be invaluable help for the blend preparation and testing [Bitadze, 2014].

The new inner detector cooling system called Thermosiphon (Figure 1.8) was designed to accommodate either pure R-218 or the blends, [Battistin *et al.*, 2015]. The speed-of-sound based analysers are integral part of the system since they would be essential to control R-116+R-218 blend composition during operation and maintenance. Half of the Thermosiphon circuit will operate below the atmospheric pressure to allow for even lower evaporation temperature and therefore the air and humidity can contaminate the refrigerant and deteriorate the cooling performance or even cause damage. For this reason, an unique purging system based on the speed of sound analyser was designed to detect and purge the air from the Thermosiphon condenser, Figures 1.9 and 1.10. The air is lighter than the refrigerant and it will accumulate on the top of the condenser. As the air displaces the R-218 in the provided accumulation volume, the speed of sound changes and when a threshold is reached the volume is released.

It turned out that the Thermosiphon condenser had a leak between the primary and secondary circuit just before the first test of the Thermosiphon with ATLAS detector in 2017[2]. Traces of the C_6F_{14} fluid from

[2]Meeting at CERN Wednesday 11 Jan 2017, 15:00 → 18:15 https://indico.cern.ch/event/595943

the secondary circuit were found in the primary R-218 circuit during a routine gas chromatography test. The contamination was low (0.04%) and the concentration was not increasing but there was a concern that the leak could suddenly increase and contaminate the primary circuit during the test with ATLAS detector. The first challenge was to predict the behaviour of the R-218+C_6F_{14} zeotropic blend in such case as no experimental data existed for such mixture. Unfortunately, the NIST REFPROP, which is the first choice for prediction of thermodynamic behaviour of refrigerant blends, is not capable of working with such mixture. A speed-of-sound based analyser was installed at the R-218 outlet of the condenser in order to detect increasing C_6F_{14} concentration and to provide early warning if the leak increased. A small amount of the fluid at the condenser outlet was evaporated and the vapour passed through the analyser before it was recondensed in the condenser. The prediction of the saturation properties of the R-218+C_6F_{14} and the speed of sound for the analyser were generated using the models and interaction coefficient correlation developed in this thesis[3].

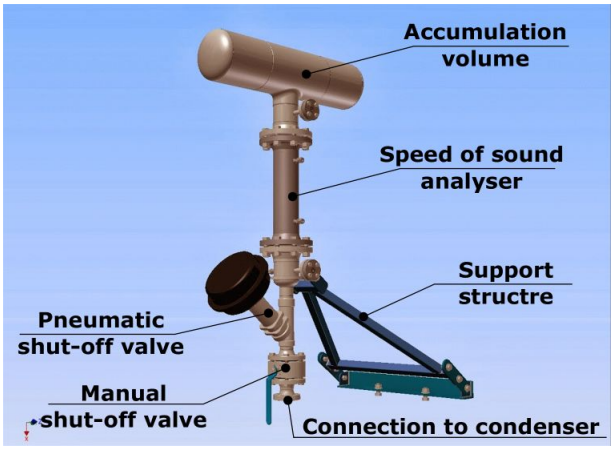

Figure 1.9: Degassing system for the Thermosiphon condenser

Figure 1.10: Photo of degassing system installed on the Thermosiphon condenser

1.5 Motivation

Refrigerant blends are formulated to mimic the thermodynamic behaviour of the phased-out fluids as close as possible or to provide even better performance. Up to six components are sometimes blended to achieve the desired properties. The modern blend components are often very different fluids and the resulting thermodynamic behaviour is quite complex. The demand for reliable thermodynamic models, that can be used for these complex blends, is high. Unfortunately, modelling properties of such mixtures is a challenging task.

The thermodynamic models in form of equations of state are often evaluated by accuracy of the speed of sound prediction. Since the calculation of the speed of sound requires partial derivatives of the equation of

[3]The matter was discussed at meetings at CERN, more information on CERN Indico pages: https://indico.cern.ch/event/588196/ and https://indico.cern.ch/event/595943

state it is a thorough test. A speed-of-sound based fluid analysis carried out with a precise instrument together with accurate prediction model can provide real-time blend composition analysis for the development and tailoring of new blends and also for operation and maintenance of cooling systems utilizing such blends.

I was a member of a group developing cooling systems for particle physics and we needed to predict properties of various mixtures of fluorocarbon refrigerants while there was no dedicated model or software tool available. For instance, when I was working on Thermosiphon cooling system at CERN ([4]) we discovered that the condenser used in the primary circuit had an internal leak and the fluid from the secondary circuit (C_6F_{14}) was contaminating the primary circuit (R-218). It was decided that the most effective way of monitoring the fluid contamination in real time was a speed-of-sound based analyser. I was facing a problem of how to predict the saturation properties (saturated pressure and composition of phases in the condenser) and the speed of sound in R-218+C_6F_{14}. The interaction coefficients for this mixture were not available and the accuracy of the speed of sound prediction was thus unknown. Similar problem arose when we were trying to detect the contamination of the primary R-218 by nitrogen (or air). Even the most common and extremely universal tool for calculations of thermodynamic properties of refrigerants, the REFPROP developed by NIST [Lemmon *et al.*, 2018], cannot predict mixtures of R-218+C_6F_{14} or R-218+nitrogen since it uses two very different equations for these two particular fluids.

The prediction of properties of R-116+R-218 blends is another example where no experimental data or proven mixture model are available. These blends are being developed as replacements for pure R-218, no vapour-liquid equilibrium or speed of sound data were available for these blends and therefore the prediction was done with estimated interaction coefficients. Although the accurate Short fundamental equation of state developed by Lemmon and Spann [Lemmon & Span, 2006] implemented in NIST REFPROP can be used for the pure fluids, the interaction coefficient are only estimated.

[4] https://edms.cern.ch/ui/file/1083852/1/Technical_Note_60kW_Thermosiphon.pdf ;
https://cds.cern.ch/journal/CERNBulletin/2013/48/News%20Articles/1629875

Bibliography

chapter 1: Introduction

[Alhamid *et al.*, 2013] Alhamid, M. I., Nasruddin, D. R. B. S., & Lubis, A. 2013. Characteristics and COP Cascade Refrigeration System using Hydrocarbon Refrigerant (Propane, Ethane and CO2) at Low Temperature Circuit (TC). *Internation Journal of Technology*, **4**(2).

[Ampel & Uzzle, 1993] Ampel, F. J., & Uzzle, T. 1993 (March). The History of Audio and Sound Measurement. *In: Audio Engineering Society Convention 94*, vol. 3598 (L1-L).

[Battistin *et al.*, 2015] Battistin, M., Berry, S., Bitadze, A., Bonneau, P., Botelho-Direito, J., Boyd, G., Corbaz, F., Crespo-Lopez, O., Riva, E. Da, Degeorge, C., Deterre, C., DiGirolamo, B., Doubek, M., Favre, G., Godlewski, J., Hallewell, G., Katunin, S., Lefils, D., Lombard, D., McMahon, S., Nagai, K., Robinson, D., Rossi, C., Rozanov, A., Vacek, V., & Zwalinski, L. 2015. The Thermosiphon Cooling System of the ATLAS Experiment at the CERN Large Hadron Collider. *International Journal of Chemical Reactor Engineering*, **13**(4), 511–521.

[Bitadze, 2014] Bitadze, A. 2014. *Thermo-dynamical measurements for ATLAS Inner Detector (evaporative cooling system)*. Ph.D. thesis, University of Glasgow.

[Lemmon *et al.*, 2018] Lemmon, E. W., Bell, I. H., Huber, M. L., & McLinden, M. O. 2018. *NIST Standard Reference Database 23: Reference Fluid Thermodynamic and Transport Properties-REFPROP, Version 10.0, National Institute of Standards and Technology*.

[Lemmon & Span, 2006] Lemmon, E.W., & Span, R. 2006. Short Fundamental Equations of State for 20 Industrial Fluids. *Journal of Chemical & Engineering Data*, **51**(3), 785–850.

[Meister, 2015] Meister, E. C. 2015. Measurement of the Temperature and Concentration Dependent Sound Velocity in Ethanol-Water Liquid Mixtures. *Physikalisch-chemisches Praktikum ETH Zurich*.

[Nasruddin. & Alhamid, 2011] Nasruddin., D. R. B. S., & Alhamid, M. I. 2011. A Cascade Refrigeration System Using Mixture of Carbon Dioxide and Hydrocarbons for Low Temperature Applications. *Journal of Engineering and Applied Sciences*, **6**(6), 379–386.

[Poncet & Dahlberg, 2011] Poncet, S., & Dahlberg, L. 2011. The legacy of Henri Victor Regnault in the arts and sciences. *International Journal of Arts and Sciences*, **4 (13)**. pp.377-400. <hal-00678894>.

[Stoltzenberg, 2004] Stoltzenberg, D. 2004. *Fritz Haber: Chemist, Nobel Laureate, German, Jew*. Chemical Heritage Press.

[Wikipedia, 2015] Wikipedia. 2015. *Firedamp whistle — Wikipedia, The Free Encyclopedia*. [Online; accessed 3-October-2015].

2 Prior art

2.1 Thermodynamic models

2.1.1 Introduction

Primary interest of this work is in models of vapour-liquid equilibrium and the speed of sound that require only few fluid-specific parameters and that can be applied to refrigerants and their blends including mixtures of unlike fluids. In addition, the models must work well in both vapour and liquid phases. Models developed specifically for a homogeneous family of fluids, hydrocarbons for example, exhibit large deviations when used to model the behaviour of other types of fluids (e.g. fluorinated refrigerants).

The selection criteria for appropriate models were following:

- The models must predict the vapour-liquid equilibrium of mixtures i.e. saturated pressure and composition of phases of zeotropic mixtures at given temperature.
- The models must be able to predict the speed of sound in mixtures consisting of more than two components. The models must be usable for both phases and also for saturation.
- It should be relatively simple to obtain the fitting parameters for the model, the model should be flexible, i.e. it should be easily applicable to new fluids and mixtures.

2.1.2 Speed of sound

The small signal (linear) theory yields following equation for propagation of a sound wave:

$$w^2 = \left(\frac{\partial p}{\partial \rho}\right)_S \quad . \tag{2.1}$$

In other words the square of the speed of sound w is equal to the partial derivative of pressure p with respect to the density ρ at constant entropy S . The constant entropy signifies that the sound propagation is adiabatic process. In ideal case, the sound propagation is accompanied by small changes in temperature (due to compression and expansion of the gas) but no heat exchange takes place since those changes are too fast. The equation can be transformed from adiabatic to isothermic using thermodynamic manipulations:

$$w^2 = \frac{c_p}{c_v}\left(\frac{\partial p}{\partial \rho}\right)_T \quad . \tag{2.2}$$

The partial derivative of pressure with respect to the density at constant temperature is easier to work with than the derivative in previous equation. It is apparent that the speed of sound depends on the heat capacities c_p and c_v or to be more precise on the ratio of the heat capacities.

The simplest approach is to assume the ideal gas with constant heat capacities which are not function of temperature c_p^{id0}, c_v^{id0}. Using ideal gas equation in the following form $pM = \rho RT$, one can write:

$$w^2 = \frac{c_p^{id0}}{c_v^{id0}} \frac{RT}{M} \quad . \tag{2.3}$$

This is a well-known equation for the speed of sound in the ideal gas. The c_p^{id0} and c_v^{id0} are related through Mayer's relation $c_p^{id0} - c_v^{id0} = R$ and the c_p^{id0} depends on the number of atoms in the gas molecule. The number of atoms dictates the rotational and translational degrees of freedom of a molecule and the ideal gas heat capacities are $c_v^{id0} = \frac{2}{3}R,\ \frac{3}{2}R\, or\, 3R$ for monoatomic, diatomic or polyatomic gas respectively.

The real heat capacities are, however, functions of the temperature due to the contribution of vibrational degrees of freedom. The statistical theory yields equation for the ideal gas heat capacity $c_p^{id} = f_{(T)}$:

$$\frac{c_p^{id}}{R} = c_p^{rot} + c_p^{trans} + c_p^{vib} = 4 + \sum_{i=1}^{3*\xi-3-n^{rot}} b_i \left(\frac{a_i}{T}\right)^2 \frac{exp\left(\frac{a_i}{T}\right)}{\left[exp\left(\frac{a_i}{T}\right)-1\right]^2} \quad , \tag{2.4}$$

where c_p^{rot}, c_p^{trans}, c_p^{vib} are the contributions of rotational, translational and vibrational motions of the molecule to the heat capacity, ξ is the number of atoms in a molecule and n^{rot} is the number of rotational degrees of freedom of the molecule. The term in the summation is also called Einstein equation and the coefficients $a_i[K]$ are called vibrational temperatures.

2.1.3 Equations of state

Classical equations of state model the relation between intensive properties: pressure p, molar volume v or density ρ and temperature T. The pressure explicit equations of state are usually in a form of:

- Power series in v
- Cubic equation
- Empirical form

The power series, for example virial equation of state, do not usually model the vapour-liquid transition. The cubic equations of state are very popular for their simplicity and accuracy in pressure calculations adequate for engineering purposes although they exhibit significant deviation in liquid density calculations. Empirical equations can provide high accuracy but they require large number of fluid-specific parameters that must be fitted to extensive experimental datasets.

Modern equations of state are in so called Helmholtz energy form. The dimensionless Helmholtz energy a is expressed as function of temperature T and number density ρ. The pressure p, heat capacities c_p, c_v and finally the speed of sound w can be then expressed through partial derivatives of Helmholtz energy as shown in Equations 2.5 to 2.8:

$$p_{(T,\rho)} = \rho^2 \left(\frac{\partial a}{\partial \rho}\right)_T \quad , \tag{2.5}$$

$$w = \sqrt{\frac{c_p}{c_v}\left(\frac{\partial p}{\partial \rho}\right)_T} \quad , \tag{2.6}$$

$$c_v^{res} = -R\left(2T\left(\frac{\partial a^{id}}{\partial T}\right)_\rho + T^2\left(\frac{\partial^2 a^r}{\partial T^2}\right)_\rho\right) \quad , \tag{2.7}$$

$$c_p = c_v + R\frac{\left(1+\rho\left(\frac{\partial a^r}{\partial \rho}\right)_T + \rho T\left(\frac{\partial^2 a^r}{\partial T \partial \rho}\right)\right)^2}{1+2\rho\left(\frac{\partial a^r}{\partial \rho}\right)_T + \rho^2\left(\frac{\partial^2 a^r}{\partial \rho^2}\right)_T} \quad . \tag{2.8}$$

The compressibility factor Z can be also obtained from Helmholtz energy:

$$Z = \frac{p}{\rho R T} = 1 + \rho\left(\frac{\partial a^r}{\partial \rho}\right)_T \quad . \tag{2.9}$$

2.1.4 Empirical equations of state

Typical example of an empirical equation of state is the BWR (Benedict–Webb–Rubin) and mBWR (modified Benedict–Webb–Rubin) equation. The BWR equation of state uses eight fitting parameters while the modified version employs up to 32 fitting parameters. Empirical equations with that many parameters were often used in past as reference equations of state for pure fluids (often for refrigerants: [Younglove & McLinden, 1994, Li *et al.*, 1999] and many others). Elaborate fitting techniques were used to obtain optimal values of the equation parameters. The resulting reference equation provide very good accuracy over wide range of temperature and pressures for the given pure compound, the equation can represent experimental data with deviation well below 1%. The Table 2.1 summarizes the accuracy of mBWR equation of state for several compounds. Note, that the saturated pressure is often represented by an ancillary equation and not by the mBWR equation of state therefore the accuracy is not shown for some of the fluids in the table.

Table 2.1: Average deviation of mBWR equation from experimental data

Fluid	Source	p_{sat}	ρ_{sat} liquid	ρ_{sat} vapour	SoS liquid	SoS vapour
		[%]	[%]	[%]	[%]	[%]
R-123	[Younglove & McLinden, 1994]	0.06	0.04	0.18	1.1	0.004
R-134a	[Huber & McLinden, 1992]	1.5	0.2	0.2		0.2-0.6
R-152a	[Outcalt & McLinden, 1996]	0.043	0.004	0.62		0.07
R-11	[Defibaugh & Moldover, 1997]		0.2			
R-22	[Defibaugh & Moldover, 1997]		0.1			
R-134a	[Defibaugh & Moldover, 1997]		0.05			
R-141b	[Defibaugh & Moldover, 1997]		0.05			
R-143a	[Defibaugh & Moldover, 1997]		0.05			
R-152a	[Defibaugh & Moldover, 1997]		0.25			
R-218	[Defibaugh & Moldover, 1997]		0.05			
R-32	[Defibaugh *et al.*, 1994]		0.02			
R-50	[Younglove & Ely, 1987]		0.2	0.3	2	0.5
R-170	[Younglove & Ely, 1987]		0.5	0.2	0.6	0.6
R-290	[Younglove & Ely, 1987]		0.1	0.04	0.5	1
R-600a	[Younglove & Ely, 1987]		0.007	0.007	0.5	1
R-600	[Younglove & Ely, 1987]		0.05	0.4	1	2

2.1.5 Virial equations of state

The acoustic virial equations of state, Equation 2.10, can be used to predict the speed of sound with high accuracy. Unfortunately, this equation of state does not model the phase change and it is therefore usable only for gases. Even though this is a major drawback, the virial equation is widely used to correlate experimental speed of sound data and to derive the ideal gas (zero-density) heat capacity ratio $\gamma^{id} = c_p/c_v$, Equation 2.11. Thanks to this, the acoustic virial coefficients are available for wide range of fluids in wide temperature ranges. Only the second B_a and third C_a virial coefficients are used to correlate the data since the higher coefficients would be obtained with large uncertainty and their contributions are negligible. The virial coefficients are functions of temperature, see the second and third nitrogen virial coefficient plotted in Fig. 2.1. It should be mentioned that apart from molecular simulations this is the only way of obtaining precise values of the ideal gas heat capacity which is absolutely essential for most of thermodynamic calculations. Relatively large amount of speed of sound data is needed to obtain the virial coefficients and the ideal gas heat capacity. The data set has to contain data points on isotherms in order to be able to employ a fitting algorithm to obtain the values of $B_{a(T)}$, $C_{a(T)}$, and $\gamma^{id}_{(T)}$ as functions of temperature.

$$w^2 = \gamma^{id}_{(T)} \frac{RT}{M} \left(1 + B_{a(T)}\rho + C_{a(T)}\rho^2 \ ...\right) \tag{2.10}$$

$$\gamma^{id}_{(T)} = \frac{1}{1 - R/c^{id}_{p(T)}} \tag{2.11}$$

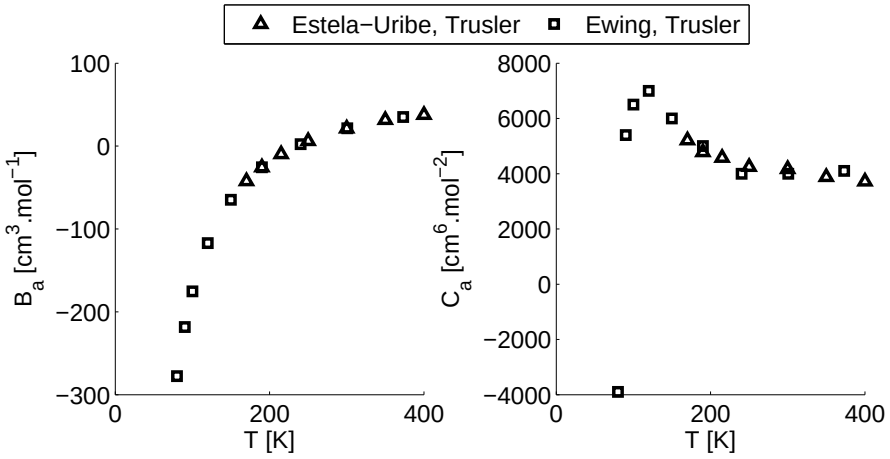

Figure 2.1: Acoustic virial coefficients of nitrogen [Estela-Uribe & Trusler, 2000, Ewing & Trusler, 1992]

The coefficients of the acoustic form of the virial equation of state are related to the coefficients of the classical density form, Equation 2.12.

$$p = \frac{RT}{v} \left(1 + B_{(T)}\rho + C_{(T)}\rho + ...\right) \tag{2.12}$$

The acoustic virial coefficients can be obtained from the classical ones through derivation with respect to temperature as is shown for the second acoustic virial coefficient B_a in Equation 2.13.

$$\frac{1}{2}B_a = B + P_a T\left(\frac{dB}{dT}\right) + Q_a T^2\left(\frac{d^2B}{dT^2}\right) \tag{2.13}$$

where:

$$P_a = (\gamma^{id} - 1) \ , \tag{2.14}$$

$$Q_a = \frac{\left(\gamma^{id} - 1\right)^2}{2}\gamma^{ig} \ . \tag{2.15}$$

It should be mentioned that unlike other equations of state, the virial equation can be directly derived from statistical mechanics. The second, third, fourth, etc. virial coefficients represent the contributions of two-body, three-body, etc. interactions. However, the virial expansion is usually truncated after the second or third coefficient even in the classical density form.

It is possible to use combination rules in order to obtain virial coefficients for mixture. The combination rules that can be employed are following:

$$M = \sum_{i=1}^{n} x_i M_i \ , \tag{2.16}$$

$$\frac{c_p^0}{R} = \sum_{i=1}^{n} x_i \frac{c_{pi}^0}{R} \ , \tag{2.17}$$

$$B = \sum_{i=1}^{n}\sum_{j=1}^{n} x_i x_j B_{ij} \ , \tag{2.18}$$

$$C = \sum_{i=1}^{n}\sum_{j=1}^{n}\sum_{k=1}^{n} x_i x_j x_k C_{ijk} \ , \tag{2.19}$$

where B_{ii} and C_{iii} are virial coefficients of the pure component i and the B_{ij} and C_{ijk} ($i \neq j \neq k$) are the cross coefficients. These coefficients are fluid specific, i.e. the coefficient is unique function of temperature for each pair of fluids i and j. Only few of these coefficients are available in literature and they cannot be omitted when reasonable accuracy is required. This is a significant limitation which renders the acoustic virial equation of state impractical for prediction of the speed of sound in various gas mixtures.

2.1.6 Cubic equations

Cubic equations are based on the Van der Wallse equation of state published in 1873 and they are widely used due to their simplicity and good performance. There is a vast list of various cubic equations of state with multitude of modifications. The cubic equations of state provide good accuracy (often better than 1%)

in terms of saturated pressure and vapour phase density but they fall short in predicting the PVT properties near critical region and the liquid density. The cubic equations usually underpredict the liquid density by approximately 10% but this deviation can reach up to 20% in some cases. Consequently, the prediction accuracy of the speed of sound in those regions is also poor. Generally, cubic equation of state can be written in following form:

$$p = \frac{RT}{v - \bar{b}} - \frac{\overline{a}}{v(v - \bar{b}) + \overline{c}(v - \overline{d})} \ , \tag{2.20}$$

where p is pressure, T is temperature, v is molar volume and R is the universal gas constant. The parameters $\bar{a}$, $\bar{b}$ and $\bar{c}$ can be fitted to vapour pressure data or they can be obtained from critical constraint by setting $\frac{\partial p}{\partial v} = \frac{\partial^2 p}{\partial v^2} = 0$. Unfortunately, the ability of the cubic equations to predict the liquid density cannot be improved by adjusting the values of the parameters since an improvement in the density prediction leads to poor performance in the critical region [Twu *et al.*, 2002].

Redlich and Kwong [Redlich & Kwong, 1949] modified the Van der Waalse equation (1949) of state into a following form:

$$p = \frac{RT}{v - \bar{b}} - \frac{\overline{a}}{\sqrt{T}} \frac{1}{v(v - \bar{b})} \ . \tag{2.21}$$

The modification introduced temperature dependence of the parameter $\overline{a}$. Subsequent cubic equations of state brought more and more complicated functions for the parameter $\overline{a}$, so called $alpha\ functions$.

Another notable successful cubic equation of state was proposed by [Soave, 1972]. The temperature-dependent parameter $\bar{a}$ can be expressed as alpha function multiplied by the value of the $\bar{a}$ at the critical point:

$$\overline{a} = \overline{\alpha}\overline{a}_c \ . \tag{2.22}$$

The Soave alpha function has following form:

$$\overline{\alpha} = \left(1 + m\left(1 - \sqrt{T_r}\right)\right)^2 \ . \tag{2.23}$$

The T_r is the reduced temperature and m is a coefficient fitted to vapour-pressures of light hydrocarbons:

$$m = 0.480 + 1.57\omega - 0.176\omega^2, \tag{2.24}$$

where ω is the acentric factor.

Another widely-used cubic equation of state is the Peng-Robinson (1976) equation, for details and background on this equation of state see the recent publication dealing with cubic equations [Lopez-Echeverry *et al.*, 2017]. It was originally developed for petrochemical industry but it is nowadays often used also for refrigerants. The pressure form of the Peng-Robinson equation of state is following:

$$p = \frac{RT}{v - b} - \frac{\overline{a}_{(T)}}{v(v + \bar{b}) + \overline{c}(v - \bar{b})} \ , \tag{2.25}$$

where

$$\overline{\alpha} = \left(1 + m\left(1 - \sqrt{T_r}\right)\right)^2 \ , \tag{2.26}$$

$$m = 0.37464 + 1.54226\omega - 0.26992\omega^2 \ . \tag{2.27}$$

The $\bar{a}$ and $\bar{b}$ can be obtained from the critical constrains:

$$\overline{a} = \frac{0.45724 R^2 T_c^2}{p_c} \ , \tag{2.28}$$

$$\overline{b} = \frac{0.07780 R T_c}{p_c} \ . \tag{2.29}$$

Comparison of the Redlich-Kwong, Soave and Peng-Robinson alpha functions can be found in Figure 2.2. Many more complicated empirical alpha functions with additional fitting parameters are available in literature. These complex functions are designed to better represent the saturated pressures of various fluids, they can use multiple parameters which are fitted directly to the vapour pressure data of the fluid.

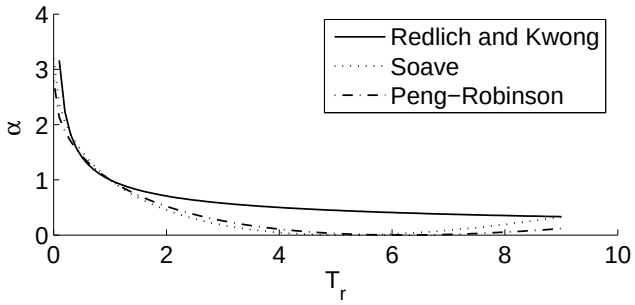

Figure 2.2: Comparison of the alpha functions

Other modifications include Patel-Teja (1982) cubic equation of state, Equation 2.30. The Patel-Teja model includes an additional parameter $\overline{c}$, Equation 2.31. This parameter is obtained from so called apparent critical compressibility factor ξ_c in Equation 2.32 (it is not equal to the true compressibility factor). Its value was empirically correlated to acentric factor in order to improve liquid volumes accuracy, Equation 2.33.

$$p = \frac{RT}{V - \overline{b}} - \frac{\overline{a}}{V^2 + \left(\overline{b} + \overline{c}\right) V - \overline{b}\overline{c}} \tag{2.30}$$

$$\overline{c} = \Omega_c \left(\frac{RT_c}{P_c}\right) \tag{2.31}$$

$$\Omega_c = 1 - 3\xi_c \tag{2.32}$$

$$\xi_c = 0.329032 - 0.0767992\omega + 0.0211947\omega^2 \tag{2.33}$$

Accuracy of various cubic equations of state are summarized in Table 2.2 in the next section.

2.1.7 Volume-translated cubic equation of state

The volume translation has been proposed in order to improve the accuracy of the cubic equation in predicting the saturated liquid phase density. The translation is in fact a correction factor $\bar{c}$ that shifts the predicted volumes [Péneloux *et al.*, 1982]. Volume-translated Peng-Robinson equation of state has following form:

$$p = \frac{RT}{v + \bar{c} - \bar{b}} - \frac{\bar{a}_{(T)}}{(v + \bar{c})(v + \bar{c} + \bar{b}) + \bar{c}(v + \bar{c} - \bar{b})} \ . \tag{2.34}$$

The volume shift does not impact the saturated pressure and the impact on the saturated vapour density is negligible since the correction is small when compared with the vapour phase volume. The simplest correction factor is temperature-independent and it is equal to the difference between the calculated v^{calc} and experimental v^{exp} molar volume at reduced temperature T_r of 0.7:

$$\bar{c} = v^{calc} - v^{exp}|_{Tr=0.7} \ . \tag{2.35}$$

The constant translation for hydrocarbons was correlated to the Rackett compressibility factor Z_{RA} by Peneloux [Péneloux *et al.*, 1982] in following way:

$$\bar{c} = 0.40768(0.29441 - Z_{RA}) \ . \tag{2.36}$$

Peneloux demonstrated that the correction results in average deviation of 5% between the predicted saturated liquid densities and the experimental values for hydrocarbons. Although this volume translation gives good results for reduced temperature below 0.6, it fails for temperatures close to the critical point. Many more sophisticated functions for the volume translation have been proposed since the first work by Peneloux. These corrections are often function of reduced temperature or some arbitrary distance from critical point. The most common approaches can be split into two groups:

- Correlations with fluid-specific fitting parameters, that have to be obtained by fitting techniques for each fluid. For example [Tsai & Y, 1998].
- Volume translations that employ correlations fitted over extensive set of fluids where the fluid properties such as the molecular weight, critical pressure, temperature and acentric factor are used as parameters. For example [Hemptinne & Ungerer, 1995].

Unfortunately, some of the volume translations cause nonphysical behaviour like prediction of negative heat capacities or crossing of isotherms but only few publications address this issue. I will focus on the second category from the short list above, since this approach eliminates the need for fluid-specific parameters.

The translation functions are often designed so that the shift is defined by the difference between the predicted critical volume v_c^{calc} and experimental critical volume v_c^{exp}:

$$\bar{c}_c = v_c^{calc} - v_c^{exp} \ . \tag{2.37}$$

A Gaussian-like temperature-dependent function $f_{(T_c)}$ is then used to obtain the translation function $\bar{c}$:

$$\bar{c} = f_{(T_c)} \cdot \bar{c}_c \ . \tag{2.38}$$

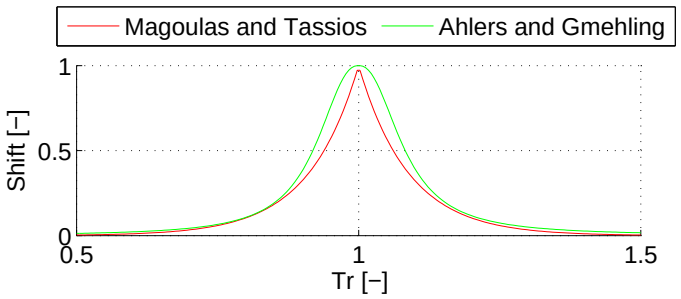

Figure 2.3: Gaussian volume translations according to [Magoulas & Tassios, 1990] and [Ahlers & Gmehling, 2001]

The function $f_{(T_c)}$ has maximum equal to one at critical temperature $T_r = 1$. The correction is therefore small far from critical point but equal to the critical volume shift $\bar{c}_c$ at the critical point. Two examples of the $f - function$ from different translation correlation are showed in Figure 2.3. Other $f - functions$ have been also evaluated (parabolic, exponential) but they have not gained that much popularity.

Table 2.2: Average deviation of cubic equations from experimental data; EoS stands for equation of state, SoS stands for Speed of Sound; Subscript sat stands for saturated

Fluid	Source	EoS*	p_{sat}	ρ_{sat} liquid	ρ_{sat} vapour	SoS liquid	SoS vapour
			[%]	[%]	[%]	[%]	[%]
R-1234yf	[Coquelet *et al.*, 2016]	PT	0.5	4.3	0.9		
R-744	[Coquelet *et al.*, 2016]	PT	3.0	4.4	3.9		
R-134a	[Coquelet *et al.*, 2016]	PT	3.6	3.3	4.6		
R-1234yf	[Coquelet *et al.*, 2016]	PR	0.9	3.9	0.8		
R-744	[Coquelet *et al.*, 2016]	PR	1.4	4.3	2.1		
R-134a	[Coquelet *et al.*, 2016]	PR	1.7	4.6	1.0		
R-50	[Salimi & Bahramian, 2014]	PR				average 28.6	
R-170	[Salimi & Bahramian, 2014]	PR				average 14.7	
R-290	[Salimi & Bahramian, 2014]	PR				average 61.2	
R-744	[Dias, 2005]	PR	0.46	2.97			
R-14	[Dias, 2005]	PR	1.32	9.5			
R-116	[Dias, 2005]	PR	0.31	6.11			
R-218	[Dias, 2005]	PR	1.68	7.81			
C_4F_{10}	[Dias, 2005]	PR	2.05	6.13			
R-290	[Ye *et al.*, 1992]	RK				23.9	
R-600	[Ye *et al.*, 1992]	RK				17.6	
R-290	[Ye *et al.*, 1992]	PR				14.9	
R-600	[Ye *et al.*, 1992]	PR				10.8	
R-290	[Tsai & Y, 1998]	VTPR	0.84	1.05			
R-600	[Tsai & Y, 1998]	VTPR	0.83	0.55			
R-600a	[Tsai & Y, 1998]	VTPR	1.07	0.47			

*PR - Peng Robinson, PT - Patel Teja, RK - Redlich and Kwong, VTPR - Volume Translated Peng Robinson

One has to be careful when using the volume-translated cubic equations of state. The volume shifts are

often designed to improve the prediction of the saturated density but the equations of state have not been tested in the one-phase regions where some nonphysical behaviour can be encountered. It is usually not recommended to use the volume translated cubic equations above the critical point or in the dense fluid region. Three selected correlation for the volume translation are discussed in section 6.2. Accuracy of volume-translated cubic equations of state together with other types of cubic equations are summarized in Table 2.2.

2.1.8 Helmholtz-energy equations of state

Modern equations of state are formulated in Helmholtz energy form as explicit functions of temperature and density. Such equations are replacing the mBWR equation of state as the reference high-accuracy equation of state for pure fluids. Models with up to 50 fitting parameters can represent the experimental density measurement with accuracy of 0.1% over wide range of temperature and pressures, [Lemmon & Roland, 2006].

Good example of equation of state in the Helmholtz energy form is the Short fundamental equation of state by Lemmon and Span [Lemmon & Roland, 2006]. This model uses 12 fitting parameters and it is optimized for industrial use as it offers fast computations at expense of small loss of accuracy. The equation of state itself is formulated in dimensionless Helmholtz energy $\alpha_{(\tau,\delta)} = \frac{a_{(T,\rho)}}{RT}$ as a function of reduced temperature $\tau = T_c/T$ and reduced density $\delta = \rho/\rho_c$. Two formulations are available; one for non-polar fluids (Equation 2.39) and one for polar fluids (Equation 2.40).

So called Multi-fluid models can combine equations of state in the Helmholtz energy form for different pure fluids into a model that describes a mixture. Perhaps the best known representative of this approach is the GERG (Groupe European de Recherches Gazires) model, which has been originally developed for natural gas and it was the first application of the Multifluid approach [Kunz & European Gas Research Group, 2007].

$$\begin{aligned}\alpha^r_{(\tau,\delta)} = {} & n_1\delta\tau^{0.25} + n_2\delta\tau^{1.125} + n_3\delta\tau^{1.5} + n_4\delta^2\tau^{1.375} + n_5\delta^3\tau^{0.25} + n_6\delta^7\tau^{0.85} \\ & + n_7\delta^2\tau^{0.625}exp(-\rho) + n_8\delta^5\tau^{1.75}exp(-\rho) + n_9\delta\tau^{3.625}exp(-\rho^2) \\ & + n_{10}\delta^4\tau^{3.625}exp(-\rho^2) + n_{11}\delta^3\tau^{14.5}exp(-\rho^3) + n_{12}\delta^2\tau^{0.625}exp(-\rho)\end{aligned} \quad (2.39)$$

$$\begin{aligned}\alpha^r_{(\tau,\delta)} = {} & n_1\delta\tau^{0.25} + n_2\delta\tau^{1.125} + n_3\delta\tau^{1.5} + n_4\delta^3\tau^{0.25} + n_5\delta^7\tau^{0.875} + n_6\delta\tau^{2.375}exp(-\rho) \\ & + n_7\delta^2\tau^{2.0}exp(-\rho) + n_8\delta^5\tau^{2.125}exp(-\rho) + n_9\delta\tau^{3.5}exp(-\rho^2) \\ & + n_{10}\delta\tau^{6.5}exp(-\rho^2) + n_{11}\delta^4\tau^{4.75}exp(-\rho^2) + n_{12}\delta^2\tau^{12.5}exp(-\rho^3)\end{aligned} \quad (2.40)$$

The model combines empirical equations of state explicit in the Helmholtz energy of natural gas components such as methane, nitrogen, carbon dioxide, propane, water and others. The Equation 2.41 shows the typical expression for the dimensionless Helmholtz energy α of a mixture. It is composed of the ideal gas Helmholtz energy α^{id}, the residual part α^r_{0j} and the mixture departure function α^r_{ij}. The F_{ij} is an adjustable factor fitted to data for binary mixtures. Finally, the x is the vector of molar composition of the mixture. The individual parts of the dimensionless Helmholtz energy are then expressed as sums of polynomial terms and exponential expressions even though they can come from different models.

$$\alpha_{(\delta,\tau,x)} = \alpha^{id}_{(\rho,T,x)} + \sum_{i=1}^{N} x_i\alpha^r_{oj(\delta,\tau)} + \sum_{i=1}^{N}\sum_{j=i+1}^{N} x_i x_j F_{ij}\alpha^r_{oj(\delta,\tau)} \quad (2.41)$$

The speed of sound can be expressed using derivatives of the dimensionless Helmholtz energy:

$$w = RT + RT\left[2\delta\left(\frac{\partial\alpha^r}{\partial\delta}\right)_\tau + \delta^2\left(\frac{\partial^2\alpha^r}{\partial\delta^2}\right)_\tau - \frac{\left[1+\delta\left(\frac{\partial\alpha^r}{\partial\delta}\right)_\tau + \delta\tau\left(\frac{\partial^2\alpha^r}{\partial\delta\partial\tau}\right)_\tau\right]^2}{\tau^2\left[\left(\frac{\partial^2\alpha^{id}}{\partial\delta^2}\right)_\delta + \left(\frac{\partial^2\alpha^r}{\partial\delta^2}\right)_\delta\right]}\right] . \tag{2.42}$$

The resulting model is very accurate; the uncertainty of the speed-of-sound prediction at temperatures above $270K$ is 0.2%. This level of accuracy is possible since each of the components can be represented by highly accurate bespoke equation of state. These models are often reference equations of state fitted to various thermodynamic properties (including caloric) with help of advanced fitting techniques. The uncertainty of the Helmholtz equations of state in prediction of the saturation properties or speed of sound for various fluids is listed in Table 2.3.

Table 2.3: Average deviation of Helmholtz equations of state from experimental data; SoS stands for Speed of Sound; Subscript sat stands for saturated

Fluid	Source	p_{sat}	ρ_{sat} liquid	ρ_{sat} vapour	SoS liquid	SoS vapour
		[%]	[%]	[%]	[%]	[%]
N. gas*	*	2	0.2	0.4	2	1-2
Xe	[Lemmon & Roland, 2006]	0.2	0.5	0.2	0.5	0.05
CO	[Lemmon & Roland, 2006]	0.2	0.13			
R-116	[Lemmon & Roland, 2006]	0.3	0.2	0.1		0.1
R-142b	[Lemmon & Roland, 2006]	0.5	0.03	0.5	2	0.2
R-218	[Lemmon & Roland, 2006]	0.5	0.2	0.5	1	1
R-32	[Tillner-Roth & Yokozeki, 1997]	0.02	0.05	0.3	0.3-0.1	0.012
R-134a	[Tillner-Roth & Baehr, 1994]	0.05	0.15	2	0.7	0.06
R-744	[Span & Wagner, 1996]	0.01	0.01	0.01		0.7

* [Kunz & European Gas Research Group, 2007] n-butane, isobutane, n-pentane, isopentane, n-hexane, n-heptane, n-octane, oxygen and argon

2.1.9 Acoustic models

The speed-of-sound predictive model by Scalabrin, Marchi and Grigiante [Scalabrin *et al.*, 2007] is an interesting alternative to the models mentioned above. Although it is an acoustic model which cannot itself predict the vapour liquid equilibrium, it could be used alongside a cubic equation of state. Such combination would make sense if the acoustic model provides significantly better accuracy in speed of sound prediction than the cubic equation. The model is based on the corresponding state principle and it requires three fluid-specific parameters. The speed of sound is expressed as a sum of the ideal gas speed of sound w^{id} and the residual part w^r. The residual term is following:

$$w^R_{(T,p)} = w^R_{(T_r,T_c,p_r,p_c)} = \zeta^R_{(T_r,p_r)}\sqrt{\frac{RT_rT_c}{M}} , \tag{2.43}$$

where ζ^R is the Dimensionless residual speed of sound and κ_i is a scaling factor introduced in order to relate the ζ^R to some reference fluid ζ^{ref}:

$$\kappa = \frac{\zeta^R_{(T_r,p_r)}}{\zeta^R_{(T_r,p_r)}|ref} \quad . \tag{2.44}$$

It turned out that the scaling parameter can be considered constant:

$$\kappa_{(T_r)}|_{sat} = \kappa_{(T_r P_r)}|_{liq,vap} = const. \tag{2.45}$$

The final term for the residual contribution is evaluated as interpolation of two dimensionless speeds of sound of two fluids:

$$\zeta^R_{(T_r,p_r,\kappa)} = \zeta^R_{1(T_r,p_r)} + \frac{\kappa - \kappa_1}{\kappa_2 - \kappa_1}\left[\zeta^R_{2(T_r,p_r)} - \zeta^R_{1(T_r,p_r)}\right] \quad . \tag{2.46}$$

The resulting speed of sound is then obtained by summation of the ideal and residual part:

$$w_{(T,T_c,p,p_c,x)} = w^{id}_{(T,x)} + \zeta^R_{(T,T_c,p,p_c,x)}\sqrt{\frac{RT}{M}} \quad . \tag{2.47}$$

The prediction accuracy of the model was tested on refrigerants R-11, R-22, R-123, R-134a, R-143a and R-152a. The average deviation of the model was 0.32% in the vapour region and 1.5% in the liquid region. Both numbers are roughly twice as high as the uncertainty of the multiparameter Helmholtz equations of state mentioned in section 2.1.8. Summary of the accuracy can be found in Table 2.4.

The model can be easily used for mixtures with help of several mixing rules. The speed of sound of a mixture is obtained from the residual dimensionless speed of sound ζ^R_m :

$$w^R_{m(T_r T_{cm},,p_r,p_{cm},x)} = \zeta^R_{m(\frac{T}{T_{cm}}{}_r,\frac{p}{p_{cm}})}\sqrt{\frac{RT}{M_m}} \quad , \tag{2.48}$$

where the subscript m denotes mixtures properties obtained from mixing rules which are listed in the original paper.

Table 2.4: Average deviation of the acoustic models by Scalabrin, Marchi and Grigiante from experimental data [Scalabrin *et al.*, 2007]

Fluid	Liquid	Vapour	Fluid	Liquid	Vapour
R-11	1.73	2.33	R-123	1.57	0.04
R-12	2.39	0.93	R-134a	0.57	0.12
R-22	2.40	0.7	R-143a	0.89	0.25
R-23	2.48	-	R-152a	1.29	0.14

2.1.10 SAFT equations of state

The SAFT (Statistical Associating Fluid Theory) models were developed by applying the perturbation theory to the equations of state of a monomer fluid. The perturbations accounts for chain formation (monomer chains), and additional terms can be added to account for association (hydrogen bonding) or polar molecules. The equations of state are in the Helmholtz energy form.

The SAFT approach has become quite popular in the last two decades since it offers good accuracy for a broad range of fluids; from simple organic or inorganic molecules to complex polymers. A great advantage of these models is the small number of fitting parameters: three or four parameters are needed for a combination of the monomer term with the chain perturbation or five to six parameters are used when the association term is included. Only a small number of vapour pressure data points and saturated liquid density data points are therefore needed in order to obtain the model parameters through a fitting procedure. A group contribution methods have been developed for selected SAFT equations of state in order to estimate the model parameters when no experimental data are available.

The idea behind the perturbation theory is following: the molecular pair potential energy u is divided into the reference term u^0 and the perturbation term u^p, Equation 2.49. The reference term is often a hard-sphere fluid (repulsive forces) and the perturbation represents the attractive forces, this model was originally used by Zwanzig [Zwanzig, 1954].

$$u_{(r)} = u^0_{(r)} + u^p_{(r)} \tag{2.49}$$

The thermodynamic models must respect associativity of fluids in order to accurately model many organic molecules and also water, which is strongly affected by hydrogen bonding. The association forces (hydrogen bonding, dipole-dipole interaction and lone-pairs of electrons) between molecules are strong and they result in formation of clusters of molecules having strong impact on the thermodynamic behaviour.

The association can also be modeled using perturbation theory by adding a correction (perturbation) terms to a reference non-associating fluid. One molecule can have number of different bonding sites which represent different kinds of associations (hydrogen bonding, dipole-dipole interactions, lone-pairs of electrons...).

The simplest first order association perturbation theory assumes that there is no interaction between the intramolecular bonds (bonding sites). A geometrical limitation allows only one molecule per one bonding site. Molecules with one bonding site can create only dimers, molecules with two bonding sites can create chains or rings and molecules with more bonding sites can create branched chains and other structures. Chains of different length are present in a fluid, however, at equilibrium some average length of chains is established. The number of monomers per chain $m[-]$ depends on the strength of association.

The Wertheim's perturbation theory (described for example in [Blas & Vega, 2001]) incorporates the forces of association directly in the pair potential which therefore consists of the reference pair potential u^0 and a sum of association forces between the association sites. The theory can be applied to the hard sphere, square-well or Lennard-Jones segments since the reference part of the pair potential and the association forces are treated separately.

The SAFT equations of state are in the Helmholtz energy form, the real gas Helmholtz energy a is composed of several contributions, typically these contributions are:

$$a^r = a^{seg} + a^{chain} + a^{assoc} \ . \tag{2.50}$$

- a^r is the residual Helmholtz energy defined as $a - a^{ig} = a^r$
- a^{seg} is the term that accounts for the hard sphere segment-segment interactions; $a^{seg} = f(m, \rho, T, \sigma, \varepsilon)$

- a^{chain} is the term that represents the covalent bonds between the segments that form the chains; $a^{chain} = f(m, \rho, d)$
- a^{assoc} is the term that describes the change of Helmholtz energy due to the site-site segment interactions such as hydrogen bonding; $a^{assoc} = (\rho, T, d, \epsilon^{AB}, \kappa^{AB})$

Table 2.5: Average deviation of SAFT equations of state from experimental data

Fluid	Source	EoS	p_{sat}	ρ liquid	SoS liquid	SoS vapour
			[%]	[%]	[%]	[%]
R-50	[Zhi-Yu *et al.*, 2000]	SAFTB				2.3
R-170	[Zhi-Yu *et al.*, 2000]	SAFTB				2.1
R-290	[Zhi-Yu *et al.*, 2000]	SAFTB				1.8
R-600	[Zhi-Yu *et al.*, 2000]	SAFTB				1.7
R-50	[Salimi & Bahramian, 2014]	SAFTB			average 2.3	
R-170	[Salimi & Bahramian, 2014]	SAFTB			average 2.1	
R-290	[Salimi & Bahramian, 2014]	SAFTB			average 1.8	
R-50	[Llovell & Vega, 2006]	SoftSAFT				2.49
R-290	[Llovell & Vega, 2006]	SoftSAFT				4.09
R-50	[Lafitte *et al.*, 2013]	SAFT-VR Mie	0.63	0.78		1.29
R-170	[Lafitte *et al.*, 2013]	SAFT-VR Mie	0.25	0.83		1.84
R-290	[Lafitte *et al.*, 2013]	SAFT-VR Mie	0.14	0.73		2.42
R-744	[Lafitte *et al.*, 2013]	SAFT-VR Mie	0.4	1.18		10.7
C_4F_{10}	[Lafitte *et al.*, 2013]	SAFT-VR Mie	0.5	1.75		5.79
$C_{45}F_{12}$	[Lafitte *et al.*, 2013]	SAFT-VR Mie	0.22	0.78		2.9
C_6H_{14}	[Lafitte *et al.*, 2013]	PC-SAFT	1.03	0.64		
$C_{15}H_{32}$	[Lafitte *et al.*, 2013]	PC-SAFT	2.26	0.77		
C_6H_{14}	[Lafitte *et al.*, 2013]	Soft-SAFT	1.56	0.70		
$C_{15}H_{32}$	[Lafitte *et al.*, 2013]	Soft-SAFT	1.96	2.90		
C_6H_{14}	[Lafitte *et al.*, 2013]	SAFT-VR Mie	1.12	0.25		
$C_{15}H_{32}$	[Lafitte *et al.*, 2013]	SAFT-VR Mie	1.76	0.60		
R-744	[Dias, 2005]	SoftSAFT	0.95	0.35		
R-14	[Dias, 2005]	SoftSAFT	14.31	1.06		
R-116	[Dias, 2005]	SoftSAFT	14.99	0.89		
R-218	[Dias, 2005]	SoftSAFT	18.59	1.39		
C_4F_{10}	[Dias, 2005]	SoftSAFT	14.41	0.77		
R-744	[Diamantonis & Economou, 2018]	SAFT	0.92	1.84		5.1
R-50	[Diamantonis & Economou, 2018]	SAFT	0.58	1.82		0.1
R-728	[Diamantonis & Economou, 2018]	SAFT	0.43	0.11		0.7
R-744	[Diamantonis & Economou, 2018]	PC-SAFT	0.49	0.83		2.3
R-50	[Diamantonis & Economou, 2018]	PC-SAFT	0.33	1.40		0.7
R-728	[Diamantonis & Economou, 2018]	PC-SAFT	0.14	1.92		1.1

The model parameters include the intermolecular potential (σ, ε), the average length of the molecule chain (m) and three parameters for the association term (d, association energy ϵ^{AB} and volume κ^{AB}).

Multitude of publications evaluating different SAFT equations of state in terms of modelling of vapour-liquid equilibrium can be found in available literature. A number of publications have also dealt with speed-of-sound prediction by various SAFT equations of state. Some comparisons with experimental speed-of-sound data can also be found among evaluations of the prediction accuracy of various thermodynamic properties in papers that present thorough studies of SAFT equations, for instance [Liang *et al.*, 2012]. A smaller number of papers deal only with the speed-of-sound predictions, for instance [Lafitte *et al.*, 2013].

2.2 Binary interaction parameters

One or more additional model parameters are introduced in order to provide better accuracy when the equations of state are used for mixtures. These parameters are called binary interaction parameters and they are employed in the mixing and combination rules which transform the model parameters of pure fluids into parameters of mixtures. The values of these binary interaction parameters are fitted to experimental data and they are specific to a certain pair of fluids (binary mixture).

Usually only one parameter is employed but some more advance models can use two or three parameters to improve accuracy. The parameter values can be either constant or temperature-dependent for higher accuracy models. For instance, the simplest mixing and combination rules for the parameters $\bar{a}$ and $\bar{b}$ corresponding to pure fluid i of the Peng-Robinson cubic equation of state can be following:

$$\overline{a}_m = \sum_i \sum_j x_i x_j \overline{a}_{ij} \quad , \tag{2.51}$$

$$\overline{b}_m = \sum_i \sum_j x_i x_j \overline{b}_{ij} \quad . \tag{2.52}$$

$$\overline{a}_{ij} = \sqrt{\overline{a}_i \overline{a}_j} k_{ij} \tag{2.53}$$

$$\overline{b}_{ij} = \frac{1}{2}(\overline{b}_i + \overline{b}_j) \tag{2.54}$$

The mixture parameters $\overline{a}_m$ and $\overline{b}_m$ are evaluated from the $\overline{a}_i$ and $\overline{b}_i$ parameters corresponding to each pure fluid i in the mixture based on the vector of mole fractions x. The interaction parameter k_{ij} is used to adjust value of $\overline{a}_{ij}$ which is assigned to each pair ij of fluid in a mixture, hence the $binary$ interaction parameter.

The value of the interaction parameters is unity (or zero if used as $\overline{a}_{ij} = \sqrt{\overline{a}_i \overline{a}_j}\,(1 - k_{ij})$) when no experimental data are available and the model is used in purely predictive mode. Otherwise the values are obtained by fitting (optimization) to vapour-liquid equilibrium data of binary mixtures consisting of temperature, saturated pressure and composition of both phases. Not many data are usually available for less-known mixtures therefore obtaining the values of the coefficient might prove difficult, this is especially the case when one wants to analyze the behaviour of the interaction parameters as a function of temperature. Unfortunately, these parameters have dramatic impact on the accuracy of the equations of state for calculation of saturation properties of mixtures.

Several methods for estimation of interaction parameters have been developed, the two main approaches are:

- group contribution methods
- correlations

The several group contribution methods have been developed for selected equations of state. The principle of the methods is that the interaction coefficient is composed of contributions from functional groups that can be found in the interacting molecules. For instance, in (linear) fluorocarbons the functional groups can be : CH_3which are the extremities of the molecules and CH_2 in the middle of the molecules, and the CH_4 for the lowest fluorocarbon R-14. The PPR78 is a predictive model that combines the Peng-Robinson equation of state with predictive contribution method for the interaction coefficients [Jaubert & Mutelet, 2004]. The model is aimed to predict the vapour-liquid equilibrium of hydrocarbons, some gases and also water, it is not intended for refrigerants although few refrigerants were added to the predictive model in the extended version of the model.

The correlations are based on relations between various properties (critical temperature, pressure etc.) and the interaction coefficients. At the end both methods can overlap since complicated correlations are very close to the simple contribution methods.

2.2.1 Correlations for estimation of interaction coefficients

The interaction coefficient k_{ij} of hydrocarbon mixtures can be estimated with correlation proposed by Chueh and Prausnitz [Chueh & Prausnitz, 1967]:

$$k_{ij} = 1 - \left[\frac{2\sqrt{v_{c_i}^{1/3} \cdot v_{c_j}^{1/3}}}{v_{c_i}^{1/3} - v_{c_j}^{1/3}} \right]^n \quad . \tag{2.55}$$

Where v_c is the critical volume and n is the number of components in the mixture.

Similar correlation was developed by Gao et al. [Gao *et al.*, 1992] on experimental data of light hydrocarbons mixtures:

$$k_{ij} = \left[1 - \frac{2\sqrt{T_{c_i}^{1/2} \cdot v_{c_j}^{1/2}}}{T_{c_i} - T_{c_j}} \right]^{Zcij} , \tag{2.56}$$

where Z_{cij} is the average critical compressibility factor:

$$Z_{cij} = \frac{Z_{ci} + Z_{cj}}{2} \quad . \tag{2.57}$$

Another correlation described in [Wong & Sandler, 1992] have following form:

$$k_{ij} = 1 - \frac{2\left(b - \frac{a}{RT}\right)_{ij}}{2\left(b_{ii} - \frac{a_{ii}}{RT}\right)_{ij} + 2\left(b_{jj} - \frac{a_{jj}}{RT}\right)_{ij}} \quad . \tag{2.58}$$

Note that the predicted coefficient k_{ij} is temperature-dependent. The a_{ii} and b_{ii} are simply the parameters of the Peng Robinson equation of state.

Unfortunately, most of the correlations were developed for hydrocarbons, only few correlations exist for refrigerants and their usability for mixtures of unlike refrigerants is very limited.

All of the correlations above use fluid properties such as the critical volume and temperature and one could think that they can be used for any fluid but this is not true. Such correlations provide reasonable results only for the groups of fluids for which they were developed and even then, the results are not very good. Correlations that use fluid-specific or type-specific constants to obtain the binary interaction coefficients perform much better.

Relatively recent work [Fateen *et al.*, 2013] proposed correlation in Equation 2.59. This correlation was developed for mixtures of hydrocarbons and other fluids. The obtained interaction coefficient is function of temperature and pressure.

$$k_{12} = 1 - \frac{1}{2}\frac{b_2}{b_1}\sqrt{\frac{a_1}{a_2}} - \frac{1}{2}\frac{b_1}{b_2}\sqrt{\frac{a_2}{a_1}} + \frac{1}{2}\frac{b_2 RT}{\sqrt{a_1 a_2}}\frac{\theta_1}{T_{r1}^{\theta_2} P_{r1}^{\theta_3}} \tag{2.59}$$

The parameters θ_1,θ_2 and θ_3 are chosen based on the types of fluids involved (alkanes/alkenes, nitrogen/aromatics etc.).

Simple correlation that employs fluid-specific constants was developed for Peng-Robinson equation of state and thirteen refrigerants by Chen et al. [Chen *et al.*, 2008]. The fluid-specific constants k are used to obtain the interaction coefficient k_{ij} by summation:

$$k_{ij} = k_i + k_j \ . \tag{2.60}$$

One of the most universal correlations that was developed for Peng Robinson equation of state and various mixtures of refrigerants can be found in [Zhang *et al.*, 2016].

Fairly extensive set of binary blends including HFO, HFC, PFC and natural refrigerants was used to develop the correlation. Each fluid was assigned the constant k_i which is the contribution of component i to k_{ij}. Second constant $\bar{w_i}$ used in the correlation is the contribution coefficient of the component j mixing with the component i, i.e., all other pure components mixing with the component i have the same contribution coefficient w_i. The binary interaction coefficient k_{ij} is then determined as the sum of the contribution coefficient of each pure component times its contribution:

$$k_{ij} = \bar{w_j} k_i + \bar{w_i} k_j \ . \tag{2.61}$$

Another correlation in Equation 2.62 developed by Hu et al. [Hu *et al.*, 2012] employs fluid-specific coefficients but also fluid properties (acentric factor ω, critical pressure P_c and critical temperature T_c) , the correlation was developed using 62 binary mixtures of 15 refrigerants including natural fluids.

$$k_{ij} = \left(\frac{\omega_j P_{c,j}^{0.5}}{T_{c,j}}\right) k_i - \left(\frac{\omega_i P_{c,i}^{0.5}}{T_{c,i}}\right) k_i \ \ with \ \ i < j \tag{2.62}$$

The accuracy of the correlations is summarized in Table 2.6 and Figure 2.4, both are adopted from [Zhang *et al.*, 2016]. One can use these correlations to obtain interaction coefficient of binary mixtures of fluids from the data set used to develop them. It is however not possible to use these correlations to predict interaction coefficient of new fluids (for example newly developed HFO refrigerants such is the CF_3I) since the fluid-specific coefficients are not known.

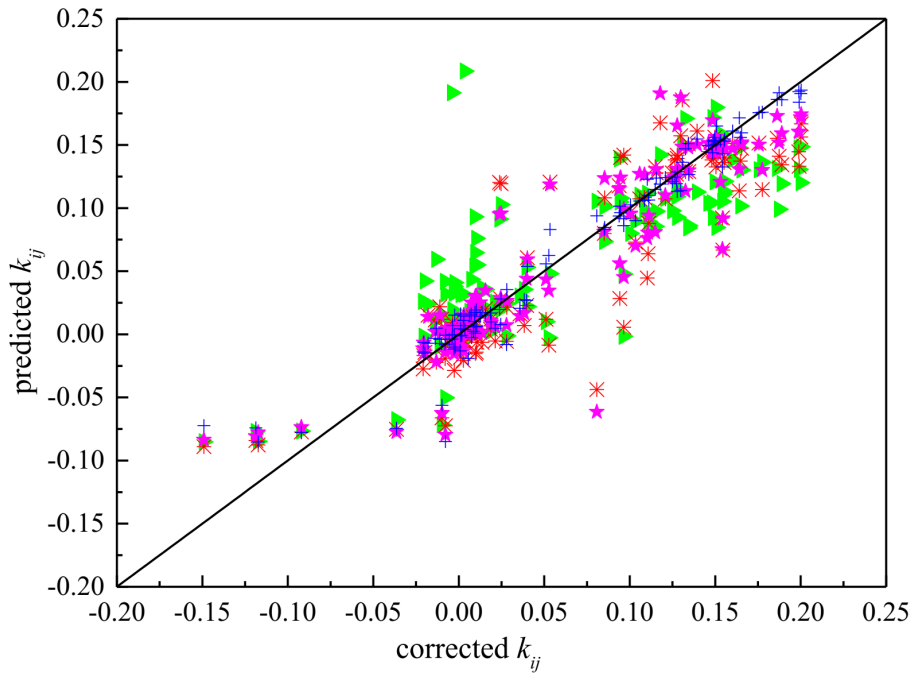

Comparisons between correlated and predicted k_{ij} calculated from different models: ▶, SPM ; ✳, ODM ; ★, MDM ; +, ZGL .

Figure 2.4: Comparison of universal correlation for interaction coefficients. The plot was adopted from [Zhang *et al.*, 2016]. Correlation references are: SPM [Chen *et al.*, 2006], ODM [Chen *et al.*, 2008], MDM [Hu *et al.*, 2012], ZGL [Zhang *et al.*, 2016]

Table 2.6: Absolute average deviation of the correlated interaction coefficients. The table was adopted from [Zhang *et al.*, 2016]. Correlation references are: SPM [Chen *et al.*, 2006], ODM [Chen *et al.*, 2008], MDM [Hu *et al.*, 2012], ZGL [Zhang *et al.*, 2016]

	ZGL	SPM	ODM	MDM
AAD [%]	0.0097	0.0341	0.0250	0.0210

An equation for prediction of the interaction coefficient for SAFT models can be derived from combination rules and intermolecular pair potential, as explained in [Tihic *et al.*, 2008]. The authors derived equation for prediction of k_{ij} coefficient for sPC-SAFT model:

$$k_{ij} = 1 - \left\{ 2^7 \left(\frac{(I_i I_j)^{1/2}}{I_i + I_j} \right) \left(\frac{\left(\sigma_{ii}^3 \sigma_{jj}^3\right)}{(\sigma_{ii} + \sigma_{jj})^6} \right) \right\} . \tag{2.63}$$

where I is the ionisation potential and σ is the parameter of the model, refer to section 6.4 for detailed description of the sPC-SAFT model.

2.3 Speed of sound measurement and fluid analysis

The instrumentation developed at SLAC National Accelerator Laboratory in the United States was a predecessor to the speed-of-sound analysers currently used at CERN. A sonar-like device with multiple sound paths was developed for the Barrel Cherenkov Ring Imaging Detector (CRID) at SLAC in late eighties and early nineties [Hallewell *et al.*, 1986]. The CRID particle detector was based on detection of Cherenkov radiation (photons) emitted when a subatomic particle transverses a radiator medium. The liquid C_6F_{14} and gaseous mixture of 70% C_5F_{12} and N_2 were used as radiators in the CRID detector. A sonar-like device was used as an acoustic fluid mixture analyser to monitor the actual ratio of the C_5F_{12} / N_2 mixture.

In fact, there were two types of analysers:

- A combined analyser-flowmeter that monitored the mixture being injected into the CRID barrel.
- Six ultrasound analysers placed directly in the detector barrel in three different heights.

The analyser-flowmeter was providing a feedback to the gas handling system which was responsible for preparation of the mixture for the detector. The speed of sound measured in the barrel was used to evaluate the refractive index of the C_5F_{12} / N_2 mixture. Local amplifiers for transmitting and receiving ultrasound transducers were located close to the transducers in remote locations in the barrel. ECL (Emitter-coupled logic) signals were used between the readout electronics and the local modules. The time-of-flight of the ultrasound between a transducer pair was measured using 4 MHz clock (timer), Figure 2.5.

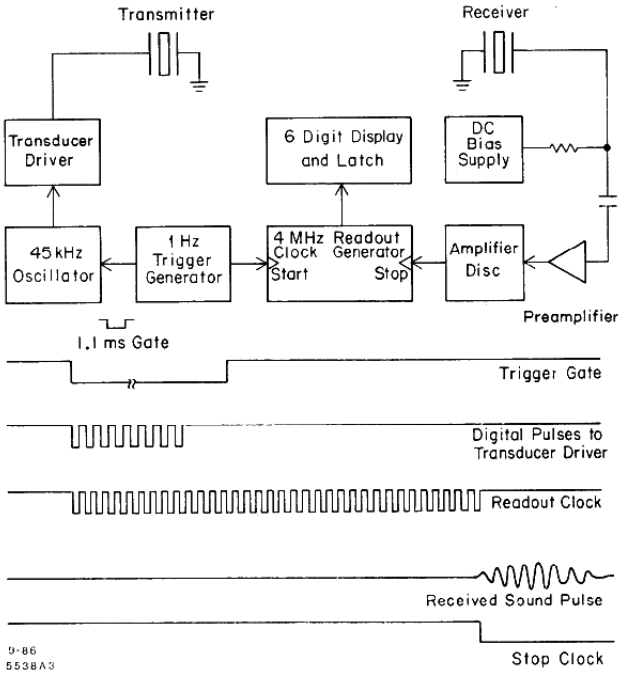

Figure 2.5: Diagram of the electronics used in the SLAC CRID detector for sonar gas mixture analyser. The diagram was adopted from [Hallewell *et al.*, 1986]

Several simple thermodynamic models were tested to be used for the analysis along the sonars. Figure 2.6 shows comparison of these models to calibration data for C_5F_{12} / N_2 mixture. It is clear that the models provide good accuracy for the pure components but very poor speed of sound prediction for the mixture. This is an example how the modelling of speed of sound can be challenging. The sonars placed at multiple

locations in the barrel revealed stratification of the mixture and indicated that the replacement of the pure N_2 gas that was used for passivation and C_5F_{12} recovery with the refractive mixture was very inefficient.

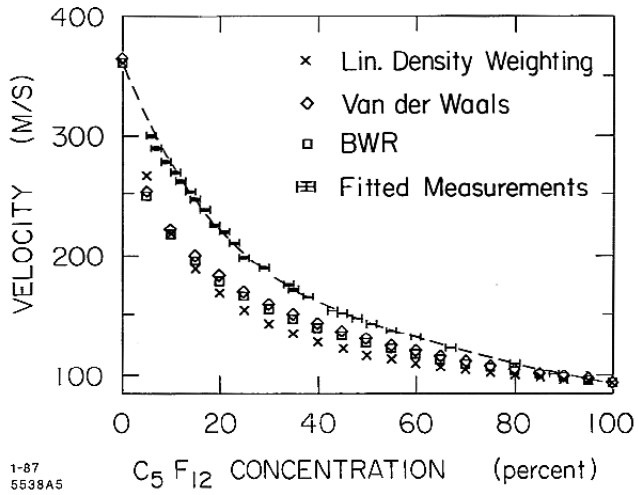

Figure 2.6: Investigation of the speed of sound in the C_5F_{12}/ N_2 mixture carried out during the development of the sonar analysers for SLAC CRID. The plot was adopted from [Hallewell *et al.*, 1986]

Subsequent RICH detectors: DELPHI, COMPASS and LHCb RICH also employed refractive gas monitoring systems based on ultrasound [Hallewell, 2011].

Other publications dealing with construction details and design proposal for speed-of-sound based mixture analysers can be traced back many decades. I have compiled following list of noteworthy publications:

- [Kniazuk & Prediger, 1955] - "Sonic gas analyser for measuring respiratory gases". A phase-shift based instrument intended for measurement CO_2 content in respiratory (exhaled) air is described.
- [Stott, 1957] - "Sonic Gas analyser for Measurement of CO_2 in Expired Air". A resonance based apparatus for speed of sound measurement is presented and continuous tracking of CO_2 during number of respiration cycles is shown. Suitability of sonic analysers for anesthetic gases is pointed out.
- [Steele & Kniazuk, 1958] - "Sonic gas analysers and their industrial uses". This publication discusses general use of sonic analysers in industrial applications, it shows examples of detection sensitivity of 20 different gases in air and elaborates on use of selective absorption to enhance the sensitivity and functionality. It should be pointed out that even though author uses water jacked to maintain the temperature of the gas in a measurement tube at 40°C, he does not elaborate on possibility of measuring speed of sound at different temperatures. He mentions that the elevated temperature prevents possible condensation inside the tube, however, he disregards the merit of having one component of the analyzed gas mixture (water vapour) condensed which could simulate use of selective absorbent and could provide more advanced analysis.
- [Garrett *et al.*, 1981] - "Helium gas purity monitor for recovery systems". Proposal and demonstration use of resonance based instrument for helium purity measurement.
- [R. *et al.*, 2005] - "Xenon measurement in breathing systems: a comparison of ultrasonic and thermal conductivity methods". Recent publication dealing with analysis of gas mixtures used for anesthesia. A comparison of different methods for analysis of the mixtures was carried out and the advantages

and disadvantages of the methods is discussed. The conclusion is that the acoustic analysis of the mixtures is more precise than the tested instrument based on thermal conductivity. The disadvantage of the acoustic method is that it is not gas specific as it assumes binary mixture of two gases if a third gas is included the analysis cannot distinguish it. Author offers techniques (water trap, soda-lime to eliminate CO_2) to overcome this disadvantage.

Steven Garett published numerous papers and developed number of instruments together with his colleagues: [Golden *et al.*, 1998b], [Garrett, 2009], [Garrett, 2008] or [Golden *et al.*, 1998a]. He presented use of his instrument for detection of hydrogen and methane from metabolic processes of anaerobic bacteria [Horta & Garrett, 2005].

Other publications from other authors that deal with construction or theoretical concept of speed-of-sound based instruments include:

- [Valdes & Cadet, 1991] - "Ultrasonic Time-of-Flight Method for On-Line Quantitation of in Situ Generated Arsine". Composition monitoring system based on an ultrasonic flow cell is used to monitor $AsH_2 + H_2$ and $Ar + He$ mixtures that are utilized during semiconductor manufacturing.

- [Giacobbe, 1993] - "Precision measurement of acoustic velocities in pure gases and gas mixtures". A design of precise instrument for measurement of speed of sound. The instrument performance is evaluated with 10 gases at two different temperatures. An accuracy from$\pm 0.15\%$ to $\pm 0.1\%$ in case of repeated measurements is concluded.

- [Joos *et al.*, 1993] - "An ultrasonic sensor for the analysis of binary gas mixtures". Authors discuss in detail sensitivity of ratio determination for binary mixtures. Authors conclude that the developed instrument is suited for use in fruit-storage halls and greenhouses where it can monitor the CO_2 content in local atmosphere.

- [Löfqvist *et al.*, 2003] - "Speed of sound measurements in gas-mixtures at varying composition using an ultrasonic gas flow meter with silicon based transducers". An ultrasonic flow meter, perhaps some commercially available type but it is not specified, is used to demonstrate measurement of the speed of sound and subsequent determination of binary mixture composition of three mixtures.

- [Liu *et al.*, 2015], [Kosterev *et al.*, 2010] - Relatively unique construction of speed of sound sensor is described. The sensor is intended as supplementary unit in a gas analyser on a principle of quartz-enhanced photoacoustic spectroscopy, Figure 2.7. The speed of sound is determined from a phase shift of continuous sine wave of variable frequency from 1 kHz to 50 kHz. The microphone that detects the phase shift are located at the ends of a U-shaped tube with constant flow of gas. The sensor was tested with number of gas mixtures and the results were compared to predictions. The standard deviation of the measured errors was found to be < 1 on a range from $260\,m/s$ to $1010\,m/s$.

One of the most in-depth publication is [Hallewell *et al.*, 1986] called "A Sonar-Based Technique for the Ratiometric Determination of Binary Gas Mixtures". In this 49-pages long paper (including the annexes) the theoretical background of sonic analyser, hardware construction and also experimental measurements are covered. A study on speed of sound in pure components and mixtures with three different equations of state (Ideal gas, Van der Waalse, BWR) is presented along with error analysis. The theoretical section is accompanied by measurement of speed of sound in pure gases and following mixtures: $Ne + He$, $CH_4 + C_4H_{10}$, $CH_4 + C_2H_6$, $N_2 + C_4H_{10}$, and $N_2 + C_5F_{12}$. The developed instrument was intended to be used at Stanford Linear Accelerator Center (SLAC) in Cerenkov Ring Imaging Detector. It can be incorporated into a control loop in the gas handling units to enable effective monitoring of the gases mixtures that are essential for the detector operation.

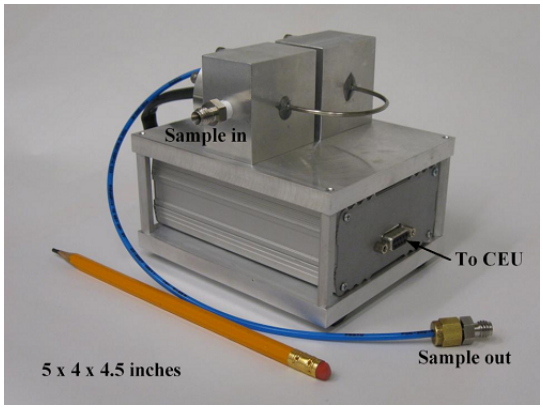

Figure 2.7: Speed of sound sensor with U-shaped tube [Liu *et al.*, 2015]

The natural gas and petrochemical industry are well-known users of acoustic analysers. Often a standard industrial ultrasonic flowmeters have secondary functions like molecular weight determination from the speed of sound although standalone analysers can be found as well:

- [Ruffine & Trusler, 2009] - "Sound-Speed Sensor for Gas Pipeline Applications". The paper present a sensor designed especially for natural gas under pipeline conditions. It is in fact a robust spherical resonator intended as alternative to chromatography and other costly and delicate instruments. The paper states that even though speed of sound measurement alone can provide only limited information about the gas it can still be used to assess the quality of natural gas in industrial environment. The instrument can deliver data that show average deviation of about 0.02% and a maximum absolute deviation of 0.06%.

- [Lansing, 2003] - "Principles of operation for ultrasonic gas flow meters". This work is dedicated to ultrasonic flowmeters for natural gas. The role of accuracy of speed of sound calculations in the flowmeter diagnostics is pointed out. The flowmeter measurement can drift in time as a consequence of pipe fouling, component malfunction or debris. Malfunction diagnostic by checks of the measured speed of sound is proposed. The paper states that firstly, all the sound paths in the pipe should show the same speed of sound. Secondly, that the measurement should be compared to highly precise calculation in order to detect possible misbehaviour of the flowmeter.

- [Sandven *et al.*, 2014] - "New Wireless IR Gas Detector for Safety Integrity Level 2 Applications Using MEMS Technology". It is a description of sensor for petroleum industry that has been extensively field tested on off-shore platform, Figure 2.8. The sensor detects presence of hydrocarbons in the air using combination of speed of sound measurement and infrared absorption. The speed of sound sensor is used for the primary alert that "something has happened" and the IR sensor then confirms the presence of hydrocarbons in the air. This is an example of sonic analyser being used as a leak detector.

Following publications represent some of the more unusual designs and applications for speed-of-sound based sensors and analysers:

- [Farrelly *et al.*, 1999] - "EARS – Environmental Acoustic Reconnaissance and Sounding: Significant scientific aspects". Proposal of acoustic instrument for the Mars Lander Mission. The instrument is designed to obtain measurements of temperature, speed of sound and sound attenuation. There would be number of operational modes for the evaluation of various quantities: Time of flight measurement,

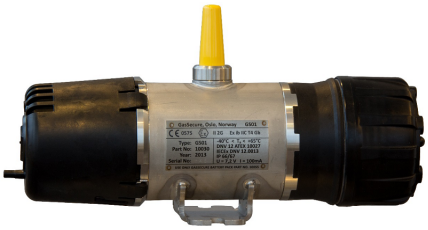

Figure 2.8: Wireless IR Gas Detector for Safety Integrity Level 2 [Sandven *et al.*, 2014]

Time of flight measurement of burst of pulses, continuous wave and resonance mode. The obtained data could be eventually used to evaluate viscosity, thermal conductivity and molecular relaxation time of the atmosphere.

- [Huang *et al.*, 2002] - "High precision, fast ultrasonic thermometer based on measurement of the speed of sound in air". A phase shift of a continuous wave is measured to obtain the speed of sound in this device. the values are then used to evaluate the temperature of air. The claimed accuracy of this non-contact rapid measurement is within $0.05°C$.

- [Olfert & Checkel, 2006] - "An ultrasonic sound speed sensor for measurement of EGR levels". Very interesting and unusual application in the combustion engine Exhaust Gas Recirculation. The EGR system becomes clogged with sooth in time limiting the flow of the recirculated exhaust gases. The proposed sensors would monitor the actual amount of the exhaust gases in the inlet manifold so that the engine management can compensate for the fouling. One-cylinder engine running on natural gas was used for demonstration. Authors conclude that it is possible to realize such sensor and use its output for the engine management. The main limitation is the resistance and stability of the selected ultrasonic sensors to high temperatures.

2.4 Commercially available instruments

Acoustic analysers are available also as commercial products. Although all ultrasonic gas and liquid flowmeters work on principle of transit time measurement, it is not common (at least outside the petrochemical industry) that they provide speed of sound measurement. Simply, there is no option to view the actual measured speed of sound on the display or to analog output proportional to the measured speed of sound. The flow speed of the gas or liquid is evaluated from the ultrasound transit times, i.e. the time needed for an ultrasound to travel between the transducers, Figure 2.9. The reciprocal difference between the up-stream t_{up} and down-stream t_{down} transit time gives the flow speed v and the average of reciprocal transit times gives the speed of sound w, Equation 2.64, the distance D between the transducers and the angle α have to be known.

$$v = \frac{D}{2sin\alpha}\left(\frac{1}{t_{down}} - \frac{1}{t_{up}}\right) \quad w = \frac{D}{2}\left(\frac{1}{t_{down}} + \frac{1}{t_{up}}\right) \tag{2.64}$$

It is apparent that the measured values needed to evaluate the speed of sound (t_{up} and t_{down}) are exactly the same as the inputs for evaluation of the flow speed. It is therefore only up to the flowmeter designer whether the speed of sound values will be available to the user alongside the flow measurements. Sometimes it might be possible to access the speed of sound measurement under some kind of service menu or in service

mode and read the value from a flowmeter display or via serial interface. Comparison of the measured speed of sound value to predictions could be advantageous for diagnostic and troubleshooting especially when fouling and deposits are suspected [Lansing, 2003].

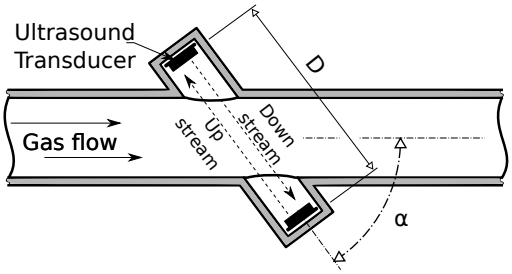

Figure 2.9: Typical industrial time-of-flight measurement instrument

The General Electrics Panametrics GF868 represents a typical ultrasonic flowmeter for the petroleum industry. It is intended for the flare gas (waste gas from refineries, chemical plants, natural gas processing plants) and it uses the speed of sound to calculate the molecular weight and subsequently the mass flow.

Various other measurement cells can be purchased from retail or wholesale companies. The cells accommodate either time-of-flight or resonance-based speed of sound measurement.

- The TTP company from the United Kingdom recently announced the SonicSense [Campbel-Baker, 2018] measurement cell, Figure 2.10. The diameter of the cell is 24 mm and the depth is 18 mm, projected price in volume production is between $\$5$ and $\$10$. The company foresees applications in methane in air monitoring, anesthesia, respiratory monitoring and even in hydrogen-cars related systems.

- Another example of an available ultrasound cell is the Compass Control Manufacturing Oxygen sensor [Com, 2018e], Figure 2.11. As the name suggests it is a product that focuses on monitoring of oxygen concentration in medical units. Although other applications such as acetylene/oxygen ratio monitoring for welding and scuba gear equipment are suggested.

- The Inficon Composer Elite Gas Concentration Monitor is a high quality precision instrument for monitoring of carrier-precursor binary mixtures, Figure 2.12. It targets the research and development but also the production processes in semiconductor industry [Com, 2018b]. The suitability for mixtures of Cp_2Mg in N_2 is emphasized. The instrument accommodates a resonance cell with precision less than $0.1\,Hz$. Such precision should translate, according to the manufacturer's specifications, to 0.00011 of $TMIn$ (trimethylindium) in H_2 . The analyzed gas mixture can be supplied to the instrument at pressures from 0.26 to $1.3\,bar$ and the cell can be maintained at temperatures up to $62°C$ with stability better than $0.01°C$.

- Another commercially available instrument is the Binary Gas Analyser BGA244 from Stanford research system [Com, 2018a] at cost around $\$4000$, Figure 2.13. Again, the resonance method is employed with cylindrical cavity. The claimed speed of sound resolution and accuracy are $0.001\,m/s$ and ± 0.01 respectively. The heaters for the measurement cell are optional and have to be purchased for additional price. Data for speed of sound prediction in 250 gases are pre-programmed and the user can add new pure gases or pseudo mixtures. The performance of the analyser in terms of various gases in air according to the data sheet is summarized in Table 2.7 . The relatively large error for nitrogen is caused by the small difference in speed of sound between air and pure nitrogen.

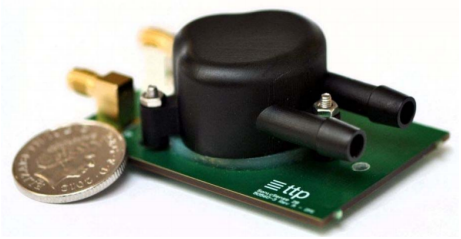

Figure 2.10: TTP's SonicSense measurement cell [Campbel-Baker, 2018]

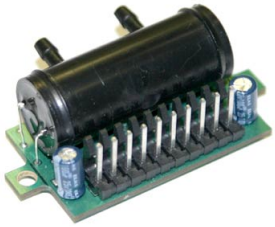

Figure 2.11: Compass Control Manufacturing Oxygen sensors [Com, 2018e]

Figure 2.12: Inficon Composer Elite Gas Concentration Monitor [Com, 2018b]

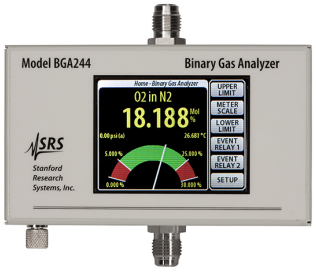

Figure 2.13: Binary Gas Analyser BGA244 [Com, 2018a]

Table 2.7: Performance of the BGA244 analyser. The table was adopted from [Com, 2018a]

Gas (mixed into air)	Composition Error
Hydrogen	±0.04 %
Helium	±0.03 %
Methane	±0.09 %
Water	±0.11 %
Neon	±0.08 %
Nitrogen	±1.03 %
Ethane	±0.09 %
Oxygen	±0.31 %
Argon	±0.13 %
Carbon dioxide	±0.05 %
Propane	±0.03 %
1,1-Difluoroethane	±0.02 %
Tetrafluoromethane	±0.01 %
Sulfur hexafluoride	±0.01 %

Instruments for laboratory and industrial speed of sound measurement in liquids are also available, namely for paper, textile, petroleum, chemical, pharmaceutical and food industry. The instrument can be used for concentration monitoring although it is also common that the purpose of the speed of sound measurement is purely to evaluate the density of the fluid. The speed of sound of petroleum products, acid solutions and food products (e.g. milk, oils) is of interest:

- Sound speed and density characterization of milk adulterated with melamine [Elvira *et al.*, 2009]
- Speed of sound in solutions of sugars, pages 369 to 371 in [Kress-Rogers & Brimelow, 2001]

Even though modern models such as the SAFT equations of state introduced in previous sections are able to model quite complex chemicals like sugars and their solutions [Ji *et al.*, 2007], such organic molecules are clearly out of the scope of this work. Following instruments can be used also for other applications outside the food industry, in applications that are closer to the subject of this thesis:

- The Centec Sonatec [Com, 2018d] holds two piezoelectric transducers and determines the speed of sound by means of time-of-flight measurement. It is suitable for measurements inside storage tanks or in tubes with flow and it integrates also a temperature probe. The range of measurement is $400 - 3000$ m/s while the accuracy is ± 0.05 m/s.
- Rhosonics ultrasonic analyser 8500 Series [Com, 2018c] determines the speed of sound in reflection or transmission mode along with the temperature. The accuracy is ± 0.1 m/s according to data sheet. The device is suitable for acids and bases such are $NaOH$, KOH, NH_4OH , H_2SO_4, $TMAH$, HCl, HNO_3 and also for mixtures with hydrocarbons: water in oil, water in glycol or for solvents and salts KCl, $NaCl$.
- Mittal Enterprises UIFL-01 [Com, 2016] is an ultrasonic interferometer for liquids, Figure 2.14. It can be used at single or multiple frequencies spanning from 1 to 12 MHz. and the required fluid sample is at least $10\,ml$. It uses typical construction with movable quartz plate (transducer) and micrometric screw. The measurement cell can be maintained at constant temperature between $-30°C$ and $+80°C$ by circulating fluid from a liquid bath thermostat. The measurement accuracy is not stated.

Figure 2.14: Mittal liquid interferometer [Com, 2016]

Figure 2.15: Centec Sonatec [Com, 2018d]

Figure 2.16: Rhosonics ultrasonic analyser 8500 Series [Com, 2018c]

2.5 Summary

The basic form of equations of state is used to calculate the pressure or Helmholtz energy from the temperature and density. The pressure as well as any other thermodynamic property can be obtained from derivation of the Helmholtz energy. The speed of sound requires derivative of pressure or Helmholtz energy including the heat capacities which are itself derivatives of pressure or Helmholtz energy but they also include the ideal gas heat capacity that needs to be evaluated experimentally. The prediction of saturated pressure and vapour density and speed of sound can be carried out with relatively simple cubic equations of state at reasonable accuracy of around 2%. The simple equation does not provide good accuracy neither for the liquid density nor for the liquid speed of sound, the deviations from experimental data are around 10% in both cases. The complex equations such as the BWR or modern Helmholtz energy equations of state which can provide accuracy better than 1% are difficult to use especially for new fluids (large experimental data sets needed for complicated fitting procedure). The SAFT approach sits in the middle, only few fluid-specific fitting constants are required while the achieved accuracy is good even in liquid phase, the deviations are often close to 1%. But the results differ for different fluids and different SAFT models. To achieve good accuracy for mixtures it is necessary to use binary interaction coefficients which are seldomly available for unusual mixture. Good estimation models are thus extremely useful. The section dedicated to speed-of-sound measuring instruments shows that there is a multitude of applications described in scientific literature. Multiple instruments for industrial speed of sound measurement exist namely in the food and petrochemical industry. To my knowledge, none of the instruments are directly intended for refrigeration applications. In my opinion, the main limitation is lack of reliable and speed of sound prediction models.

Bibliography

chapter 2: Prior art

[Com, 2016] 2016. *Ultrasonic Interferometer For Liquids*. Mittal enterprises, New Patel Nagar, Delhi, 110008 India, http://www.mittalenterprises.com/products/index/ultrasonic-interferometer-for-liquids_3238.html.

[Com, 2018a] 2018a (October). *Binary Gas Analyzer BGA244*. SRS Stanford Research Systems, 1290-D Reamwood Ave. Sunnyvale CA 94089 USA, http://thinksrs.com/products/BGA244.htm.

[Com, 2018b] 2018b (October). *Composer Elite Gas Concentration Monitor*. INFICON Holding AG, Hintergasse 15B CH-7310 Bad Ragaz Switzerland, http://products.inficon.com/en\protect\discretionary{\char\hyphenchar\font}{}{}us/Product/Detail/Composer\protect\discretionary{\char\hyphenchar\font}{}{}Elite.

[Com, 2018c] 2018c (October). *Composer Elite Gas Concentration Monitor*. INFICON Holding AG, Hintergasse 15B CH-7310 Bad Ragaz Switzerland, http://products.inficon.com/en\protect\discretionary{\char\hyphenchar\font}{}{}us/Product/Detail/Composer\protect\discretionary{\char\hyphenchar\font}{}{}Elite.

[Com, 2018d] 2018d (October). *Determination of Concentration by Sound Velocity*. Centec, Wilhelm-Röntgen-Strasse 10 63477 Maintal Germany, http://www.centec.de/sensors/power-plants/sonatec/.

[Com, 2018e] 2018e (September). *Oxygen sensor*. Compass Controls Manufacturing Inc., 9645 Lackman Rd Lenexa, KS 66219 USA, http://compassmanufacturing.com/monitoring.html.

[Ahlers & Gmehling, 2001] Ahlers, J., & Gmehling, J. 2001. Development of an universal group contribution equation of state: I. Prediction of liquid densities for pure compounds with a volume translated Peng-Robinson equation of state. *Fluid Phase Equilibria*, **191**(1), 177 – 188.

[Blas & Vega, 2001] Blas, F. J., & Vega, L. F. 2001. Thermodynamic properties and phase equilibria of branched chain fluids using first- and second-order Wertheim's thermodynamic perturbation theory. *The Journal of Chemical Physics*, **115**(8), 3906–3915.

[Campbel-Baker, 2018] Campbel-Baker, A. 2018 (January). *Press Release SonicSense*. TTP plc., Melbourn Science Park Melbourn Hertfordshire SG8 6EE UK, http://www.ttp.com/news/2014/01/sonic_sense.

[Chen *et al.*, 2006] Chen, J., Chen, Z., & Hu, P. 2006. *J. Univ. Sci. Technol. China*, **36**, 656–659. cited By 1.

[Chen *et al.*, 2008] Chen, J.-X., Hu, P., & Chen, Z.-S. 2008. Study on the Interaction Coefficients in PR Equation with vdW Mixing Rules for HFC and HC Binary Mixtures. *International Journal of Thermophysics*, **29**(6), 1945–1953.

[Chueh & Prausnitz, 1967] Chueh, P. L., & Prausnitz, J. M. 1967. Vapor-liquid equilibria at high pressures: Calculation of partial molar volumes in nonpolar liquid mixtures. *AIChE Journal*, **13**(6), 1099–1107.

[Coquelet *et al.*, 2016] Coquelet, Ch., Houriez, C., & El Abbadi, J. 2016. Prediction of thermodynamic properties of refrigerant fluids with a new three-parameter cubic equation of state. *International Journal of Refrigeration*, **69**, 418–436.

[Defibaugh & Moldover, 1997] Defibaugh, D. R., & Moldover, M. R. 1997. Compressed and Saturated Liquid Densities for 18 Halogenated Organic Compounds. *Journal of Chemical & Engineering Data*, **42**(1), 160–168.

[Defibaugh *et al.*, 1994] Defibaugh, D. R., Morrison, G., & Weber., L. A. 1994. Thermodynamic Properties of Difluoromethane. *Journal of Chemical & Engineering Data*, **39**(2), 333–340.

[Diamantonis & Economou, 2018] Diamantonis, N., & Economou, I. 2018. Evaluation of SAFT and PC-SAFT EoS for the calculation of thermodynamic derivative properties of fluids related to carbon capture and sequestration. 05.

[Dias, 2005] Dias, A. M. A. 2005. *Thermodynamic Properties of Blood Substituting Liquid Mixtures*. Ph.D. thesis.

[Elvira *et al.*, 2009] Elvira, L., Rodriguez, J., & Lynnworth, L. C. 2009. Sound speed and density characterization of milk adulterated with melamine. *The Journal of the Acoustical Society of America*, **125**(5), EL177–EL182.

[Estela-Uribe & Trusler, 2000] Estela-Uribe, J. F., & Trusler, J. P. M. 2000. Acoustic and Volumetric Virial Coefficients of Nitrogen. *International Journal of Thermophysics*, **21**(5), 1033–1044.

[Ewing & Trusler, 1992] Ewing, M. B., & Trusler, J. P. M. 1992. Second acoustic virial coefficients of nitrogen between 80 and 373 K. *Physica A: Statistical Mechanics and its Applications*, **184**(3), 415 – 436.

[Farrelly *et al.*, 1999] Farrelly, F. A., Flamini, E., Petri, A., Pitolli, L., & Pontuale, G. 1999 (September). EARS - Environmental Acoustic Reconnaissance and Sounding: Significant scientific aspects. *In: 2nd International Workshop on "The Italian role and perspectives for the exploration of Mars"*.

[Fateen *et al.*, 2013] Fateen, S.-E. K., Khalil, M. M., & Elnabawy, A. O. 2013. Semi-empirical correlation for binary interaction parameters of the Peng-Robinson equation of state with the van der Waals mixing rules for the prediction of high-pressure vapor-liquid equilibrium. *Journal of Advanced Research*, **4**(2), 137 – 145.

[Gao *et al.*, 1992] Gao, G., Daridon, J.-L., Saint-Guirons, H., Xans, P., & Montel, F. 1992. A simple correlation to evaluate binary interaction parameters of the Peng-Robinson equation of state: binary light hydrocarbon systems. *Fluid Phase Equilibria*, **74**, 85 – 93.

[Garrett, 2008] Garrett, S. L. 2008. Sonic gas analyzer for hydrogen and methane. *The Journal of the Acoustical Society of America*, **123**(5), 3372–3372.

[Garrett, 2009] Garrett, S. L. 2009 (January). Sonic Gas Analysis. *In: ETHOS Conference proceedings*. Session 5: Science of Stoves.

[Garrett *et al.*, 1981] Garrett, S. L., Swift, G. W., & Packard, R. E. 1981. Helium gas purity monitor for recovery systems. *Physica B+C*, **107**(1), 601 – 602.

[Giacobbe, 1993] Giacobbe, F. W. 1993. Precision measurement of acoustic velocities in pure gases and gas mixtures. *The Journal of the Acoustical Society of America*, **94**(3), 1200–1210.

[Golden *et al.*, 1998a] Golden, M. V., Keoliarr, R. M., & Garrett, S. L. 1998a. Sonic Gas Analysis. *Pages 1705–1706 of: Proceedings 16th International Congress on Acoustics and 135th Meeting Acoustical Society of America*, vol. III.

[Golden *et al.*, 1998b] Golden, M. V., Keolian, R. M., & Garrett, S. L. 1998b. Sonic gas analyzers. *The Journal of the Acoustical Society of America*, **103**(5), 2944–2944.

[Hallewell, 2011] Hallewell, G. 2011. *Aspects de lutilisation de fluides fluorocarbures saturees dans la physique des hautes energies*. Université de la Méditerranée Aix-Marseille II. Habilitation a diriger des recherches.

[Hallewell *et al.*, 1986] Hallewell, G., Crawford, G., Mcshurley, D., Oxoby, G., & Reif, R. 1986. A Sonar-Based Technique for the Ratiometric Determination of Binary Gas Mixtures. *SLAC - PUB*, **4122**(October).

[Hemptinne & Ungerer, 1995] Hemptinne, J. C., & Ungerer, P. 1995. Accuracy of the volumetric predictions of some important equations of state for hydrocarbons, including a modified version of the Lee-Kesler method. *Fluid Phase Equilibria*, **106**(1), 81 – 109.

[Horta & Garrett, 2005] Horta, M. A., & Garrett, S. L. 2005. Sonic gas analyzer for microbiological metabolic measurements. *The Journal of the Acoustical Society of America*, **118**(3), 1945–1945.

[Hu *et al.*, 2012] Hu, P., Chen, L.-X., & Chen, Z,-S. 2012. A modified differential-model for interaction parameters in PR EoS with vdW mixing rules for mixtures containing HFCs and HCs. *Fluid Phase Equilibria*, **324**, 64 – 69.

[Huang *et al.*, 2002] Huang, K. N., Huang, C. F., Li, Y. C., & Young, M. S. 2002. High Precision, Fast Ultrasonic Thermometer Based on Measurement of the Speed of Sound in Air. *Review of Scientific Instruments*, **73**(4022).

[Huber & McLinden, 1992] Huber, M. L., & McLinden, M. O. 1992. Thermodynamic Properties of R134a (1,1,1,2-tetrafluoroethane). *International Refrigeration and Air Conditioning Conference*.

[Jaubert & Mutelet, 2004] Jaubert, J.-N., & Mutelet, F. 2004. VLE predictions with the Peng-Robinson equation of state and temperature dependent kij calculated through a group contribution method. *Fluid Phase Equilibria*, **224**(2), 285 – 304.

[Ji *et al.*, 2007] Ji, Peijun, Feng, Wei, & Tan, Tianwei. 2007. Density Calculation of Sugar Solutions with the SAFT Model. *Journal of Chemical & Engineering Data*, **52**(1), 135–140.

[Joos *et al.*, 1993] Joos, M., Müller, H., & Lindner, G. 1993. An ultrasonic sensor for the analysis of binary gas mixtures. *Sensors and Actuators B: Chemical*, **16**(1), 413 – 419.

[Kniazuk & Prediger, 1955] Kniazuk, M., & Prediger, F. R. 1955. Sonic gas analyzer for measuring respiratory gases. *ISA Proc.*, **II**(55-9-2). 5 pages.

[Kosterev *et al.*, 2010] Kosterev, A. A., Dong, L., Thomazy, D., Tittel, F.K., & Overby, S. 2010. QEPAS for Chemical Analysis of Multi-Component Gas Mixtures. *Appl Phys B*, **101**, 649–659.

[Kress-Rogers & Brimelow, 2001] Kress-Rogers, E., & Brimelow, C.J.B. 2001. *Instrumentation and Sensors for the Food Industry*. Woodhead Publishing Series in Food Science, Technology and Nutrition. Woodhead.

[Kunz & European Gas Research Group, 2007] Kunz, O., & European Gas Research Group. 2007. *The GERG-2004 Wide Range Equation of State for Natural Gases and Other Mixtures: GERG TM15 2007*. Fortschrittberichte VDI / 6: Energietechnik. VDI-Verlag.

[Lafitte *et al.*, 2013] Lafitte, T., Apostolakou, A., Avendano, C., Galindo, A., Adjiman, C. S., Müller, E. A., & Jackson, G. 2013. Accurate statistical associating fluid theory for chain molecules formed from Mie segments. *The Journal of Chemical Physics*, **139**(15), 154504.

[Lansing, 2003] Lansing, J. 2003 (September). Principles of Operation for Ultrasonic Gas Flow Meters. *Pages 50 – 60 of: American School of Gas Measurement Technology*, vol. 38. American School of Gas Measurement Technology, Houston, texas.

[Lemmon & Roland, 2006] Lemmon, E. W., & Roland, S. 2006. Short Fundamental Equations of State for 20 Industrial Fluids. *Journal of Chemical & Engineering Data*, **51**(3), 785–850.

[Löfqvist *et al.*, 2003] Löfqvist, T., Sokas, K., & Delsing, J. 2003. *Speed of Sound Measurements in Gas-Mixtures at Varying Composition Using an Ultrasonic Gas Flow Meter With Silicon Based Transducers*. Tech. rept. 11th Conference on Flow Measurement Groningen, NETHERLANDS.

[Li *et al.*, 1999] Li, J., Tillner-Roth, R., Sato, H., & Watanabe, K. 1999. An Equation of State for 1,1,1-Trifluoroethane (R-143a). *International Journal of Thermophysics*, **20**(6), 1639–1651.

[Liang *et al.*, 2012] Liang, X., Maribo-Mogensen, B., Thomsen, K., Yan, W., & Kontogeorgis, G. M. 2012. Approach to Improve Speed of Sound Calculation within PC-SAFT Framework. *Industrial & Engineering Chemistry Research*, **51**(45), 14903–14914.

[Liu *et al.*, 2015] Liu, K., Dong, L., & Tittel, F. K. 2015. Compact Sound-Speed Sensor for Quartz Enhanced Photoacoustic Spectroscopy Based Applications. *Review Of Scientific Instruments*, **86**(044903).

[Llovell & Vega, 2006] Llovell, F., & Vega, L. F. 2006. Prediction of Thermodynamic Derivative Properties of Pure Fluids through the Soft-SAFT Equation of State. *The Journal of Physical Chemistry B*, **110**(23), 11427–11437. PMID: 16771416.

[Lopez-Echeverry *et al.*, 2017] Lopez-Echeverry, J. S., Reif-Acherman, S., & Araujo-Lopez, E. 2017. Peng-Robinson equation of state: 40 years through cubics. *Fluid Phase Equilibria*, **447**, 39 – 71.

[Magoulas & Tassios, 1990] Magoulas, K., & Tassios, D. 1990. Thermophysical properties of n-Alkanes from C1 to C20 and their prediction for higher ones. *Fluid Phase Equilibria*, **56**(Supplement C), 119 – 140.

[Olfert & Checkel, 2006] Olfert, J. S., & Checkel, M. D. 2006. An Ultrasonic Sound Speed Sensor For Measuring EGR Levels. *Proc. IMechE*, **221**(November). Part D J. Automobile Engineering.

[Outcalt & McLinden, 1996] Outcalt, S. L., & McLinden, M. O. 1996. A Modified Benedict-Webb-Rubin Equation of State for the Thermodynamic Properties of R152a (1,1-difluoroethane). *Journal of Physical and Chemical Reference Data*, **25**(2), 605–636.

[Péneloux *et al.*, 1982] Péneloux, A., Rauzy, E., & Fréze, R. 1982. A consistent correction for Redlich-Kwong-Soave volumes. *Fluid Phase Equilibria*, **8**(1), 7 – 23.

[R. *et al.*, 2005] R., King, M., Bretland, A., Wilkes, & J., Dingley. 2005. Xenon measurement in breathing systems: a comparison of ultrasonic and thermal conductivity methods. *Anaesthesia*, **60**(12), 1226–1230.

[Redlich & Kwong, 1949] Redlich,)., & Kwong, J. N. S. 1949. On the Thermodynamics of Solutions. V. An Equation of State. Fugacities of Gaseous Solutions. *Chemical Reviews*, **44**(1), 233–244. PMID: 18125401.

[Ruffine & Trusler, 2009] Ruffine, L., & Trusler, J. P. M. 2009. Sound-Speed Sensor for Gas Pipeline Applications. *Int. J. Thermophys*, **30**(January), 1106 –1117.

[Salimi & Bahramian, 2014] Salimi, M., & Bahramian, A. 2014. The Prediction of the Speed of Sound in Hydrocarbon Liquids and Gases: The Peng-Robinson Equation of State Versus SAFT-BACK. *Petroleum Science and Technology*, **32**(4), 409–417.

[Sandven *et al.*, 2014] Sandven, K., Sagberg, H., Fismen, B., & Aakvaag, N. 2014. New Wireless IR Gas Detector for Safety Intergrity Level 2 Applications Using Mems Technology. *In: ISA 59th Analysis Division Symposium*. International Society of Automation, Baton Rouge, LA USA. Session 05-2.

[Scalabrin *et al.*, 2007] Scalabrin, G., Marchi, P., & Grigiante, M. 2007. Speed of sound predictive modeling in a three-parameter corresponding states format: Application to pure and mixed haloalkanes. *Experimental Thermal and Fluid Science*, **31**(3), 261 – 278.

[Soave, 1972] Soave, G. 1972. Equilibrium constants from a modified Redlich-Kwong equation of state. *Chemical Engineering Science*, **27**(6), 1197 – 1203.

[Span & Wagner, 1996] Span, R., & Wagner, W. 1996. A New Equation of State for Carbon Dioxide Covering the Fluid Region from the Triple-Point Temperature to 1100 K at Pressures up to 800 MPa. *Journal of Physical and Chemical Reference Data*, **25**(6), 1509–1596.

[Steele & Kniazuk, 1958] Steele, D. I., & Kniazuk, M. 1958. Sonic gas Analyzers and their Industrial Uses. *Industrial Electronics, IRE Transactions on*, **PGIE-6**(May), 64–67.

[Stott, 1957] Stott, F. D. 1957. Sonic Gas Analyzer for Measurement of CO2 in Expired Air. *Review of Scientific Instruments*, **28**(11), 914–915.

[Tihic *et al.*, 2008] Tihic, A., Kontogeorgis, G., Michelsen, M. L., von Solms, N., & Constantinou, L. 2008. *Group Contribution sPC-SAFT Equation of State*. Ph.D. thesis.

[Tillner-Roth & Baehr, 1994] Tillner-Roth, R., & Baehr, H. D. 1994. An International Standard Formulation for the Thermodynamic Properties of 1,1,1,2-Tetrafluoroethane (HFC-134a) for Temperatures from 170 K to 455 K and Pressures up to 70 MPa. *Journal of Physical and Chemical Reference Data*, **23**(5), 657–729.

[Tillner-Roth & Yokozeki, 1997] Tillner-Roth, R., & Yokozeki, A. 1997. An International Standard Equation of State for Difluoromethane (R-32) for Temperatures from the Triple Point at 136.34 K to 435 K and Pressures up to 70 MPa. *Journal of Physical and Chemical Reference Data*, **26**(6), 1273–1328.

[Tsai & Y, 1998] Tsai, J.-C., & Y, P. Chen. 1998. Application of a volume-translated Peng-Robinson equation of state on vapor-liquid equilibrium calculations. *Fluid Phase Equilibria*, **145**(2), 193 – 215.

[Twu *et al.*, 2002] Twu, C. H., Sim, W. D., & Tassone, V. 2002. Getting a Handle on Advanced Cubic Equations of State. *Chemical Engineering Progress*, **98**(22), 58–56.

[Valdes & Cadet, 1991] Valdes, J. L., & Cadet, G. 1991. Ultrasonic time-of-flight method for on-line quantitation of in situ generated arsine. *Analytical Chemistry*, **63**(4), 366–369.

[Wong & Sandler, 1992] Wong, D. S. H., & Sandler, S. I. 1992. A theoretically correct mixing rule for cubic equations of state. *AICh*, **38**(5), 671–680.

[Ye *et al.*, 1992] Ye, S., Lagourette, B., Alliez, J., Saint-Guirons, H., Xans, P., & Montel, F. 1992. Comparison with experimental data of ultrasound velocity in pure hydrocarbons calculated from equations of state. *Fluid Phase Equilibria*, **74**, 157 – 175.

[Younglove & Ely, 1987] Younglove, B. A., & Ely, J. F. 1987. Thermophysical Properties of Fluids. II. Methane, Ethane, Propane, Isobutane, and Normal Butane. *Journal of Physical and Chemical Reference Data*, **16**(4), 577–798.

[Younglove & McLinden, 1994] Younglove, B. A., & McLinden, M. O. 1994. An International Standard Equation of State for the Thermodynamic Properties of Refrigerant 123 (2,2-Dichloro-1,1,1-Trifluoroethane). *Journal of Physical and Chemical Reference Data*, **23**(5), 731–779.

[Zhang *et al.*, 2016] Zhang, H., Gong, M., Li, H., Zhao, Y., Zhong, Q., Dong, X., Shen, J., & Wu, J. 2016. A simple model for temperature-independent kij of the PR-vdW model for mixtures containing HCs, HFCs, PFCs, HFOs, CO2, RE170 and R13I1. *Fluid Phase Equilibria*, **425**, 374 – 384.

[Zhi-Yu *et al.*, 2000] Zhi-Yu, Z., Ji-Chu, Y., & Yi-Gui, L. 2000. The use of statistical associating fluid theory to improve the BACK equation of state: I. Pure fluids. *Fluid Phase Equilibria*, **172**(2), 111 – 127.

[Zwanzig, 1954] Zwanzig, R. W. 1954. High-Temperature Equation of State by a Perturbation Method. I. Nonpolar Gases. *The Journal Of Chemical Physics*, **22**(8), 1420–1426.

3 Speed of sound measurement

The great advantage of the speed of sound is that it can be measured with astounding accuracy relatively easily. I will describe only the measurement methods that are utilized for high quality scientific or industrial measurements. Following are the main speed of sound measurement principles that are the most common and that can be encountered in many instruments and scientific publications:

- Time-of-flight, Sing around, Pulse-echo - methods based on sound propagation over a distance
- Resonance, Interferometry - methods based on resonance

There are also other methods such as phase shift measurement or dynamic light scattering, however, they are rarely used for scientific or industrial purposes. The time-of-flight and pulse-echo methods are often used for ultrasonic ranging i.e. distance measurement. In those applications the sound transmitting medium is air or liquid (level measurement) and the distance is evaluated from known speed of sound and measured time-of-flight.

Although the above listed measurement methods are based on different principles there is a common limit to the achievable accuracy stemming from the purity of the analyzed fluid. For precise measurement a correction of the results has to be made to account for the contaminants which are always present. A chromatography analysis must be carried out to identify the real composition of the analyzed fluid. In any case, thorough flush and evacuation of all the instrument piping and the measurement cell is a must.

3.1 Speed of sound measurement techniques

3.1.1 Resonance methods

The resonators offer the highest accuracy from all known measurement methods, the order of uncertainty of the obtained speed of sound is as small as 10^{-5} ([Wilhelm & Letcher, 2010], [Goodwin *et al.*, 2003] page 241). Various resonators are the instruments of choice for obtaining speed of sound values for thermodynamic characterization of fluids. Other thermodynamic properties such as the ideal gas heat capacity or viscosity can be then reliably derived thanks to the exceptional measurement accuracy.

The resonance of closed cavity filed with gas, Figure 3.1, is governed by the cavity geometry, thermophysical properties and the speed of sound of the gas. Two values can be obtained from the resonance measurements :

- Resonance frequencies f_i
- Resonance half-widths $\triangle f_i$

The resonance frequencies are used to determine the speed of sound and the resonance half-widths are related to the viscosity, thermal conductivity and energy losses. A resonance quality can be characterized by ratio of the resonance bandwidth relative to the center frequency called the quality factor , Equation 3.1. The lower is the quality factor the more damped is the resonance.

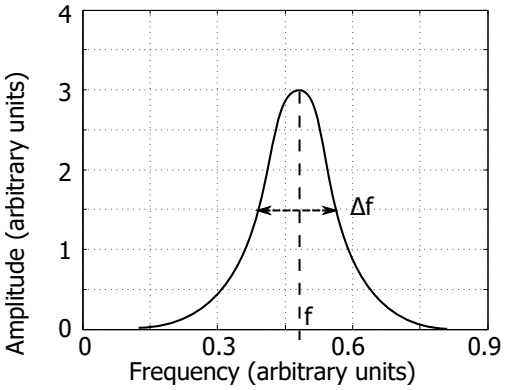

Figure 3.1: Resonance

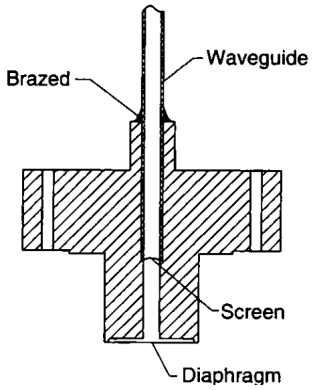

Figure 3.2: Wave guide construction [Gillis, 1994]

$$Q_f = \frac{f}{\triangle f} \tag{3.1}$$

The uncertainty of the obtained ideal gas heat capacity depends on the uncertainty of the molar mass and mainly on contamination of the measured fluid [Wilhelm & Letcher, 2010]. In order to achieve the best results for the speed of sound, the resonators are designed so that a narrow frequency-amplitude peaks are obtained. The opposite approach is taken when the focus is on transport properties and the geometry of the cavity is designed so that it produces wide peaks allowing for more precise determination of the haft-widths [Assael *et al.*, 2014]. Sound frequency of several kilohertz is used for gases, liquids are measured at several megahertz. The diameter of the spherical cavity or the length of the cylindrical resonator is selected so that convenient resonance frequencies at the lower modes are obtained. Common values are approximately 10 cm, such size ensures that the low-order resonance modes occur at audio frequencies.

The rest of this section will describe resonators and techniques for speed of sound measurement in gases since the instrument developed in this work is intended for gases. The resonance cavity is filled with measured vapour and equipped with two transducers, an acoustic emitter (loudspeaker) and microphone. Arrangement with only one transducer is also possible especially for cylindrical resonators. In this case the transducer is being excited and its admittance i.e. the driving current is measured instead of measuring the cavity response with a microphone. The transducers have to be able to withstand the pressures and temperatures in the cavity and they should be corrosion resistant and chemically inert. Although, wave guides (Figure 3.2) that connect the cavity with external transducers can be used to keep the transducers at room temperature, atmospheric pressure and to separated them from the measured gas. The heat dissipation of the transducers has to be minimal and they have to allow for installation that disturbs the cavity surface as little as possible. Both the loudspeaker and the microphone can be custom made elements.

The signal-to-noise ratio depends on the sensitivity of the transducers and it will generally suffer at low and high pressures. A precise frequency generator is used to excite the loudspeaker. The excitation signal might need high voltage DC bias or a large amplitude depending on what type of transducer is used.

The signal from the microphone is amplified and a band-pass filter can be used to eliminate unwanted low and high frequency components. The amplitude and phase of the received signal is compared with the excitation signal by a dedicated amplitude and phase detector or lock-in amplifier, Figure 3.3. The frequency sweep is usually carried out in a few steps in a narrow range of frequencies around the resonance frequency. Sweep back and forth should point out to possible temperature drifts.

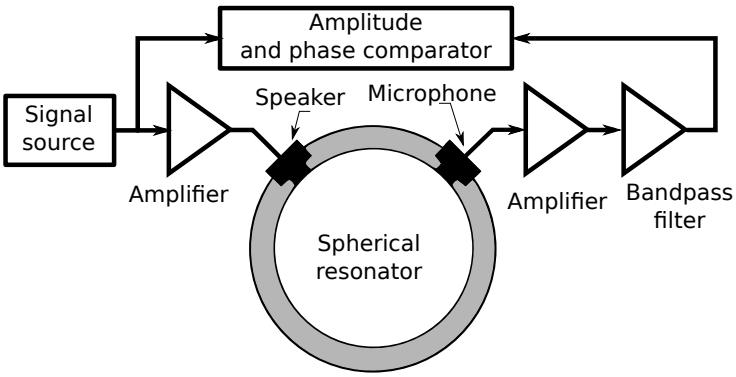

Figure 3.3: Typical arrangement for the resonance frequency measurement

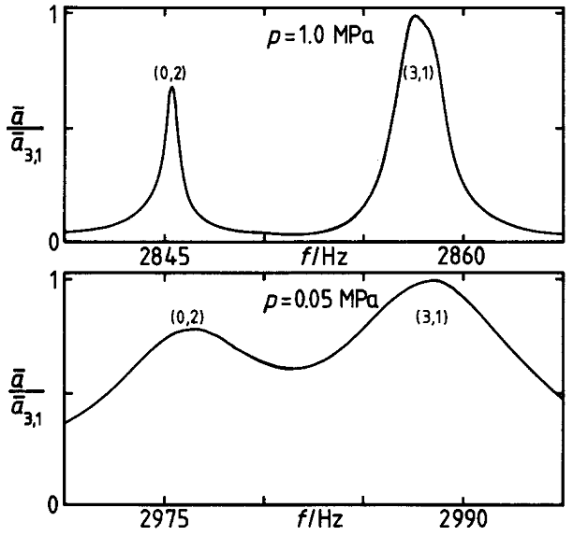

Figure 3.4: Signal amplitudes recorded in CF_4 at $250K$ and pressures of 1 and $0.05MPa$. The plot was adopted from [Ewing & Trusler, 1989a]

The resonator cavity is usually spherical although cylindrical [Younglove & Frederick, 1990] or annular [Jarvis *et al.*, 1996] cavities are sometimes used as well, Figure 3.5. Naturally, the highest quality surface and geometric precision are desirable. While best measurement accuracy can be achieved with the spherical resonators, the spherical cavity is difficult to manufacture and therefore expensive. The cylindrical resonators are cheaper to manufacture, however, a sphere has better surface-to-volume ratio. The resonance in a cylindrical cavity has lower quality factor due to the damping at the wall and the measurements are usually carried out at few lower resonance modes, especially the longitudinal modes are of interest.

An annular geometry is used for fluids that exhibit high attenuation due to slow molecular thermal relaxation and also for measurements close to the critical point. Annular resonator allows for measurement at very low frequencies that would otherwise require large sphere diameters [Wilhelm & Letcher, 2010, page 207] and they are especially suitable for measurement at low pressures.

The speaker and the microphone are accommodated flush with the inner surface in order not to disturb the geometry of the cavity and they should be as small all possible so that only small fraction of the cavity surface is affected. The same applies to the gas port through which the resonator can be evacuated and filled with the measured fluid. For the best result the gas port should be constructed as a needle valve so that the tip

of the needle is flush with the inner surface when closed. The position of the acoustic transducers on the end walls in the cylindrical resonator is not important for the longitudinal resonance modes. The transducers can be both located on one end of the cylindrical cavity or they can be opposite to each other on both ends.

The resonator cavity shell is often made of aluminum, stainless steel, copper or bronze. High purity material should be used so that the thermal expansion and the compressibility can be precisely accounted for. In case of the spherical resonator the shell consists of two hemispheres and the transducers mounting holes are most often drilled in the top hemisphere as shown the Figure 3.5.

For measurements at precisely defined temperature the resonator is accommodated inside a thermostat/cryostat with liquid bath as shown in the Figure 3.5. Thermostat itself can be pressurized or the resonator is placed in a pressure cell that is submerged in a bath, often low temperature silicon oil. The goal is to have the same pressure inside and outside of the resonator so that resonator shell is not stressed and its radius depends only on the temperature. A platinum or other precise thermometer is attached to the resonator shell from outside.

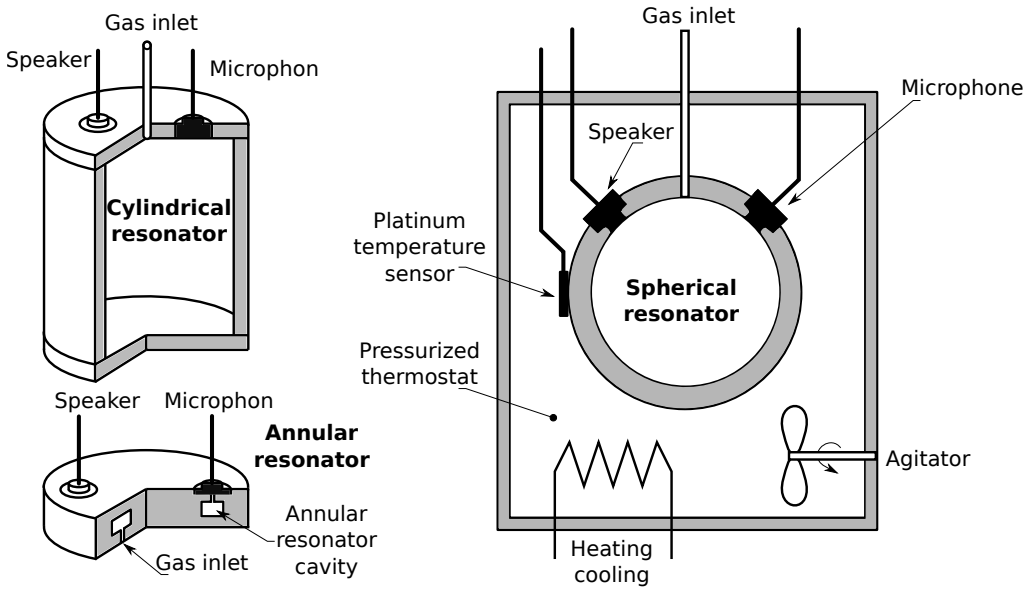

Figure 3.5: Cylindrical, spherical and annular resonator. The spherical resonator is inside a pressurized thermostatic vessel to prevent geometry changes.

Only radial (breathing) modes are of interest for the cylindrical resonator. Therefore the indices of the spherical cavity resonant modes l, m and n are reduced to n alone since the $l = m = 0$. The $n = 1$ is the zero frequency radial mode. Measurement at one resonant mode is enough to obtain the speed of sound although measurement at different resonant modes can reduce measurement errors and provide information about the speed of sound dispersion.

An important source of measurement error is the thermal relaxation described in section 6.6 and so called precondensation effect which occurs at temperatures and pressure close to saturation and it can cause the measurement error up to few percent. The effect is more pronounced at low frequencies ($2 - 20kHz$) and in resonators with large surface-to-volume ratios [Mehl & Moldover, 1982]. The walls of the resonator cavity can adsorb measured vapour and a layer of condensate appears on the machined surface even though pressure and temperature during the measurement are not significantly approaching the saturation line. The pressure and temperature fluctuation during the sound cycle will induce a mass transfer between the phases that results in sound attenuation and sound speed dispersion.

A first order acoustic model is usually used for the spherical resonators . The natural (observed) frequency f_n of the $n-th$ radial mode is expressed as

$$f_n = f_n^0 - i\,\tilde{g}_{0n} \ . \tag{3.2}$$

The imaginary part $\tilde{g}$ represents losses and it is related to the resonance half-widths that were explained in the Figure 3.1. The equation can be expressed using perturbation terms $(\triangle f - i\,g)_j$:

$$f_n = \frac{\nu_{0n} w}{2\pi r} + \sum_j \left(\triangle f - i\,\tilde{g}\right)_j \ . \tag{3.3}$$

Where the $\frac{\nu_{0n} w}{2\pi a}$ is the unperturbed resonance frequency f_n^0. The ν_{0n} is tabulated eigenvalue corresponding to the resonance mode, r is the sphere radius and w is the speed of sound. The diameter of the cavity has to be known as a function of temperature and pressure, it can be either calculated using a model or obtained from calibration carried out with a well-known gas. The perturbations (corrections) account for a shift in the resonance frequency and contribute to the resonance half-width.

A model based solely on the unperturbed resonance frequency would provide measurement accuracy in the order of 0.01% [Hess, 1989]. A resonance model that employs the perturbations can increase the accuracy up to 0.0001% [Hess, 1989].

The most often used perturbations are:

1. Thermal boundary layer: For many gases the most important perturbation. The boundary condition of the radial modes requires temperature to be continuous at the gas/wall interface. The sound propagation, which is otherwise adiabatic process, becomes isothermal process at the wall, [Hess, 1989].

2. Bulk absorption and molecular relaxation: The correction terms incorporate viscous diffusivity and vibrational-relaxation contribution to the bulk diffusivity [Trusler, 1984, page 179]. In case of negligible sound speed dispersion this term influences only the resonance half-widths.

3. Openings in the resonator cavity wall for filling ports and transducers. The opening can be divided into cylindrical (tube of certain diameter and length) and annular (slits around the transducers).

4. Shell motion: The elastic response: (breathing) of the resonator spherical isotropic shell to an internal acoustic mode. This perturbation contributes mainly to the resonance frequency shift [Trusler, 1984, page 180]. The breathing frequency of the resonator is found experimentally with helium making use of its very high speed of sound. Measured perturbations of the radial resonant frequency are compared to frequencies far and close to the resonator shell breathing frequency [Boyes, 1992, page 12].

5. Geometric imperfection: The inner cavity is never an ideal sphere. An imperfection arises from the machining and polishing process. Also the cavity is always assembled from two hemispheres therefore it is not ideally symmetric due to a step at the hemispheres joint.

The thermal boundary layer correction can be calculated from Equation 3.4. The first term in the equation is the loss at a plane surface, the second term accounts for the curvature of the actual resonator surface. The last, third, term is the correction for the temperature jump effect that is a result of different thermal conductivity of a gas near the wall.

$$(\triangle f - i\,g) = -\,(1+i)\,\frac{\gamma-1}{2a}\sqrt{\frac{D_t f_{0,n}}{\pi}} + i\frac{(\gamma-1)\,D_t}{2\pi a^2} + (\gamma-1)\,\frac{f_{0,n} l_a}{a} \tag{3.4}$$

where γ is the ratio of heat capacities, D_t is the thermal diffusivity coefficient:

$$D_t = \frac{\gamma M}{\rho C_p} \ . \tag{3.5}$$

and l_a is the accommodation length:

$$l_a = \frac{k}{p}\sqrt{\frac{\pi M T}{2R}}\frac{(2-h)/h}{C_v/R + 1/2} \ . \tag{3.6}$$

where p is the pressure, k is the thermal conductivity and M is the molar mass. The thermal accommodation coefficient h spans from 0 to 1. It is a ratio of energy actually transported over the vapour-solid interface and energy that would be transported over the interface if all molecules were in thermal equilibrium. The values of the coefficient are 0.91 for an aluminum resonator and 1 for a stainless steel resonator of diameter 40 and $45mm$ respectively [Boyes, 1992].

A simple equation can be used for the cylindrical resonator provided only longitudinal resonance modes are considered:

$$w = \frac{2Lf}{n} \quad n = 1, 2, 3.... \tag{3.7}$$

The n corresponds to the resonant mode and L is the resonator length. The speed of sound w obtained from the Equation 3.7 can be corrected for various effects in similar way as described above for the spherical resonator:

$$w_{corr} = \frac{w}{(1 - \delta w)} \ , \tag{3.8}$$

$$\delta = \frac{\phi + \varphi}{2\pi f} \ . \tag{3.9}$$

The correction coefficient δ is composed of two components [Younglove & Frederick, 1990]:

- ϕ is the attenuation coefficient for the wall losses:

$$\phi = \frac{1}{r.w}\left\{\left(\frac{\mu}{\rho}\right)^{0.5} + (\gamma - 1)\left(\frac{k}{e.C_p}\right)^{0.5}\right\}(\pi f)^{0.5} \ . \tag{3.10}$$

- φ is accounting for the energy loss at the end walls of the cylinder:

$$\varphi = \frac{1}{L.u}(\gamma - 1)\left(\frac{k}{e.C_p}\right)^{0.5}(\pi f)^{0.5} \ . \tag{3.11}$$

Where μ is the viscosity, γ is the ratio of heat capacities, k is the thermal conductivity, ρ is the density, r is the cylinder radius and L is the cylinder length (L is a function of the temperature and also pressure).

3.1.2 Interferometric method

The interferometric method was widely used for laboratory measurement in the past. It is still used even today in a simple table-top instrument for determination of the sound speed in liquids like vegetable oils and subsequent evaluation of compressibility β=$1/\rho w^2$, [Pankaj & Bhatt, 2010] and [Voleisiene & Voleisis, 2008].

The principle and instrumentation is similar to a cylindrical resonator, the difference being that with the interferometer the excitation frequency is fixed and the geometry (length) of the measurement cell varies instead. The excitation frequency can have few discrete values for more advanced measurements. The fixed excitation frequency allows for efficient use of a piezoelectric plates as transducers. The plates are selected so that they can be used at their first resonant modes usually between 1 and 20 MHz. Two or one transducer arrangement can be used the same way as in the above mentioned cylindrical resonators.

Some means of precise mechanical positioning and measurement such as micrometric screw or optical interferometer have to be used in order to be able to change the length of the measurement cell. This moving parts are clearly a big disadvantage which disqualifies the method from practical applications outside a laboratory. Nowadays, when even cheap electronic components can provide very precise time measurement and advanced signal processing this method has fallen out of favor.

Identical sources of errors as for the above described resonators can be identified when the interferometer is used for gases. Namely the precondensation can cause significant error when the measurement is carried out close to saturation state.

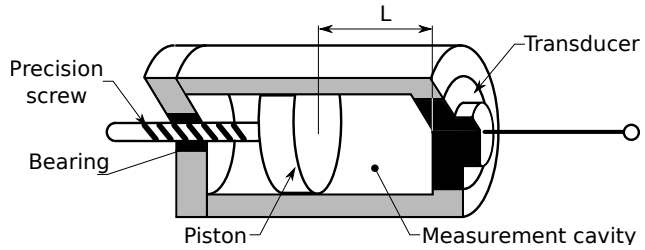

Figure 3.6: Interferometer for speed of sound measurement

The example of an acoustic gas interferometer is shown in Figure 3.6. A piston is positioned with a setting screw inside a cylinder with a crystal transducer on the opposite side to the piston. This transducer is excited with a frequency signal while its admittance is measured to detect the resonance.

The speed of sound w is determined from the excitation frequency f and the measured wavelength λ:

$$w = \lambda f \quad . \tag{3.12}$$

The adiabatic compressibility β is an important property, it can be evaluated provided the density is known:

$$\beta = \frac{1}{w^2 \rho} \quad . \tag{3.13}$$

This equation is other form of the sound velocity equation:

$$w^2 = \left(\frac{\partial p}{\partial \rho}\right)_s = \frac{1}{\beta \rho} \quad . \tag{3.14}$$

Where p is the pressure and the acoustic impedance Z is then

$$Z = \rho w \ . \tag{3.15}$$

When the viscosity μ is known the ultrasonic attenuation α_a is calculated as

$$\frac{\alpha_a}{f^2} = \frac{8\pi^2\mu}{3\rho w^2} \ . \tag{3.16}$$

Lastly the equation for the relaxation time $\hat{\tau}$ which is the time for transfer of energy from translation to vibration:

$$\hat{\tau} = \frac{4\mu}{3\rho c^2} \ . \tag{3.17}$$

3.1.3 Time of flight

The time-of-flight method is very suitable for liquids and somewhat less for gases. The reason being the high energy losses on the gas-transducer interface that make it more difficult to obtain fast response and good quality signal from the transducers. One the other hand, the method has four significant advantages:

1. The measurement principle is robust, no delicate components are required.
2. Required instrumentation is simple and cheap.
3. The speed of sound is measured in a real time.
4. It can be combined with flow measurement.

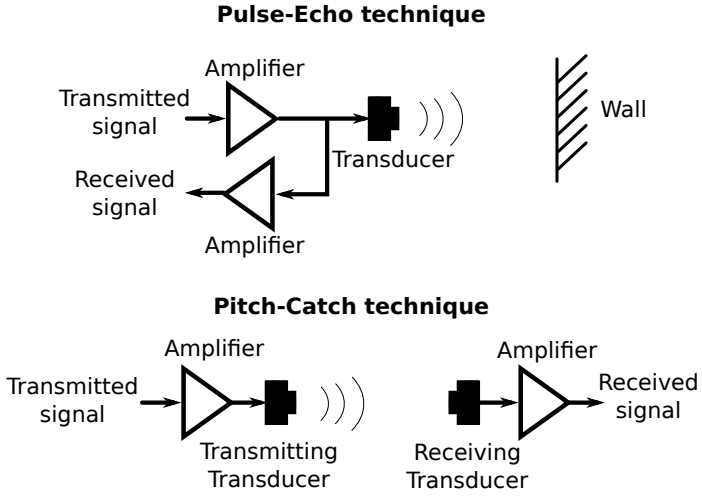

Figure 3.7: Time-of-flight measurement principles

The advantages of the time-of-flight method are exploited in industrial applications where it is widely used. The pulse-echo technique, Figure 3.7, is used for thickness measurements of solid materials, level

measurement and distance measurement. The pitch-catch technique is used for liquid and gas flowmeters and composition sensors. Section 2 provides an overview of various sensors and commercially available instruments many of which are based on time of flight methods.

A typical measurement set-up consist of a cylindrical measurement cell with ultrasonic transducer at the ends, Figure 3.8. A short acoustic burst (signal A) is transmitted from one transducer and received (signal B) by the other one. The time it takes for the sound to propagate from one to the other side is precisely measured. The speed of sound is obtained immediately by dividing the travelled distance between the transducers by the measured time of flight. The typical transmitted and received signals are shown in Figure 3.9. The transmitted burst of pulses (on the left) is short and with high amplitude followed by a short period of ringing of the transmitting transducer. The received pulses (on the right) have smaller amplitude and the detection of the first received pulse might be difficult at small signal to noise ratios.

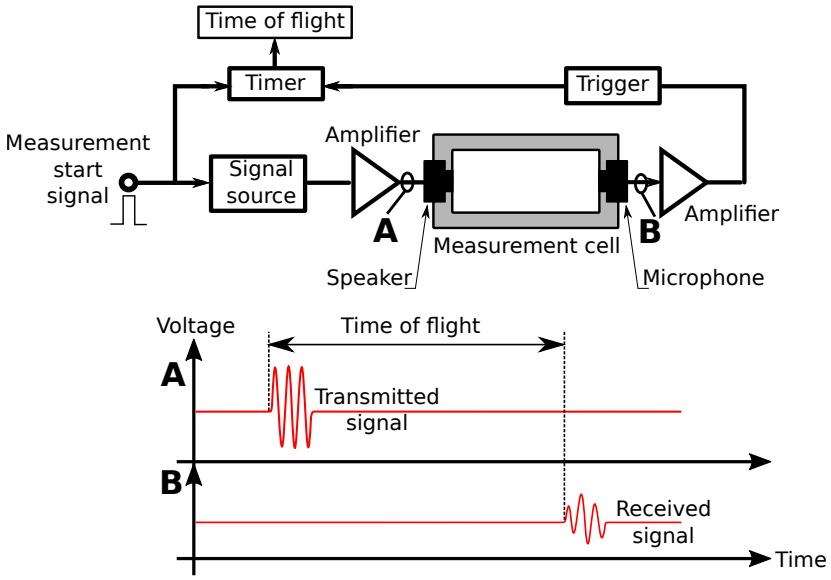

Figure 3.8: Pitch-catch speed of sound measurement

The "Sing around" technique was popular before precise time measurement with fast microcontrollers became available for custom applications. A short burst of sound pulses is transmitted on one side of measurement cell when a receiving circuitry detects a signal on the other side of the cell, Figure 3.10. This means that the sound bursts are transmitted repeatedly at frequency proportional to the speed of sound in the measurement tube. The faster the speed of sound the more often is the signal generator triggered by the receiving circuitry.

3.2 Instrumentation for speed of sound measurement

Various types of acoustic transducers are used in all the speed-of-sound measurement methods discussed in the previous section. Generally, the same transducer can be used to convert electric signal to sound (transmitting transducers) and sound to electric signal (receiving transducer). There is a large selection of commercially available transducers that have been designed for general or very specific applications. In most cases the operation frequency is in ultrasound region between $20\,kHz$ and several megahertz. The physical size spans from large and very powerful ultrasonic transducers that are used for cleaning to miniature arrays of hundreds of transducers for ultrasound imaging. Typical power output of ultrasonic transducers for ranging

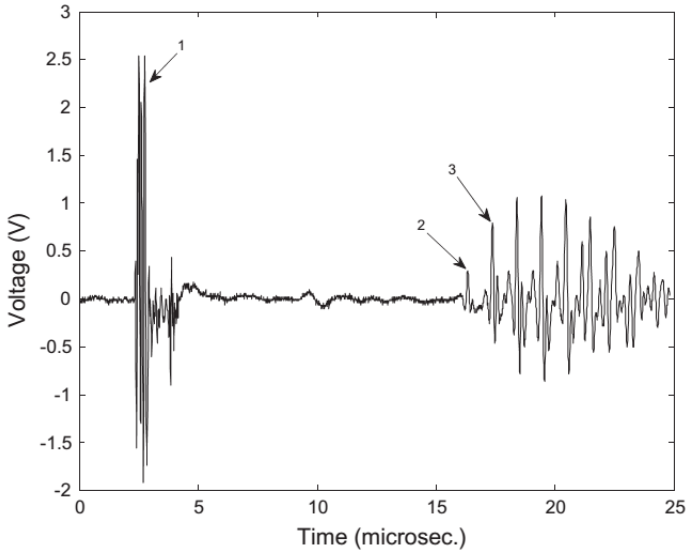

Figure 3.9: Example of the acoustic signals in liquid. The figure was adopted from [Lopes *et al.*, 2014]

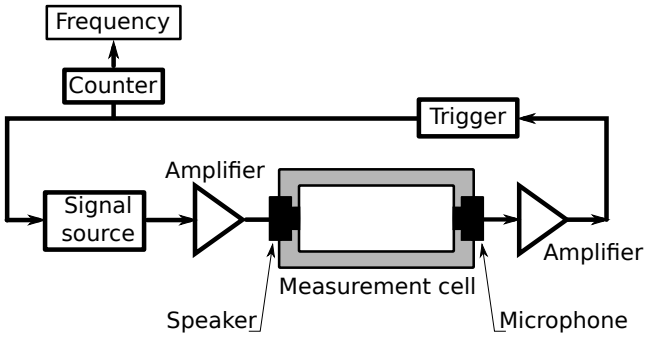

Figure 3.10: Sing around measurement principle

application, flow or speed of sound measurement is approximately $1\,W/cm^2$.

There is an extensive research focusing on ultrasound transducers for defectoscopy and medical applications. Some portion of the results from this field are applicable also to the transducers for thermodynamic measurements. However, the defectoscopy is focusing on measurements in solid phase and the medical applications are predominantly using phase array imaging method.

The temperature and pressure range of operation and possibly corrosive or chemically reactive atmosphere are unique conditions that are not found in many different fields where the acoustic transducers are being used and developed. In other words, the environmental conditions the transducers can be exposed to in the acoustic analysers can be very harsh. Very little information can be found about performance of commercial transducers and their components outside usual conditions that are defined by atmospheric pressure, temperature from 0 to $+50°C$ and air or water environment. Tests at elevated pressure in particular, that would be so important for the acoustic analysers, are conducted very rarely.

The transducers suitable for thermodynamic measurements, Figure 3.11, are based on following principles:

- Piezoelectric
- Electrostatic (capacitive), MEMS

The main component of piezoelectric transducers is a piezoelectric material, quartz or piezo ceramics. Such material responds to an electrical field with mechanical strain (deformation). The piezo elements for acoustic applications have usually one or few significant resonance frequencies with very high quality factors. The usable frequency range spans from tens of kilohertz to hundreds of megahertz. The ceramic piezoelectric transducers have relatively low sensitivity on acceptance. Due to this the piezo transducers are more suitable for liquids than gases where more energy is coupled from the fluid. The fact that the piezo transducers perform best at discrete (resonant) frequencies predetermines their use for interferometric and time-of-flight measurements methods. The disadvantages of piezo ceramics such as the high acoustic impedance and narrow bandwidth can be improved by piezo composites and PVDF (ferroelectric polymer polyvinylidene fluoride), which are combination of ceramics with passive layers or spheres of polymers or epoxy resins.

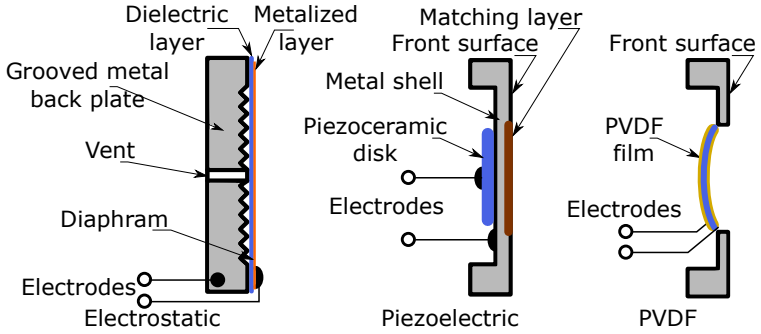

Figure 3.11: Types of acoustic transducers

The capacitive or electrostatic transducers are composed of a thin membrane and a solid metal back plate, Figure 3.11, the membrane moves when electric charge is applied. The back plate is made of metal with a grooved pattern that improves the sensitivity and frequency response. The electrostatic transducers are used only for gases, they have wide bandwidth and high sensitivity on acceptance due to the thin membranes but they also require high voltage to operate.

The MEMS (Micro Electro Mechanical Systems) transducers are micromachined elements of very small dimensions. The micromachined ultrasound arrays are used for medical ultrasound applications. The MEMS microphones found its way to thin mobile phones, laptops and hearing aids.

Summary of the transducers properties can be found in Table 3.1.

Table 3.1: Ultrasonic transducers properties. The table was adopted from [Kazakov, 2008]

		Capacitive	Piezoceramic (with matching layer)	Composite (kit of layers)	PVDF
Sensitivity on acceptance	mV/Pa	2	1	0.1	0.4
Frequency range	kHz	200	500	500	200
Freq. band	%	30	2	30	30
Temperatures (max)	°C	80	>100	>100	80
Stability to environment	-	low	high	high	low
Stability	-	moderate	low	moderate	high

3.3 Sound transmission losses

Time-of-flight and pulse-echo measurement in gases are very demanding on the transducers, namely on the piezo transducers. The energy transfer between the fluid and solid piezoceramic transducer is poor especially at high frequencies due to large difference in the specific acoustic impedance[1] of the solid transducer and air which results in high reflection loses. The capacitive transducers with thin membranes have the smallest transmission loses hence they are very efficient for application with gases. The solid piezocermic crystals exhibit very high transmission loses and they are most suitable for applications with liquids while the flexible PVDF materials are somewhere in the middle.

Assuming a longitudinal sound wave, the reflection loss on a boundary of two materials under $90°$ incidence angle (sound arriving perpendicularly to the boundary) can be calculated with following equation:

$$R = \frac{I_r}{I_t} = \left(\frac{Z_2 - Z_1}{Z_2 + Z_1}\right)^2 \quad . \tag{3.18}$$

Where R is the reflection coefficient, it represents the ratio of reflected wave intensity I_r to the transmitted wave intensity I_t , Z is the acoustic impedance of the material. Subscript 1 corresponds to the material in which the signal originates and index 2 is the material that creates the boundary.

Consequently the transmission coefficient is equal to

$$\tau = \frac{I_t}{I_r} = 1 - R = 4\frac{Z_2 Z_1}{(Z_2 + Z_1)^2} \quad . \tag{3.19}$$

In order to express the transmission coefficient in decibels one has to take is decadic logarithm and multiply it by 10. The acoustic impedance is a product of the density ρ and acoustic velocity w:

$$Z = \rho.w \quad . \tag{3.20}$$

The specific acoustic impedance is an intensive[2] material properties while the acoustic impedance depends on the material, geometry and frequency.

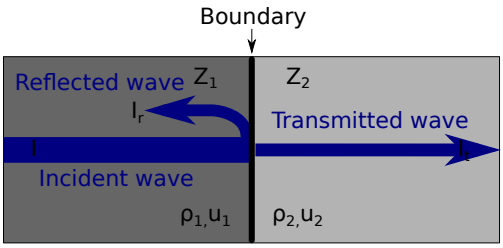

Figure 3.12: Reflection loss on a boundary

It is apparent from the Equation 3.19 that the highest transmission loses will be encountered when the sound travels from low acoustic impedance to a medium with high impedance. Gases have the lowest acoustic impedance, metals have very high impedance and liquids and some plastics are in between. Acoustic impedance of some selected materials can be found in Table 3.2.

[1] "Acoustic impedance and specific acoustic impedance are measures of the opposition that a system presents to the acoustic flow resulting of an acoustic pressure applied to the system. The SI unit of acoustic impedance is the Pascal second per cubic meter ($Pa \cdot s/m^3$) or the Rayl per square meter ($rayl/m^2$), while that units of specific acoustic impedance are Pascal second per meter ($Pa \cdot s/m$) or the $rayl$." [Wikipedia, 2015]

[2] An intensive property does not depend on the volume of a substance

Table 3.2: Acoustic impedance. The table was adopted from [Mea, 2018b]

Gas	Acoustic impedance $[kg.m^{-2}s^{-1}10^3]$	Liquid	Acoustic impedance $[kg.m^{-2}s^{-1}10^3]$	Material (solid)	Acoustic impedance $[kg.m^{-2}s^{-1}10^3]$
Air	0.4286	Water	1483	Polyethylene	1760
Ammonia	0.320	Fluorinert FC-40	1860	Mylar	3000
Argon	0.569	C_6F_{14}	860	Alumina	40600
Carbon dioxide	0.512	Gasoline	1000	Piezo ceramics	3000
Methane	0.308	Oil - castor	1430	PVDF	3900

The metal-gas boundary causes major losses since it reflects large portion of the sound passing through. For example, the acoustic impedance of aluminium is $40600\ kg.m^{-2}s^{-1}10^3$ and that of air is $0.43\ kg.m^{-2}s^{-1}10^3$, using Equation 3.18 one can calculate the reflection loss for this combination:

$$R = \left(\frac{0.43 - 40600}{0.43 + 40600}\right)^2 = 0.99996 \ . \tag{3.21}$$

It is apparent that almost all the sound energy is reflected and only very little is transmitted through. The metal-liquid boundary causes less significant loss to the transmitted sound signal. The acoustic impedance of water is $1483\ kg.m^{-2}s^{-1}10^3$ and the resulting transmission coefficient is then

$$R = \left(\frac{0.43 - 1483}{0.43 + 1483}\right)^2 = 0.86401 \ . \tag{3.22}$$

In other words, more than 86% of the signal is reflected and 14% passes through, this is much better result than for the air. The severe loss on the solid-gas boundary can be improved by adding one or several interfacing layers of a material with lower acoustic impedance. The so called matching layers located between the high impedance material of the piezo ceramics transducers and the gas are often composed of plastic material, aerogel or silicon rubber with lower acoustic impedance ([Kommareddy, 2003], [Alvarez-Arenas, 2013] and [Stosel, 2004]). Part of the incidence sound is reflected back on the boundary and the reflected wave interacts with the the incident one, Figure 3.13. The resulting interference can have intensifying of weakening effect depending on the phase. The transmission coefficient of a plate T_p is thus function not only of the acoustic impedance but also of the thickness of the layer D_p [Kommareddy, 2003]:

$$T_p = \frac{1}{\sqrt{1 + \frac{1}{4}(\frac{Z_1}{Z_2} - \frac{Z_2}{Z_1})^2 sin^2 \frac{2\pi D_p}{\lambda}}} \ . \tag{3.23}$$

The plate transmission coefficient is high when the thickness is equal to $1/4\lambda$, $3/4\lambda$, $5/4\lambda\, etc.$ where λ is the wave length of the incidence wave. Matching layers of $1/4\lambda$ thickness are common. A major drawback is immediately apparent, the matching layer limits the transducer bandwidth.

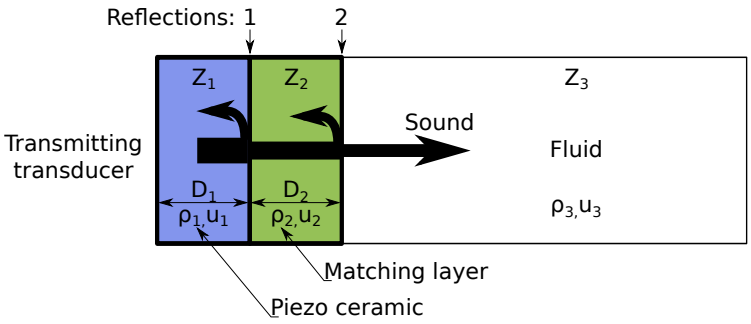

Figure 3.13: Reflection losses in transducer with matching layer

3.3.1 Piezoelectric transducers

The piezo transducers can be based on ceramic or polymers. Commonly used ceramics include Lead Zirconate-Titanite, Barium Titanate and some others. The polymeric materials are porous polymeric ferroelectret films, often made of polypropylene, polyvinylidene fluoride and some other. PVDF is a ferroelectric polymer polyvinylidene fluoride that is used for construction of piezoelectric transducers. Conveniently, only a low to moderate driving voltage is necessary to excite the piezo ceramic transducer. Ferroelectricity is a property of materials that have a permanent electric polarization and have a piezoelectric response. The PVDF transducers require higher driving voltage than the ceramic ones. The PVDF material is usually in a form a flexible film or sheet that exhibit piezoelectric effect, in other words the film deforms when an electric potential difference is applied. The thickness of the PVDF film spans from $9\,\mu m$ to $1\,mm$ and the properties of PVDF are stable up to $90°C$ [Mea, 2018a]. Another advantages are relative chemical inertness, mechanical strength and low acoustic impedance which ensures high sensitivity. The PVDF ultrasonic transducers have relatively flat frequency response when compared to piezo ceramics, however, some PVDF materials can have pressure sensitive resonant frequency [Álvarez Arenas, 2014].

The piezo transducers can be excited by square wave in simple applications although harmonics are introduced to the sound this way. This is not a problem for time-of-flight measurement. A sine wave excitation have to be used for some transducers to minimize harmonics that may excite the overtone mode (vibration at multiples of the resonant frequency). The piezo ultrasonic transmitters for ranging and other acoustic application typically dissipates $200\,mW\ RMS$. Typical driving circuit capable of transmitting any kind of signal (square, sine, sawtooth ...) consists of two bridged operational amplifiers with higher driving current capability, Figure 3.14. The bridge arrangement helps to excite the piezo transducer with signal of sufficient amplitude even when only a low voltage is available. In case of unipolar construction, shown in the Figure 3.14, both electrodes of the transducer are at the same potential which is not equal to the ground (GND) when idle. This offset of the amplifiers outputs is called virtual ground and it is usually set to $VCC/2$ by setting the divider resistor R6, R7 and R1, R2 to the same values. When a positive signal is introduced to the input of bridge amplifier, the IC1 acts as an inverting amplifier and sets its output proportionally below the offset and the IC2 sets its output proportionally above the offset through the feedback resistor R4. The excitation amplitude is therefore effectively doubled.

Receiving piezo transducers have a high impedance therefore they require an amplifier with very high input impedance. Either a JFET[3] transistor or operational amplifier can be used to convert the piezo charge to voltage. When dropped or upon impact, the piezo crystal can generate voltages that can be dangerous for sensitive JFET circuitry therefore a protection consisting of two anti-parallel clamping diodes connected in parallel with the transducers is recommended. In some cases, especially when long cables are used, a

[3] Junction field effect transistor

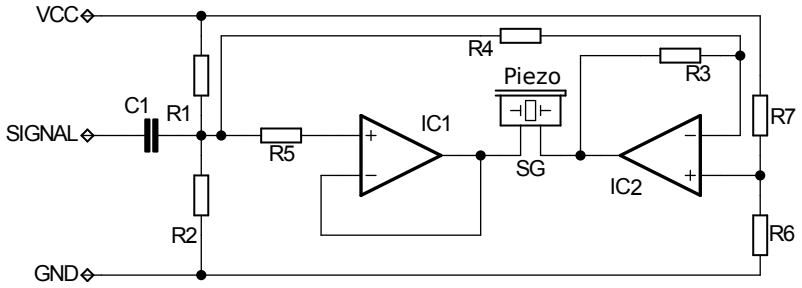

Figure 3.14: Typical driver for piezo transducers

simple JFET charge pre-amplifier is integrated into the transducer case or located nearby to increase the signal-to-noise ratio. There are many application lists and technical notes from semiconductor and transducer manufactures that deal with amplifiers and circuitry for interfacing piezo elements, for example [Mea, 2006, Karki, 2000]. The charge amplifier constructed with operational amplifier is a common front end for various sensors based on piezo elements with frequency range up to hundreds of kilohertz. For frequencies above one megahertz the voltage amplifier if preferred. The high frequency limit (cut of frequency) of the voltage amplifier is given only by the resistor and capacitor in the amplifier feedback while the high frequency limit of the charge amplifier is dictated by the capacitance of the transducer and connecting cable [Karki, 2000]. For the low frequency cut-off the situation is inverse. The advantage of the charge amplifier is that gain is not influenced by the capacitance of the transducer and connecting cable. The voltage amplifier is therefore used only when it can be located very close to the transducer.

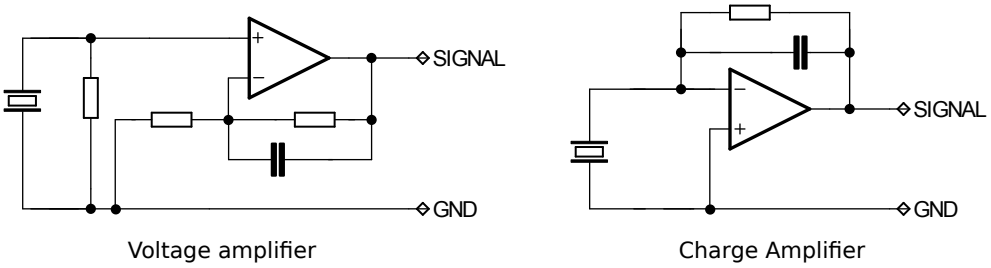

Figure 3.15: Amplifiers for piezo transducers

A simple model of the charge amplifier coupled via cable to a piezo transducer is shown in Figure 3.16. The transducer is modeled as a piezo crystal SG with charge Q and a parallel capacitance C2. The cable is represented by a capacitor C3 and resistor R2 while the charge amplifier is constructed with an operational amplifier IC1 with open-loop gain A and parallel combination of capacitor C1 and resistor R1 in the feedback.

The output signal U_{out} can be expressed as:

$$U_{out} = -\frac{Q}{C_1} \ . \tag{3.24}$$

Where the Q is the charge on the piezo element SG, the charge is a result of the pressure applied on the element which has certain sensitivity specified in Coulombs per Pascal. The time constant of the charge amplifier is $\tau_{RC} = R_1 \cdot C_1$. The upper cut-off frequency is

$$f_H = \frac{1}{2\pi R_2 \left(C_2 + C_3\right)} \ . \tag{3.25}$$

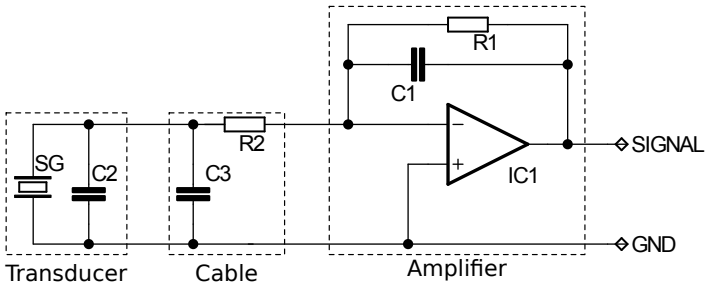

Figure 3.16: Charge amplifier for piezo transducers

Voltage amplifier is a typical non-inverting operational amplifier:

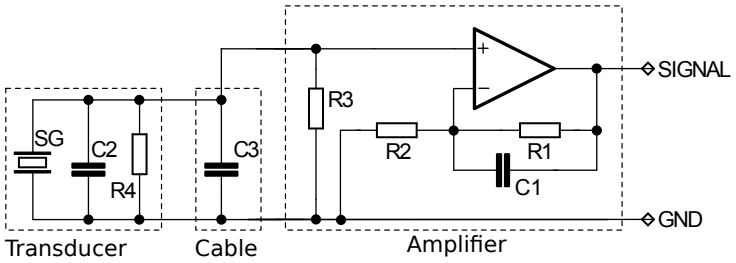

Figure 3.17: Voltage amplifier for piezo transducers

And the output voltage of such circuit is:

$$U_{out} = -\frac{Q}{C_2 + C_3}\left(1 + \frac{R_1}{R_2}\right) \quad . \tag{3.26}$$

The upper cut-off frequency f_H is

$$f_H = \frac{1}{2\pi R_1 C_1} \quad . \tag{3.27}$$

The piezoelectric elements used in the transducers can have various shapes, most common are circular discs but also strips and rings can be found in certain types of transducers. The discs have two main resonance modes: the radial and thickness mode, Figure 3.18. The piezo disc is excited either by an electric field applied on the disc electrodes or by a stress applied to the disc. The response in a form of a distortion (reverse piezoelectric effect) or polarization (piezoelectric effect) is linear.

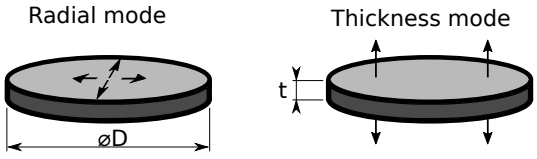

Figure 3.18: Resonant modes of piezo disc

The piezo ceramic materials are characterized by a radial, axial (thickness) and longitudinal frequency constants N_R, N_T and N_L . The radial f_R and thickness f_T resonant frequencies of the disc can be then evaluated from the dimensions of the element:

$$f_R = \frac{N_R}{\phi D} \ . \tag{3.28}$$

$$f_T = \frac{N_T}{T} \tag{3.29}$$

The thickness mode is the dominant resonance mode in acoustic applications while the radial modes that can be encountered at lower frequencies are undesirable. Typical frequency characteristic of piezo disc is shown in Figure 3.19. From the Equation 3.29 it is apparent, that the thinner the disc the higher the thickness resonant frequency.

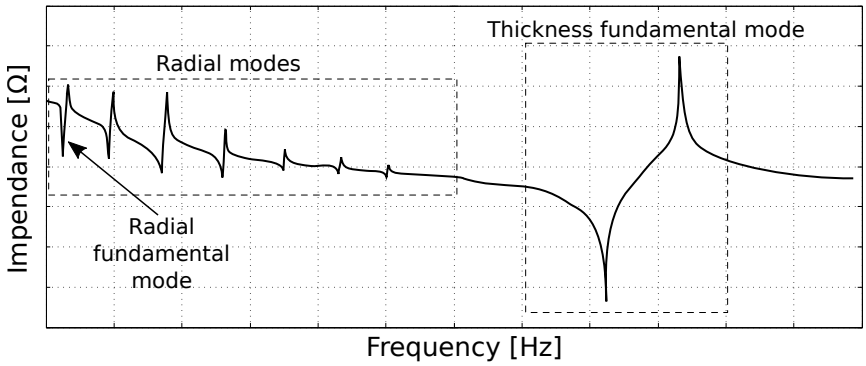

Figure 3.19: Resonant plot of piezo transducer

3.3.2 Electrostatic transducers

Thanks to their high sensitivity the electrostatic or capacitive transducers are the preferred type in applications with gases at frequencies up to one hundred kilohertz. They consist of a thin plastic diaphragm (polyvinyl or polyester) with a metalized layer on one side acting as an electrode. A metal back-plate is behind the non-metalized side of the diaphragm, Figure 3.21. A capacitor-like arrangement is thus created in the form of metal electrodes - back-plate and metalized layer - with the dielectric material in the middle. Such arrangement requires relatively high driving voltage when used as a speaker, and high bias voltage when used as a microphone. One example of a simple high voltage driver is shown in Figure 3.20. Driving square wave signal drives the transducers periodically to the ground by switching the transistor Q1. The circuit is designed for time of flight measurements where a short burst of few pulses is used. The circuit can be tuned so that the amplitude of the pulses in the burst decreases which can be advantageous for pulse-echo applications. The condenser C3 which stores the high voltage for the burst is charged via the resistor R3. If the resistance is high enough the charging rate is slow and the capacitor is being gradually discharged by every pulse in the burst and the pause between the burst is used to recharge it. The pulses in the burst have then decreasing amplitude as is shown on the right hand side of the Figure 3.20. The receiving circuit for electrostatic transducers is fairly simple, a high voltage bias is provided via the resistor and a decoupling capacitor or pulse transformer followed by a common voltage amplifier are used.

Unlike with the piezoelectric transducers, the resonance frequency of the electrostatic transducers is not given by the diameter of the membrane. Instead, the back plates are either grooved, micromachined or etched so that the membrane can vibrate on the back-plate surface pattern, Figure 3.22. A metal back-plate can have

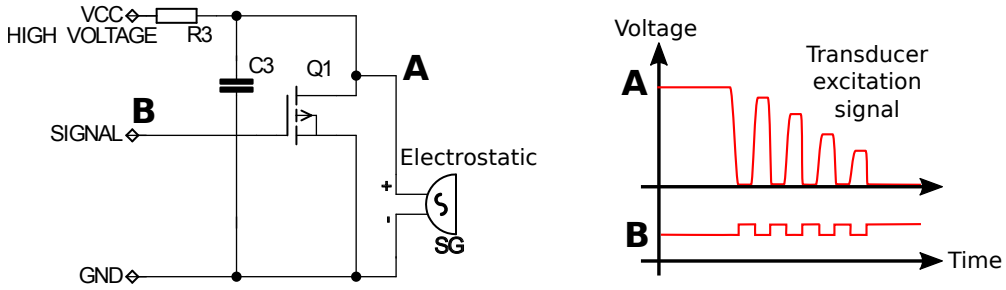

Figure 3.20: High voltage driver for electrostatic transducer

a circular v-groove pattern, so that the membrane can vibrate between the elevated rims of the v-groove, [Rafiq & Wykes, 1991]. For higher resonant frequencies, just the "natural" roughness of the surface of the flat metal back plate provides adequate pattern for the membrane resonance, Figure 3.21. This has been proved by experiments which demonstrated that the depth of the grooves or the depth of the surface roughness have no effect on the transducers resonance, Figure 3.22. It is the groove width or width of the "valleys" and "hills" on the rough surface together with membrane thickness and the applied bias voltage that determine the transducer resonant frequency, [Carr & Wykes, 1993]. The groove geometry has also an impact on the transducer sensitivity and bandwidth. The change of charge ΔQ on the electrostatic transducer can be calculated from the thickness of the air gap between the membrane and the plate L, change of the thickness due to movement of the membrane ΔL, membrane surface area A, permittivity of free space ε_0 and bias voltage U [Hutchins & Neild, 2012]:

$$\Delta Q = -\frac{\Delta L \epsilon_0 A}{L^2} U \quad . \tag{3.30}$$

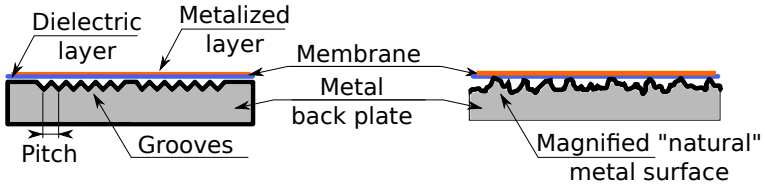

Figure 3.21: Construction of electrostatic transducer with different backing plates

For precise measurements in laboratory instruments, tailor-made transducers are sometimes used. A detail drawing of a custom electrostatic transducer together with a J-FET pre-amplifier is shown in Figure 3.23. The thin membrane is facing into the measurement chamber of a resonator and its metalized layer is electrically connected to the cavity body (2). The electrode behind the membrane is connected to the feedthrough connection (1) by a spring. The backplate is insulated from the body by a ceramic ring. An example of a high precision J-FET input amplifier for a bespoke transducer used in a spherical resonator is shown in in Figure 3.24.

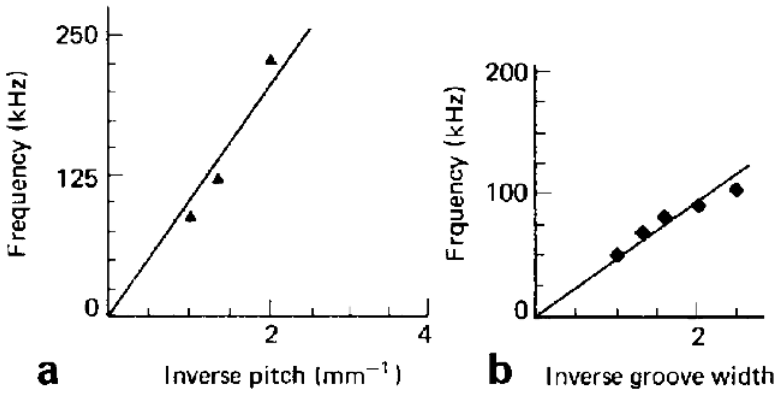

Figure 3.22: Resonant frequency of two electrostatic transducers with different back-plates [Carr & Wykes, 1993]

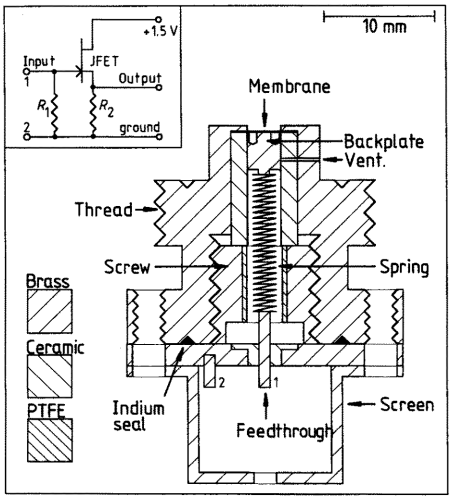

Figure 3.23: Custom made electrostatic transducer. The figure was adopted from [Ewing & Trusler, 1989b]

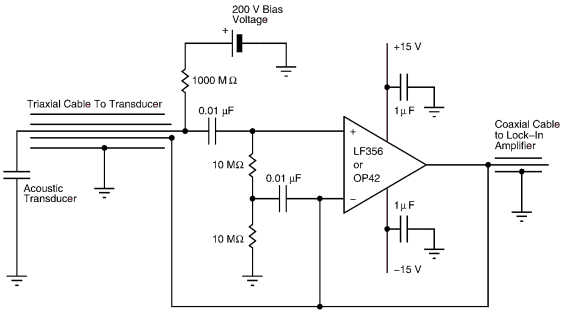

Figure 3.24: Input amplifier for electrostatic transducer used in spherical resonator. The figure was adopted from [Perkins & McLinden, 2015]

Bibliography

chapter 3: Speed of sound measurement

[Mea, 2006] 2006 (March). *Interfacing Piezo Film to Electronics*. Rev b edn. MEAS Measurement Specialties, 1000 Lucas Way, Hampton, VA 23666. Application Note 01800004-000.

[Mea, 2018a] 2018a. *Piezoelectric films technical information*. PIEZOTECH S.A.S. Polymeres pyro et piezoelectriques [Online; accessed 01-January-2016] `https://www.piezotech.fr`.

[Mea, 2018b] 2018b. *Tables of Acoustic Properties of Materials*. Onda, 592 Weddell Drive, Suite 7, Sunnyvale, California 94089, USA, `http://www.ondacorp.com/tecref_acoustictable.shtml`.

[Alvarez-Arenas, 2013] Alvarez-Arenas, T. E. Gomez. 2013. Air-Coupled Piezoelectric Transducers with Active Polypropylene Foam Matching Layers. *Sensors*, **13**(5), 5996.

[Assael *et al.*, 2014] Assael, M. J., Goodwin, A. R. H., Vesovic, V., & Wakeham, W. A. (eds). 2014. *Experimental Thermodynamics Volume IX*. The Royal Society of Chemistry.

[Boyes, 1992] Boyes, S. J. 1992 (February). *The speed of sound in gases with application to equations of state and sonic nozzles*. Ph.D. thesis.

[Carr & Wykes, 1993] Carr, H., & Wykes, C. 1993. Diagnostic measurements in capacitive transducers. *In:* [Carr & Wykes, 1993], 13–30.

[Ewing & Trusler, 1989a] Ewing, M. B., & Trusler, J. P. M. 1989a. Speeds of sound in CF4 between 175 and 300 K measured with a spherical resonator. *The Journal of Chemical Physics*, **90**(2), 1106–1115.

[Ewing & Trusler, 1989b] Ewing, M. B., & Trusler, J. P. M. 1989b. Speeds of sound in CF4 between 175 and 300 K measured with a spherical resonator. *The Journal of Chemical Physics*, **90**(2), 1106–1115.

[Gillis, 1994] Gillis, K.A. 1994. Thermodynamic properties of two gaseous halogenated ethers from speed-of-sound measurements: Difluoromethoxy-difluoromethane and 2-difluoromethoxy-1,1,1-trifluoroethane. *International Journal of Thermophysics*, **15**(5), 821–847.

[Goodwin *et al.*, 2003] Goodwin, A. R. H, Marsh, K. N., & Wakeham, W. A. (eds). 2003. *Measurement of the thermodynamic properties of single phases*. Experimental thermodynamics, vol. VI. Elsevier. ISBN 0-444-50931-3.

[Hess, 1989] Hess, P. 1989. *Photoacoustic, Photothermal and Photochemical Processes in Gases*. Vol. 46. Springer Berlin Heidelberg.

[Hutchins & Neild, 2012] Hutchins, D. A., & Neild, A. 2012. *Airborne ultrasound transducers*. Woodhead Publishing Limited.

[Jarvis *et al.*, 1996] Jarvis, G. K., Johnson, K. A., & Walmsley, S. L. 1996. An Annular Resonator Used To Measure the Speed of Sound in Gaseous Fluoroalkanes: Trifluoromethane and Hexafluoroethane. *Journal of Chemical & Engineering Data*, **41**(2), 222–230.

[Karki, 2000] Karki, J. 2000 (September). *Signal Conditioning Piezoelectric Sensors*. Texas Instruments. Application Report SLOA033A.

[Kazakov, 2008] Kazakov, V. V. 2008 (October 27-31). On particularities of choice of ultrasonic transducers features at air location. XX Session of the Russian Acoustical Society.

[Kommareddy, 2003] Kommareddy, V. K. R. 2003. *Air-coupled Ultrasonic Measurements in Composites*. Ph.D. thesis, Iowa state university. Retrospective Theses and Dissertations. Paper 236.

[Lopes *et al.*, 2014] Lopes, A. F.G., Talavera-Prieto, M. del Carmen, Ferreira, A. G.M., Santos, J. B., Santos, M. J., & Portugal, A. T.G. 2014. Speed of sound in pure fatty acid methyl esters and biodiesel fuels. *Fuel*, **116**(Complete), 242–254.

[Álvarez Arenas, 2014] Álvarez Arenas, T. E. Gómez. 2014 (May). Pressure sensitivity response of polymeric ferroelectret foam films. *Pages 1–4 of: Applications of Ferroelectrics, International Workshop on Acoustic Transduction Materials and Devices Workshop on Piezoresponse Force Microscopy (ISAF/IWATMD/PFM), 2014 Joint IEEE International Symposium on the*.

[Mehl & Moldover, 1982] Mehl, J. B., & Moldover, M. R. 1982. Precondensation phenomena in acoustic measurements. *The Journal of Chemical Physics*, **77**(1), 455–465.

[Pankaj & Bhatt, 2010] Pankaj, K. S., & Bhatt, S. C. 2010. Investigation of Acoustical Parameters of Polyvinyl Acetate. *Applied Physics Research*, **2**(1), 35–45.

[Perkins & McLinden, 2015] Perkins, Richard A., & McLinden, Mark O. 2015. Spherical resonator for vapor-phase speed of sound and measurements of 1,1,1,2,2,3,3-heptafluoro-3-methoxypropane (RE347mcc) and trans-1,3,3,3-tetrafluoropropene [R1234ze(E)]. *The Journal of Chemical Thermodynamics*, **91**(Supplement C), 43 – 61.

[Rafiq & Wykes, 1991] Rafiq, M., & Wykes, C. 1991. The performance of capacitive ultrasonic transducers using v-grooved backplates. *Meas. Sci. Technol.*, **2**, 168–174.

[Stosel, 2004] Stosel, R. 2004. *Air-Coupled Ultrasound Inspection as a New Non-Destructive Testing Tool for Quality Assurance*. Ph.D. thesis, Stuttgart university, Institut für Kunststofftechnik.

[Trusler, 1984] Trusler, J. P. M. 1984 (March). *The speed of sound in gases*. Ph.D. thesis, University of London, department of chemistry.

[Voleisiene & Voleisis, 2008] Voleisiene, B., & Voleisis, A. 2008. Ultrasound velocity measurements in liquid media. *Ultragarsas (ultrasound)*, **63**(4), 7–19. ISSN 1392-2114.

[Wikipedia, 2015] Wikipedia. 2015. *Acoustic impedance — Wikipedia, The Free Encyclopedia*. [Online; accessed 23-February-2016] `https://en.wikipedia.org/w/index.php?title=Acoustic_impedance&oldid=688890317`.

[Wilhelm & Letcher, 2010] Wilhelm, E., & Letcher, T. M. (eds). 2010. *Heat Capacities*. The Royal Society of Chemistry.

[Younglove & Frederick, 1990] Younglove, B. A., & Frederick, N. V. 1990. Sound speed measurements on gas mixtures of natural gas components using a cylindrical resonator. *International Journal of Thermophysics*, **11**(5), 897–910.

4 Problem statement and goals

4.1 Problem statement

A universal thermodynamic model (not necessarily but likely an equation of state) that would combine accurate prediction of the speed of sound and saturation properties of mixtures of unlike components across wide range of conditions does not exist. The very accurate equations of state carefully developed for pure fluid are available only for common fluids (including widely-used refrigerants). It takes a significant effort and large experimental data sets to fit such equations to new or less-common fluids. Unfortunately, sufficient data sets are seldomly available for such fluids. Universal models with few fluid-specific parameters (fitting parameters) such as the cubic equation of state or SAFT model can be used relatively easily for many different fluids although their accuracy varies widely. It is often the case that some models are applicable to blends of fluids from one family (hydrocarbons, hydrofluorocarbons) but fail when used for fluids from other families. At the same time the accuracy of many existing models in terms of prediction of speed of sound in both phases and also under saturated conditions is largely unknown for many common fluids.

When using the equations of state for mixtures, another parameters called binary interaction coefficients are needed to accurately predict saturation properties. For the most common mixtures (fluid pairs) and common equations of state these parameters are usually known, either they have been obtained by fitting experimental data or from molecular simulations. Since the values are unique for fluid pairs and the given model, there are many combinations for which the parameters are unknown, either because there are no experimental data or no one has ever fitted the parameters of the specific model (equation of state). Some more or less universal methods exists to estimate the interaction coefficients for some equations of state but the applications are often very limited and the accuracy is questionable.

4.2 Goals

In the previous sections I have outlined the scope and the motivation for this work. The problems addressed in this thesis are concentrated around the speed of sound measurement and real application of the thermodynamic modelling of cooling fluids used for particle detectors and high tech electronics cooling. The thesis consists of the experimental and theoretical parts.

The goals of the experimental part are:

- to design an apparatus for high accuracy speed of sound measurement that can provide high accuracy at lower complexity;
- to carry out speed of sound measurements in binary mixtures of R-116, R-218 and nitrogen since no such data exist in available literature and the mentioned binary mixtures have direct applications in the cooling systems of particle detectors.

The theoretical part includes modelling of vapour liquid equilibrium of pure fluid and various refrigerant mixtures with emphasis on the accuracy of the speed of sound prediction, the specific goals are:

- to benchmark various thermodynamic models on representative sets of pure fluids and mixtures in order to find the applicability range of the saturated properties and speed of sound predictions;

- to develop new correlations for the prediction of binary interaction coefficients for mixtures of unlike fluids with emphasis on fluorocarbons that will allow to work more accurately with blends for which no experimental data or molecular simulation exist. The correlations shall be applicable to model for which no group-contribution methods (that would allow the estimation of the binary interaction coefficients) are available. The developed correlation will therefore be the only way for prediction of the interaction coefficients for this model.

5 Development of high accuracy speed-of-sound measurement apparatus

I began the development of the apparatus together with the data acquisition in my Bachelor thesis [Doubek, 2012], I have continued the work in my Master's thesis [Doubek, 2014] and this chapter describes the latest development that lead to the current instrument that can be used for mixtures and that delivers accuracy close to resonators as shown in chapter 5.8.

The goal from the very beginning was to develop an instrument for high-accuracy measurement of speed of sound in gases over wide range of temperature and pressure. The time-of-flight measurement method was selected for the measurement apparatus due to its relative simplicity and low cost. The developed setup includes control system that allows for semi-automated measurement of the speed of sound along isochors but also along isotherms due to a precise temperature control. The speed of sound data on isotherms are essential for the derivation of ideal gas heat capacities.

The use of capacitive ultrasound transducers was inevitable due to their high sensitivity on acceptance. Standard piezoelectric transducers were also tested but they have very low sensitivity, exhibit long ringing and generally are not suitable for applications in gases where a high precision triggering on the received signal is needed. Senscomp 600 transducers (previously made by Polaroid) were selected to be used from the few available models. This type of transducers is most sensitive at $50\,kHz$ although the frequency response is fairly flat between $40\,kHz$ and $100\,kHz$. The gold-plated membrane ensures good corrosion and chemical resistance.

I have used the ELMB data acquisition system for temperature and pressure sensor readout together with my custom made electronics which takes care of the actual speed of sound measurement. The SCADA software running on dedicated computer is in charge of data visualization and archiving as well as temperature regulation and other control functions.

5.1 Setup Overview

The new setup allows for preparation of binary mixtures directly inside the measurement cell. Two gas cylinders provide the pure gases (mixture components) A and B, Figure 5.1. Since the setup is intended for refrigerants the pressures inside the gas cylinders are not supposed to be very high and therefore pressure regulators on the cylinders are not needed. Omitting the pressure regulator eliminates complicated purging procedures to prevent gas contamination from air or other gases trapped inside the regulators. Since the pressures inside the gas cylinders were expected to be different in each cylinder (mixing of two different refrigerants at room temperature) there was a risk of contamination of the gas inside the cylinder at the lower pressure due to wrong manipulation with valves in the setup. Two accumulators (coils of 1.5 meters of $12\,mm$ tubing) were provided for each gas to store some amount of the pure gas so that the gas cylinders could be shut off with cylinder valves during the preparation of the mixtures. With this arrangement only the gas inside the accumulator would be contaminated while the gas in the cylinder would remain intact. The pressure inside each accumulator was monitored with a pressure sensor. The high precision Keller 33X pressure sensor was used to monitor the pressure inside the measurement cell. The temperature inside the cell was monitored by Pt1000 Class A sensors manufactured by IST Innovative Sensor. The rotary oil vacuum

pump was used to evacuated the cell and both accumulators before the preparation of each mixture. The three-way valve in front of the pump was used to shut-off the pump and to allow atmospheric air to break the vacuum at the pump suction preventing the oil from the pump to be sucked inside the piping.

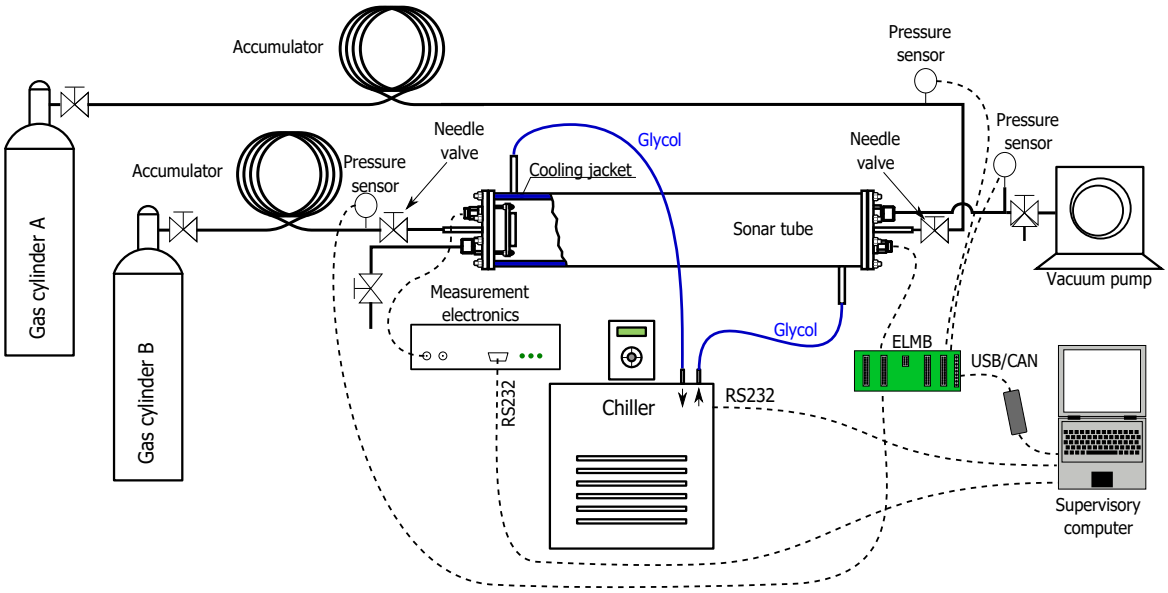

Figure 5.1: Constructed measurement setup for mixtures

The temperature of the measurement cell was controlled by liquid bath chiller filled with glycol. The glycol circulated through the double wall of the measurement cell. The ELMB data acquisition system was connected to the computer via USB/CAN interface while the speed-of-sound measurement electronics communicated via the serial port.

The WinCC SCADA environment running on the computer was executing custom scripts I had written specifically for this application. The scripts provided data archivation in SQL-like database, data visualization through various charts and graphical panels and temperature regulation of the chiller. The fine-tuned PI regulation was needed to repeatedly achieve temperature precisely equal to the provided set point inside the measurement cell despite changes in room temperature.

All the instrumentation was installed in a rack with the measurement cell mounted vertically to save space, Figure 5.2. One can notice the thick insulation that is necessary for measurements at low temperature but the proper insulation also helps to achieve better homogeneity of the temperature along the cell.

5.2 Mechanical design

The measurement cell is a stainless steel tube with flanges on both ends, Figure 5.3. The length of the cell is $560\,mm$ and the diameter is $120\,mm$. The tube has two coaxial walls, the cooling/heating fluid circulates in the space between the walls in order to maintain the gas inside the tube at the desired temperature ("cooling jacket"). Each flange has two connection ports, one is realized as a$12\,mm$ weld fitting and the second is a $8\,mm$ welded tube stud. The fittings are used to connect the vacuum pumps, pressure sensor and for gas release to decrease the pressure inside the cell. The tube studs welded to the middle of the flanges are used to introduce the investigated gases. Needle valves are used to precisely gauge the amount of gas to be added, the valves must be placed as close to the test cell as possible, see section 5.4 for more details. A sealed electrical connector in each flange interconnects the data acquisition system with the sensors and the

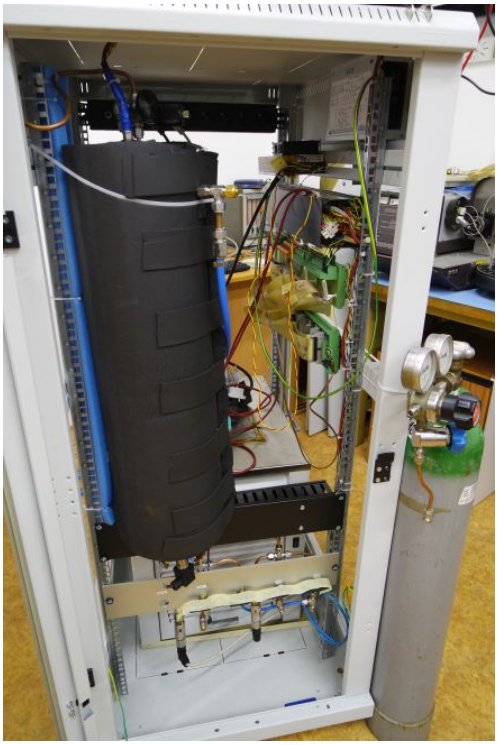

Figure 5.2: Constructed setup inside a rack

ultrasound transducers inside the tube. The flanges are sealed with indium seals which ensure leak tightness even at very low temperatures.

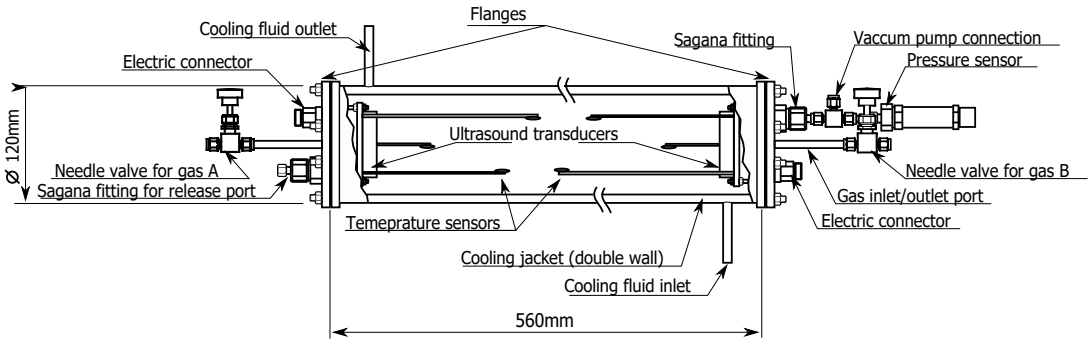

Figure 5.3: Measurement cell

5.3 Electronics

I started the development of the speed-of-sound measurement electronics in my Bachelor's and Master's thesis, the first prototype was simple with one channel and single triggering. In this work I have continued the development in pursuit of higher accuracy using more advanced design and high speed components. This section is focused on description of the improvements to the triggering mechanism which the unique key element that ensures the high accuracy of the time-of-flight measurement.

The general block schematics of the electronics I have designed for the time-of-flight speed of sound measurement are in Figure 5.4. The electronics is based on ATmega1248 microcontroller that is equipped with two 16 bit counters clocked at $20\,MHz$. Each counter has an input capture unit which is used to measure timing of external events. The frequency of $20\,MHz$ provides time resolution of $50\,ns$ but due to delays in the time input circuits the effective resolution is $100\,ns$.

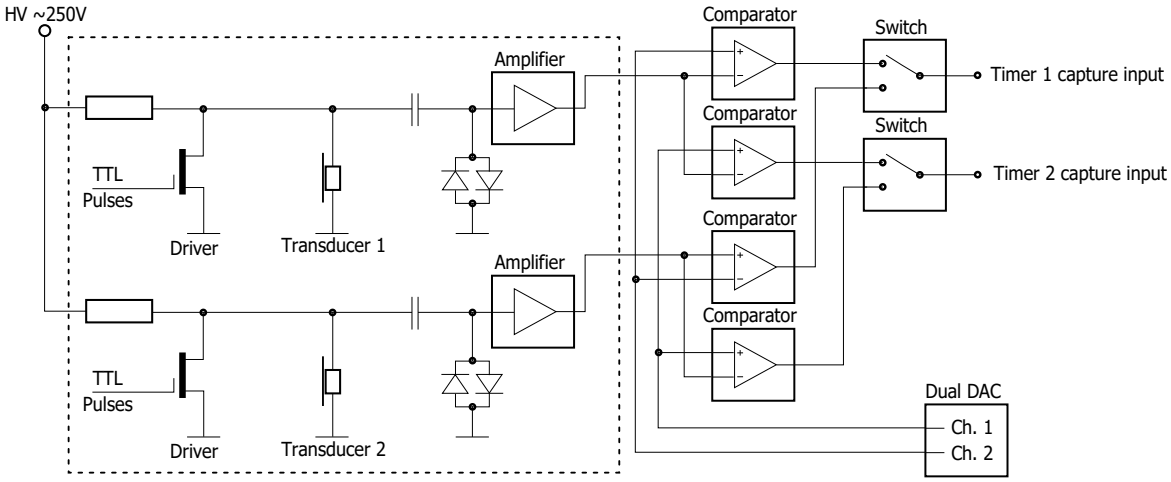

Figure 5.4: Block diagram of measurement electronics

There are two identical analog channels, each for one of the transducers. The drivers that make the transducers transmit a burst of ultrasound pulses are fairly simple. A high voltage FET transistor is driving the bias voltage to the ground through current-limiting resistor. Since the current flowing through the transistor is very low it is possible to drive the gate with TTL pulses directly from the microcontroller. There is a separate high speed amplifier in the inverting configuration for each transducer. The drivers and amplifiers are located on separate piggy board so that they can be replaced with different design during testing and prototyping, this separate module for the analog channels is visible in Figure 5.5. The amplifiers are decoupled with mica capacitors and protected with back to back diodes. The amplified signal from each channel is then compared with two threshold levels generated by a DAC (Digital to Analog Converter). The ultra high speed comparators AD8561 with $7\,ns$ delay were used for this purpose. All the amplifiers and comparators are powered with symmetric supply $\pm 5\,V$.

Figure 5.5: Speed-of-sound measurement electronics

The selection of the input amplifier is important to achieve stability and minimum signal delays. The common operational amplifiers are too slow, the signals delays are clearly visible in the measured times of

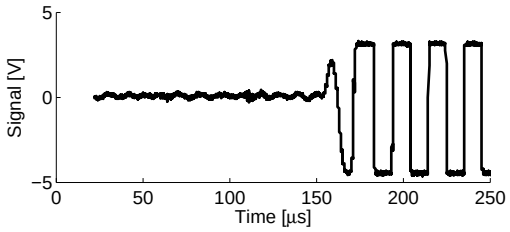

Figure 5.6: Received signal

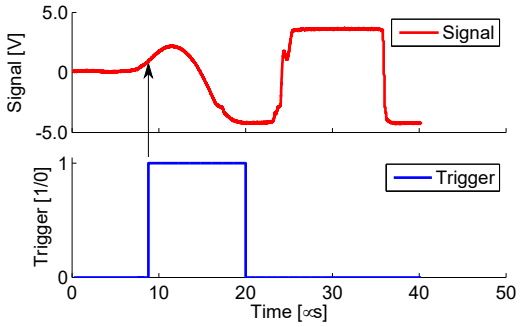

Figure 5.7: Trigger on received signal

flight. On the other hand, high speed operational amplifiers with too much bandwidth are noisy, unstable and often very expensive. Most of the high speed amplifiers for special applications come in 8-pin DIP sockets. After testing several high speed amplifiers, the most suitable one for this application seemed to be LT1220. The amplifier gain was set to 100 and the DC blocking capacitor of $220\,pF$ provided the optimal frequency response.

In order to achieve the best signal-to noise ratio, the ultrasonic transducers were connected to the electronics with high voltage shielded twisted pair cable with BNC connectors. Even though it was possible to reduce the electric noise to very low levels when the transducers were disconnected, some noise was always present when the transducers were connected. The frequency of the noise was approximately $50\,kHz$ and after some investigation it turned out that it was caused by vibration of the transducer membranes that were excited by tiny vibration from the environment (people working around the setup, fluid flowing through the measurement cell double wall, chiller fridge running nearby etc.). Unfortunately, this noise did not disapper even after attempts to isolate the measurement cell from the table vibrations with dampening foam.

The level of this noise in comparison with the received $50\,kHz$ ultrasound after amplification is shown in Figure 5.6. Fortunatelly, with proper grounding and shielding the actual received ultrasound signal was clear of any noise or superimposed signals even after amplification as can be seen in Figure 5.7. The triggering on the first rising edge of a clear signal thus exhibited minimal jitter.

If only one threshold level is used for the triggering it must be set above the noise to prevent false triggers. However, the higher the level the higher the delay between the moment when the ultrasound pulses arrive (ultrasound transition time) to the transducer and when they are actually detected. If this delay was constant under every measurement condition it would be eliminated by calibration. Unfortunately, it is not constant, slight changes in the slope of the rising edge with pressure and density translate into significant timing errors. For this reason, the two threshold levels are used. The first level is set just above zero while the other is set relatively high. The first threshold does not clear the noise level but it does not matter since it is only the crossing of the higher level that can trigger the time measurement. Every time the lower level is crossed a time (counter state) is stored but no event is generated. Only when the higher level is crossed the last stored value of the lower threshold crossing is used for the time-of-flight calculation.

It turned out that even the use of two threshold times cannot provide the desirable accuracy that would be guaranteed under wide range of conditions (pressure, temperature, type of gas). By studying the variations of the received signal under different conditions I have developed a correction that can be applied to the measured transition time (low threshold) in order to increase the timing accuracy. Three crossing times are recorded on the lower threshold level; first rising edge, first falling edge and second rising edge. These three crossing times are used to obtain the t_x and T values as shown in Figure 5.8 for the threshold level of $210\,mV$.

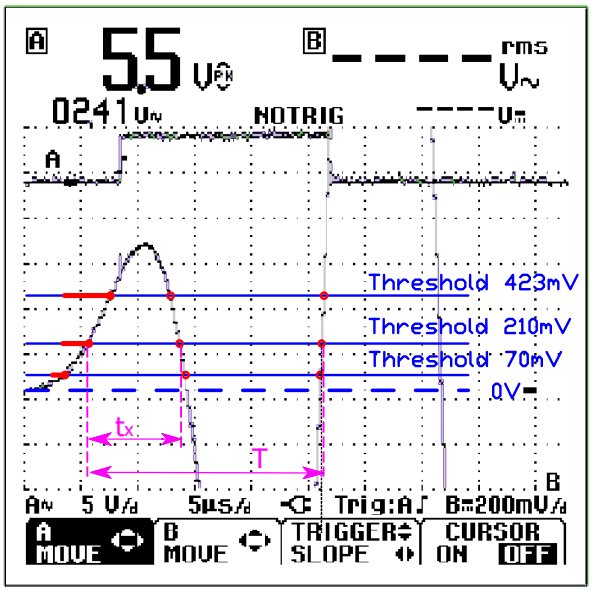

Figure 5.8: Correction of triggering on first received rising edge

The correction c_t is then calculated as follows:

$$c_t = \left(\frac{T}{2} - t_x\right) \quad . \tag{5.1}$$

The Figure 5.8 shows corrections (red bold lines) for three different threshold levels (blue lines). Notice how the correction for $70\,mV$ corresponds to the very beginning of the signal rising edge. The great advantage of this approach is that only time measurements are needed. It is not necessary to measure the amplitude of the signal which would significantly complicate the design of the electronics. The measured transit times T, the resulting correction c_t and the corrected transition time are showed in Table 5.1. The lines in the table represent subsequent measurements in one-second intervals at stable conditions. The $70\,mV$ threshold represents the typical value used for the measurements, one can see that the variations in the corrected transit times are about $125\,ns$. This shows that the correction, which is based on three time measurements, does not introduce too much jitter into the resulting transit time.

Table 5.1: Corrected transition times for different threshold levels

T $[\mu s]$	c_t $[\mu s]$	T_{time} $[ms]$	T $[\mu s]$	c_t $[\mu s]$	T_{time} $[ms]$	T $[\mu s]$	c_t $[\mu s]$	T_{time} $[ms]$
Threshold 423 mV			Threshold 210 mV			Threshold 70 mV		
18.15	3.875	0.645575	21.05	1.925	0.645575	22.35	1.075	0.644775
18.20	4.350	0.645350	20.65	2.075	0.645825	22.35	1.075	0.644725
18.35	4.625	0.645625	20.40	2.200	0.645400	22.55	0.925	0.644675
18.50	4.650	0.645450	20.35	2.225	0.645925	22.40	1.050	0.644750
18.85	4.025	0.645625	20.85	2.125	0.64565	22.70	0.900	0.644650

5.4 Design optimization for mixtures

The first attempts to measure the speed of sound in a mixture prepared inside the measurement cell provided results quite far from the expected speed of sound. It took hours for the measured speed of sound to stabilize even though the temperature and pressure were stable (since the pressure was stable the gradual change in the speed of sound was not caused by a leaking valve). Whether the measured speed of sound was slowly decreasing or increasing depended on the order of the mixture components injections. I have studied the behaviour with R-218+N_2 mixture.

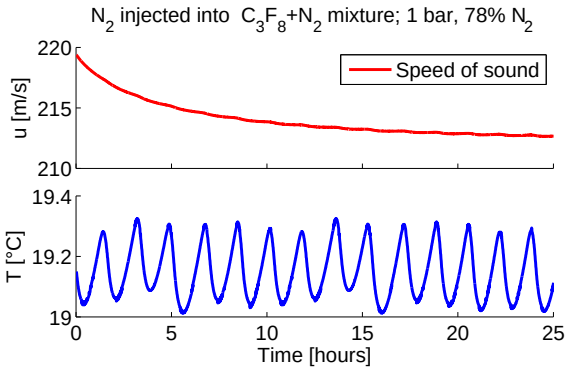

Figure 5.9: Speed of sound after mixture preparation - injecting N_2

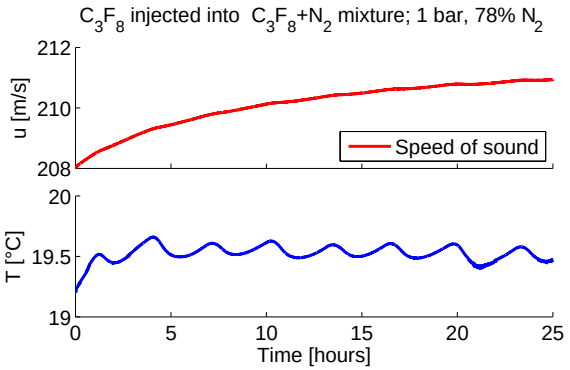

Figure 5.10: Speed of sound after mixture preparation - injecting R-218

When nitrogen was injected inside the measurement cell filled with R-218 the speed of sound kept decreasing during a whole day, Figure 5.9. When R-218 was injected into nitrogen the speed of sound kept increasing, Figure 5.10. It was apparent that the two components were mixing very slowly by diffusion, perhaps due to trapped volumes (virtual leaks) inside the measurement cell. Obviously, this has not been observed with the pure gases that were measured before the mixtures. I have significantly reduced the length of all the connection pipes for the pressure sensor, vacuum pump, safety relief valve and the mixing needle valve so that all the valves were as close to the measurement cell as the insulation allowed. Further, I filled the dead space of the threaded blind holes in the flanges with indium and removed all the unnecessary insulation from the electric connections inside the measurement cell. The effect of reduced virtual leaks was immediately apparent as the speed of sound stabilization time reduced from hours to seconds, Figure 5.11.

Another concern was the stratification of mixture components with large differences in molecular weights. A test carried with mixture of 52 R-218 and 48% of R-116 with the measurement cell mounted vertically did not reveal any changes in speed of sound even after more than 15 hours, Figure 5.12. Any subsequent measurement did not reveal a possible stratification therefore it is possible to mount the measurement cell vertically.

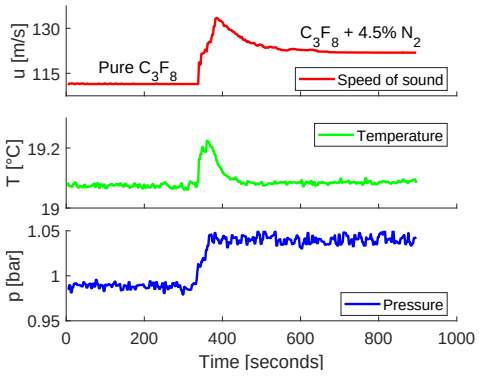

Figure 5.11: Speed of sound after mixture preparation - modified measurement cell

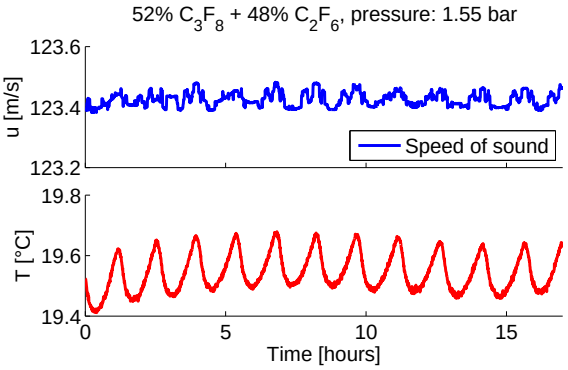

Figure 5.12: Stratification test with vertical test tube

5.5 Calibration and measurement procedure

The calibration was carried out before the actual measurement, the calibration is the same no matter if the instrument is used for pure fluids or mixtures. The result of the calibration was a linear relationship of the calibrated distance D and temperature T. Although a good insulation together with careful positioning of the temperature sensors helped to minimized the impact of temperature variations along the ultrasound fly path, the temperature distribution inside the measurement tube is not perfect since the cooling/heating fluid exhibits a temperature gradient along the length of the tube (fluid inlet is on one side of the tube and outlet is on other side) and the flanges do not have any fluid passages. The average of all the six sensors inside the tube was used for the calibration and all the presented measurements. The slope of the obtained linear relationship agreed with the coefficient of thermal expansion stainless steel (material of the measurement tube) confirming that placement of the temperature sensors was chosen well as it represented the average temperature distribution along the sound tube.

There was no clear correlation between the pressure and the distance D. Although the pressure has some impact on the length of the tube it also affects the shape of the signal from the receiving transducer. The two effects interact and mostly cancel each other in the range of pressures used for the calibration.

Nitrogen was used for the calibration since high purity samples are readily available and due to the fact that the speed of sound in nitrogen can be calculated with very low uncertainty using equation of state implemented in the NIST REFPROP [Lemmon *et al.*, 2018],

In total, 281 data points were obtained for the calibration with nitrogen in the temperature range from $-22.1°C$ to $51.5°C$ and pressure range from $0.94\ bar_{absolute}$ to $2.7\ bar_{absolute}$, Figure 5.13. The range of the measured transition times was from $1.348\ ms$ to $1.534\ ms$. The calibrated distance was calculated from the speed of sound from NIST REFPROP for each data point separately and linear regression was used to obtain the distance as a function of temperature, Equation 5.2. The uncertainty of the linear fit is $\pm 0.4\%$.

$$D\,[m] = \left\{T\,[°\mathrm{C}]\cdot 5.2226\cdot 10^{-6} + 0.4957\right\}\ \pm 0.4\%. \tag{5.2}$$

5.6 Measurement uncertainty

The type A uncertainties u_A of the measured pressure, temperature and speed of sound are listed in Table 5.2. This uncertainty is a standard deviation of three hundred samples recorded by the ELMB data acquisition

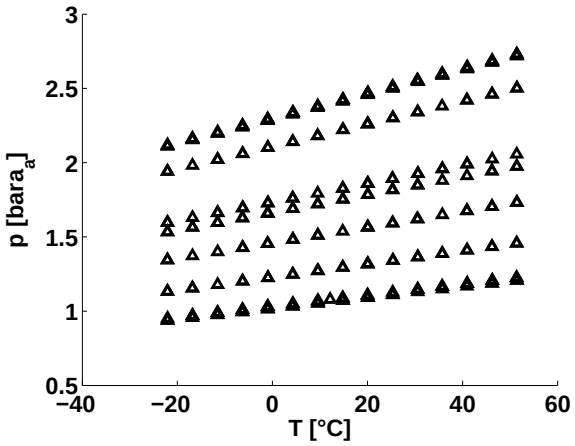

Figure 5.13: Data points used for the calibration (nitrogen)

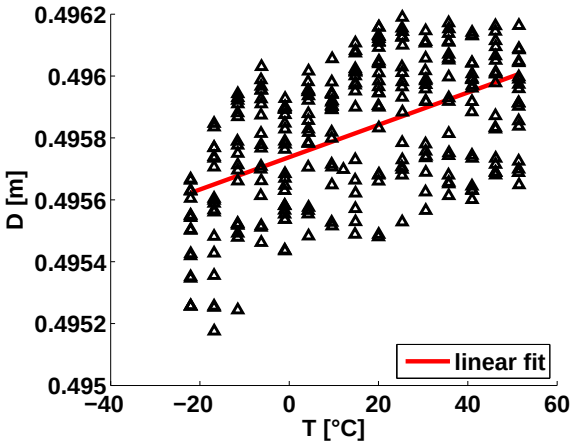

Figure 5.14: Calibrated distance D

system over an interval of five minutes. The type B uncertainties u_B of the temperature and pressure measurements correspond to the sensor calibration uncertainties taken from the data sheets.

Additional measurement error is introduced by the inhomogeneity of the temperature distribution inside the 500mm-long tubular measurement cell. Six temperature sensors distributed along the sound path were used in order to reduce this error as much as possible. The temperature distribution is homogeneous when the measurements are carried out at the ambient temperature but the measurement error increases when the temperature of the cell is increased or decreased since the cooling jacket is not perfectly symmetric and the end flanges are not in contact with the cooling liquid. To account for the temperature inhomogeneity the combined uncertainty of the temperature measurement was expanded by coverage factor of 3. The pressure transducer 33X manufactured by Keller had a usable range of $0.3\,MPa$ and the type-B uncertainty of the pressure is given by the full scale and reading uncertainty. The type-B uncertainty of the temperature measurement comes from a calibration of the internal Pt1000 sensor which was carried out against the precise Tinsley Pt25 thermometer.

The speed of sound is obtained from the calibrated distance, which is a function of temperature, and the measured time of flight. The uncertainty of the calibrated distance is much higher than the uncertainty of the time measurement despite the precise calibration procedure described in the previous section. The time measurement itself is precise and fairly straightforward: a crystal provides the $24.000\,MHz$ for the counter and the trigger delay can be evaluated with high precision due to the use of ultra-high $7\,ns$ speed amplifiers and comparators. In contrast, there is a lot of sources of error that influence the calibrated distance and even though some of them cancel themselves out the calibrated distance is the main source of uncertainty that influences the resulting speed of sound. The type-B uncertainty of the speed of sound is thus given predominantly by the uncertainty of the calibrated distance which is a result of a linear regression of the transit times, measured at different temperatures in nitrogen, and the speed of sound predicted with uncertainty of 0.005% using NIST REFPROP [Lemmon *et al.*, 2018] . The coverage factor of two was used for the expanded uncertainty U of the speed of sound to accommodate for a variation in slew rate of input amplifier. The measurement uncertainties are summarized in Table 5.2

The composition of the prepared mixtures and the purity of the fluid are often the biggest sources of error in the speed of sound data. The fluid purity was verified by chromatography which was carried out by the producers before shipping, Table 5.3. The composition of the prepared mixtures was evaluated based

Table 5.2: Measurement uncertainties

		u_A	u_B	u_C	U
Temperature	K	0.013	0.03	0.03	0.1
Pressure	Pa	19	300	301	
Speed of sound	m/s	0.008	0.04	0.05	0.09
Composition	%		0.15	0.15	

on the mixing partial pressures that were corrected with compressibility factors. The uncertainty of the mixture composition is thus combination of pressure measurement uncertainty and the uncertainty of the compressibility factors.

A short fundamental equation of state developed by Lemmon and Span [Lemmon & Span, 2006] was used to obtain the compressibility factors of R-116, R-218 and $N_2$with uncertainty of 0.5. The composition uncertainty is the same for both mixtures since very similar mixing procedure was used. Firstly, the evacuated measurement cell was filled with the R-218 and then small amount of the second component (R-116 or N_2) was added. A correction has to be made since the partial pressure of the pure component that is filled first is not equal its partial pressure in the mixture after the second component is added. This is due to the compressibility being different from unity. The actual partial pressure of the first component in the mixture is to the pressure after filling multiplied by the compressibility factor at the total pressure of the mixture.

Table 5.3: Purity of the fluids in cylinders that were used for measurement

Fluid	Source	Mass fraction purity	Analysis method
C_2F_6(R-116)	Air Liquide	>99.99%	Gas Chromatography
C_3F_8(R-218)	Astor	>99.99%	Gas Chromatography
N_2	Linde	>99.99%	Gas Chromatography

5.7 Measured data

New and unique data for mixture R-218+R-116 and R-218+N_2 are reported here. These mixtures were chosen since they are of high interest for the cooling applications at CERN as is discussed in first chapter 1, the obtained data are used for model evaluation in the chapter 6. The measurement of the speed of sound in the reference pure fluids R-218 and R-116 without the transit time corrections, uncertainty analysis and comparison with similar data from literature was reported in my Master's thesis [Doubek, 2014]. The new comparison shows that with the correction, the developed apparatus is achieving accuracy close to the spherical resonators which are the most precise speed-of-sound measurement instruments. The speed of sound measured in the mixtures can be thus used for models evaluations.

The measurement of the mixtures was semi-automatic. Firstly, the measurement tube was evacuated and flushed with a small amount of the prevalent mixture component in order to prevent contamination and ensure purity of the investigated sample. The tube was then filled with the prevalent mixture component and when the temperature inside the tube stabilized the pressure was noted down and the other component was added. The final pressure of the mixture was noted down after the temperature stabilized again and an automatic measurement procedure was started. The control algorithm was adjusting the temperature set point of the liquid bath chiller and when a stable predefined temperature was achieved 300 readings of the speed of sound, pressure and temperature were taken during 5-minute long interval. All the data points on one

isochore across the whole temperature range were obtained during one measurement cycle. A pressure inside the measurement tube was then decreased and the whole cycle was repeated.

I have obtained vapour-phase speed of sound for two mixtures: 5.6 molar R-116 in R-218 and a mixture consisting of R-218 and 6.4 molar nitrogen. On average, more than 330 data points were measured for each mixture. The pressure and temperature ranges of the acquired data sets are from $0.06\,MPa$ to $0.3\,MPa$ (absolute), and from $-22°C$ to $+52°C$ as shown in Figures 5.15 and 5.16. The range of the acquired speed of sound was from 102.5 to $144.8\,m\,.\,s^{-1}$. Each data point was acquired twice, once in a measurement cycle with increasing temperature and then during a cycle with decreasing temperature. Fifteen isotherms were obtained for each fluid. The standard deviation of the data point temperatures on each of the isotherms was lower than 0.052 K. The Peng Robinson equation of state discussed in the chapter 6 was used to obtain the vapour density ρ from the temperature and pressure values of each data point to illustrate the isochors and density range of the measurement. The calculated vapour-phase density should be within 1 from a true value based on comparison of the Peng Robinson equation of state prediction with existing vapour density measurement of pure refrigerants under similar conditions.

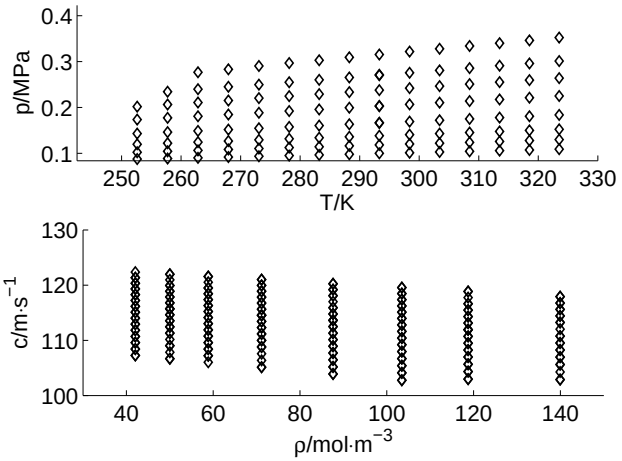

Figure 5.15: Speed of sound measured in mixture of R-218 and 5.6% R-116

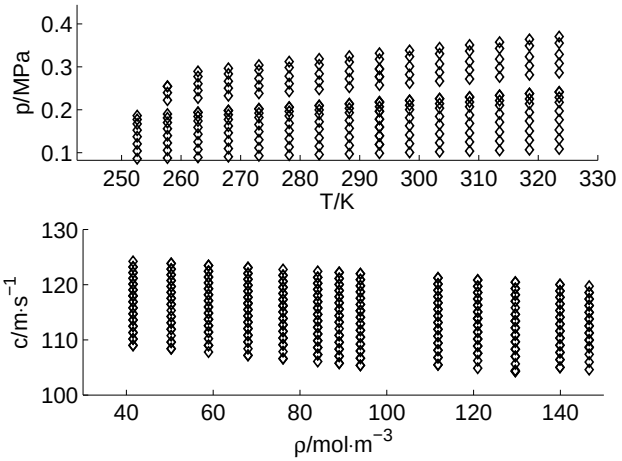

Figure 5.16: Speed of sound measured in mixture of R-218 and 6.4% N_2

As is customary, the measured data were correlated with the acoustic virial equation, Equation 2.10. The zero-density heat capacity ratio γ^{id0} was determined from a linear extrapolation of the measured speed of sound to zero density and the value of the second acoustic virial coefficient B_a was obtained for each isotherm. The results are listed in Table 5.4. The average deviation of the obtained fit is 0.008. The fitted acoustic virial equation allows for interpolation between the measured data points since the fitted acoustic virial coefficients B_a are smooth function of temperature, as can be seen in Figure 5.17.

Table 5.4: Second acoustic virial coefficients obtained from correlation of the measured data

T [K]	B_a $[1e^6 * m^3/mol]$			
	R-218	R-116	5.6% R-218 94.4% R-116	93.6% R-218 6.4% N_2
252.0	-1327.3	-606.67	-1292	-1203
262.0	-1206	-558.23	-1178	-1086
272.0	-1103.8	-515.18	-1079	-996
282.0	-1014.2	-476.14	-990	-916
292.0	-934.34	-440.73	-914	-847
302.0	-863.47	-408.81	-840	-777
312.0	-800.33	-379.79	-777	-718
322.0	-741.14	-351.99	-722	-664

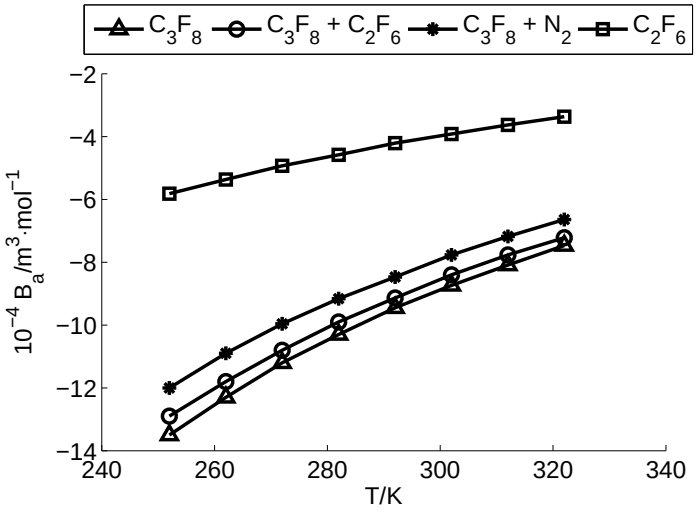

Figure 5.17: Acoustic virial coefficients obtained through regression of the experimental data

5.8 Comparison of measured data

The new corrected data of the speed of sound in pure fluids were compared to several data sets from literature. Hurly used cylindrical resonator in [Hurly, 1999] and [Hurly *et al.*, 2003] while Jarvis used annular resonator [Jarvis *et al.*, 1996] to measure speed of sound in R-116. Data set obtained by [Vacek *et al.*, 2013] with previous, less precise, version of the presented apparatus is also included in the comparison. The R-116 speed of sound data points are shown in the top plot in Figure 5.18. The uncertainty of the speed of sound measured with the cylindrical resonator is claimed to be 0.01% while the uncertainty for the annular resonator is claimed to be 0.05%. The data set by [Hurly, 1999] is by far the most accurate, for this reason it was taken as a reference for comparison with all other datasets. The bottom plot in the Figure 5.18 shows the deviation w_{diff} between the speed of sound correlation w^{virial} of data by [Hurly, 1999] and the other data sets. The deviation w_{diff} was calculated as follows:

$$w_{diff}[\%] = \frac{w_i - w^{virial}}{w_i} 100 \ . \tag{5.3}$$

The coefficients of the acoustic virial equation used to correlate the speed of sound data from the cylindrical resonator in [Hurly, 1999] were fitted by the authors and the fit represents the original dataset with accuracy better than 0.1%. The comparison shown in the Figure 5.18 reveals that the difference between the data obtained with the cylindrical and annular resonator is very high considering the claimed uncertainties of 0.04% and 0.05% respectively. The average deviation of the speed of sound data from the cylindrical resonator ([Hurly *et al.*, 2003]) is 0.33% while the average deviation of the data from this work with the data from the cylindrical resonator is 0.25%.

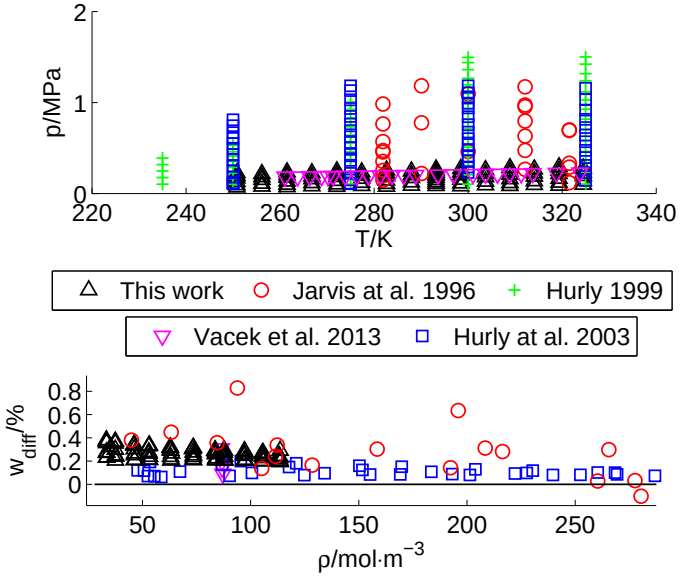

Figure 5.18: Comparison of experimental data of speed of sound in gaseous R-116

A comparison of the speed of sound measured in R-218 is shown in Figure 5.19. The speed of sound measured using the instrument described in this work was taken as a base line and two data sets obtained with older and simpler time-of-flight instrument [Vacek *et al.*, 2001, Vacek *et al.*, 2013] were included in the comparison. The correlation in form of the virial equation of state described in the section above was used

to compare the data sets. It is clearly visible that the apparatus used by [Vacek *et al.*, 2001] exhibits large spread of the measured data.

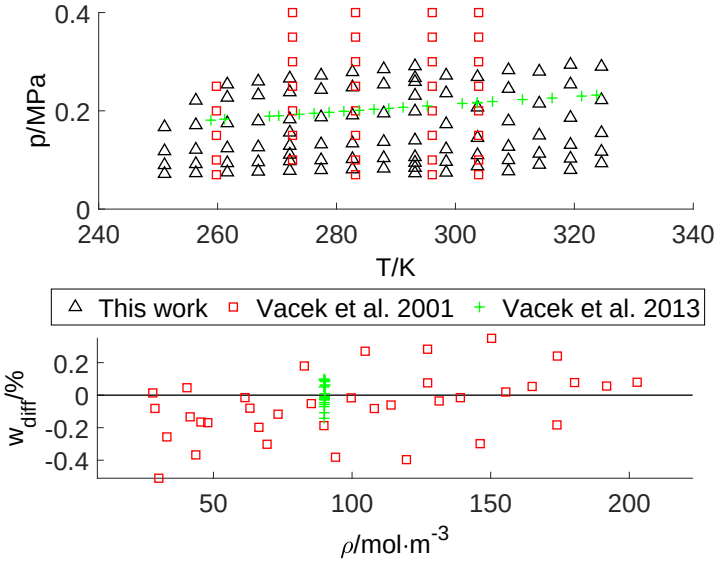

Figure 5.19: Comparison of experimental data of speed of sound in gaseous R-218

Bibliography

chapter 5: Development of high accuracy speed-of-sound measurement apparatus

[Doubek, 2012] Doubek, M. 2012. *Studie zarizeni pro merení rychlosti zvuku v plynne fazi*. Bachelor's thesis, Czech Technical University, Faculty of Mechanical Engineering.

[Doubek, 2014] Doubek, M. 2014. *Thermophysical properties of fluids experiment and simulations*. Master's thesis, Czech Technical University, Faculty of Mechanical Engineering.

[Hurly, 1999] Hurly, J. J. 1999. Thermophysical Properties of Gaseous CF4 and C2F6 from Speed-of-Sound Measurements. *International Journal of Thermophysics*, **20**(2), 455–484.

[Hurly *et al.*, 2003] Hurly, J. J., Gillis, K. A., Mehl, J. B., & Moldover, M. R. 2003. The Viscosity of Seven Gases Measured with a Greenspan Viscometer. *International Journal of Thermophysics*, **24**(6), 1441–1474.

[Jarvis *et al.*, 1996] Jarvis, G. K., Johnson, K. A., & Walmsley, S. L. 1996. An Annular Resonator Used To Measure the Speed of Sound in Gaseous Fluoroalkanes: Trifluoromethane and Hexafluoroethane. *Journal of Chemical & Engineering Data*, **41**(2), 222–230.

[Lemmon & Span, 2006] Lemmon, E. W., & Span, R. 2006. Short Fundamental Equations of State for 20 Industrial Fluids. *Journal of Chemical & Engineering Data*, **51**(3), 785–850.

[Lemmon *et al.*, 2018] Lemmon, E. W., Bell, I. H., Huber, M. L., & McLinden, M. O. 2018. NIST Standard Reference Database 23: Reference Fluid Thermodynamic and Transport Properties-REFPROP, Version 10.0, National Institute of Standards and Technology.

[Vacek *et al.*, 2001] Vacek, V., Hallewell, G., & Lindsay, S. 2001. Velocity of sound measurements in gaseous per-fluorocarbons and their mixtures. *Fluid Phase Equilibria*, **185**(1), 305 – 314. Proceedings of the 14th symposium on thermophysical properties.

[Vacek *et al.*, 2013] Vacek, V., Vítek, M., & Doubek, M. 2013. Velocity of sound in Perfluoropropane (C3F8), Perfluoroethane (C2F6) and their mixtures. *Fluid Phase Equilibria*, **351**, 53 – 60. Special Issue covering the Eighteenth Symposium on Thermophysical Properties.

6 Thermodynamic Models

6.1 Peng-Robinson equation of state

I have included the Peng Robinson equation of state in the tested models since it is widely used and it can be considered as the reference model. It exhibits the common drawback of cubic equations of state in that it underestimates the liquid density by up to 10%. Nevertheless, the Peng-Robinson equation of state provides good accuracy in the vapour region and good prediction of saturated pressure of pure fluids and mixtures. The pressure-specific form of the equation of state is discussed in chapter 2.

Since I used the same framework of Helmholtz-energy partial derivatives for all the thermodynamic models which are introduced in this section, I worked with the Helmholtz-energy form of the Peng-Robinson equation of state, Equation 6.1, instead of the usual pressure-specific form.

$$\frac{a^r}{RT} = ln\left(\frac{1}{1-b\rho}\right) - \frac{\overline{a}}{2\sqrt{2}RT} ln\left(\frac{1+\left(\sqrt{2}+1\right)\overline{b}\rho}{1-\left(\sqrt{2}-1\right)\overline{b}\rho}\right) \tag{6.1}$$

When the cubic equations are used for mixtures the a_m and b_m coefficients have to be obtained using simple Van der Waalse mixing rules:

$$\overline{a_m} = \sum_i \sum_j x_i x_j \overline{a}_{ij} \ , \tag{6.2}$$

$$\overline{b}_m = \sum_i \sum_j x_i x_j \overline{b}_{ij} \ , \tag{6.3}$$

$$\overline{a}_{ij} = \sqrt{\overline{a}_i \overline{a}_j}(1-k_{ij}) \ , \tag{6.4}$$

$$\overline{b}_{ij} = \frac{1}{2}(\overline{b}_i + \overline{b}_j) \ . \tag{6.5}$$

The Van der Waalse mixing rules are suitable only for mixtures of non-polar or slightly polar fluids. The binary interaction parameter k_{ij} in Equation 6.4 is used to improve the vapour-liquid equilibrium prediction. Some authors proposed composition-dependent mixing rules to improve the accuracy of prediction of the vapour-liquid equilibrium of mixtures, temperature-dependent coefficients, rules for polar fluids [Iwai *et al.*, 1988] and also rules for associating fluids [Medeiros & Tellez-Arredondo, 2008]. I chose to use the simplest rules since the more complicated mixing rules often provide better results for certain fluids but they are less universal.

6.2 Volume-translated Peng-Robinson equation of state

The volume translation technique for the cubic equations of state is introduced in chapter 2. I have included the volume-translated Peng-Robinson equation of state in the tested models since it promises to overcome the main drawback of the cubic equations while still keeping the model equations and derivatives relatively simple. Unfortunately, the volume-translated models often exhibit over-crossing of isotherms at high pressures rendering the models suitable only for modelling of phase-equilibrium but not for one-phase regions. A simple mixing rule is used for the volume translation of a mixture:

$$\overline{c}_m = \sum_i^n x_i \overline{c}_i \ . \tag{6.6}$$

6.2.1 Volume translation by Magoulas and Tassios

This temperature-dependent volume translation represented by Equations 6.7 to 6.10 was developed for n-alkanes by [Magoulas & Tassios, 1990]. The focus was on prediction of the saturated pressure, liquid volume and enthalpy of vapourization. The volume translation provides improvement in prediction of the saturated pressure especially at low pressures.

$$\overline{c}_c = \frac{RT_c}{P_c}\left(0.3074 - Z_c\right) \tag{6.7}$$

$$\overline{c}_o = \frac{RT_c}{P_c}\left(-0.014471 + 0.067498\omega - 0.084852\omega^2 + 0.067298\omega^3 - 0.017366\omega^4\right) \tag{6.8}$$

$$\beta = -10.244700 - 28.631200\omega \tag{6.9}$$

$$\overline{c} = \overline{c}_0 + (\overline{c}_c - \overline{c}_0)e^{(\beta|1-T_r|)} \tag{6.10}$$

6.2.2 Volume translation by Ahlers and Gmehling

The Volume translation by Ahlers and Gmehling [Ahlers & Gmehling, 2001] (equations 6.11 to 6.17) was developed on a dataset containing various fluids, from simple molecules like CO_2 to complex molecules including refrigerants. Average deviation of 2.47% was achieved with this correlation in prediction of the saturated liquid density. However, the authors point out that the volume translation cannot be used in wider pressure range due to the nonphysical over-crossing isotherms at high pressures. This is especially the case for the critical isotherm and for large molecules where, in both cases, the volume translation (correction) is the biggest.

$$\overline{c} = C - \frac{0.35\overline{c}_c}{0.35 + (\eta|\alpha - T_r|)^\gamma} \tag{6.11}$$

$$\overline{c}_c = \frac{RT_c}{P_c}\left(0.3074 - Z_c\right) \tag{6.12}$$

$$C = \frac{0.252RT_c}{P_c}\left(-0.4024 - 1.5448Z_c\right) \tag{6.13}$$

$$\eta = 26.966 - 74.458Z_c \tag{6.14}$$

$$\gamma = 12.67 - 107.21Z_c + 246.78Z_C^2 \tag{6.15}$$

$$m = 0.37464 + 1.54226\omega - 0.26992\omega^2 \tag{6.16}$$

$$\overline{\alpha} = \left[1 + m\left(1 - \sqrt{T_r}\right)\right]^2 \tag{6.17}$$

6.2.3 Volume translation by Lin and Duan

This third presented correlation for volume translation selected from broad variety of correlations available in contemporary literature was developed on significantly larger data-set then the previous two. The data-set includes, among others, 35 Halogenated hydrocarbons. The correlation achieved the average deviation of 1.37% between the predicted saturated liquid density and experimental data [Lin & Duan, 2005]. What is more, the authors even tested the correlation on mixtures and achieved significant improvement over the standard Peng-Robinson equation of state. The correlation represented by equations 6.18 to 6.21 was developed as a function of critical parameters.

$$\overline{c_c} = \frac{RT_c}{P_c}\left(0.3074 - Z_c\right) \tag{6.18}$$

$$\gamma = 0.1735 - 2.8431e^{[-64.2184(0.3074 - Z_c)]} \tag{6.19}$$

$$\beta = -99.2558 + 301.6201Z_c \tag{6.20}$$

$$\overline{c} = \overline{c}_0\left[\gamma + (1-\gamma)e^{(\beta|1-T_r|)}\right] \tag{6.21}$$

6.3 SoftSAFT

The soft-SAFT model consists of a reference fluid with Lennard-Jones pair potential and a contribution term that accounts for bonding in a chain-like molecules. I have selected the Lennard-Jones fluid model developed by [Johnson *et al.*, 1993] who fitted the 33 parameters of the mBWR (Modified Benedict-Webb-Rubin) equation of state to molecular simulation data. The associativity (chain formation) is modeled by the first order Wertheim's theory [Blas & Vega, 2001]. The fluid-specific parameter m represents the average length of the chains in the fluid. The soft-SAFT equation of state is in the Helmholtz energy form composed of following terms:

$$\frac{a^r}{RT} = \frac{A^r}{n_c RT} = \frac{A^r}{NkT} = \frac{A^{ref}}{NkT} + \frac{A^{CHAIN}}{NkT} = m\frac{A^{LJ}}{NkT} + \frac{A^{CHAIN}}{NkT} \quad . \tag{6.22}$$

The soft-SAFT model uses three fitting constants:

- σ characterizes the distance of zero potential
- ε characterizes the potential minimum
- m is the number of monomers per chain

$$A^{LJ} = \sum_{i=1}^{8} \frac{a_i \rho^{*i}}{i} + \sum_{i=1}^{6} b_i G_i \tag{6.23}$$

The reference Lennard-Jones Helmholtz energy term A^{LJ} , Equation 6.23, is based on the mBWR equations. The coefficients a_i, b_i and G_i are given in Tables 6.1 and 6.2. The T^* and ρ^* in coefficients equations are the reduced temperature, Equation 6.24, and reduced pressure, Equation 6.25, and the k_B is the Boltzmann constant.

$$T^* = \frac{k_B T}{\epsilon} \tag{6.24}$$

$$\rho^* = \rho\sigma^3 \tag{6.25}$$

The contribution from chain formation of a mixture of n components is given by Equation 6.26. The x_i is the vector of mole fractions of the mixture components and g_{ij} is pair radial distribution function, Equation 6.27. The coefficients $c_{ij}$of the chain formation term can be found in Table 6.3. More information on the radial distribution function can be found in my Master's thesis [Doubek, 2014].

$$A^{CH} = RT \sum_{i=1}^{n} x_i (1 - m_i) ln\left(g_{LJ}^{ii}\right) \tag{6.26}$$

$$g_{LJ} = f_{(\sigma^i)} = 1 + \sum_{i=1}^{5}\sum_{j=1}^{5} c_{ij} \left(\rho^*\right)^i \left(T^*\right)^{1-j} \tag{6.27}$$

Table 6.1: SoftSAFT model coefficients a_i and b_i

i	a_i
1	$x_1 T^* + x_2\sqrt{T^*} + x_3 + x_4/T^* + x_5/T^{*2}$
2	$x_6 T^* + x_7 + x_8/T^* + x_9/T^{*2}$
3	$x_{10} T^* + x_{11} + x_{12}/T^*$
4	x_{13}
5	$x_{14}/T^* + x_{15}/T^{*2}$
6	x_{16}/T^*
7	$x_{17}/T^* + x_{18}/T^{*2}$
8	x_{19}/T^{*2}

i	b_i
1	$x_{20}/T^{*2} + x_{21}/T^{*3}$
2	$x_{22}/T^{*2} + x_{23}/T^{*3}$
3	$x_{24}/T^{*2} + x_{25}/T^{*3}$
4	$x_{26}/T^{*2} + x_{28}/T^{*3}$
5	$x_{28}/T^{*2} + x_{29}/T^{*3}$
6	$x_{30}/T^{*2} + x_{31}/T^{*3} + x_{32}/T^{*4}$

Table 6.2: SoftSAFT model coefficients G_i

i	G_i
1	$(1 - F) \,/\, (2\gamma)$
2	$-\left(F\rho^{*2} - 2G_1\right) / (2\gamma)$
3	$-\left(F\rho^{*4} - 2G_2\right) / (2\gamma)$
4	$-\left(F\rho^{*6} - 2G_3\right) / (2\gamma)$
5	$-\left(F\rho^{*8} - 2G_4\right) / (2\gamma)$
6	$-\left(F\rho^{*10} - 2G_5\right) / (2\gamma)$
$F = exp(-\gamma\rho^{*2})$	

Table 6.3: SoftSAFT model coefficients c_{ij}

i/j	1	2	3	4	5
1	0.493043466	2.152834989	-15.95568233	24.03599967	-8.643795851
2	-0.470319831	1.147164749	37.88982802	-84.66712149	39.64391411
3	5.032548624	-25.91539923	-18.86225131	107.6370738	-66.60264974
4	-7.363315043	51.55356534	-40.51936926	-38.79669265	44.6051392
5	2.90436073	-24.41881287	31.50018677	-5.336892037	-9.518344018

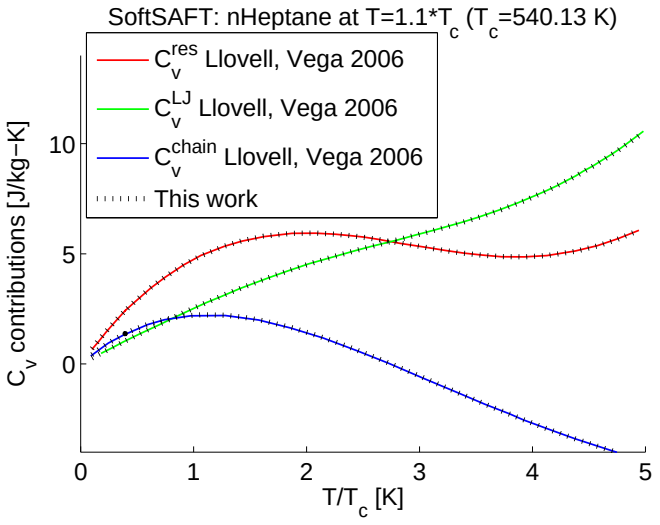

Figure 6.1: First comparison of my implementation of SoftSAFT model to results from literature [Llovell & Vega, 2006]

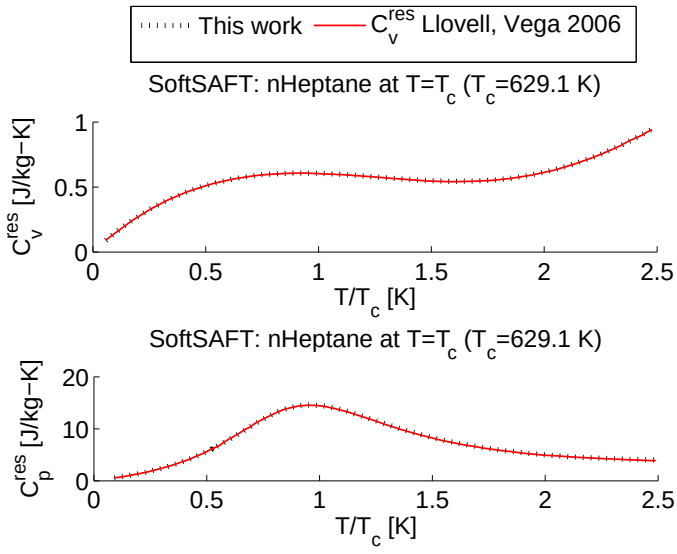

Figure 6.2: Second comparison of my implementation of SoftSAFT model to results from literature [Llovell & Vega, 2006]

I have validated my MATLAB code of the Soft-SAFT model against test data from literature [Llovell & Vega, 2006], the results shown in the Figures 6.1 and 6.2 indicate that the model, including the derivatives needed for the calculations of heat capacities, are implemented correctly.

Equations 6.28 to 6.30 represent the mixing and combination rules that I used for the soft-SAFT model.

$$m = \sum_{i=1}^{n} m_i x_i \tag{6.28}$$

$$\sigma_m^3 = \sum_{i=1}^{n}\sum_{j=1}^{n} x_i x_j \sigma_{ij}^3 \tag{6.29}$$

$$\epsilon_m \sigma_m^3 = \sum_{i=1}^{n}\sum_{j=1}^{n} x_i x_j \varepsilon_{ij} \sigma_{ij}^3 \tag{6.30}$$

Conventional (Lorentz-Berthold) combination rules with one binary interaction parameter k_{ij} were used for the size and energy parameters:

$$\sigma_{ij} = \frac{\sigma_{ii} + \sigma_{jj}}{2} \quad , \tag{6.31}$$

$$\epsilon_{ij} = (1 - k_{ij}) \left(\varepsilon_{ii} \epsilon_{jj}\right)^{1/2} \quad . \tag{6.32}$$

6.4 sPC-SAFT

The PC-SAFT equation of state was originally published by Gross and Sadowski [Gross & Sadowski, 2001]. The molecules are considered to be chains of spheres interacting with the square-well potential. The potential is divided into a reference repulsive part and a perturbation part that accounts for the attractive interactions. The hard-chain fluid is characterized by the sphere-segments diameter σ and by the average number of segments in the chain m. The interaction between two chain-like molecules is considered to be the sum of the whole interaction between individual atoms - spherical segments. The chain molecules are also considered to be spherical, the first and second order perturbation terms are used to account for attractive interactions between the chain molecules. A group contribution method has been developed for the sPC-SAFT equation of state [Tihic *et al.*, 2008]. The method provides a relatively good estimate of the fitting parameters namely for polymer molecules.

The residual Helmholtz free energy A^r (Equation 6.33) consists of two terms: the hard-chain reference part A^{hc} and the perturbation part A^{pert} which is further split into the first and second order perturbations A^1 and A^2.

$$\frac{a^r}{RT} = \frac{A^r}{nRT} = \frac{A^r}{Nk_BT} = \frac{A^{hc}}{Nk_BT} + \frac{A^{pert}}{Nk_BT} = \frac{A^{hc}}{Nk_BT} + \frac{A_1}{Nk_BT} + \frac{A_2}{Nk_BT} \tag{6.33}$$

The PC-SAFT model uses three fitting parameters:

- σ - characterizes the distance of zero potential
- ε - characterizes the potential minimum
- m - is the number of monomers per chain

The terms in the Equation 6.33 have following forms:

$$\frac{A_{hc}}{RT} = m\frac{\eta(4-3\eta)}{(1-\eta)^2} - (m-1)\,ln\left(\frac{1-0.5\eta}{(1-\eta)^3}\right) \quad , \tag{6.34}$$

$$\frac{A_1}{RT} = -2\pi\rho\sigma^3 m^2 \left(\frac{\varepsilon}{kT}\right) I_{1(m,\eta)} \quad , \tag{6.35}$$

$$\frac{A_2}{RT} = -\frac{\pi\rho\sigma^3 m^3 \left(\frac{\varepsilon}{kT}\right)^2}{1 + m(8\eta - 2\eta^2)/(1-\eta)^4 - (m-1)\,\frac{(20\eta - 27\eta^2 + 12\eta^3 - 2\eta^4)}{(2-\eta)^2(1-\eta)^2}} I_{2(m,\eta)} \quad , \tag{6.36}$$

$$I_{1(\eta,m)} = \sum_{i=0}^{6} a_i(m).\eta^i \quad , \tag{6.37}$$

$$I_{2(\eta,m)} = \sum_{i=0}^{6} b_i(m).\eta^i \quad . \tag{6.38}$$

where η is the radial distribution function. A simplified version of the original PC-SAFT, [Solms *et al.*, 2006], has been used for all the calculation in this work. The simplified equation (sPC-SAFT) assumes that the segment diameters d_i of different species are very similar, and that a simplified radial distribution function η can therefore be employed in the chain term:

$$\eta = \left(\frac{\sum_i x_i m_i d_i^3}{\sum_i x_i m_i}\right) \quad . \tag{6.39}$$

The universal constants a_{i0} and b_{i0} in equations 6.40 and 6.41 are tabulated and can be found in [Gross & Sadowski, 2001].

$$a_{(m)} = a_{0i} + \frac{m-1}{m}a_{1i} + \frac{m-1}{m}\frac{m-2}{m}a_{2i} \tag{6.40}$$

$$b_{(m)} = b_{0i} + \frac{m-1}{m}b_{1i} + \frac{m-1}{m}\frac{m-2}{m}b_{2i} \tag{6.41}$$

The coefficients a_i and b_i are tabulated.

The Chen-Kreglewski segment diameter d_i is calculated followingly:

$$d_i = \sigma_i \left[1 - 0.12exp\left(\frac{-3\varepsilon_i}{kT}\right)\right] \quad . \tag{6.42}$$

The models equations including the second and first derivatives are quite complex, the implementation in MATLAB language was therefore verified against PC-SAFT simulations from literature [Diamantonis &

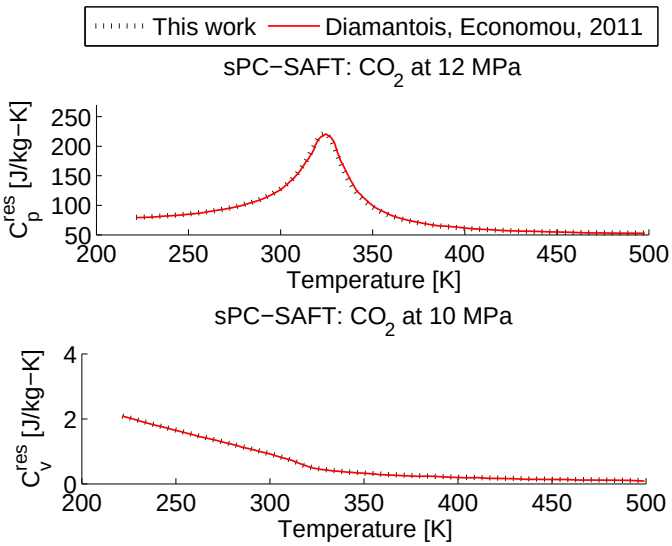

Figure 6.3: Comparison of my implementation of sPC-SAFT model to results from literature [Diamantonis & Economou, 2011]

Economou, 2011]. Figure 6.3 shows that the model works correctly, including the derivatives for calculations of heat capacities.

Conventional combination rules with one binary interaction parameter k_{ij} were used for the mixtures, equations 6.43 and 6.44.

$$\sigma_{ij} = \frac{\sigma_{ii} + \sigma_{jj}}{2} \tag{6.43}$$

$$\epsilon_{ij} = (1 - k_{ij}) \left(\varepsilon_{ii}\epsilon_{jj}\right)^{1/2} \tag{6.44}$$

Note that the term for the equations for the segment diameter d_i and packing fraction η already takes into account the species in the mixture.

6.5 SAFT-BACK

The BACK (Boublik–Alder–Chen–Kreglewski) equation of state [Boublik, 2007] is an augmented van der Waals equation of state. The equation of state was developed on a statistical description of non-spherical convex molecules. It has been proven that BACK is quite suitable for simple non-associating fluids such as methane, nitrogen, hydrogen and their mixtures. The BACK equation of state provides good prediction even close to the critical point and in the supercritical region. The statistical association fluid theory was applied to this equation to obtain a model for more complex molecules and associating fluids [Zhi-Yu *et al.*, 2000]. As a result, the molecule is modeled as a chain of hard convex body segments. The residual Helmholtz energy, Equation 6.45, is divided into four parts: the hard convex body contribution A^{hc}, the chain formation term $A^{chain,hcb}$, the dispersion term A^{dis} and the dispersion due to chain formation $A^{chain,dis}$. The SAFT-BACK model uses four fitting parameters:

- $\tilde{\alpha}$ - geometry of a hard convex body (nonsphericity)
- m - segment number
- u^0 - segment dispersion parameter (energetic parameter)
- v^{00} - segment volume parameter

$$\frac{a^{res}}{RT} = \frac{A^{res}}{nRT} = \frac{A^{res}}{Nk_BT} = \frac{A^{hcb}}{Nk_BT} + \frac{A^{chain,hcb}}{Nk_BT} + \frac{A^{dis}}{Nk_BT} + \frac{A^{chain,dis}}{Nk_BT} \tag{6.45}$$

The first term is the Helmholtz energy of a hard convex body as defined by Boublik [Boublik, 2007]:

$$\frac{A^{hcb}}{Nk_BT} = m\left[\frac{\tilde{\alpha}^2}{(1-\eta)^2} - \frac{\tilde{\alpha}^2 - 3\tilde{\alpha}}{1-\eta} - (1-\tilde{\alpha}^2)ln\left(1-\eta-3\tilde{\alpha}\right)\right] \ . \tag{6.46}$$

The m is the segment parameter number, η is the packing fraction and α is a parameter related to geometry of hard a convex body. The packing factor is defined in following way:

$$\eta = \frac{1}{6}\pi N_{AV} m \rho d^3 \ . \tag{6.47}$$

The segment diameter d is calculated using the model parameter u^0 called the segment dispersion and σ which is evaluated from another model parameter ν^{00} called segment volume parameter:

$$d = \sigma\left[1 - 0.12exp\left(-\frac{3u^0}{k_BT}\right)\right] \ , \tag{6.48}$$

$$\sigma = \sqrt[3]{6\frac{\nu^{00}}{\pi N_{AV}}} \ . \tag{6.49}$$

Next term is the contribution from the chain of hard convex bodies:

$$\frac{A^{hcb}}{Nk_BT} = (1-m)\, lng^{hcb} \ . \tag{6.50}$$

where the g^{hcb} is the mean radial distribution function:

$$g^{hcb}_{(d)} = \frac{1}{1-\eta} + \frac{3\alpha\,(1+\tilde{\alpha})\,\eta}{(1-\eta)^2\,(1+3\tilde{\alpha})} + \frac{2\tilde{\alpha}^2\eta^2}{(1-\eta)^3\,(1+3\tilde{\alpha})} \ . \tag{6.51}$$

The dispersion term comes from work of Aldler [Alder *et al.*, 1972]:

$$\frac{A^{dis}}{Nk_BT} = m\sum_i\sum_j D_{ij}\left(\frac{u}{k_BT}\right)^i\left(\frac{\eta}{\sqrt{2}\pi/6}\right)^j \ . \tag{6.52}$$

Table 6.4: The D constants for SAFT-BACK model

D11	-8.8043	D21	2.9396	D27	-1535.3224
D12	4.164627	D22	-6.0865383	D28	1221.4261
D13	-48.203555	D23	40.137956	D29	-409.1053
D14	140.4362	D24	-76.230797	D31	-2.8225
D15	-195.23339	D25	-133.70055	D32	4.7600148
D16	113.515	D26	860.25349	D33	11.257177

The D_{ij} are universal constants listed in 6.4 and u is the interaction energy:

$$u = u^0 \left(1 + \frac{e}{k_B T}\right) \ . \tag{6.53}$$

For small molecules $m = 1$ and $e/k_B = 1$ otherwise $e/k_B = 10.0$.
Finally, the dispersion term from chain formation has following form:

$$\frac{A^{chain,dis}}{N k_B T} = m \frac{\lambda A^{chain,hcb}}{A^{hcb}} \sum_i \sum_j D_{ij} \left(\frac{u}{k_B T}\right)^i \left(\frac{\eta}{\sqrt{2}\pi/6}\right)^j \ . \tag{6.54}$$

The $\lambda = 1.75$ for non-polar fluids.

The implementation of the SAFT-BACK equation of state in MATLAB was tested against literature simulations from [Maghari & Najafi, 2010] in order to validate the code. The comparison of heat capacities in Figure 6.4 shows that the model works correctly.

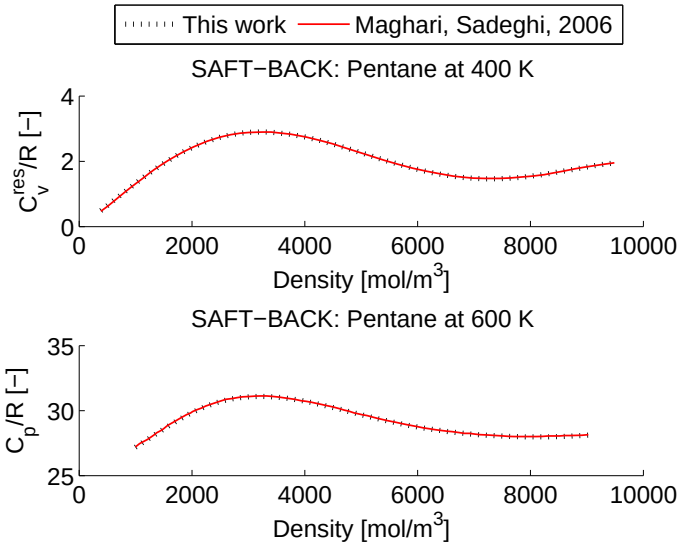

Figure 6.4: Comparison of my implementation of SAFT-Back model to results from literature [Maghari & Najafi, 2010]

Mixing rules with one binary interaction parameter k_{ij} proposed by Hoda Tahani in [Tahani, 2011] were adopted for the SAFT-BACK model in this work, equations 6.55 to 6.59.

$$m = \sum_{i=1}^{n} m_i x_i \tag{6.55}$$

$$\alpha_m = \frac{\sum_{j=1}^{n} \alpha_i m_i x_i}{\sum_{j=1}^{n} m_i x_i} \tag{6.56}$$

$$\left(\frac{u_o}{k_B}\right)_m = \sum_{i=1}^{n}\sum_{j=1}^{n} x_i x_j \varepsilon_{ij} \left(\frac{u_o}{k_B}\right)_{ij} \tag{6.57}$$

$$\left(\frac{u_o}{k_B}\right)_{ij} = \sqrt{\left(\frac{u_o}{k_B}\right)_i \left(\frac{u_o}{k_B}\right)_j}\,(1 - k_{ij}) \tag{6.58}$$

The mixing rule for the segment diameter is following:

$$d_m = \left(\frac{\sum_{j=1}^{n} d_i^3 m_i x_i}{\sum_{j=1}^{n} m_i x_i}\right)^{1/3} , \tag{6.59}$$

where d_i is the segment diameter d of mixture component i.

6.6 Speed of sound and molecular relaxation

The actual measured speed of sound in polyatomic gases is a function of frequency since the sound-wave propagation is not purely isoentropic. The dispersion effects cause an increase in entropy and result in sound absorption and speed of sound shift (dispersion). The so called molecular relaxation is characterized by molecular relaxation time $\hat{\tau}$ and it causes the strongest speed of sound dispersion among the various phenomena that affect the speed of sound. The sound absorption due to the molecular relaxation is highest when the sound frequency $\omega = 2\pi f$ approaches the relaxation frequency ($\omega\hat{\tau} = 1$) and it is zero at low or high frequencies, this enables the experimental investigation of the relaxation times. Note that the absorption due to the molecular relaxation superimposes on the classical absorption (dissipation of sonic energy into heat given by the Stokes-Kirchhoff relation) due to the viscosity and heat conduction. The sound intensity I_L in the distance L decreases from the source intensity I_0 in following manner:

$$I_L = I_0 e^{-2\alpha_a L} , \tag{6.60}$$

where α_a is the attenuation coefficient that consist of viscous and thermal contribution and it can be evaluated from the viscosity, density, coefficient of thermal expansion, specific heats, speed of sound and frequency. The equations of states discussed in section 2.1 give so called zero-frequency speed of sound which is a speed of sound that would correspond to a sound wave with frequency of zero hertz. One can imagine this values as an extrapolation of sound speed measured at various frequencies. The variation between the zero-hertz frequency speed of sound and infinite-frequency speed of sound is usually around 10%.

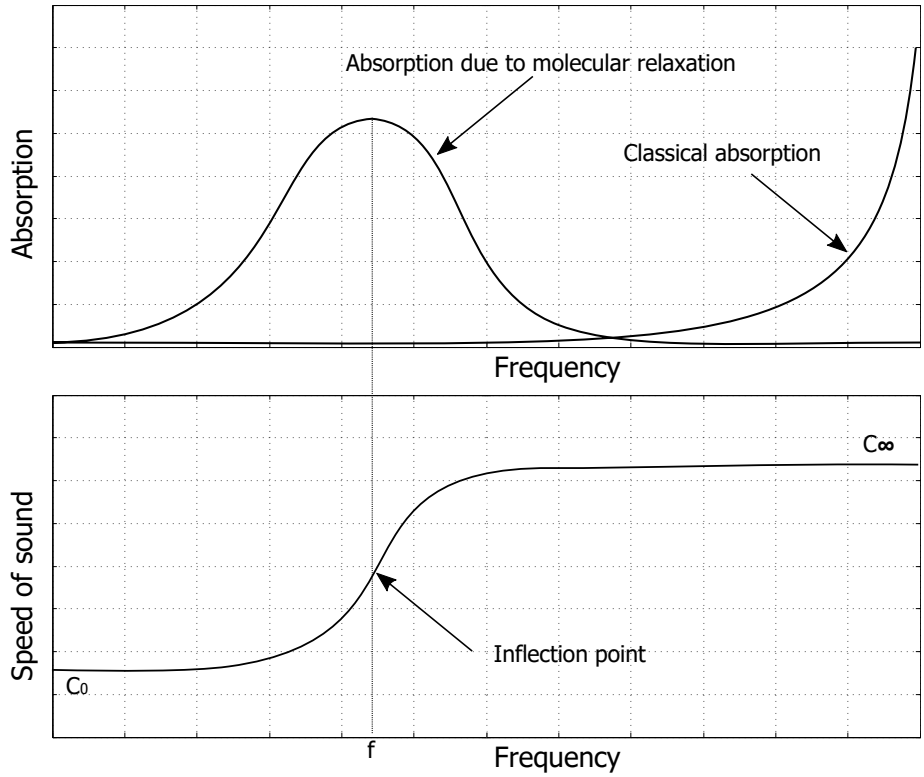

Figure 6.5: Sound speed dispersion

The propagation of sound through a gas is a translational motion of the gas molecules which results in a varying density - sound wave propagation. The molecular relaxation is a phenomenon that is present in polyatomic gases where the energy of the moving sound wave is transferred into the vibrational degrees of freedom of gas molecules. This energy transfer results in the absorption of the sound waves and sound speed dispersion. The speed of sound is affected since the vibrational degrees of freedom contribute to the heat capacity, Equation 2.6. The frequency dependence of the heat capacities arises from the fact that at low sound frequencies a thermal equilibrium can be established in the propagating sound wave while at high frequencies the molecules do not have enough time to transfer the energy into the vibrational degrees of freedom and to deactivate the vibrational mode by collisions with other molecules. It has been proven that the vibrational degrees of freedom exhibit hundredfold slower energy exchange than the translational and rotational degrees of freedom, [Dwyer, 1939]. The vibrational modes contribute to the heat capacities below so called relaxation frequency which is a reciprocal value of relaxation time $\hat{\tau}$. Even though molecules with more vibrational modes have relaxation times corresponding to each of these modes, only one relaxation time is usually observed experimentally, [Olson & Legvold, 1963]. For most gases the relaxation times $\hat{\tau}$ are between $10^{-4}$and 10^{-8} seconds [Olson & Legvold, 1963]. It should be noted that at very high frequencies (hundreds of megahertz) even the rotational degrees of freedom cannot follow the temperature fluctuations and they don't contribute to the specific heat of a gas [Henderson, 1963].

It is now apparent that at very low frequencies the heat capacity has value c_0 and different value c_∞can be observed at very high frequencies. The vibrational mode does not contribute the to the heat capacity at high frequency:

$$c_{v\infty} = c_{v0} - c_{v\,vib} \quad . \tag{6.61}$$

The heat capacity can be expressed as a function of the complex frequency $\hat{\omega}$:

$$c_{v\omega} = c_{v\infty} + \frac{c_{v\,vib}}{1 + i\hat{\omega}\hat{\tau}} \quad . \tag{6.62}$$

In fact, there are multiple vibrational modes and each has a corresponding relaxation time $\hat{\tau}_i$

$$c_{v\omega} = c_{v\infty} + \sum_i \frac{c_{v\,vib_i}}{1 + i\hat{\omega}\hat{\tau}_i} \quad . \tag{6.63}$$

However, as mentioned above only one relaxation time is usually observed experimentally. The real part of the heat capacity is equal to

$$c_{v\omega} = \frac{c_{vo}^2 + \hat{\omega}^2\hat{\tau}^2 c_{v\infty}^2}{c_{vo} + \hat{\omega}^2\hat{\tau}^2 c_{v\infty}} \quad . \tag{6.64}$$

The relations above apply to pure gas. Unfortunately, the processes in a mixture of relaxing gasses are not fully understood. Several thorough investigations of the sound dispersion in moist air can be found in scientific literature, for instance [Dean, 1979]. Number of models have been proposed to evaluate the relaxation time and consequently the sound absorption and dispersion of a mixture (for instance [Liu *et al.*, 2017] and [Zhang *et al.*, 2014]). Many of this models are very complex and are out of the scope of this work, which is focused es on easy-to-use reliable models. The simplest approach is to use following mixing rules for binary mixture of relaxing (component A) and nonrelaxing gas:

$$c_{v\omega}^{mix} = c_{v\infty}^{mix} + \frac{x c_{v\,vib}^{A}}{1 + i\hat{\omega}\hat{\tau}^{A}} \quad . \tag{6.65}$$

Where x is the mole fraction of the relaxing component A. In similar manner, the simplest approach leads to the following term for the specific heat of mixture of two relaxing gases with one dominant relaxation time:

$$c_{v\omega}^{mix} = c_{v\infty}^{mix} + \frac{x c_{v\,vib}^{A}}{1 + i\hat{\omega}\hat{\tau}^{A}} + \frac{(x-1) c_{v\,vib}^{B}}{1 + i\hat{\omega}\hat{\tau}} \quad . \tag{6.66}$$

Fortunately, the dispersion effect due to the molecular relaxation can be avoided by carefully choosing the sound frequency for the speed of sound measurements. A frequency sweep can be used to evaluate the sound attenuation and if a peak is found a much higher or lower frequency can be used to measure the speed of sound to avoid the dispersion region. A wide-range of frequencies from several kilohertz to one megahertz can be used with the time-of-flight measurement methods.

6.6.1 Relaxation times

The vibrational relaxation times increase with the temperature and decrease with pressure. The speed of sound against frequency divided by pressure is used on the horizontal axis (units are then cycle per second-atmosphere) and the square of sound velocity is plotted on the vertical axis of plots describing the relaxation behaviour. The Landau-Teller relation can be used to express the relaxation time $\hat{\tau}$ as a function of pressure p and temperature T:

$$\hat{\tau} = \frac{K_1}{p} e^{(\frac{K_2}{\sqrt[3]{T}})} \quad , \tag{6.67}$$

where $K_1$and K_2 are the fluid specific constants. The relaxation times are usually obtained experimentally from an inflection in the sound absorption curve. Relaxation times $\hat{\tau}$ for selected fluids are listed in table 6.5, the relaxation frequency $f = 1/\hat{\tau}$ is also included since it gives better picture about the gas behaviour for our purposes. As a reminder, the relaxation frequency corresponds to the sound absorption peak caused by molecular relaxation. Most of the simple gases such as nitrogen (R-728) and oxygen exhibit very long relaxation times. However, the CO_2 (R-744) and methane (R-50) exhibit relaxation and strong ultrasound absorption at very inconvenient frequencies. The sound dispersion with these two gases can be expected when common measurement techniques are employed. One can see that most of the refrigerants have short relaxation times and therefore the sound dispersion is not a concern with usual speed of sound measurement techniques that work with ultrasound at few tens of kilohertz.

Table 6.5: Relaxation times at atmospheric pressure

Gas	Temperature [K]	Relaxation time [s]	Relaxation frequency [MHz/atm]	Source
R-50	299.15	1.36E-06	0.735	[Zhang *et al.*, 2014]
R-50	293.9	1.42E-06	0.704	[Zhang *et al.*, 2014]
R-50	300	1.30E-06	0.8	[Goodwin, 1998]
R-50	255	2.33E-06	0.4	[Goodwin, 1998]
R-50	350	7.80E-07	1.3	[Goodwin, 1998]
Cl_2	296.2	4.69E-06	0.213	[Zhang *et al.*, 2014]
R-744	296.15	5.01E-06	0.200	[Zhang *et al.*, 2014]
R-744	298.15	4.90E-06	0.204	[Zhang *et al.*, 2014]
R-170	296.4	1.39E-08	72	[Valley & Legvold, 1960]
R-170	298.15	1.79E-08	56	[Holmes *et al.*, 1964]
R-170	297.15	1.39E-08	72	[Holmes *et al.*, 1964]
R-170	303.15	1.50E-08	67	[Holmes *et al.*, 1964]
R-600a	300	1.90E-09	526	[Goodwin, 1998]
R-728	297	5.80E+00	1.724E-07	[Zhang *et al.*, 2014]
R-600	300	1.30E-09	769	[Goodwin, 1998]
O_2	303.2	1.49E-02	6.711E-05	[Zhang *et al.*, 2014]
C_5H_{12}	300	9.00E-08	11	[Goodwin, 1998]
R-290	303.15	1.56E-08	64	[Holmes *et al.*, 1964]
R-1270	303.15	1.48E-08	68	[Holmes *et al.*, 1964]
R-12	298	8.33E-08	12	[Boade & Legvold, 1965]
R-134a	270	9.00E-08	11	[Zhu *et al.*, 1993]
R-134a	340	7.20E-08	14	[Zhu *et al.*, 1993]
R-134a	233	5.50E-08	18	[Goodwin & Moldover, 1990]
R-14	298	8.20E-07	1.2	[Boade & Legvold, 1965]
R-152a	296.1	3.37E-09	297	[Valley & Legvold, 1960]
R-21	298	2.67E-08	37	[Boade & Legvold, 1965]
R-23	298	6.00E-07	1.7	[Boade & Legvold, 1965]
R-32	298	3.99E-08	25	[Boade & Legvold, 1965]

6.7 Vapour-liquid equilibrium

The calculation of vapour-liquid equilibrium of pure fluids requires to solve a system of three equations which describes the coexistence of the two phases: the temperatures of the liquid phase T' and the vapour phase T'' must be the same as well as the pressures p and chemical potentials μ of the liquid and vapour phases:

$$\begin{cases} T' = T'' = T \\ p' = p'' = p \\ \mu' = \mu'' \end{cases} . \tag{6.68}$$

The Gibbs' phase rule dictates that there is one degree of freedom (independent variable) in the vapour-liquid equilibrium of a pure fluid. For this reason, the set of equations 6.68 reduces to the equality of the chemical potential and pressures of the two phases since the temperature is the independent variable i.e. the input of the equations of state. In case of the a pure fluid, the chemical potential can be expressed as Gibbs energy per atom:

$$\mu = \frac{G}{N} = a + \frac{p}{\rho} - T \ . \tag{6.69}$$

An iterative algorithm is used to solve these equations by adjusting density estimates for the two phases ρ' and ρ'' in an attempt to minimize the difference in pressures $abs(p' - p'')$ and chemical potential $abs(\mu' - \mu'')$ at fixed temperature $T = T' = T''$.

The vapour-liquid equilibrium of mixtures is more complicated, the number of equations that need to be satisfied depends on the number of components in the mixture i. The set of equations 6.70 represents equality of the temperature, pressure and chemical potential of all the components in both phases.

$$\begin{cases} T' = T'' = T \\ p' = p'' = p \\ \mu_i' = \mu_i'' \end{cases} \tag{6.70}$$

The Gibbs phase rule dictates that there are two degrees of freedom in the vapour-liquid equilibrium of a binary mixture (mixture of two components). One can choose different combinations of the independent variables (input parameters for the calculation):

- Temperature T and mole fraction of component i in the liquid phase x_i' (bubble point pressure calculations).
- Temperature T and mole fraction of component i in the vapour phase x_i'' (dew-point pressure calculations).
- Pressure p and mole fraction of component i in the liquid phase x_i' (bubble point temperature calculations).
- Pressure p and mole fraction of component i in the vapour phase x_I'' (dew-point temperature calculations).

I chose a relatively unique approach to the solution of the binary mixtures vapour liquid equilibrium in that my input variables are the temperature and pressure and the compositions of the phases are the unknowns to be solved. The reason for choosing this approach is that in practice (i.e. refrigeration plant, industrial process plant, etc.) the pressure and temperature are process parameters that can be easily measured while the exact composition of the fluid is often unknown. To solve the equilibrium at the given pressure and temperature I have implemented an algorithm described by [Privat *et al.*, 2013]. It should be obvious, that this algorithm is not suitable for mixtures where there are several solutions in terms of composition for the same combination of temperature and pressure, i.e mixtures with azeotrope as shown in Figure 6.6. This can be overcome by providing an appropriate initial guess for the solution iterative algorithm.

So called $\varphi - \varphi$ approach is used when solving the phase equilibrium using an equation of state (as opposed to $\gamma - \varphi$ which employs activity coefficients for the liquid phase). The fugacity coefficient φ is defined as ratio of the species fugacity in the mixture to the ideal gas reference state:

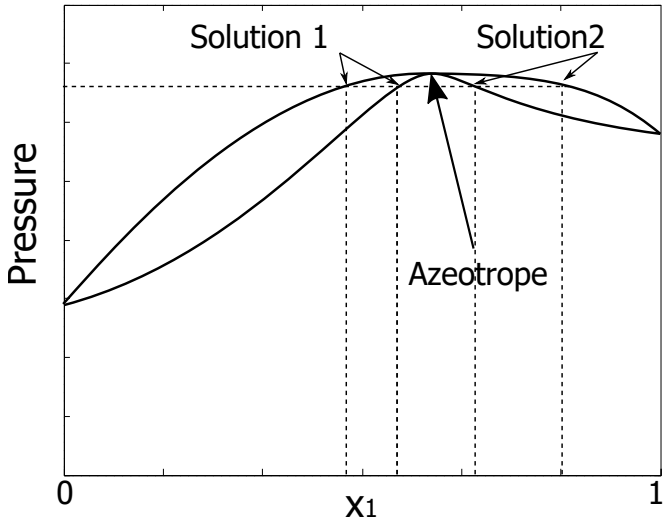

Figure 6.6: Phase diagram of binary mixture with azeotrope

$$\varphi = \frac{\phi_i}{x_i P} \quad . \tag{6.71}$$

The Volume-translated Peng-Robinson equation of state yields following expression for the fugacity of a component in mixture (component-specific fugacity):

$$ln\phi_i = \frac{b_i}{B}(Z + \hat{t} - 1) - ln(Z + \hat{t} - B) - \frac{A}{2\sqrt{2}B}\left[\frac{2\sum_j^n x_j a_{ij}}{A} - \frac{b_i}{B}\right] ln\left[\frac{Z + \hat{t} + \left(\sqrt{2}+1\right)B}{Z + \hat{t} + \left(\sqrt{2}-1\right)B}\right] \quad , \tag{6.72}$$

where

$$A = \frac{Pa}{R^2T^2} \quad , \tag{6.73}$$

$$B = \frac{Pb}{RT} \quad , \tag{6.74}$$

$$\hat{c} = \frac{Pc_m}{RT} \quad . \tag{6.75}$$

Expression for the classical Peng-Robinson equation of state is obtained simply by setting the mixture volume translation $c_m = 0$.

Partial derivatives with respect to the composition have to be evaluated in order to obtain the fugacity of a component in a mixture of the SAFT models:

$$ln\phi_i = \frac{\partial}{\partial n_i}\left[n \cdot ln\phi\right]_{T,P,n_j} \quad . \tag{6.76}$$

Where n is the total number of moles, n_i is the number of moles of the component i and n_j is the number of moles of other components j. Since the equations of SAFT models are quite complex, the partial derivation with respect to composition are usually solved numerically: [Rand, 2004]:

$$ln\phi_i = \frac{(1+dx_i)ln\phi_{+dn_i} - (1-dx_i)ln\phi_{-dn_i}}{2dx_i} \ . \tag{6.77}$$

I have used following expressions to obtain the component-specific fugacity from the SAFT equations of state from partial derivative of Helmholtz energy with respect to the composition:

$$ln\phi_i = \frac{\mu_i^{res}}{kT} - lnZ \ , \tag{6.78}$$

$$\frac{\mu_i^{res}}{kT} = a^{res} + (Z-1) + \left[\frac{\partial a^{res}}{\partial x_i}\right]_{T,\rho,x_{j\neq i}} - \sum x_k \left[\frac{\partial a^{res}}{\partial x}\right]_{T,\rho,x_{k\neq j}} \ . \tag{6.79}$$

To solve the vapour-liquid equilibrium of a binary mixture using the $\varphi - \varphi$ approach and with the pressure P and temperature T as the input variables one has to solve following set of equations [Privat *et al.*, 2013]:

$$\begin{cases} x_1'\varphi_1' = x_1''\varphi_1'' \\ (1-x_1')\,\varphi_2' = (1-x_1'')\,\varphi_2'' \end{cases} \ . \tag{6.80}$$

The fugacity coefficients φ are obtained from equations of state:

$$\varphi_i' = \varphi_{\left(T,\rho',x_i'\right)} \ . \tag{6.81}$$

The vapour and liquid phase densities ρ'' and ρ' are obtained from the known pressure and temperature for a given composition in each step of the iterative algorithm:

$$P = P_{(T,\rho',x')} = P_{(T,\rho'',x'')} \ . \tag{6.82}$$

The set of equations 6.80 can be rewritten in a matrix notation:

$$\begin{bmatrix} \varphi_1' & -\varphi_1'' \\ -\varphi_2' & \varphi_2'' \end{bmatrix} \begin{bmatrix} x_1' \\ x_1'' \end{bmatrix} = \begin{bmatrix} 0 \\ \varphi_2'' - \varphi_2' \end{bmatrix} \ . \tag{6.83}$$

This can be written in a matrix notation and we get a classical linear form:

$$\left[A_{(x)}\right][x] = \left[B_{(x)}\right] \ . \tag{6.84}$$

A simple iteration algorithm can be employed to solve the linear form. Firstly, an initial guess of the vector of vapour and liquid x^1 compositions is used for the first iteration. Subsequent iterations update the composition vector using following iteration scheme:

$$\left[x^{k+1}\right] = \left[A_{(x)}\right]^{-1} \left[B_{(x)}\right] \ . \tag{6.85}$$

The iterations are stopped when a convergence criterion is fulfilled:

$$\delta = \left[\left|x_1'' \varphi_1'' - x_1' F_1'\right| + \left|\left(1 - x_1''\right) \varphi_2'' - \left(1 - x_1'\right) F_2'\right|\right] \leq 10^{-5} \ . \tag{6.86}$$

The important properties of the iteration algorithm for a solution of vapour-liquid equilibrium are:

- The algorithm is robust with respect the to initial guess of the composition vector. The iteration will converge even with an initial guess far from the solution;
- The algorithm is relatively slow. It can take more than ten thousand iterations to converge when the temperature is close to the critical temperature of the mixture;
- A trivial solution is reached when the temperature is above the critical temperature of the mixture.

The algorithm is also slow (it requires large number of iterations) when solving the equilibrium at temperature above the critical point of some of the components. Trying to solve the equilibrium of a mixture above its critical point will lead to unphysical results.

Bibliography

chapter 6: Thermodynamic Models

[Ahlers & Gmehling, 2001] Ahlers, J., & Gmehling, J. 2001. Development of an universal group contribution equation of state: I. Prediction of liquid densities for pure compounds with a volume translated Peng-Robinson equation of state. *Fluid Phase Equilibria*, **191**(1), 177 – 188.

[Alder *et al.*, 1972] Alder, B. J., Young, D. A., & Mark, M. A. 1972. Studies in Molecular Dynamics. X. Corrections to the Augmented van der Waals Theory for the Square Well Fluid. *The Journal of Chemical Physics*, **56**(6), 3013–3029.

[Blas & Vega, 2001] Blas, F. J., & Vega, L. F. 2001. Thermodynamic properties and phase equilibria of branched chain fluids using first- and second-order Wertheim's thermodynamic perturbation theory. *The Journal of Chemical Physics*, **115**(8), 3906–3915.

[Boade & Legvold, 1965] Boade, R. R., & Legvold, S. 1965. Sound Dispersion in Binary Mixtures of Halomethane Gases. *The Journal of Chemical Physics*, **42**(2), 569–573.

[Boublik, 2007] Boublik, T. 2007. BACK equation of state for simple compounds. *Journal of Molecular Liquids*, **134**(1), 151 – 155. EMLG/JMLG 2005 Special Issue.

[Dean, 1979] Dean, E. A. 1979. *Atmospheric Effects on the Speed of Sound*. Battelle Columbus Labs Durham Nc.

[Diamantonis & Economou, 2011] Diamantonis, N. I., & Economou, I. G. 2011. Evaluation of Statistical Associating Fluid Theory (SAFT) and Perturbed Chain-SAFT Equations of State for the Calculation of Thermodynamic Derivative Properties of Fluids Related to Carbon Capture and Sequestration. *Energy & Fuels*, **25**(7), 3334–3343.

[Doubek, 2014] Doubek, M. 2014. *Thermophysical properties of fluids experiment and simulations*. Master's thesis, Czech Technical University, Faculty of Mechanical Engineering.

[Dwyer, 1939] Dwyer, R. J. 1939. The Persistence of Molecular Vibration in Collisions. *The Journal of Chemical Physics*, **7**(1), 40–44.

[Goodwin, 1998] Goodwin, A. R. H. 1998 (February). *Thermophysical Properties of Chlorine from Speed-of-Sound Measurements*. Ph.D. thesis, University of London.

[Goodwin & Moldover, 1990] Goodwin, A. R. H., & Moldover, M. R. 1990. Thermophysical properties of gaseous refrigerants from speed of sound measurements. I. Apparatus, model, and results for 1,1,1,2-tetrafluoroethane R134a. *The Journal of Chemical Physics*, **93**(4), 2741–2753.

[Gross & Sadowski, 2001] Gross, J., & Sadowski, G. 2001. Perturbed-Chain SAFT: An Equation of State Based on a Perturbation Theory for Chain Molecules. *Industrial & Engineering Chemistry Research*, **40**(4), 1244–1260.

[Henderson, 1963] Henderson, M. C. 1963. Sound in Air: Absorption and Dispersion. *Sound: Its uses and Control*, **2**(6), 28–36.

[Holmes *et al.*, 1964] Holmes, R., Jones, G. R., & Pusat, N. 1964. Vibrational Relaxation in Propane, Propylene, and Ethane. *The Journal of Chemical Physics*, **41**(8), 2512–2516.

[Iwai *et al.*, 1988] Iwai, Y., Margerum, M. R., & Lu, B. C.-Y. 1988. A new three-parameter cubic equation of state for polar fluids and fluid mixtures. *Fluid Phase Equilibria*, **42**, 21 – 41.

[Johnson *et al.*, 1993] Johnson, J. K., Zollweg, J. A., & Gubbins, K. E. 1993. The Lennard-Jones equation of state revisited. *Molecular Physics*, **78**(3), 591–618.

[Lin & Duan, 2005] Lin, H., & Duan, Y.-Y. 2005. Empirical correction to the Peng-Robinson equation of state for the saturated region. *Fluid Phase Equilibria*, **233**(2), 194 – 203.

[Liu *et al.*, 2017] Liu, T., Wang, S., & Zhu, M. 2017. Decomposition of effective specific heat of molecular relaxation for gas detection in a mixture. *The Journal of the Acoustical Society of America*, **141**(3), 1844–1851.

[Llovell & Vega, 2006] Llovell, F., & Vega, L. F. 2006. Prediction of Thermodynamic Derivative Properties of Pure Fluids through the Soft-SAFT Equation of State. *The Journal of Physical Chemistry B*, **110**(23), 11427–11437. PMID: 16771416.

[Maghari & Najafi, 2010] Maghari, Ali, & Najafi, Mohsen. 2010. On the Calculation of Surface Tensions of n-Alkanes Using the Modified SAFT-BACK-DFT Approach. *Journal of Solution Chemistry*, **39**(1), 31–41.

[Magoulas & Tassios, 1990] Magoulas, K., & Tassios, D. 1990. Thermophysical properties of n-Alkanes from C1 to C20 and their prediction for higher ones. *Fluid Phase Equilibria*, **56**(Supplement C), 119 – 140.

[Medeiros & Tellez-Arredondo, 2008] Medeiros, M., & Tellez-Arredondo, P. 2008. Cubic Two-State Equation of State for Associating Fluids. *Ind. Eng. Chem. Res*, **47**(15), 5723–5733.

[Olson & Legvold, 1963] Olson, J. R., & Legvold, S. 1963. Sound Dispersion in Substituted Methane-inert Gas Mixtures. *The Journal of Chemical Physics*, **39**(11), 2902–2908.

[Privat *et al.*, 2013] Privat, R., Jaubert, J.-N., & Privat, Y. 2013. A simple and unified algorithm to solve fluid phase equilibria using either the gamma-phi or the phi-phi approach for binary and ternary mixtures. *Computers & Chemical Engineering*, **50**, 139 – 151.

[Rand, 2004] Rand, M. 2004 (12). *Practical Equation of State for Non-Spherical and Asymetric Systems*. Dissertation thesis, University of Stellenbosch.

[Solms *et al.*, 2006] Solms, N., Kouskoumvekaki, I. A., Michelsen, M. L., & Kontogeorgis, G. M. 2006. Capabilities, limitations and challenges of a simplified PC-SAFT equation of state. *Fluid Phase Equilibria*, **241**(1), 344 – 353. A Festschrift in Honor of John M. Prausnitz.

[Tahani, 2011] Tahani, H. 2011 (November). *Determination of the Velocity of Sound in Reservoir Fluids Using an Equation of State*. Submitted for the degree of Doctor of Philosophy in Petroleum Engineering, Heriot-Watt University, Institute of Petroleum Engineering.

[Tihic *et al.*, 2008] Tihic, Amra, Kontogeorgis, Georgios M., von Solms, Nicolas, Michelsen, Michael L., & Constantinou, Leonidas. 2008. A Predictive Group-Contribution Simplified PC-SAFT Equation of State: Application to Polymer Systems. *Industrial & Engineering Chemistry Research*, **47**(15), 5092–5101.

[Valley & Legvold, 1960] Valley, L. M., & Legvold, S. 1960. Sound Dispersion in Ethane and 1,1-Difluoroethane. *The Journal of Chemical Physics*, **33**(2), 627–629.

[Zhang *et al.*, 2014] Zhang, K.-S., Ou, W., Jiang, X., Long, F., & Hu, M. 2014. Calculation of vibrational relaxation times in multi-component excitable gases. *Journal of the Korean Physical Society*, **65**(7), 1028–1035.

[Zhu *et al.*, 1993] Zhu, M. S., Han, L. Z., Zhang, K. Z., & Zhou, T. Y. 1993. Sound velocity and ideal-gas specific heat of gaseous 1,1,1,2-tetrafluoroethane (R134a). *International Journal of Thermophysics*, **14**(5), 1039–1050.

7 Evaluations of models

7.1 Introduction

This thesis focuses on fluids that are used in cooling of particle physics experiments, this include fluorocarbons and carbon dioxide. The higher fluorocarbons are used as heat transfer liquids (mono-phase coolants) in radiation environments and so far only one suitable ecological friendly replacement called Novec 649[1] have been identified. The carbon dioxide can be used as refrigerant and also as heat transfer fluid but the design of the pumping system is significantly more complex and expensive than for Novec or fluorocarbons liquids. The carbon dioxide triple point is relatively high (-56°C) and it presents a limitation for the lowest achievable evaporation temperature. Mixtures or R-744 with other fluids namely hydrocarbons are being tested to improve certain properties and efficiency for cooling systems and heat pumps and to lower the minimum evaporation temperature, for example [Sarkar & Bhattacharyya, 2009] or [Zhang *et al.*, 2017]. The mixtures of hydrocarbons with fluorocarbons are interesting for various applications spanning from solvent separation, organic Rankine cycles and most importantly for mixed-gases Joule-Thomson refrigerators (for example [Gong *et al.*, 2004]).

7.2 Fluids

I have included following types of refrigerants in the evaluations of the thermodynamic models:

- Saturated fluorocarbons from CF_4 (R-14) to C_6F_{14}
- Hydrocarbons from R-50 (ethane) to R-600 (nbutane)
- Nitrogen R-728
- Carbon dioxide R-744
- Heat transfer fluid Novec 649

Although fluorocarbons have very high GWP they are still used for special applications where more ecological fluids cannot be used for some reasons. The fluorocarbons have applications as solvents in microelectronic industry, as fire extinguishing gases, blood substitutes (!) and as refrigerants. Needles to say that they are being replaced with more ecological fluids wherever possible. The saturated fluorocarbons are non-toxic, odorless, inert and they do not conduct electricity. Their chemical formula is C_nF_{2n+2}, starting from CF_4 (Tetrafluoromethane R-14), continuing through C_2F_6 (Hexafluoroethane R-116), C_3F_8 (Octafluoropropane R-218) and so on. Since the fluorocarbons do not contain chlorine or bromine they have zero ozone depleting potential. Their GWP is high, 12010 and 8690 for R-116 and R-218 respectively. The fluids up to C_4F_{10} can be considered refrigerants as they can be used in evaporative cooling circuits while the fluids with higher carbon numbers are used as heat transfer liquids. The fluorocarbons can be found in numerous commercially available refrigerant blends:

[1] Heat transfer fluid manufactured by 3M

- R-508A: 39% R-23 and 61% R-116
- R-508B: 46% R-23 and 54% R-116
- R-403A: 5% R-290 75% R-22 and 20% R-218
- R-403B: 5% R-290 56% R-22 and 39% R-218
- R-412A: 10% R-22 5% R-218 and 25% R-142b
- R-413A: 9% R-218 88% R-134a 3% R-600a
- R-509A: 44% R-22 and 56% R-218

The C-F bond is very strong and notably it is the only bond in the fluorocarbon molecules. As a result the molecules are radiation hard. This has two consequences; on one hand the molecules have extremely long atmospheric life time, thousands of years, on the other hand they are suitable for uses in particle detectors as cooling fluid or radiation gases. The strong bond prevents formation of acids and toxic products in the cooling system even after long exposure to radiation. The R-218 proved to be a suitable refrigerant for multiple evaporative cooling circuits that removes heat from particle detector installed in the Large Hadron Collider at CERN, [Attree *et al.*, 2008] and [Haug, 2005]. Thanks to the favorable saturated pressure the R-218 is employed in oil-free cooling systems with water-cooled condensers capable of dealing with loads up to tens of kilowatts at evaporation temperatures down to -32°C. I did not include fluorocarbons with carbon number above six since they are not used as refrigerants nor as heat transfer fluids. The lowest saturated fluorocarbon with carbon number 1 is R-14. The R-116, R-218 refrigerants have carbon number two and three respectively, higher fluorocarbons are not assigned with refrigerant designation. Some higher fluorocarbons such is the C_6F_{14} are sometimes referred to by commercial name FC-72[2].

The saturated hydrocarbons (alkenes) C_nH_{2n+2} are used as ecological refrigerants with very low GWP (<26). Unfortunately, the flammability is limiting their use inside buildings and other closed spaces. But they can be added in small amounts to other non flammable refrigerants in order to create blends with interesting properties. One example is already mentioned low-temperature blend of carbon dioxide with small amount of ethane that is currently being developed. The saturated hydrocarbons start with methane R-50 (carbon number 1) and the series progresses with ethane R-170, propane R-290 and (n)butane R-600 and so on. I have not included hydrocarbons with higher carbon numbers since the normal boiling point is getting too high for refrigeration applications.

Nitrogen is rarely used as refrigerant outside cryogenic applications but it can be used in mixtures to model behaviour of air-contaminated refrigerants. The speed of sound in mixtures of fluorocarbons with nitrogen (R-728) are interesting since they can model air contamination of refrigerants and provide models for leak detection systems utilizing speed of sound measurement.

The carbon dioxide is a popular ecological refrigerant with two significant limitations: firstly, critical temperature is relatively low (31°C) which means that in hotter climates the refrigeration/air-conditioning systems with R-744 must run in trans-critical mode. Secondly, the triple point of carbon dioxide relatively high (-56°C). The carbon-dioxide molecule is very stable and it is thus radiation hard. Many new systems designs utilizing the R-744 are emerging nowadays including slush circuits and oil-less systems.

The Novec 649 is a new low GWP (<2) fluoroketone heat transfer fluid with properties closely matching the C_6F_{14} fluorocarbon in every respect (density, viscosity etc.) but the molecules are quite different. The fluid is relatively radiation hard and it is used in some new low-temperature cooling system for particle detectors in order to replace the environmentally unfriendly C_6F_{14} .

[2]The C_6F_{14} is produced under this name by 3M

The thermophysical properties of all the mentioned fluids can be found in Table 7.1. The C_6F_{14} molecule is the longest linear chain in the fluid set while the Novec is by far the most complex molecule as can be seen in the table.

Table 7.1: Fluids included in this study

Fluid	Formula	M [g/mol]	T_c [K]	P_c [MPa]	ρ_c [mol/m^3]	Accentric factor
R-14	CF_4	88.005	227.51	3.75	7109.4	0.1785
R-116	C_2F_6	138.01	293.03	3.048	4444.0	0.2566
R-218	C_3F_8	188.02	345.02	2.64	3340.0	0.3172
C_4F_{10}	C_4F_{10}	238.03	386.33	2.3234	2520.0	0.374
C_5F_{12}	C_5F_{12}	288.03	420.56	2.045	2116.0	0.423
C_6F_{14}	C_6F_{14}	338.04	448.77	1.868	1650.0	0.500
R-50	CH_4	16.043	190.56	4.5992	10139.0	0.0114
R-170	CH_3CH_3	30.069	305.32	4.8722	6856.9	0.0995
R-290	$CH_3CH_2CH_3$	44.096	369.89	4.2512	5000.0	0.152
R-600	CH_3-2(CH_2)-CH_3	58.122	425.13	3.796	3922.8	0.201
R-728	N_2	28.013	126.19	3.3958	11184.0	0.037
R-744	CO_2	44.01	304.13	7.3773	10625.0	0.224
Novec 649	$CF_3CF_2C(O)CF(CF_3)_2$	316.04	441.81	1.869	2022.2	0.471

7.3 Model parameter fitting

Firstly, vapour-liquid equilibrium data of the pure fluids were used to obtain the SAFT model parameters through multiparameter fitting. The same data were than used to evaluate the models. Somewhat unusually, the saturated pressure p and density of saturated vapour and liquid (ρ_V and ρ_L respectively) were used in the fitting procedure since the models were evaluated both in vapour and liquid region. Having the vapour density with weight of 0.5 in the function to be minimized, Equation 7.1, stabilized the results and the models then provided more balanced accuracy in both phases. The calculated properties from NIST REFPROP were used for some fluids as can be seen in Table 7.2 since there were no reliable data of saturated vapour density in convenient temperature range. The columns in the Table shows number of data points and maximum and minimum reduced temperature $T_r = T/T_c$.

$$CF = \sum_n \left| \frac{p_i^{exp} - p_i^{calc}}{p_i^{exp}} \right| + \sum_n \left| \frac{\rho_{Li}^{exp} - \rho_{Li}^{calc}}{\rho_{Li}^{exp}} \right| + 0.5 \sum_n \left| \frac{\rho_{Vi}^{exp} - \rho_{Vi}^{calc}}{\rho_{Vi}^{exp}} \right| \tag{7.1}$$

Saturated vapour and liquid density data-points at the same temperatures were used as input data even though it is not required by the fitting procedure. Although the selected thermodynamic models use only few fitting parameters (three or four) six $p - \rho_L - \rho_V$ data points were used for the fitting. The data points were evenly spaced on the temperature range stated in Table 7.2. The simplex algorithm was used as it provided more consistent results in comparison with the Levenberg-Marquardt algorithm for various number and spacing of input data points. To avoid problems with the initial estimates the Latin hyper cube was used to generate one hundred initial parameters sets in a wide range of the parameter values. The simplex algorithm was then run for each of the initial parameters set and the best result was selected. The obtained SAFT models parameters are listed in Table 7.3. The parameters of the Peng-Robinson and the Volume Translated

Peng-Robinson models were calculated from the critical properties of the fluids which are listed in 7.1 (see the model descriptions in chapter 6 for details).

Table 7.2: vapour-liquid equilibrium data sources

Fluid	Source	Datapoints	max T_r [K]	min T_r [K]
R-14	NIST REFPROP	14	1	0.53
R-116	NIST REFPROP	22	1	0.65
R-218	NIST REFPROP	29	1	0.61
C_4F_{10}	NIST REFPROP	18	1	0.6
C_5F_{12}	NIST REFPROP	20	1	0.57
C_6F_{14}	Equation by E.W. Lemmon*	22	1	0.56
R-50	[Friend *et al.*, 1989]	17	0.99	0.48
R-170	[Younglove & Ely, 1987]	9	0.98	0.46
R-290	[Glos *et al.*, 2004]	10	0.92	0.43
R-600	NIST REFPROP	12	0.99	0.47
R-728	[Jacobsen & Stewart, 1973]	30	0.98	0.53
R-744	NIST REFPROP	9	0.99	0.72
Novec 649	[McLinden *et al.*, 2015]	21	1	0.57

* This equation was provided privately by E. Lemmon as preliminary fit for NIST REFPROP 8.0

Table 7.3: Fitted model parameters

Model	sPC-SAFT			SoftSAFT			SAFT-BACK			
	m	ε/k_b	σ	m	ε/k_b	σ	m	v^{00}	u^0/k_b	α
Fluid	$[-]$	$[J]$	[Å]	$[-]$	$[J]$	[Å]	$[-]$	[ml/mol]	[K]	$[-]$
R-14	2.260	120.0	3.090	2.210	123.2	3.170	1.280	18.00	231.0	1.030
R-116	2.830	139.9	3.300	2.810	144.5	3.350	1.480	24.26	311.7	1.050
R-218	3.330	153.8	3.440	3.190	162.9	3.500	1.620	29.24	381.2	1.090
C_4F_{10}	3.890	161.1	3.520	3.800	170.5	3.540	1.810	33.66	431.1	1.080
C_5F_{12}	4.550	165.4	3.530	4.480	176.2	3.530	2.040	36.07	479.1	1.090
C_6F_{14}	4.930	172.2	3.620	4.460	191.1	3.760	1.980	41.95	537.6	1.180
R-50	1.010	148.8	3.690	1.080	142.5	3.650	1.000	15.93	191.2	1.010
R-170	1.620	189.9	3.510	1.880	176.1	3.400	1.090	21.19	309.7	1.040
R-290	2.000	208.3	3.620	1.950	212.2	3.720	1.240	25.46	387.4	1.050
R-600	2.330	222.9	3.710	2.130	237.7	3.870	1.340	29.88	457.9	1.070
R-728	1.250	88.89	3.290	1.300	86.27	3.300	1.000	14.02	128.9	1.030
R-744	2.560	152.1	2.560	2.680	153.4	2.530	1.350	10.95	324.3	1.070
Novec 649	4.620	173.7	3.660	4.650	183.3	3.630	1.990	40.89	517.9	1.150

7.4 Model evaluations - saturation properties of pure fluids

The models were compared against the vapour-liquid equilibrium data listed in the previous section. The absolute average deviation in Equation 7.2 was used to evaluate the models, Q represents either the saturated pressure, saturated vapour density or saturated liquid density. The algorithm for vapour liquid equilibrium calculations is described in section 6.7.

$$AAD\,[\%] = \sum_i \left| \frac{Q_i^{exp} - Q^{calc}}{Q_i^{exp}} \right| 100 \tag{7.2}$$

Firstly, I focused on the accuracy of the Volume Translated models. Only the saturated liquid density is affected by the volume translation, the calculated saturated vapour density and saturated pressure are practically unaffected and therefore almost identical to the Peng-Robinson equation of state. The comparison in Table 7.4 reveals that the volume translation by Magoulas and Tassios is by far the most accurate. The other two translations proved to be very inaccurate. The deviation of the saturated liquid density predicted by the Magoulas and Tassios model is below 5%. As a consequence only this model was used in further evaluations.

All of the translations do well with the common fluids such as carbon dioxide (R-744), nitrogen (R-728), methane (R-50) etc. This is because these fluids were always included in the datasets used during the development of the translations. The presented results indicate whether the translations can be used with fluids outside of the development set since the saturated fluorocarbons were not in any of these datasets. One should notice the poor results for the C_6F_{14} and Novec 649 which are caused by large deviations from the experimental data at low temperatures, below $T_r = 0.7$.

Table 7.4: Absolute average deviations of saturated liquid prediction - volume translated Peng-Robinson equation of state

	AAD [%]		
Fluid	Magoulas and Tassios	Lin and Duan	Ahlers and Gmehling
R-14	3.943	1.791	2.698
R-116	4.403	0.728	0.991
R-218	5.223	1.07	1.452
C_4F_{10}	5.646	24.758	28.06
C_5F_{12}	5.041	24.749	2.868
C_6F_{14}	3.914	90.636	92.745
R-50	1.449	0.562	1.986
R-170	0.809	1.013	1.449
R-290	0.96	32.772	0.872
R-600	0.827	0.654	0.921
R-728	1.267	0.76	1.667
R-744	1.454	0.773	0.592
Novec 649	1.312	7.206	91.714
Average	3.038	13.473	16.49

The absolute average deviations of the saturated pressure and saturated vapour density in Tables 7.5 and 7.6 reveal that the simple Peng-Robinson cubic equation of state achieves very good accuracy in prediction

of these properties. The accuracy is on par with the complicated SAFT modes, sometimes even better. This is in line with what is known about the general behaviour of the different equations of state. The cubic equations exhibit large deviations in liquid region. One can see in the Table 7.7 that the average deviation of the Peng-Robinson equation is quite large, more than 6%. The volume translated Peng-Robinson model which aims to improve the prediction of the liquid density provided better results with the average deviation of 3.1%.

The Soft-SAFT model is the worst from the three tested SAFT models, especially the large deviation in the prediction of saturated vapour density is striking. The results for R-116 and R-218 presented in my Master's thesis ([Doubek, 2014]) already indicated that the Soft-SAFT model is probably not a good choice for the saturated fluorocarbons. It is surprising that the models exhibits large deviation in the saturated vapour density prediction even for the hydrocarbons and carbon dioxide (R-744).

One advantage of the cubic equations over the SAFT models is that the cubic equations are generally more accurate close to the critical point. The inaccuracy of the SAFT models in the critical region is clearly visible in the evaluation plots in Annexes (section 9). There is one exception, however: the SAFT-BACK model is very accurate even close to the critical point (T_r close to 1). In fact, the little-known SAFT-BACK model outperforms even the well-known and accurate sPC-SAFT model, and it is the most accurate model in all the presented evaluations so far.

Table 7.5: Absolute average deviations of saturated pressure prediction. PR stands for Peng-Robinson; VTPR for Volume Translated Peng-Robinson - Magoulas and Tassios, sPC for Simplified PC-SAFT, SS for SoftSAFT and SB for SAFT-BACK

	AAD [%]				
Fluid	PR	VTPR	sPC	SS	SB
R-14	0.42	0.42	0.33	1.42	0.59
R-116	0.35	0.35	0.21	1.34	0.4
R-218	0.46	0.46	0.43	1.73	0.43
C_4F_{10}	0.66	0.66	1.09	2.32	0.62
C_5F_{12}	5.36	5.36	2.13	1.85	1.72
C_6F_{14}	6.34	-	2.32	2.89	0.89
R-50	0.64	0.64	1.3	1.04	0.73
R-170	0.91	0.91	1.29	6.5	1.48
R-290	1.86	1.86	1.56	1.27	2.2
R-600	0.96	0.96	0.36	1.75	0.47
R-728	0.73	0.73	1.52	0.93	1.24
R-744	0.48	0.48	1.53	0.77	0.72
Novec 649	1.49	1.49	1.34	2.39	0.7
Average	1.59	1.19	1.19	2.02	0.94

Table 7.6: Absolute average deviations of saturated vapour density prediction

	AAD [%]				
Fluid	PR	VTPR	sPC	SS	SB
R-14	2.18	2.07	3.41	7.61	2.04
R-116	1.7	1.91	2.61	7.32	1.69
R-218	1.52	1.37	3.44	9.03	1.63
C_4F_{10}	1.64	1.51	3.03	9.62	2.6
C_5F_{12}	7.08	7.47	3.98	8.42	2.91
C_6F_{14}	6.19	-	3.75	11.71	4.32
R-50	1.22	1.92	1.51	5.34	2.2
R-170	1.29	1.88	1.55	8.13	2.6
R-290	2.12	2.18	1.18	1.95	2.61
R-600	1.35	1.99	2.42	6.75	1.49
R-728	2.02	1.92	1.87	1.25	1.07
R-744	1.12	2.07	1.94	9.38	1.83
Novec 649	2.61	2.87	3.7	8.9	3.75
Average	2.46	2.43	2.65	7.34	2.36

Table 7.7: Absolute average deviations of saturated liquid density prediction

	AAD [%]				
Fluid	PR	VTPR	sPC	SS	SB
R-14	8.12	3.94	2.4	4.36	2.28
R-116	6.15	4.40	1.85	3.63	1.77
R-218	5.97	5.22	2.49	3.94	0.78
C_4F_{10}	6.45	5.65	3.41	5.35	2.43
C_5F_{12}	4.77	5.04	2.32	4.66	4.01
C_6F_{14}	3.47	3.91	5.61	7.91	5.16
R-50	9.04	1.45	1.02	1.65	0.98
R-170	7.35	0.81	0.93	1.69	1.02
R-290	5.29	0.96	0.19	2.17	1.24
R-600	5.2	0.83	0.62	1.51	0.62
R-728	9.4	1.27	1.29	0.89	1.38
R-744	4.44	1.45	0.39	1.35	0.52
Novec 649	4.92	1.31	2.18	4.07	2.84
Average	6.2	3.04	1.9	3.32	1.93

7.5 Model evaluations - Speed of sound

The density evaluations presented in the previous section already indicate the performance of the models in terms of the speed of sound prediction. If a model accurately predicts the saturated vapour density it is likely that it will be accurate in prediction of the vapour-phase speed of sound. The accuracy of the models near the critical point can indicate the model performance for the speed of sound above the critical point (nitrogen,

carbon dioxide).

Every equation of state is evaluated in terms of prediction accuracy of saturation properties of common fluids during the development and these evaluations are available in literature. The vapour-phase speed of sound is sometimes included too since the experimental data are extremely accurate and the speed of sound calculations require partial derivatives of the equations of state which reveals whether the model is consistent. Most equations of state exhibit large deviations in the liquid phase speed of sound prediction and this might be the reason why it is rarely included in the models evaluations. I have found numerous vapour phase speed of sound experimental data (Table 7.9) and several liquid phase speed of sound data (Table 7.8) for the presented evaluations. The vapour-phase speed (Tables 7.9 and 7.10) of sound also includes the data obtained in the experimental part of this work. The vapour-phase speed of sound data gathered from literate were obtained with resonators and the claimed uncertainties are well below 1%. The liquid phase speed of sound was mostly obtained with pulse-echo techniques and the uncertainties differ greatly, on average the uncertainty should be better than 3% (note that the liquid phase speed of sound is higher than the vapour phase speed of sound). Some of the data sets in the Table 7.9 contain data-points in the vapour-region or in gas region above the critical point or both as indicated by the ranges of reduced temperature and reduced pressure in the table. The plots in the Annexes (section 9) show the data points in the (p-T) plot together with the saturation curve and critical points so that one can immediately see what kind of data are in the data-set.

The data always consist of the temperature, pressure and speed of sound but the equations of state require the temperature and density as an input for calculations. This means that an iterative algorithm had to be used to find the density for a given pressure and temperature. A Newton search algorithm was employed, the initial estimate for the vapour phase density was $1\,mol/m^3$ while the initial estimate for the liquid phase density was derived from the Rackett equation which estimates the saturated liquid density based on critical properties:

$$1/\rho = \left(\frac{1}{\rho_c}\right)\left[\frac{p_c}{T_c\rho_c R}\right]^{(1-Tr)^{0.2857}} . \tag{7.3}$$

Table 7.8: Liquid speed of sound data sources

	Fluid	Source	Datapoints	max T_r [K]	min T_r [K]	max p_r [MPa]	min p_r [MPa]
19	C_5F_{12}	[Kallepally & Mallikharjuna, 1989]	1	0.71	0.71	0.05	0.05
20	C_5F_{12}	[Cochran *et al.*, 1974]	5	0.6	0.55	0.05	0.05
21	C_6F_{14}	[Marsh *et al.*, 2002]	6	0.71	0.65	0.06	0.055
22	C_6F_{14}	[Cusco & Trusler, 1995]	4	0.68	0.61	0.06	0.055
23	R-290	[Meier & Kabelac, 2012]	298	1.14	0.65	23.56	0.306
24	R-600	[Hawary & Meier, 2016]	197	1.01	0.47	4.64	0.066
25	Novec 649	[McLinden *et al.*, 2015]	7	0.7	0.63	0.04	0.044

Table 7.9: vapour speed of sound data sources

	Fluid	Source	Datapoints	max T_r [K]	min T_r [K]	max p_r [MPa]	min p_r [MPa]
1	R-14	[Hurly, 1999]	81	1.87	1.32	0.4	0.027
2	R-14	[Ewing & Trusler, 1989]	59	1.32	0.77	0.27	0.021
3	R-116	This work	174	1.11	0.86	0.1	0.023
4	R-116	[Hurly *et al.*, 2003]	171	1.62	0.72	0.49	0.033
5	R-218	[Vacek *et al.*, 2001]	64	0.88	0.74	0.15	0.004
6	R-218	This work	180	0.94	0.73	0.11	0.024
7	C_4F_{10}	[Vacek *et al.*, 2000]	26	0.78	0.66	0.04	0.004
8	R-50	[Goodwin, 1988]	47	1.84	1.34	1.56	0.01
9	R-50	[Friend *et al.*, 1989]	140	2.1	0.63	2.17	0.022
10	R-50	[Younglove & Ely, 1987]	133	2.62	1.05	0.09	0.002
11	R-170	[Estrada-Alexanders & Trusler, 1997]	187	1.47	0.72	2.15	0.003
12	R-290	[He *et al.*, 2002]	24	0.87	0.79	0.16	0.048
13	R-290	[Trusler & Zarari, 1996]	68	1.01	0.61	0.2	0.002
14	R-728	[Gomes & Trusler, 1998]	68	2.77	1.98	8.86	0.029
15	R-728	[Estela-Uribe & Trusler, 2000]	58	3.17	1.35	0.42	0.007
16	R-728	[Boyes, 1992]	71	2.57	2.34	1.96	0.015
17	R-744	[Liu *et al.*, 2014]	61	1.48	0.72	1.92	0.042
18	Novec 649	[McLinden *et al.*, 2015]	75	1.13	0.74	0.93	0.029

The Table 7.10 reveals that all the models perform very well in in the vapour phase speed of sound prediction, the average deviations are below 1%. Even the SoftSAFT model which did not perform well in saturated vapour density prediction delivers average deviation below 1%. It means that the derivatives needed to calculate the speed of sound are correct even though the saturated vapour density exhibits larger deviations. The deviation of the data obtained in the experimental part of this work (datasets 3 and 6 in Tables 7.9 and 7.10) is comparable with the deviations of vapour-phase speed of sound data for other fluids in the table. Since the other data were obtained with spherical resonators it is another confirmation that the developed measurement technique is very accurate.

The liquid phase results in Table 7.11 indicate very poor accuracy of the Peng-Robinson equations of state which is no surprise but the volume-translated model is even worse. The reason is that the translated models are developed with strong focus on the saturated density and they can exhibit very strange behaviour in the compressed liquid region. The SAFT-BACK model stands out in terms of prediction accuracy in the vapour and liquid phases. It is already clear that the little known and rarely used SAFT-BACK model is clearly superior to the other models in the presented tests. Especially the accuracy for C_6F_{14} and Novec 649 where all other models fail is impressive. It is true that the SAFT-BACK model has certain advantage in that it uses four fluid-specific parameters unlike the other SAFT models which use only three.

Table 7.10: Absolute average deviations of vapour speed of sound predictions. PR stands for Peng-Robinson; VTPR for Volume Translated Peng-Robinson - Magoulas and Tassios, sPC for Simplified PC-SAFT, SS for SoftSAFT and SB for SAFT-BACK

	AAD [%]					
	Fluid	PR	VTPR	sPC	SS	SB
1	R-14	0.34	0.11	0.37	0.36	0.2
2	R-14	0.41	1.12	0.26	0.41	0.05
3	R-116	0.42	0.37	0.37	0.1	0.14
4	R-116	0.49	0.39	0.54	0.69	0.14
5	R-218	0.59	0.49	0.58	0.83	0.57
6	R-218	0.38	0.15	0.33	0.46	0.13
7	C_4F_{10}	1.3	1.3	1.31	1.24	1.26
8	R-50	0.65	0.42	0.38	0.43	0.11
9	R-50	0.52	1	0.28	0.43	0.1
10	R-50	0.05	0.03	0.02	0.02	0.01
11	R-170	0.78	1.79	0.48	1.97	0.44
12	R-290	0.34	0.39	0.2	0.69	0.28
13	R-290	0.26	1.47	0.12	0.37	0.12
14	R-728	2.3	0.64	0.51	1.06	0.47
15	R-728	0.11	0.05	0.06	0.06	0.05
16	R-728	0.34	0.25	0.18	0.25	0.12
17	R-744	0.91	2.88	0.59	2.47	0.25
18	Novec 649	0.61	0.8	1.16	2.71	0.8
Average		0.56	0.73	0.40	0.70	0.28

Table 7.11: Absolute average deviations of liquid speed of sound predictions. PR stands for Peng-Robinson; VTPR for Volume Translated Peng-Robinson - Magoulas and Tassios, sPC for Simplified PC-SAFT, SS for SoftSAFT and SB for SAFT-BACK

	AAD [%]					
	Fluid	PR	VTPR	sPC	SS	SB
19	C_5F_{12}	29.55	28.73	16.97	13.92	0.94
20	C_5F_{12}	22.4	20.58	20.51	14.48	5.11
21	C_6F_{14}	25.38	25.88	16.42	13.45	2.85
22	C_6F_{14}	23.61	23.93	18.03	14.48	1.82
23	R-290	15.05	22.98	6.67	4.18	2.19
24	R-600	16.61	20.01	8.06	6.03	6.14
25	Novec 649	25.09	25.21	17.38	14.15	1.46
Average		10.20	10.99	6.70	5.56	1.45

7.6 Mixtures

I gathered vapour-liquid equilibrium data of mixtures containing saturated fluorocarbons from available literature, Table 7.12. The data contain the saturated pressure, temperature and composition of both liquid (molar fractions x_i) and vapour (molar fractions y_i) phase. Unfortunately, I found only one data set of fluorocarbon-fluorocarbon mixture (R-116+C_6F_{14}), the rest are mixtures of fluorocarbons with hydrocarbons, nitrogen or carbon dioxide. The data sets were used to obtain the binary interaction coefficients k_{12} through optimization. The function minimized during the optimization was following:

$$CF = \sum_n \left| \frac{x_i^{exp} - x_i^{calc}}{x_i^{exp}} \right| + \sum_n \left| \frac{y_i^{exp} - y_i^{calc}}{y_i^{exp}} \right|. \tag{7.4}$$

In other words, the optimization algorithm (Newton search in this case) was searching for the optimal value of the interaction coefficient k_{12} in order to minimize the deviation of the calculated vapour (y_i) and liquid phase composition (x_i) from the input experimental data. Somewhat unusual algorithm was used to calculate the vapour-liquid equilibrium: the inputs to calculate the equilibrium were the pressure and temperature while the algorithm was searching for the composition of the phases, detailed description can be found in section 6.7. Although it is more common to use composition as one of the inputs, especially in chemical process design, this work is focused on fluid analysis and identification where the composition is the unknown. The optimal values of the binary interaction coefficients are listed in Table 7.13.

The average deviations of the vapour and liquid phase compositions for each evaluated mode can be found in Table 7.14. The results are very similar, the sPC_SAFT exhibits the lowest deviation in the vapour composition predicition while the SAFT-BACK exhibits the highest deviation but the differences are relatively small for this kind of data.

Table 7.12: Mixture vapour-liquid equilibrium data sources

Pair	Fluid	Fluid	Source	Datapoints	max T [K]	min T [K]
1	R-744	R-728	[Brown *et al.*, 1989]	17	270	250
2	R-50	R-728	[Stryjek *et al.*, 1974]	23	161	138
3	R-728	R-170	[Stryjek *et al.*, 1974]	15	194	194
4	R-728	R-290	[Yucelen & Kidnay, 1999]	32	330	240
5	R-728	R-600	[Brown *et al.*, 1989]	24	270	250
6	R-744	R-50	[Wei *et al.*, 1995]	13	270	270
7	R-744	R-170	[Wei *et al.*, 1995]	8	207	207
8	R-744	R-290	[Katsuyuki *et al.*, 2009]	33	290	260
9	R-744	R-600	[Kalra *et al.*, 1976]	10	283	283
10	R-728	C_4F_{10}	[Tshibangu, 2017]	11	333	333
11	R-744	R-116	[Valtz *et al.*, 2007]	12	273	253
12	R-744	C_6F_{14}	[Tochigi *et al.*, 2010]	12	303	303
13	R-170	R-50	[Wei *et al.*, 1995]	25	250	230
14	R-50	R-290	[May *et al.*, 2015]	8	244	244
15	R-50	R-600	[Sage *et al.*, 1940]	42	328	294
16	R-170	R-600	[Mehra & Thodos, 1965]	13	394	366
17	R-600	R-290	[Yohei *et al.*, 2005]	16	310	270
18	R-50	C_4F_{10}	[Tshibangu, 2017]	34	333	293
19	R-50	C_6F_{14}	[Tshibangu, 2017]	58	333	293
20	R-170	R-116	[Zhang *et al.*, 2006]	14	253	193
21	R-170	R-218	[Tshibangu *et al.*, 2013]	50	308	264
22	R-116	R-290	[Ramjugernath *et al.*, 2009]	9	263	263
23	R-600	R-116	[Ramjugernath *et al.*, 2017]	9	288	288
24	R-116	C_6F_{14}	[Bengesai *et al.*, 2016]	98	313	273

Table 7.13: Optimized binary interaction parameters

Pair	Fluid	Fluid	PR	VTPR	sPC	SS	SB
1	R-744	R-728	1.02	0.99	1.05	1.04	1.11
2	R-50	R-728	0.95	0.95	0.98	0.97	0.98
3	R-728	R-170	0.99	0.83	0.99	1.01	1.03
4	R-728	R-290	0.93	0.86	0.95	0.96	1.13
5	R-728	R-600	0.90	0.82	0.93	0.93	1.21
6	R-744	R-50	0.91	0.89	0.99	0.92	0.99
7	R-744	R-170	0.87	0.87	0.95	0.88	0.90
8	R-744	R-290	0.88	0.87	0.95	0.87	0.89
9	R-744	R-600	0.88	0.97	0.95	0.85	0.96
10	R-728	C_4F_{10}	1.00	0.82	0.97	0.99	1.29
11	R-744	R-116	0.91	0.91	0.96	0.91	0.89
12	R-744	C_6F_{14}	0.98	0.94	0.99	0.90	0.97
13	R-170	R-50	0.99	0.97	1.00	1.00	1.06
14	R-50	R-290	0.88	0.93	0.91	0.92	1.00
15	R-50	R-600	0.74	1.43	0.83	0.79	0.97
16	R-170	R-600	0.96	0.95	0.98	0.99	1.01
17	R-600	R-290	1.00	0.99	1.00	1.00	1.00
18	R-50	C_4F_{10}	0.75	0.65	0.84	0.81	1.02
19	R-50	C_6F_{14}	0.87	0.67	0.90	0.86	1.23
20	R-170	R-116	0.87	0.87	0.92	0.90	0.89
21	R-170	R-218	0.89	0.89	0.93	0.93	0.92
22	R-116	R-290	0.86	0.88	0.92	0.92	0.88
23	R-600	R-116	0.85	0.85	0.92	0.90	0.92
24	R-116	C_6F_{14}	1.00	1.36	0.98	0.95	0.99

Table 7.14: Evaluation of the mixture composition prediction

			AAD [%]									
	Fluids		PR		VT		sPC		SS		SB	
	1	2	x_1	y_1	x_1	y_1	x_1	y_1	x_1	y_1	x_1	y_1
1	R-744	R-728	0.49	0.71	1.22	1.22	0.45	0.56	0.46	3.89	0.14	1.19
2	R-50	R-728	1.38	1.09	0.73	0.73	0.67	0.86	1.92	6.98	0.38	0.45
3	R-728	R-170	2.41	2.94	6.31	6.31	4.09	3.88	3.71	5.92	9.23	4.1
4	R-728	R-290	0.4	0.65	0.98	0.98	0.45	1.04	0.62	1.87	0.3	1.22
5	R-728	R-600	0.19	0.11	0.3	0.3	0.21	0.07	0.22	0.44	0.14	0.14
6	R-744	R-50	0.37	0.78	0.82	0.82	1.25	0.94	1.04	4.18	1.64	0.92
7	R-744	R-170	0.88	1.21	0.7	0.7	0.63	0.52	1.11	2.92	0.64	0.89
8	R-744	R-290	0.5	1.21	0.97	0.97	0.89	0.89	1.06	2.43	2.12	1.02
9	R-744	R-600	1.22	0.66	1.43	1.43	0.82	0.51	2.73	1.27	7.44	1.35
10	R-728	C_4F_{10}	0.32	1.48	1.58	1.58	0.1	2.47	0.85	2.47	0.65	0.65
11	R-744	R-116	0.59	0.38	0.44	0.44	0.94	0.55	0.6	1.73	1.43	0.86
12	R-744	C_6F_{14}	0.86	0.6	0.61	0.61	0.31	0.7	1.2	1.31	6.68	0.83
13	R-170	R-50	0.24	0.44	0.82	0.82	0.47	0.66	1.21	2.48	2.04	1.78
14	R-50	R-290	16.19	0.56	0.55	0.55	20.3	0.64	15.63	0.64	13.17	0.92
15	R-50	R-600	3.49	26.24	26.56	26.56	2.71	23.84	3.97	28.05	3.16	22.66
16	R-170	R-600	1.09	1.8	2.22	2.22	0.55	0.95	0.34	5.2	0.77	0.77
17	R-600	R-290	1.06	0.74	0.9	0.9	0.86	0.85	0.81	0.83	1	0.75
18	R-50	C_4F_{10}	2.86	7.8	9.49	9.49	2.85	7	4.38	10.43	4.64	5.17
19	R-50	C_6F_{14}	0.38	1.92	1.88	1.88	0.53	1.82	0.5	1.87	1.07	2.04
20	R-170	R-116	2.12	0.76	1.2	1.2	2.05	1.63	6.09	3.14	6.68	4.56
21	R-170	R-218	1.26	1.13	1.47	1.47	0.79	0.66	0.86	1.06	2.14	2.88
22	R-116	R-290	2.15	1.68	2.12	2.12	2.05	1.12	4.83	2.38	2.57	1.29
23	R-600	R-116	1.34	0.87	0.67	0.67	1.18	0.82	1.38	1.55	4.16	1.25
24	R-116	C_6F_{14}	6.27	9.53	2.39	2.39	2.07	2.54	4.25	2.17	7.6	0.78
Average			2	2.72	2.77	2.77	1.97	2.31	2.49	3.97	3.32	2.44

7.7 Correlations of binary interaction coefficients

There are several papers dealing with the Peng-Robinson, sPC-SAFT and Soft-SAFT equations of state that focus on mixtures relatively close to the mixtures studied in this work although in most cases higher fluorocarbons and alkanes are involved. There is a thorough work [Qian *et al.*, 2017] dealing with accurate prediction models that consist of Peng-Robinson equation of state coupled with model for prediction of binary interaction coefficients. The use of sPC-SAFT model for mixtures of higher alkenes and carbon dioxide is studied in [Ma *et al.*, 2015] . Several papers are dealing with Soft-SAFT model and higher alkenes and perfluorocarbons [Varanda *et al.*, 2008, Dias *et al.*, 2006, Dias *et al.*, 2004]. To my knowledge there is no publication that would evaluate the SAFT-BACK model for similar mixtures or publication which would provide correlation or other approach for interaction coefficient prediction for this model. The Figure 7.1 shows that the interaction coefficients for the SAFT-BACK model have different values for some of the mixtures than the other models. Thus not it is not possible to use the correlations developed for other SAFT models. For this reason I have developed three correlations that can be used to estimate the binary interaction

parameters of the SAFT-BACK model for certain mixtures.

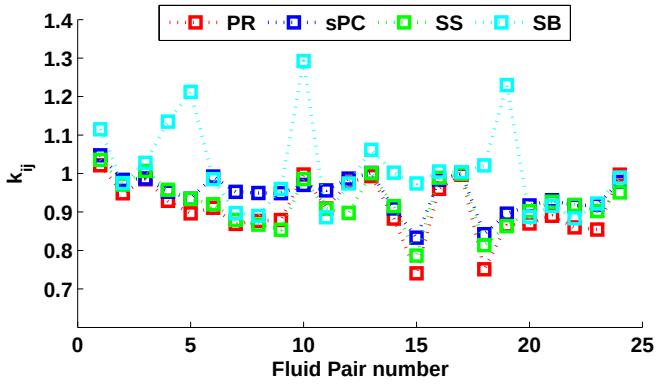

Figure 7.1: Correlated interaction coefficients k_{12}

Firstly I divided the fluids from section 7.6 into three groups, Table 7.15. The first group contains saturated fluorocarbons, the second group contains hydrocarbons and finally the third group contains nitrogen and carbon dioxide. The lowest fluorocarbon R-14 and lowest hydrocarbon R-50 were not separated into their own groups although one might argue that they behave differently in mixtures due to the shape of the molecules which is closer to a sphere in contrast to the higher fluorocarbon molecules which are linear chains. Having separate groups for R-50 and R-14 would likely increase the accuracy of the correlations but the correlations would be less universal.

By studying the existing correlations described in chapter 2, I came to a conclusion that the interaction coefficient should be correlated using fluid properties such as the molecular weight or critical temperature and group-specific constants in order for the correlation to have prediction ability. The correlation should also be consistent, meaning that the coefficient of the same fluids should be unity or at least close to unity. I have used an optimization algorithm to search for the optimal correlation from the possible equations 7.5 to 7.10. The equations contain group-specific constants a and b. The fluid property Y that were tested in the correlation can be found in equations 7.11 to 7.15. The constants and fluid properties are always plugged into the correlations so that $Y_1 > Y_2$

The optimization algorithm selected the best combination of equation and fluid property and found the group-specific constants for the groups in Table 7.15. The results are in Table 7.16 and in Figures 7.2 to 7.4. The same equation is used for all three fluid groups combinations. The equation inherently gives the interaction coefficients of 1 for the same fluids. The accentric factor is used as a fluid property for the mixture of Group 1 + Group 2 and the Equation 7.15 is used as a fluid property for the other two group combinations. One can compare the results in Figures 7.2 to 7.4 with the Figure 2.4 to see that the accuracy of the developed correlations is similar to other universal correlations. The correlation can be used to estimate the interaction coefficient of fluids from the same group, unfortunately very few data exist for the fluorocarbon+fluorocarbon mixtures. The Group1+Group3 model is recommended for the fluorocarbon+fluorocarbon since it is likely to be the most accurate due to the fact that it is not influenced by large number of "cross-group" interactions like the Group1+Group2 model.

Table 7.15: Fluid groups

Group 1					
R-14	R-116	R-218	C_4F_{10}	C_5F_{12}	C_6F_{14}
Group2					
R-50	R-170	R-290	R-600		
Group 3					
R-728	R-744				

$$k_{12} = a_1 Y_1^{b_1} \pm a_2 Y_2^{b_2} \tag{7.5}$$

$$k_{12} = \left(a_1 + Y_1^{b_1}\right) \pm \left(a_2 + Y_2^{b_2}\right) \tag{7.6}$$

$$k_{12} = \left[\left(a_1 Y_1^{b_1}\right) / \left(a_2 Y_2^{b_2}\right)\right]^{b1+b2} \tag{7.7}$$

$$k_{12} = \left[\left(a_1 Y_1^{b_1}\right) / \left(a_2 Y_2^{b_2}\right)\right] \tag{7.8}$$

$$k_{12} = \left[\left(a_1 + Y_1^{b_1}\right) / \left(a_2 + Y_2^{b_2}\right)\right]^{b1+b2} \tag{7.9}$$

$$k_{12} = \left(a_1 + Y_1^{b_1}\right) / \left(a_2 + Y_2^{b_2}\right) \tag{7.10}$$

$$Y_i = \omega_i \,;\, M_i \,;\, T_{ci} \,;\, P_{ci} \,;\, \rho_{ci} \,;\, m_i \,;\, \alpha_i \,;\, u_i^0 \,;\, v_i^{00} \,;\, \vartheta_i^0 \tag{7.11}$$

$$Y_i = \omega_i / T_{ci} \tag{7.12}$$

$$Y_i = \omega_i P_{ci} \tag{7.13}$$

$$Y_i = \omega_i P_{ci} / T_{ci} \tag{7.14}$$

$$Y_i = \omega_i P_{ci}^{0.5} / T_{ci} \tag{7.15}$$

Table 7.16: Developed correlations for SAFT-BACK interaction coefficients

Mixture	Group1+Group2	Group1+Group3	Group2+Group2
Correlation	$\left[\left(a_1 + Y_1^{b_1}\right) / \left(a_2 + Y_2^{b_2}\right)\right]^{b1+b2}$		
Property	$Y_i = \omega_i$	$Y_i = \omega_i P_{ci}^{0.5}/T_{ci}$	$Y_i = \omega_i P_{ci}^{0.5}/T_{ci}$
First group constant a_1	2.8079	1.4008	-0.9836
First group constant b_1	1.7085	0.3141	0.0067
Second group constant a_2	2.1551	1.3729	-1.0592
Second group constant b_2	0.0755	0.8598	0.1560

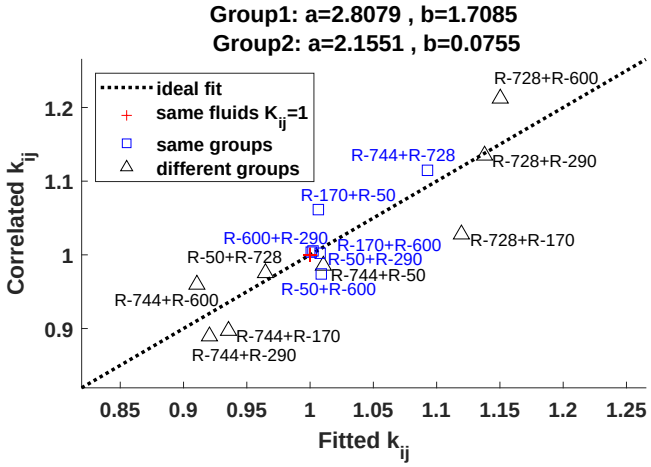

Figure 7.2: Correlation of interaction coefficients k_{ij} for fluids from Group1 and Group2

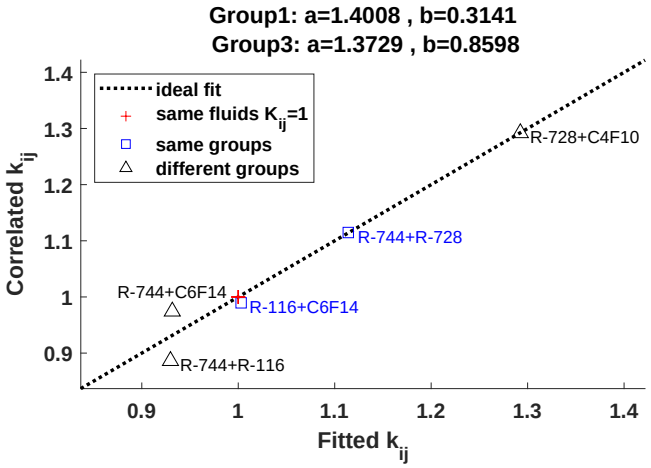

Figure 7.3: Correlation of interaction coefficients k_{ij} for fluids from Group1 and Group3

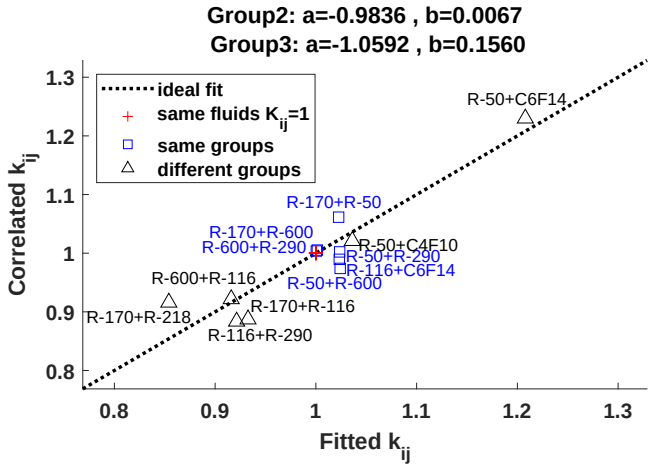

Figure 7.4: Correlation of interaction coefficients k_{ij} for fluids from Group2 and Group3

7.8 Speed of sound in mixtures

I have measured speed of sound in mixtures of R-116+R-218 and R-218+R-728 in the experimental part of this thesis. The binary interaction coefficients of these mixtures cannot be fitted directly to vapour liquid equilibrium since no data are available. The correlation developed in previous section can be used to estimate the interaction coefficient of the SAFT-BACK which performed the best in the previous evaluations. The correlation Group1+Group3 from Table table 7.16 was used to obtain interaction coefficient for both the mixtures:

$$k_{R116+R218} = \left[\frac{1.3729 + \left\{ \frac{0.2566 \cdot 3048000^{0.5}}{293.0300} \right\}^{0.8598}}{1.3729 + \left\{ \frac{0.3172 \cdot 2640000^{0.5}}{345.02} \right\}^{0.8598}} \right]^{0.8598+0.8598} . \tag{7.16}$$

$$k_{R218+R728} = \left[\frac{1.3729 + \left\{ \frac{0.3172 \cdot 2640000^{0.5}}{345.02} \right\}^{0.8598}}{1.4008 + \left\{ \frac{0.0372 \cdot 3395800^{0.5}}{126.1900} \right\}^{0.3141}} \right]^{0.8598+0.3141} . \tag{7.17}$$

The average deviation of the calculated and measured speed of sound with and without the correlated interaction coefficient can be found in Table 7.17. The predicted interaction coefficient of the R-116+R-218 mixtures is close to unity which is to be expected since the fluid are very similar. The average deviation between calculated and measured speed of sound of the R-218+R-728 (N_2) mixture benefits from appropriate interaction coefficient much more, the correlated coefficient $k_{12} = 1.3$ results in significant improvement from 1.07% to 0.89%. The speed of sound deviation as function of reduced density are shown in Figures figure 7.5 and figure 7.6.

Table 7.17: Evaluation of SAFT-BACK model for prediction of speed of sound in mixtures measured in this work

Mixture		Without correlation		Correlated	
Fluid 1	Fluid 2	k_{ij}=1	AAD [%]	k_{ij}	AAD [%]
R-116	R-218	1.000	0.76	1.018	0.76
R-218	R-728 (N_2)	1.000	1.073	1.300	0.89

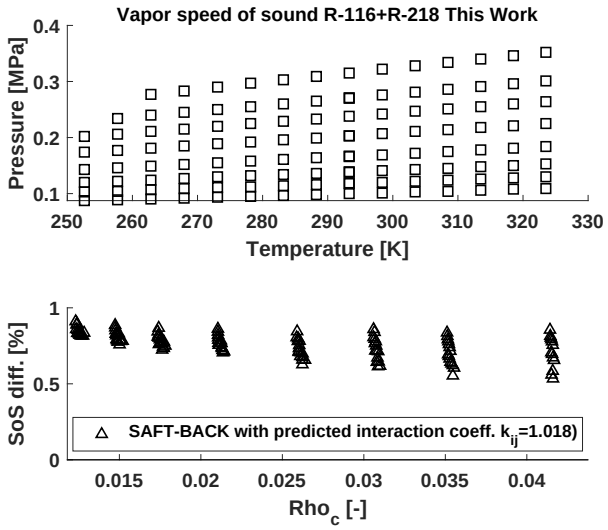

Figure 7.5: Evaluation of SAFT-BACK model for prediction of speed of sound in a mixture of R-116+R-218 measured in this work

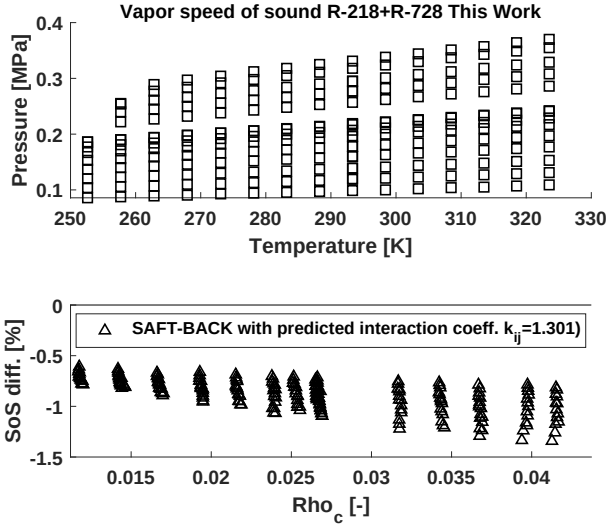

Figure 7.6: Evaluation of SAFT-BACK model for prediction of speed of sound in a mixture of R-218+R-728 (N_2) measured in this work

Bibliography

chapter 7: Evaluations of models

[Attree *et al.*, 2008] Attree, D, Anderson, B, Anderssen, E C, Akhnazarov, V, Apsimon, R J, Barclay, P, Batchelor, L E, Bates, R L, Battistin, M, Bendotti, J, Berry, S, Bitadze, A, Bizzel, J P, Bonneau, P, Bosteels, M, Butterworth, J M, Butterworth, S, Carter, A A, Carter, J R, Catinaccio, A, Corbaz, F, Danielsson, H O, Danilevich, E, Dixon, N, Dixon, S D, Doherty, F, Dorholt, O, Doubrava, M, Egorov, K, Einsweiler, K, Falou, A C, Feraudet, P, Ferrari, P, Fowler, K, Fraser, J T, French, R S, Galuska, M, Gannaway, F, Gariano, G, Gibson, M D, Gilchriese, M, Giugni, D, Godlewski, J, Gousakov, I, Gorski, B, Hallewell, G D, Hartman, N, Hawkings, R J, Haywood, S J, Hessey, N P, Ilyashenko, I, Infante, S, Jackson, J N, Jones, T J, Kaplon, J, Katunin, S, Lindsay, S, Luisa, L, Massol, N, McEwan, F, McMahon, S J, Menot, C, Mistry, J, Morris, J, Muskett, D M, Nagai, K, Nichols, A, Nicholson, R, Nickerson, R B, Nielsen, S L, Nordahl, P E, Olcese, M, Parodi, M, Perez-Gomez, F, Pernegger, H, Perrin, E, Rossi, L P, Rovani, A, Ruscino, E, Sandaker, H, Smith, A, Sopko, V, Stapnes, S, Stodulski, M, Tarrant, J, Thadome, J, Tovey, D, Turala, M, Tyndel, M, Vacek, V, van der Kraaij, E, Viehhauser, G H A, Vigeolas, E, Wells, P S, Wenig, S, & Werneke, P. 2008. The evaporative cooling system for the ATLAS inner detector. *Journal of Instrumentation*, **3**(07), P07003.

[Bengesai *et al.*, 2016] Bengesai, P. N., Nelson, W. M.l, & Naidoo, P.and Ramjugernath, D. 2016. Phase Equilibria for Perfluoroethane + (n-Perfluorohexane or n-Perfluorooctane) Binary Systems: Measurement and Modeling. *Journal of Chemical & Engineering Data*, **61**(9), 3363–3370.

[Boyes, 1992] Boyes, S.J. 1992. *The speed of sound in gases with application to equations of state and sonic nozzles*. Ph.D. thesis, University of London.

[Brown *et al.*, 1989] Brown, T. S., Niesen, V. G., Sloan, E. D., & Kidnay, A. J. 1989. Vapor-liquid equilibria for the binary systems of nitrogen, carbon dioxide, and n-butane at temperatures from 220 to 344 K. *Fluid Phase Equilibria*, **53**, 7 – 14. Proceedings of the Fifth International Conference.

[Cochran *et al.*, 1974] Cochran, M. A., North, A. M., & Pethrick, R. A. 1974. Ultrasonic studies of perfluoro-n-alkanes. *J. Chem. Soc., Faraday Trans. 2*, **70**, 1274–1279.

[Cusco & Trusler, 1995] Cusco, L., & Trusler, J. P. M. 1995. Identification of environmentally acceptable low-sound speed liquids. *International Journal of Thermophysics*, **16**(3), 675–685.

[Dias *et al.*, 2004] Dias, A. M. A., Pamies, J. C., Coutinho, J. A.P., Marrucho, I. M., & Vega, L. F. 2004. SAFT Modeling of the Solubility of Gases in Perfluoroalkanes. *The Journal of Physical Chemistry B*, **108**(4), 1450–1457.

[Dias *et al.*, 2006] Dias, A. M. A., Carrier, H., Daridon, J. L., Pamies, J. C., Vega, L. F., Coutinho, J. A. P., & Marrucho, I. M. 2006. VaporâLiquid Equilibrium of Carbon DioxideâPerfluoroalkane Mixtures:â Experimental Data and SAFT Modeling. *Industrial & Engineering Chemistry Research*, **45**(7), 2341–2350.

[Doubek, 2014] Doubek, M. 2014. *Thermophysical properties of fluids experiment and simulations*. Master's thesis, Czech Technical University, Faculty of Mechanical Engineering.

[Estela-Uribe & Trusler, 2000] Estela-Uribe, J. F., & Trusler, J. P. M. 2000. Acoustic and Volumetric Virial Coefficients of Nitrogen. *International Journal of Thermophysics*, **21**(5), 1033–1044.

[Estrada-Alexanders & Trusler, 1997] Estrada-Alexanders, A. F., & Trusler, J. P. M. 1997. The speed of sound and derived thermodynamic properties of ethane at temperatures between 220 K and 450 K and pressures up to 10.5 MPa. *The Journal of Chemical Thermodynamics*, **29**(9), 991 – 1015.

[Ewing & Trusler, 1989] Ewing, M. B., & Trusler, J. P. M. 1989. Speeds of sound in CF4 between 175 and 300 K measured with a spherical resonator. *The Journal of Chemical Physics*, **90**(2), 1106–1115.

[Friend *et al.*, 1989] Friend, G. D., Ely, J. F., & Ingham, H. 1989. Thermophysical Properties of Methane. **18**(04), 583–638.

[Glos *et al.*, 2004] Glos, S., Kleinrahm, R., & Wagner, W. 2004. Measurement of the (p,Ï,T) relation of propane, propylene, n-butane, and isobutane in the temperature range from (95 to 340) K at pressures up to 12 MPa using an accurate two-sinker densimeter. *The Journal of Chemical Thermodynamics*, **36**(12), 1037 – 1059.

[Gomes & Trusler, 1998] Gomes, M. F. C., & Trusler, J. P. M. 1998. The speed of sound in nitrogen at temperatures betweenT=250 K andT=350 K and at pressures up to 30 MPa. *The Journal of Chemical Thermodynamics*, **30**(5), 527 – 534.

[Gong *et al.*, 2004] Gong, M., Wu, J., Luo, E., Qi, Y., & Zhou, Y. 2004. Study of the single-stage mixed-gases refrigeration cycle for cooling temperature-distributed heat loads. *International Journal of Thermal Sciences*, **43**(1), 31 – 41.

[Goodwin, 1988] Goodwin, A. R. H. 1988. *Thermophysical properties from speed of sound*. Ph.D. thesis, University of London.

[Haug, 2005] Haug, F. 2005. Studies on cooling of the TOTEM particle detector at the LHC. 12.

[Hawary & Meier, 2016] Hawary, A. E., & Meier, K. 2016. Measurements of the Speed of Sound in Liquid n-Butane. *Journal of Chemical & Engineering Data*, **61**(11), 3858–3867.

[He *et al.*, 2002] He, M. G., Liu, Z. G., & Yin, J. M. 2002. Measurement of Speed of Sound with a Spherical Resonator: HCFC-22, HFC-152a, HFC-143a, and Propane. *International Journal of Thermophysics*, **23**(6), 1599–1615.

[Hurly, 1999] Hurly, J. J. 1999. Thermophysical Properties of Gaseous CF4 and C2F6 from Speed-of-Sound Measurements. *International Journal of Thermophysics*, **20**(2), 455–484.

[Hurly *et al.*, 2003] Hurly, J. J., Gillis, K. A., Mehl, J. B., & Moldover, M. R. 2003. The Viscosity of Seven Gases Measured with a Greenspan Viscometer. *International Journal of Thermophysics*, **24**(6), 1441–1474.

[Jacobsen & Stewart, 1973] Jacobsen, R. T., & Stewart, R. B. 1973. Thermodynamic Properties of Nitrogen Including Liquid and Vapor Phases from 63K to 2000K with Pressures to 10,000 Bar. *Journal of Physical and Chemical Reference Data*, **2**(4), 757–922.

[Kallepally & Mallikharjuna, 1989] Kallepally, N. L., & Mallikharjuna, S. K. 1989. Ultrasonic velocity in and adiabatic compressibility for some fluorocarbon liquid mixtures. *Journal of Chemical & Engineering Data*, **34**(1), 19–21.

[Kalra *et al.*, 1976] Kalra, H., Krishnana, T. R., & Robinson, D. B. 1976. Equilibrium-phase properties of carbon dioxide-butane and nitrogen-hydrogen sulfide systems at subambient temperatures. *Journal of Chemical & Engineering Data*, **21**(2), 222–225.

[Katsuyuki *et al.*, 2009] Katsuyuki, T., Yukihiro, H., Ryo, A., Yohei, K., & Kenich, F. 2009. Measurements of the VaporâLiquid Equilibrium for the CO2 + R290 Mixture. *Journal of Chemical & Engineering Data*, **54**(3), 1029–1033.

[Liu *et al.*, 2014] Liu, Q., Feng, X., An, B., & Duan, Y. 2014. Speed of Sound Measurements Using a Cylindrical Resonator for Gaseous Carbon Dioxide and Propene. *Journal of Chemical & Engineering Data*, **59**(9), 2788–2798.

[Ma *et al.*, 2015] Ma, M., Chen, S., & Abedi, J. 2015. Binary interaction coefficients of asymmetric CH4, C2H6, and CO2 with high n-alkanes for the simplified PC-SAFT correlation and prediction. *Fluid Phase Equilibria*, **405**, 114 – 123.

[Marsh *et al.*, 2002] Marsh, J. N., Hall, Ch. S., Wickline, S. A., & Lanza, G. M. 2002. Temperature dependence of acoustic impedance for specific fluorocarbon liquids. *The Journal of the Acoustical Society of America*, **112**(6), 2858–2862.

[May *et al.*, 2015] May, E. F., Guo, J. Y., Oakley, J. H., Hughes, T. J., Graham, B. F., Marsh, K. N., & Huang, S. H. 2015. Reference Quality VaporâLiquid Equilibrium Data for the Binary Systems Methane + Ethane, + Propane, + Butane, and + 2-Methylpropane, at Temperatures from (203 to 273) K and Pressures to 9 MPa. *Journal of Chemical & Engineering Data*, **60**(12), 3606–3620.

[McLinden *et al.*, 2015] McLinden, M. O., Perkins, R. A., Lemmon, E. W., & Fortin, T. J. 2015. Thermodynamic Properties of 1,1,1,2,2,4,5,5,5-Nonafluoro-4-(trifluoromethyl)-3-pentanone: Vapor Pressure, (p, Ï, T) Behavior, and Speed of Sound Measurements, and an Equation of State. *Journal of Chemical & Engineering Data*, **60**(12), 3646–3659.

[Mehra & Thodos, 1965] Mehra, V. S., & Thodos, G. 1965. Vapor-Liquid Equilibrium in the Ethane-n-Butane System. *Journal of Chemical & Engineering Data*, **10**(4), 307–309.

[Meier & Kabelac, 2012] Meier, K., & Kabelac, S. 2012. Thermodynamic Properties of Propane. IV. Speed of Sound in the Liquid and Supercritical Regions. *Journal of Chemical & Engineering Data*, **57**(12), 3391–3398.

[Qian *et al.*, 2017] Qian, J.-W., Privat, R., Jaubert, J.-N., Coquelet, Ch., & Ramjugernath, D. 2017. Fluid-phase-equilibrium prediction of fluorocompound-containing binary systems with the predictive E-PPR78 model. *International Journal of Refrigeration*, **73**, 65 – 90.

[Ramjugernath *et al.*, 2009] Ramjugernath, D., Valtz, A., Coquelet, C., & Richon, D. 2009. Isothermal VaporâLiquid Equilibrium Data for the Hexafluoroethane (R116) + Propane System at Temperatures from (263 to 323) K. *Journal of Chemical & Engineering Data*, **54**(4), 1292–1296.

[Ramjugernath *et al.*, 2017] Ramjugernath, D., Valtz, A., Richon, D., Williams-Wynn, M. D., & Coquelet, C. 2017. Isothermal VaporâLiquid Equilibrium Data for the Hexafluoroethane (R116) + n-Butane System at Temperatures from 273 to 323 K. *Journal of Chemical & Engineering Data*, **62**(10), 3483–3487.

[Sage *et al.*, 1940] Sage, B. H., Budenholzer, R. A., & Lacey, W. N. 1940. Phase Equilibria in Hydrocarbon Systems Methaneân-Butane System in the Gaseous and Liquid Regions. *Industrial & Engineering Chemistry*, **32**(9), 1262–1277.

[Sarkar & Bhattacharyya, 2009] Sarkar, J., & Bhattacharyya, S. 2009. Assessment of blends of CO2 with butane and isobutane as working fluids for heat pump applications. *International Journal of Thermal Sciences*, **48**(7), 1460 – 1465.

[Stryjek *et al.*, 1974] Stryjek, R., Chappelear, P. S., & Kobayashi, R. 1974. Low-temperature vapor-liquid equilibriums of nitrogen-methane system. *Journal of Chemical & Engineering Data*, **19**(4), 334–339.

[Tochigi *et al.*, 2010] Tochigi, K., Namae, T., Suga, T., Matsuda, H., Kurihara, K., Ramos, M. C., & McCabe, C. 2010. Measurement and prediction of high-pressure vaporâliquid equilibria for binary mixtures of carbon dioxide+n-octane, methanol, ethanol, and perfluorohexane. *The Journal of Supercritical Fluids*, **55**(2), 682 – 689. 100th year Anniversary of van der Waals' Nobel Lecture.

[Trusler & Zarari, 1996] Trusler, J. P. M., & Zarari, M. P. 1996. The speed of sound in gaseous propane at temperatures between 225 K and 375 K and at pressures up to 0.8 MPa. *The Journal of Chemical Thermodynamics*, **28**(3), 329 – 335.

[Tshibangu, 2017] Tshibangu, M. M. 2017. *Investigation Of Perfluorocarbons As Potential Physical Solvents For Flue Gas Cleaning*. Ph.D. thesis, University of KwaZulu-Natal.

[Tshibangu *et al.*, 2013] Tshibangu, M. M., Courtial, X., Coquelet, C., Naidoo, P., & Ramjugernath, D. 2013. Isothermal VaporâLiquid Equilibrium Data and Modeling for the Ethane (R170) + Perfluoropropane (R218) System at Temperatures from (264 to 308) K. *Journal of Chemical & Engineering Data*, **58**(5), 1316–1320.

[Vacek *et al.*, 2000] Vacek, V., Hallewell, G., Ilie, S., & Lindsay, S. 2000. Perfluorocarbons and their use in cooling systems for semiconductor particle detectors. *Fluid Phase Equilibria*, **174**(1), 191 – 201.

[Vacek *et al.*, 2001] Vacek, V., Hallewell, G., & Lindsay, S. 2001. Velocity of sound measurements in gaseous per-fluorocarbons and their mixtures. *Fluid Phase Equilibria*, **185**(1), 305 – 314. Proceedings of the 14th symposium on thermophysical properties.

[Valtz *et al.*, 2007] Valtz, A., Coquelet, Ch., & Richon, D. 2007. Vaporâliquid equilibrium data for the hexafluoroethane + carbon dioxide system at temperatures from 253 to 297 K and pressures up to 6.5 MPa. **258**(09), 179–185.

[Varanda *et al.*, 2008] Varanda, F. R., Vega, L. F., Coutinho, J. A.P., & Marrucho, I. M. 2008. Liquidâliquid equilibrium of substituted perfluoro-n-octane+n-octane systems. *Fluid Phase Equilibria*, **268**(1), 85 – 89.

[Wei *et al.*, 1995] Wei, M. S.-W., Brown, T. S., Kidnay, A. J., & Sloan, E. D. 1995. Vapor + Liquid Equilibria for the Ternary System Methane + Ethane + Carbon Dioxide at 230 K and Its Constituent Binaries at Temperatures from 207 to 270 K. *Journal of Chemical & Engineering Data*, **40**(4), 726–731.

[Yohei *et al.*, 2005] Yohei, K., Kenichi, F., & Yukihiro, H. 2005. VaporâLiquid Equilibrium (VLE) Properties for the Binary Systems Propane (1) + n-Butane (2) and Propane (1) + Isobutane (3). *Journal of Chemical & Engineering Data*, **50**(2), 579–582.

[Younglove & Ely, 1987] Younglove, B. A., & Ely, J. F. 1987. Thermophysical Properties of Fluids. II. Methane, Ethane, Propane, Isobutane, and Normal Butane. *Journal of Physical and Chemical Reference Data*, **16**(4), 577–798.

[Yucelen & Kidnay, 1999] Yucelen, B., & Kidnay, A. J. 1999. VaporâLiquid Equilibria in the Nitrogen + Carbon Dioxide + Propane System from 240 to 330 K at Pressures to 15 MPa. *Journal of Chemical & Engineering Data*, **44**(5), 926–931.

[Zhang *et al.*, 2017] Zhang, Xianping, Wang, Fang, Liu, Zhiming, Gu, Junjie, Zhu, Feiyu, & Yuan, Qiuyan. 2017. Performance Research on Heat Pump Using Blends of R744 with Eco-friendly Working Fluid. *Procedia Engineering*, **205**, 2297 – 2302. 10th International Symposium on Heating, Ventilation and Air Conditioning, ISHVAC2017, 19-22 October 2017, Jinan, China.

[Zhang *et al.*, 2006] Zhang, Y., Gong, M.-Q., Zhu, H.-B., & Wu, J.-F. 2006. Vaporâliquid equilibrium measurements and correlations for an azeotropic system of ethane+hexafluoroethane. *Fluid Phase Equilibria*, **240**(1), 73 – 78.

8 Summary and conclusions

8.1 Development of high accuracy speed-of-sound measurement apparatus

The experimental part of this thesis presents the time-of-flight based instrument for speed of sound measurement I have developed. The instrument was adopted for mixtures so that two gases can be mixed directly inside the measurement chamber. A custom electronics I have designed and continuously improved is used for the speed of sound measurement. I have implemented a new triggering technique which eliminates errors in the transit time measurements to achieve the best accuracy. The comparison of the speed of sound I have measured in pure R-116 and R-218 with the most accurate data from literature, which were measured with extremely precise but expensive and difficult to build spherical resonators, indicated mutual deviation smaller than 0.4%. Although only the extremely accurate data from spherical resonators can be used to safely derive other thermodynamic properties such as the heat capacities, the deviation of 0.4% is smaller than deviations between experimental data and the speed of sound calculated by commonly used equations of state for refrigerants.

8.2 Evaluations of models

I have compiled numerous experimental data from literature in order to evaluate the selected thermodynamic models for accuracy in terms of prediction of saturation properties and speed of sound in both phases. The evaluation focused on fluorocarbons and their mixtures with unlike fluids including carbon dioxide (R-744) that will be used in most of the new cooling applications at CERN. The evaluation of thermodynamic models for speed of sound prediction demonstrated that the simple cubic equations such as the Peng-Robinson equation of state can be used for the vapour-phase speed of sound prediction, for prediction of the saturated pressure and phase compositions. A well-known fact that the cubic equations fail to predict the correct liquid density and consequently the liquid speed of sound was confirmed. The volume translated Peng-Robinson equation of state somewhat improves the accuracy for saturated liquid density prediction but otherwise is very unreliable with large deviations in speed of sound prediction in both liquid and vapour regions. The well-known sPC-SAFT proved to be a universal model with good accuracy in all the evaluated disciplines. The Soft-SAFT model exhibited large deviation in the vapour density and cannot be recommended for fluorocarbons. The little-known SAFT-BACK model was by far the best model with a small deviation below 2% even in the liquid region and close to the critical point where other models failed. The only discipline where the model gave slightly worse results was the saturated vapour phase composition of mixtures. This is because the predicted vapour phase composition of R-744+C_6F_{14} and C_6F_{14}+R-116 mixtures deviate from the experimental data (see figures in annexes). These deviations are most likely caused by the mixing and combination rules. Unfortunately, there is no proposal for different mixing rules for this model. The next step in the development of the very accurate universal model for speed of sound prediction in mixtures can be thus development of better mixing rules for the SAFT-BACK model.

I have used the vapour-equilibrium data of mixtures containing saturated fluorocarbons, hydrocarbons, nitrogen and carbon dioxide to obtain the binary interaction coefficients of the evaluated models. The

obtained coefficients of the SAFT-BACK model are especially valuable since they have not been reported in the available literature. Further, I have developed correlations for estimation of the binary interaction coefficients for the SAFT-BACK model since there is no publications dealing with prediction of those coefficients. The correlation was shown to provide significant improvement for the speed of sound prediction for the R-218+R-728 mixture which was measured in the experimental part of the thesis. The correlation also correctly predicts the interaction coefficient very close to unity for R-116+R-218 mixture since it is a mixture of very similar fluids.

As a result, this work provides unique model parameters of 13 refrigerants for the very accurate but little-known SAFT BACK model and binary interaction coefficients of 24 mixtures and 3 correlations that can be used to predict the interaction coefficients for mixtures of saturated fluorocarbons, hydrocarbons, nitrogen and carbon dioxide. Neither the fluid parameters for the saturated fluorocarbons nor any of the binary interaction coefficients have been published in the available literature so far.

8.3 Applications

The developed instrument was used to obtain the speed of sound in R-116+R-218 and R-218+R-728 mixtures over wide range of temperatures and pressures, the obtained data were published in Journal of Chemical Engineering Data ([Doubek & Vacek, 2016b]) and in proceedings of the Proceedings of 13th International Conference on Properties and Phase Equilibria for Products and Process Design ([Doubek & Vacek, 2016a]) and 24th IIR International Congress of Refrigeration ([Doubek & Vacek, 2015]). These mixtures are interesting for the cooling systems currently used at CERN for particle detectors ([Battistin *et al.*, 2015]). The R-116+R-218 blend might be used as a replacement for pure R-218 in the refrigeration systems in order to decrease evaporation temperatures to protect the particle detectors from thermal runaways as they accumulate more and more radiation damage, [Bates *et al.*, 2015] and . The R-218+R-728 mixture is interesting for leak detection and modelling of performance of contaminated refrigerants. The nitrogen (R-728) can represent air mixing with a refrigerant during operation of the cooling plant. In all cases, accurate speed-of-sound measurements and prediction models provide valuable tool for online composition monitoring of refrigerant blends and real-time leak and contamination detection. I have participated in several projects that benefited from the speed-of-sound based analysis of refrigerants as is demonstrated in number of publications: The measurement of R-116+R-218 heat transfer ([Doubek *et al.*, 2017b] and [Doubek *et al.*, 2017a]) benefited from concentration monitoring based on speed of sound which was used to adjust the blend composition in order to evaluate impact of the increasing R-116 level. The Thermosiphon cooling system at CERN is currently using speed-of-sound based analyser I helped to develop to detect refrigerant contamination by air ([Alhroob *et al.*, 2017a], [Alhroob *et al.*, 2015] and [Alhroob *et al.*, 2017b]), the developed simulations models can be used to further increase the detection accuracy.

The measurement apparatus and the simulation models presented in this work can also be used for commercial refrigerants, especially for modern ecological blends or for monitoring and leak detection systems in industrial refrigeration plants. I have described several such applications as a co-author of the contribution presented on the IEEE SENSORS 2016 conference ([Doubek *et al.*, 2016]).

Bibliography

chapter 8: Summary and conclusions

[Alhroob *et al.*, 2015] Alhroob, M., Battistin, M., Berry, S., Doubek, M., *et al.* 2015. Development of a custom on-line ultrasonic vapour analyzer and flow meter for the ATLAS inner detector, with application to Cherenkov and gaseous charged particle detectors. *Journal of Instrumentation*, **10**(03), C03045.

[Alhroob *et al.*, 2017a] Alhroob, M., Battistin, M., Berry, S., Doubek, M., *et al.* 2017a. Custom real-time ultrasonic instrumentation for simultaneous mixture and flow analysis of binary gases in the CERN ATLAS experiment. *Nuclear Instruments and Methods in Physics Research Section A: Accelerators, Spectrometers, Detectors and Associated Equipment*, **845**, 273 – 277. Proceedings of the Vienna Conference on Instrumentation 2016.

[Alhroob *et al.*, 2017b] Alhroob, M., Battistin, M., Berry, S., Doubek, M., *et al.* 2017b. Custom ultrasonic instrumentation for flow measurement and real-time binary gas analysis in the CERN ATLAS experiment. *Journal of Instrumentation*, **12**(01), C01091.

[Bates *et al.*, 2015] Bates, R., Battistin, M., Berry, S., Doubek, M., *et al.* 2015. The cooling capabilities of C2F6/C3F8 saturated fluorocarbon blends for the ATLAS silicon tracker. *Journal of Instrumentation*, **10**(03), P03027.

[Battistin *et al.*, 2015] Battistin, M., Berry, S., Bitadze, A., Doubek, M., *et al.* 2015. The Thermosiphon Cooling System of the ATLAS Experiment at the CERN Large Hadron Collider. *International Journal of Chemical Reactor Engineering*, **13**(4), 511–521.

[Doubek & Vacek, 2015] Doubek, M., & Vacek, V. 2015 (August). Thermodynamic properties of fluorocarbons: simulations and experiment. *In: Proceedings of the 24th IIR International Congress of Refrigeration*. IIF, Yokohama, Japan.

[Doubek & Vacek, 2016a] Doubek, M., & Vacek, V. 2016a (05). Experimental study of refrigerants and their mixtures. *In: Proceedings of 13th International Conference on Properties and Phase Equilibria for Products and Process Design*.

[Doubek & Vacek, 2016b] Doubek, M., & Vacek, V. 2016b. Speed of Sound Data in Pure Refrigerants R-116 and R-218 and Their Mixtures: Experiment and Modeling. *Journal of Chemical & Engineering Data*, **61**(12), 4046–4056.

[Doubek *et al.*, 2016] Doubek, M., Vacek, V., Hallewell, G., & Pearson, B. 2016 (Oct). Speed-of-sound based sensors for environmental monitoring. *Pages 1–3 of: 2016 IEEE SENSORS*.

[Doubek *et al.*, 2017a] Doubek, M., Haubner, M., Houska, D., Vacek, V., Battistin, M., Hallewell, G., Katunin, S., & Robinson, D. 2017a (July). Experimental investigation and modelling of flow boiling heat transfer of C3F8/C2F6 blends. *In: proceedings of the 13th International Conference on Heat Transfer*.

[Doubek *et al.*, 2017b] Doubek, M., Haubner, M., Vacek, V., Battistin, M., Hallewell, G., Katunin, S., & Robinson, D. 2017b. Measurement of heat transfer coefficient in two phase flows of radiation-resistant zeotropic C2F6/C3F8 blends. *International Journal of Heat and Mass Transfer*, **113**, 246 – 256.

9 Annexes

The annexes include detailed plots comparing the evaluated models to experimental data. The differences visible in the plots indicate accurcies of the models which were summarized in form of absolute average deviations in the tables in chapter 7.

9.1 Vapour liquid equilibrium plots

The vapour liquid evaluations consisted of saturated pressure, liquid density and vapour density comparisons. It is particularly interesting to see how the deviations between the models and the experimental data increases in proximity of the critical point ($T_r = 1$).

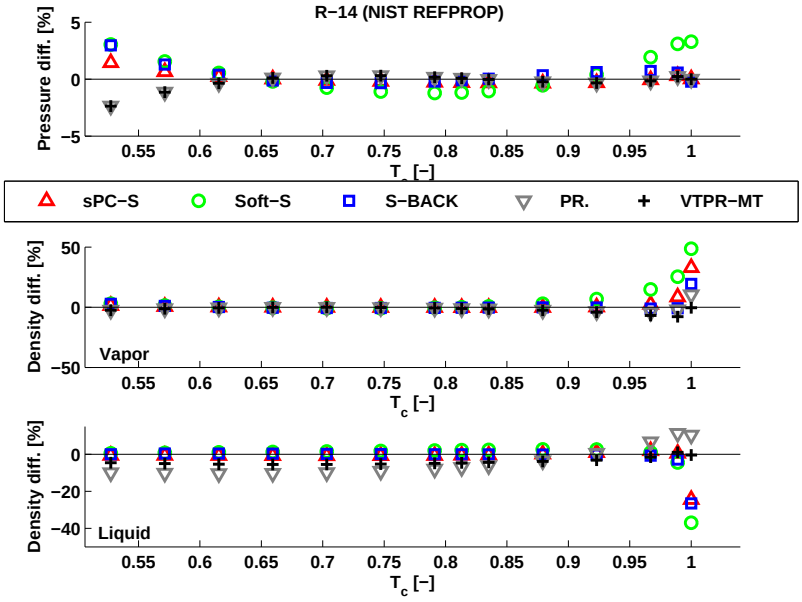

Figure 9.1: R-14 vapour-liquid equilibrium evaluation

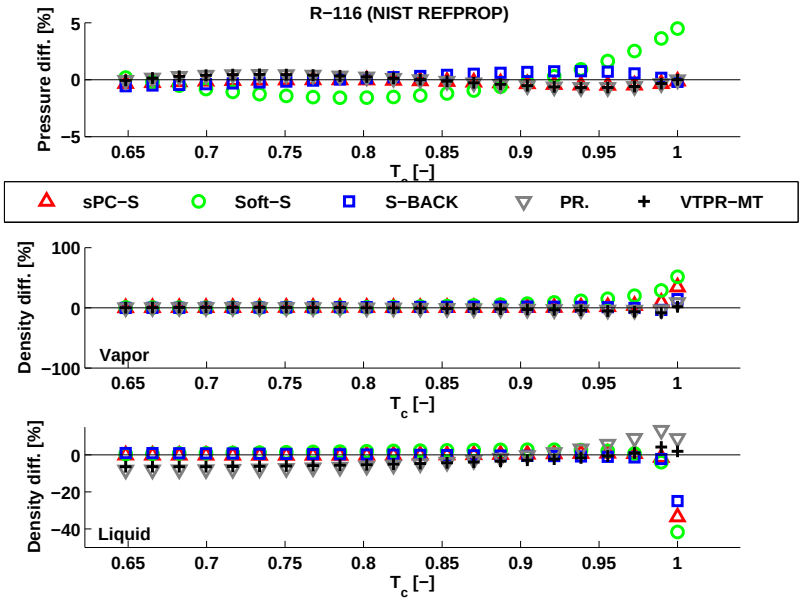

Figure 9.2: R-116 vapour-liquid equilibrium evaluation

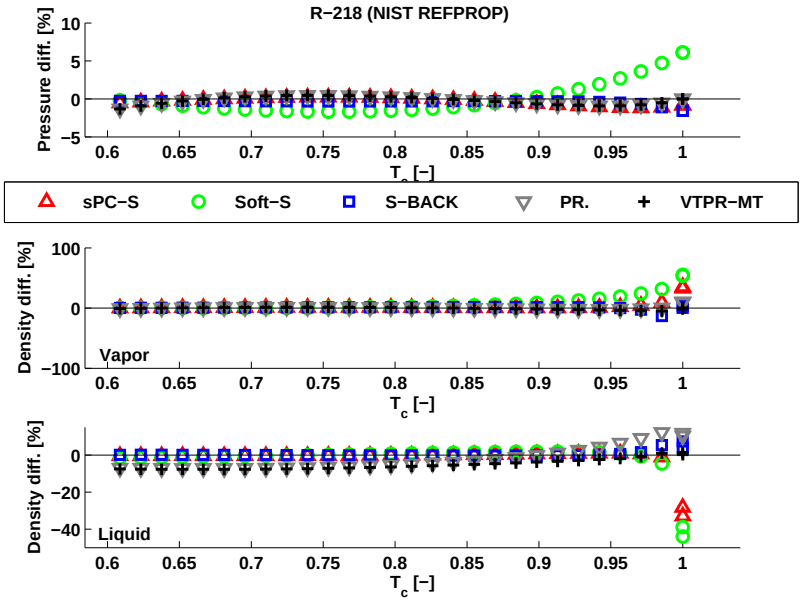

Figure 9.3: R-218 vapour-liquid equilibrium evaluation

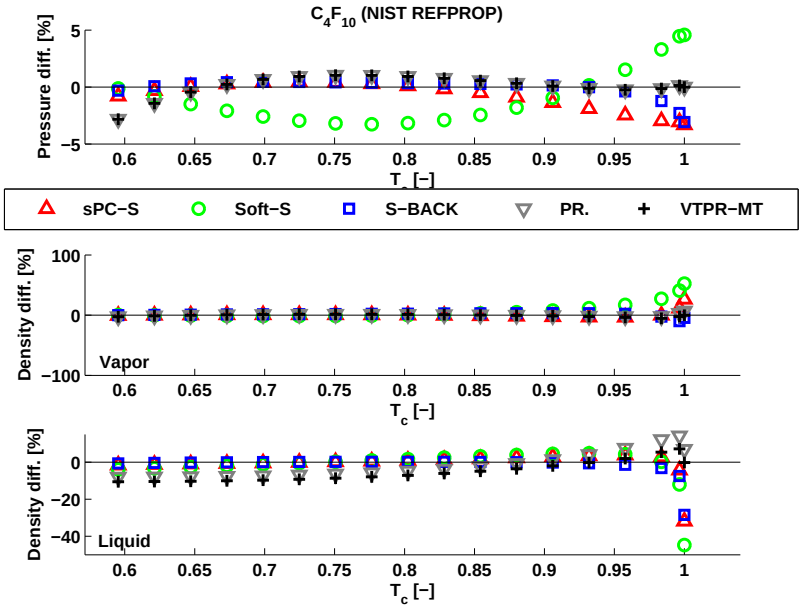

Figure 9.4: C_4F_{10} vapour-liquid equilibrium evaluation

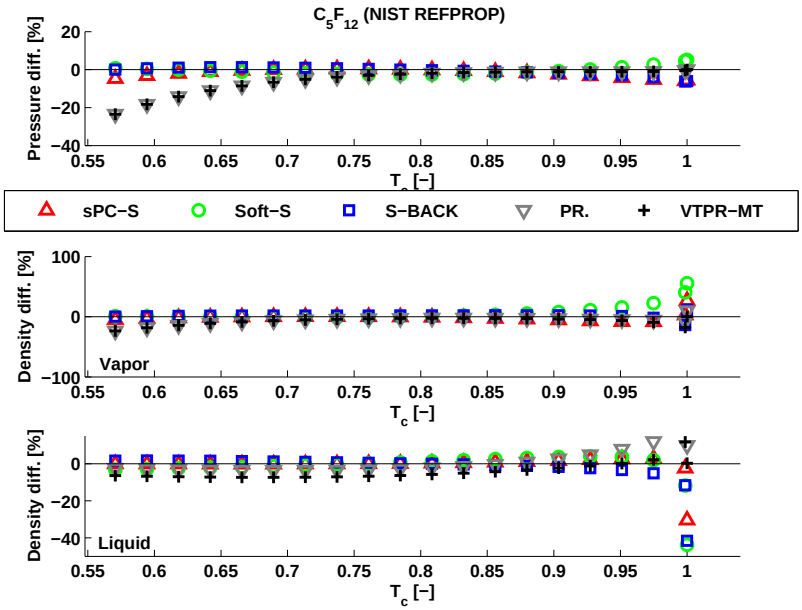

Figure 9.5: C_5F_{12} vapour-liquid equilibrium evaluation

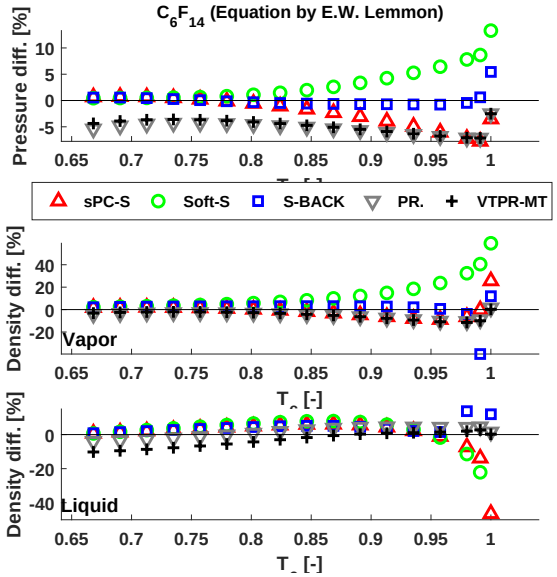

Figure 9.6: C_6F_{14} vapour-liquid equilibrium evaluation

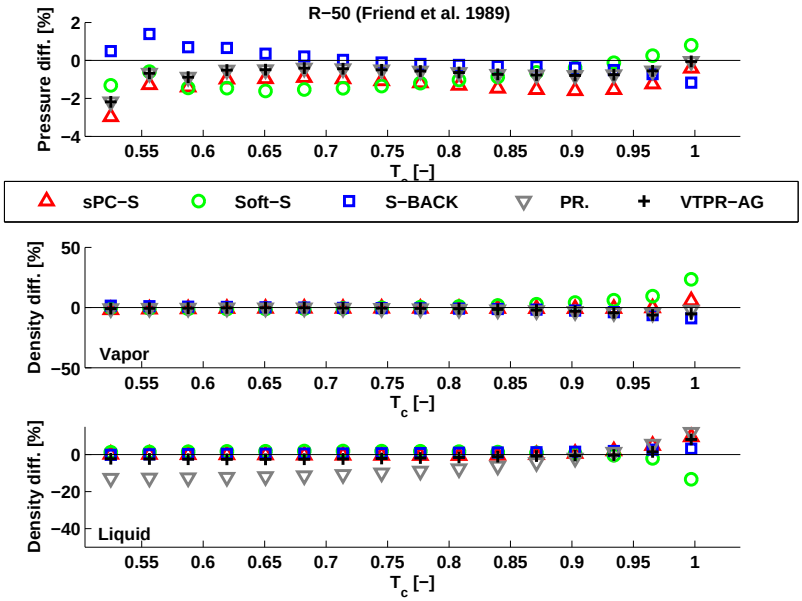

Figure 9.7: R-50 vapour-liquid equilibrium evaluation

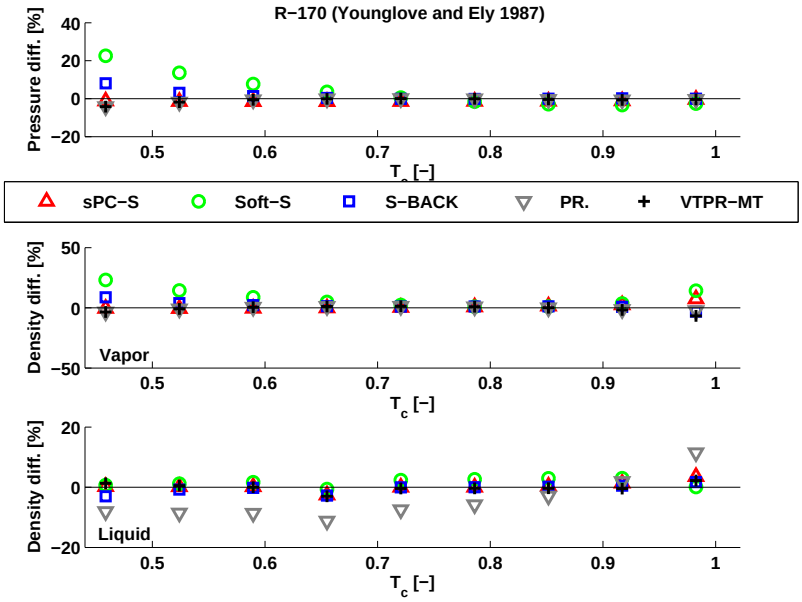

Figure 9.8: R-170 vapour-liquid equilibrium evaluation

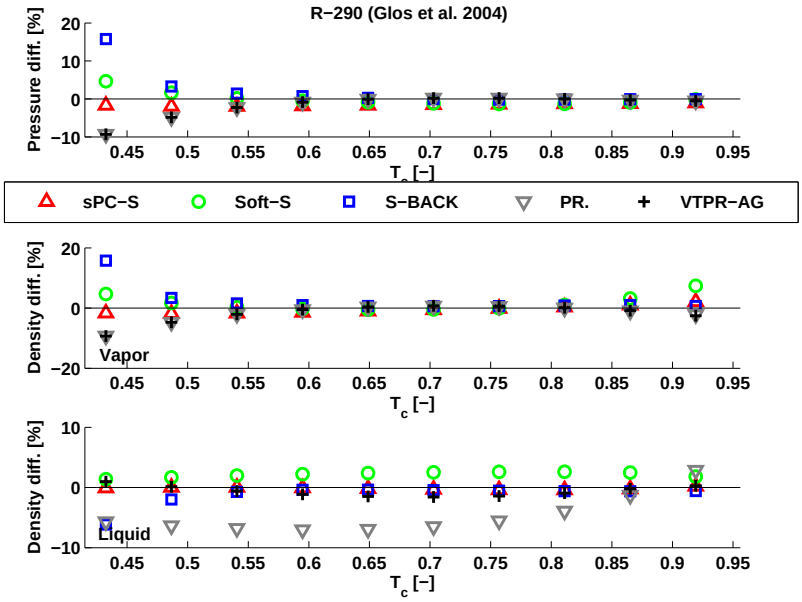

Figure 9.9: R-290 vapour-liquid equilibrium evaluation

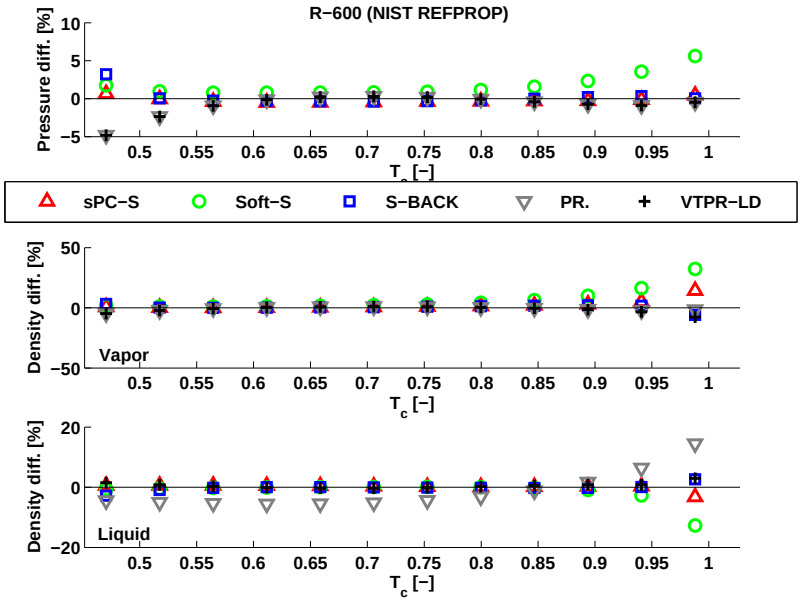

Figure 9.10: R-600 vapour-liquid equilibrium evaluation

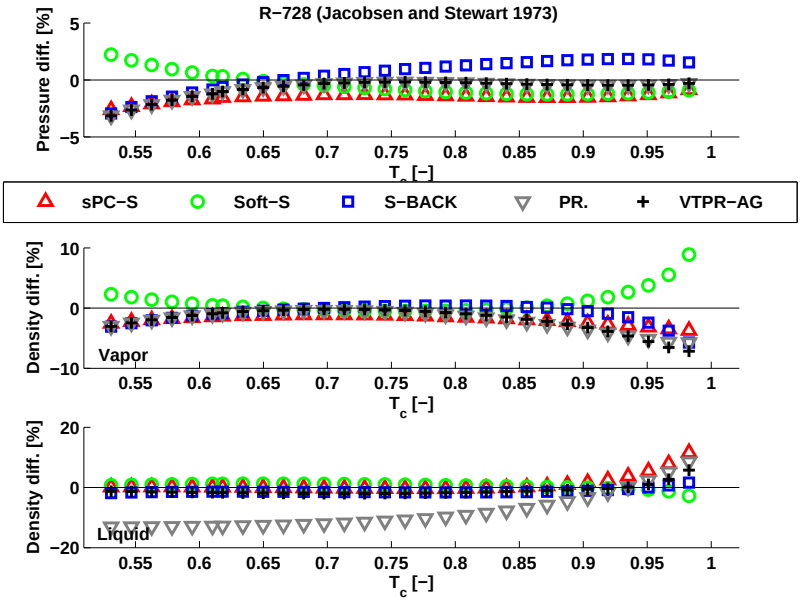

Figure 9.11: R-728 vapour-liquid equilibrium evaluation

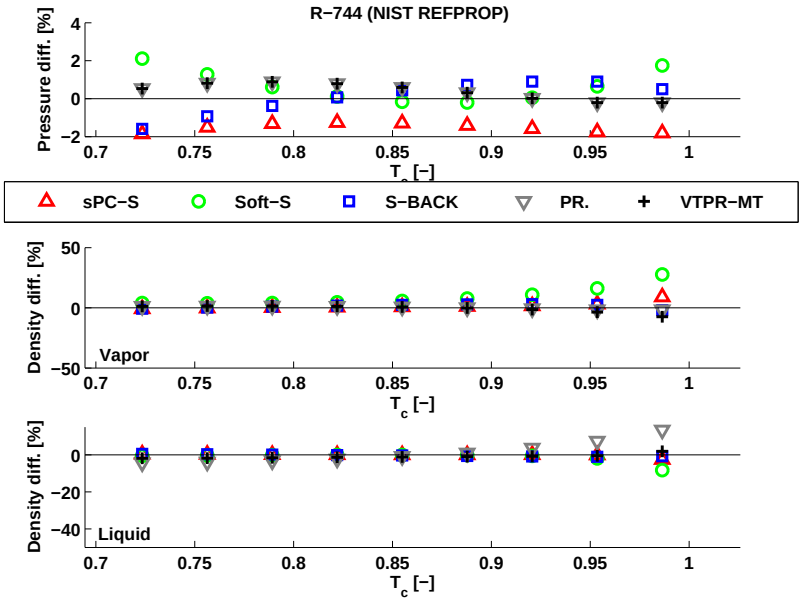

Figure 9.12: R-744 vapour-liquid equilibrium evaluation

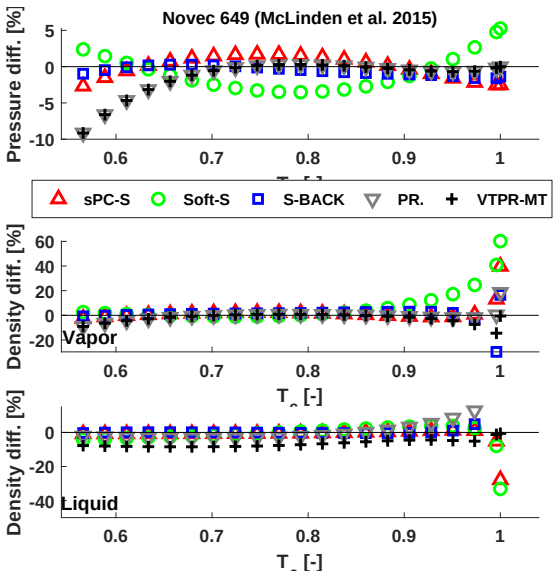

Figure 9.13: Novec 649 vapour-liquid equilibrium evaluation

9.2 Speed of sound plots

The evaluation plots show the data points in temperature-pressure state space. The saturation curve with critical point is shown in the plots in order to indicate the position of the data points with respect to the saturation curve. The liquid speed of sound (data points above the saturation curve) and vapour speed of sound were evaluated separately. The vapour speed speed of sound data can be further divided into data below and above critical pressure and temperatures. The deviations of the models from the experimental

speed of sound are plotted as function of reduced density. The combination of the pressure-temperature plot and the density-deviation plot provides comprehensive overview of the input data used for the evaluation.

9.2.1 vapour phase

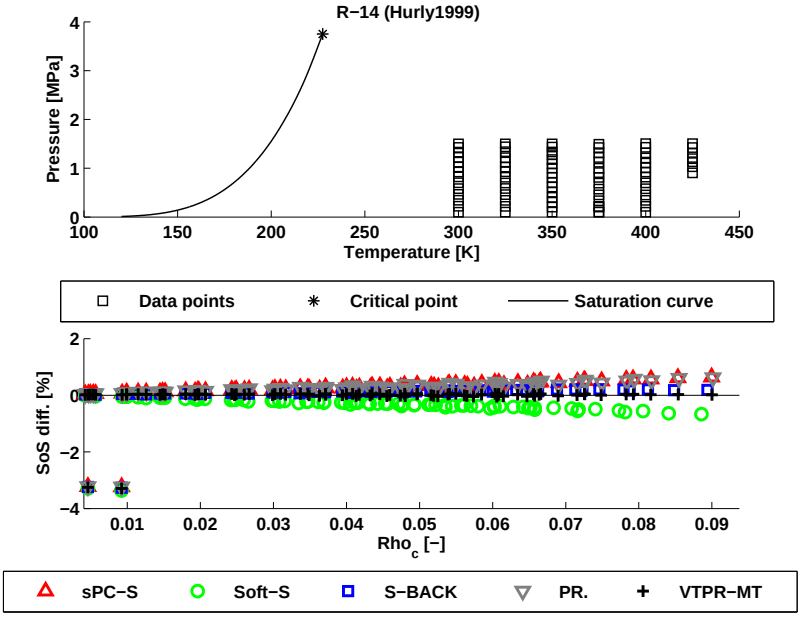

Figure 9.14: Speed of sound evaluation No1: R-14

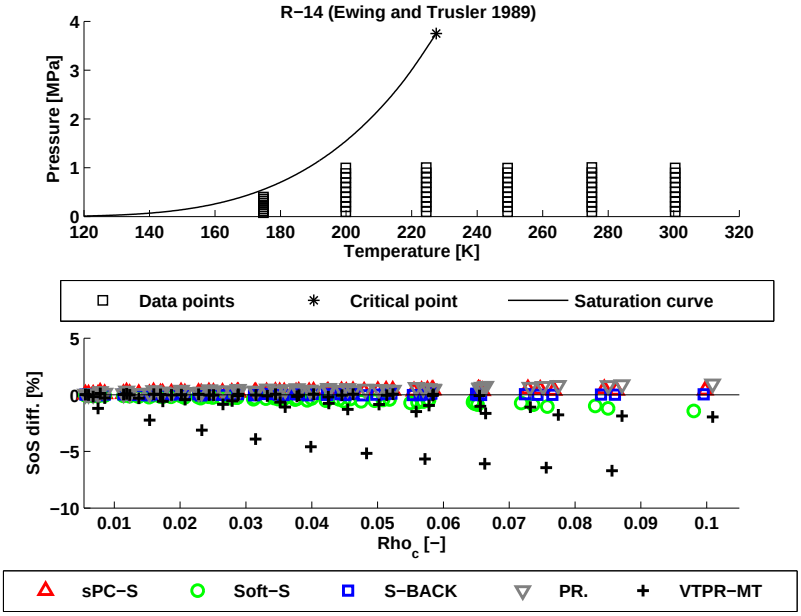

Figure 9.15: Speed of sound evaluation No2: R-14

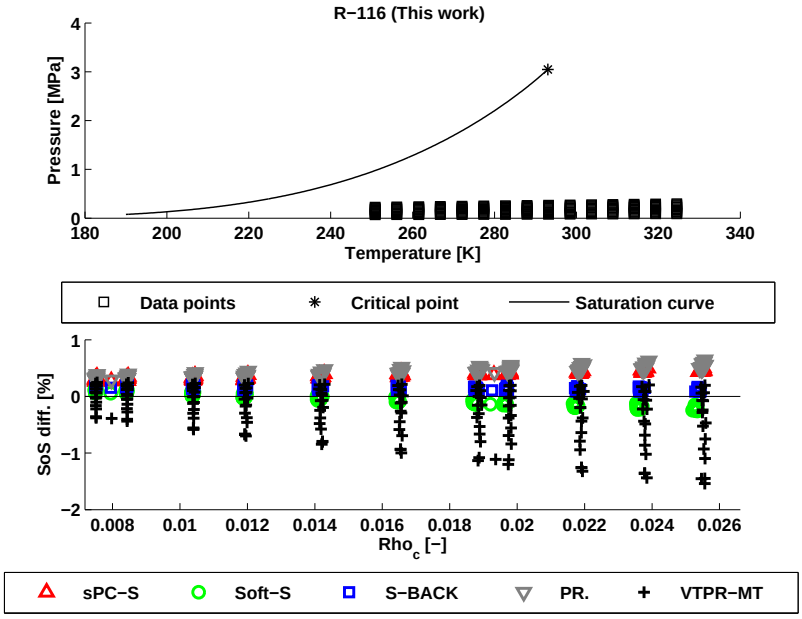

Figure 9.16: Speed of sound evaluation No3: R-116

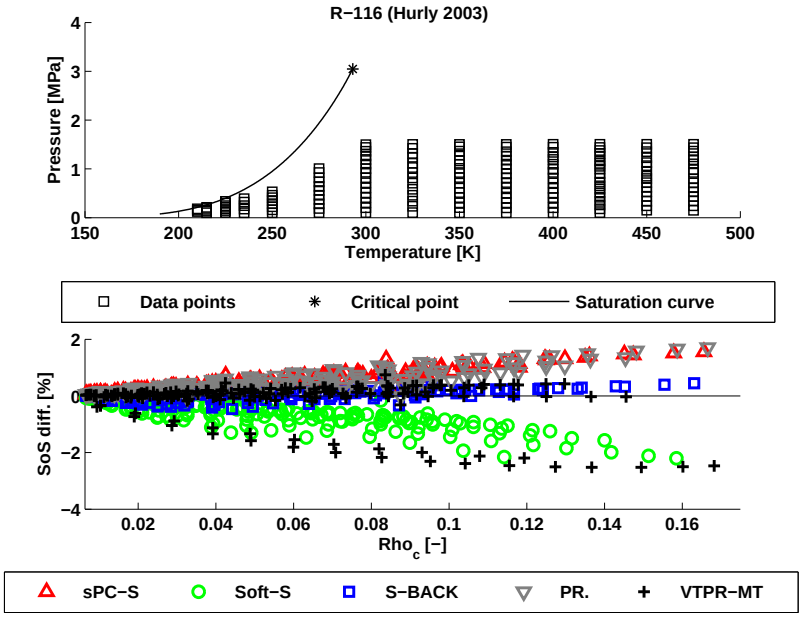

Figure 9.17: Speed of sound evaluation No4: R-116

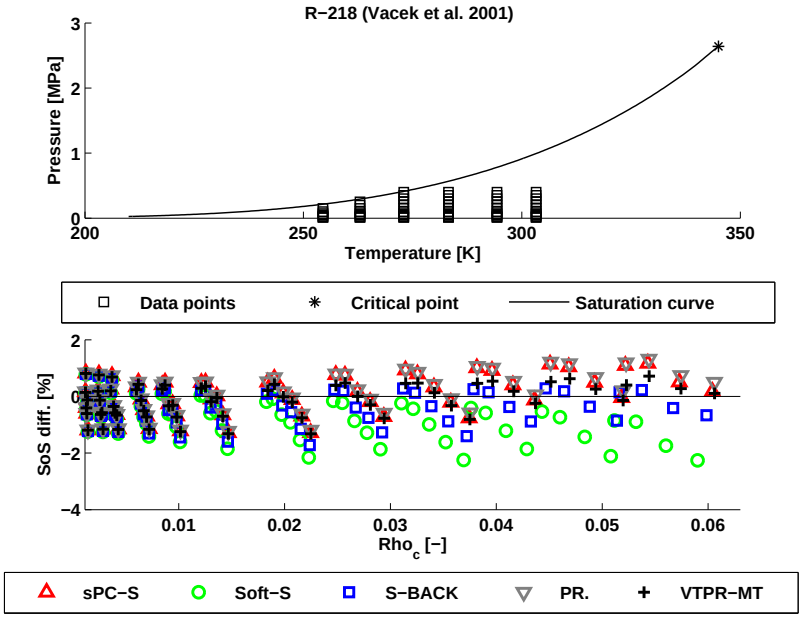

Figure 9.18: Speed of sound evaluation No5: R-218

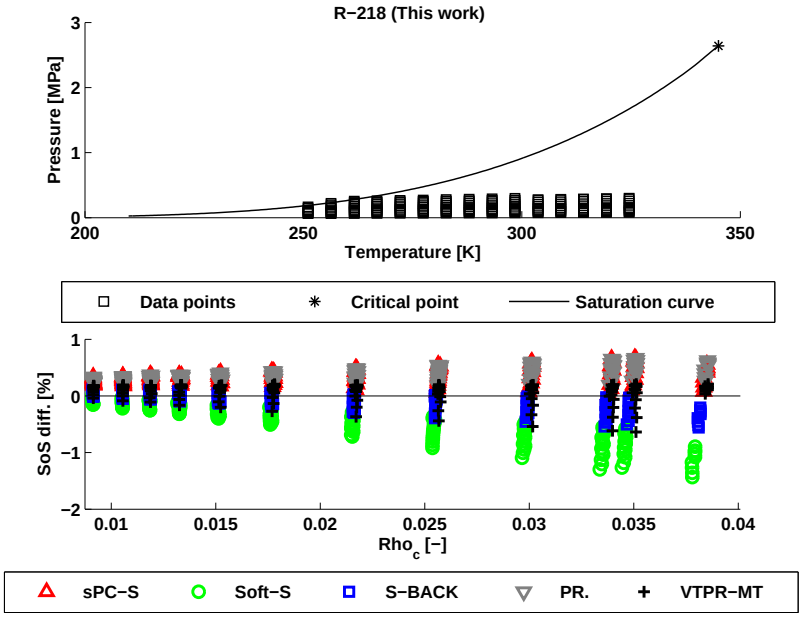

Figure 9.19: Speed of sound evaluation No6: R-218

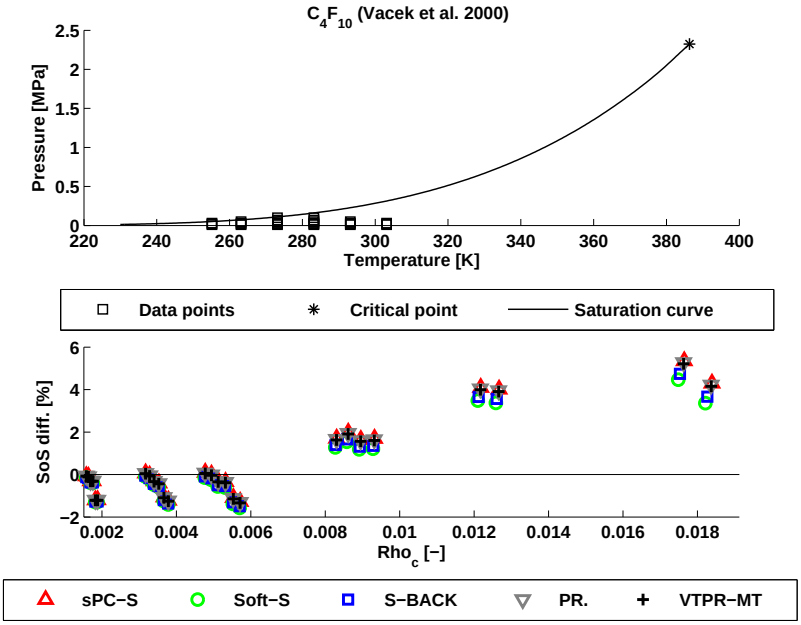

Figure 9.20: Speed of sound evaluation No7: C_4F_{10}

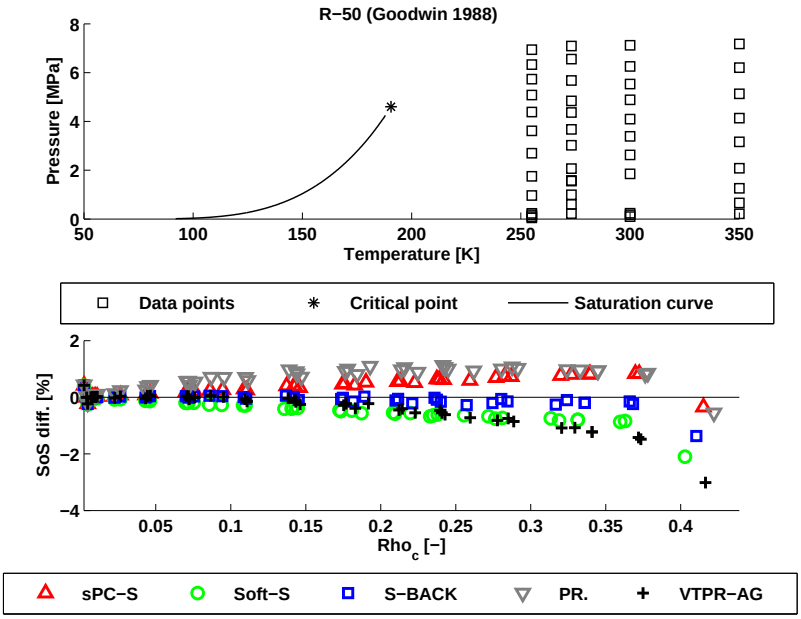

Figure 9.21: Speed of sound evaluation No8: R-50

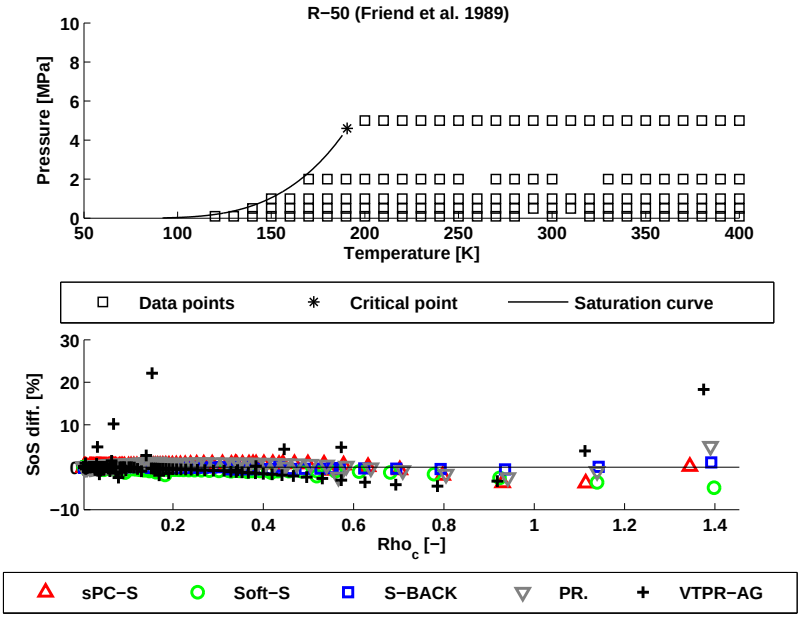

Figure 9.22: Speed of sound evaluation No9: R-50

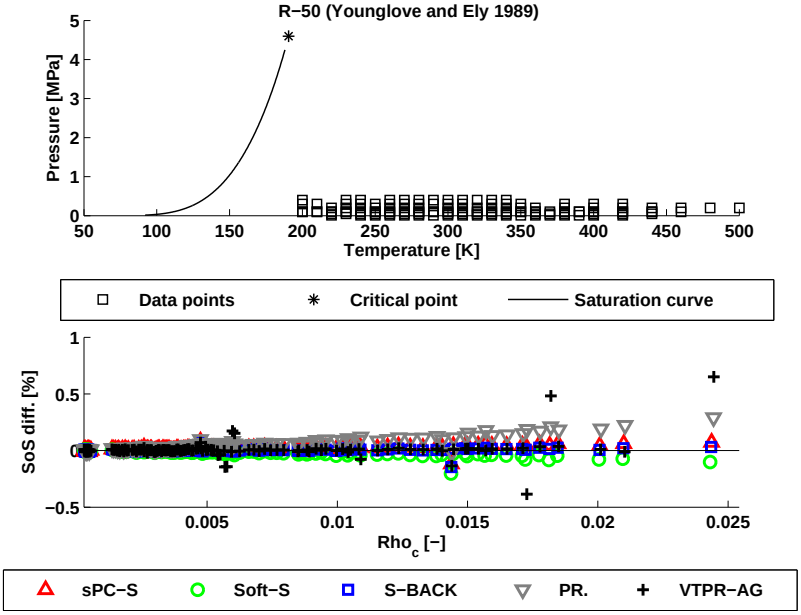

Figure 9.23: Speed of sound evaluation No10: R-50

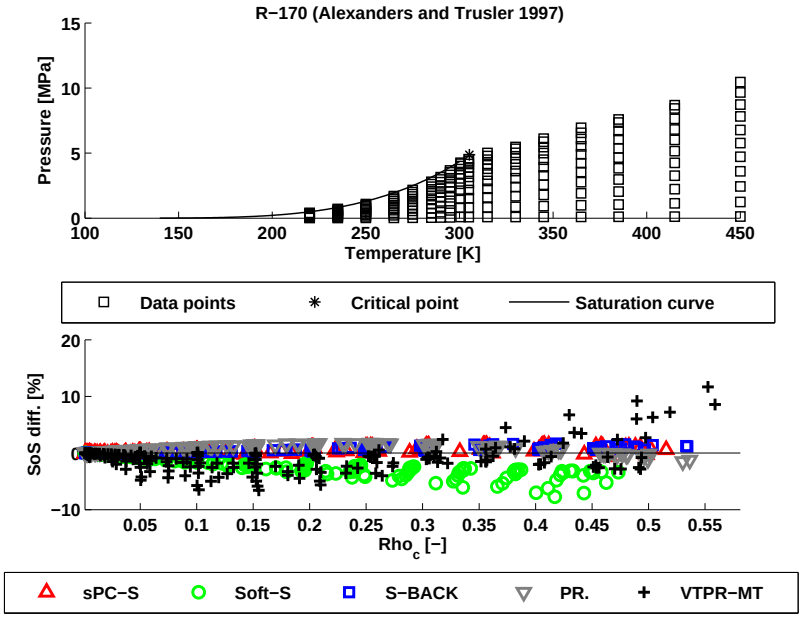

Figure 9.24: Speed of sound evaluation No11: R-170

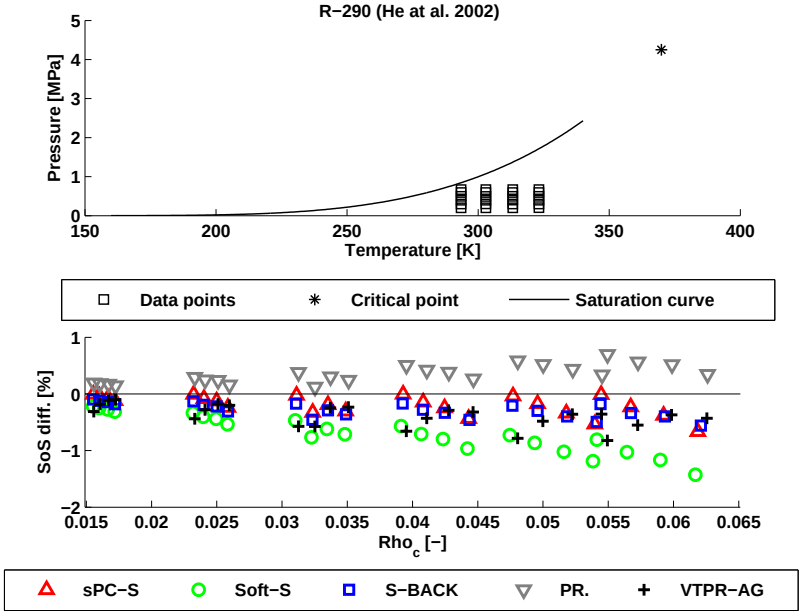

Figure 9.25: Speed of sound evaluation No12: R-290

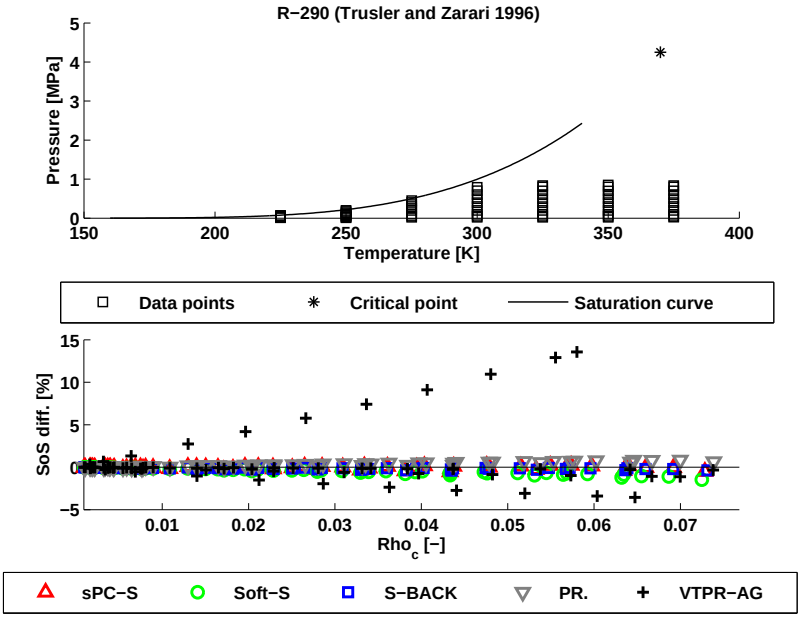

Figure 9.26: Speed of sound evaluation No13: R-290

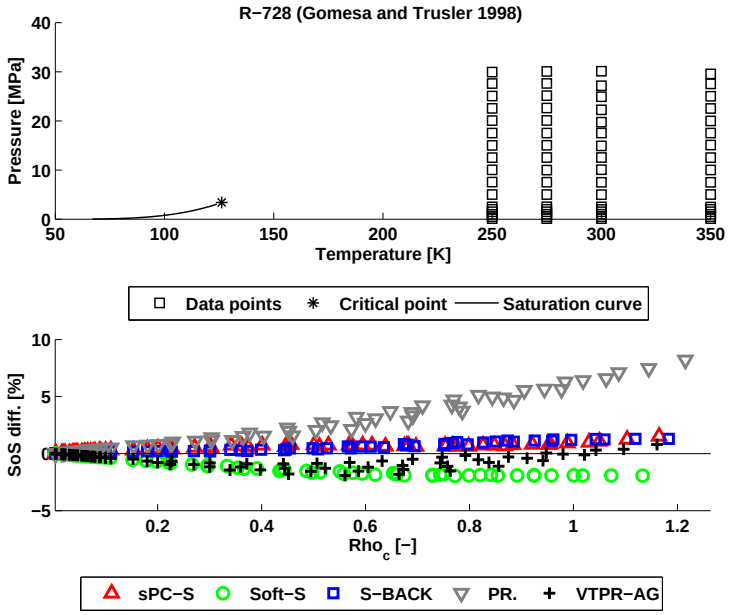

Figure 9.27: Speed of sound evaluation No14: R-728

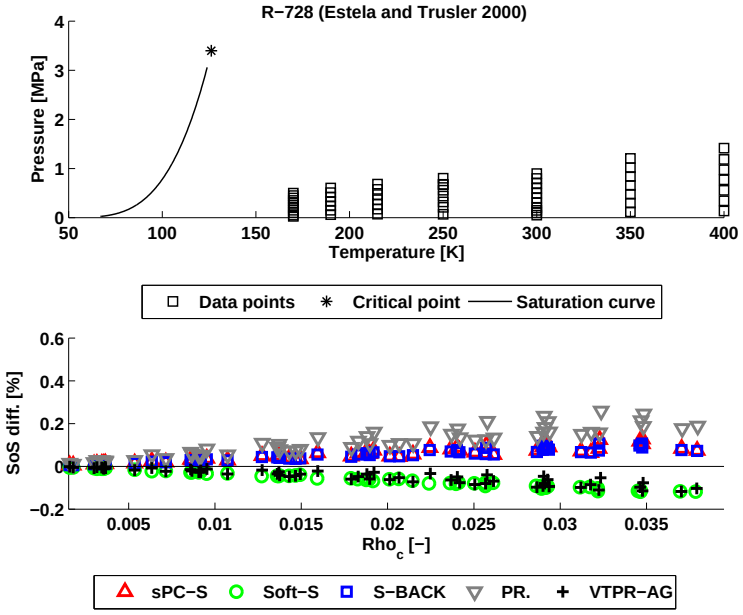

Figure 9.28: Speed of sound evaluation No15: R-728

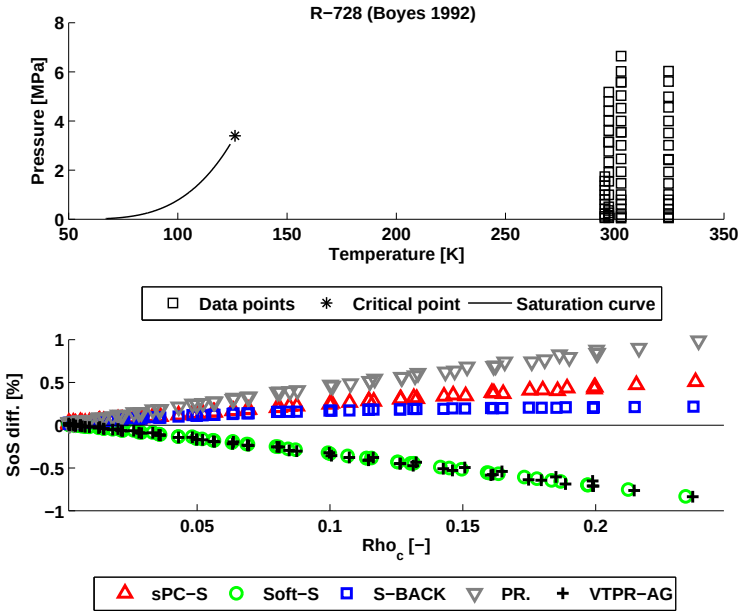

Figure 9.29: Speed of sound evaluation No16: R-728

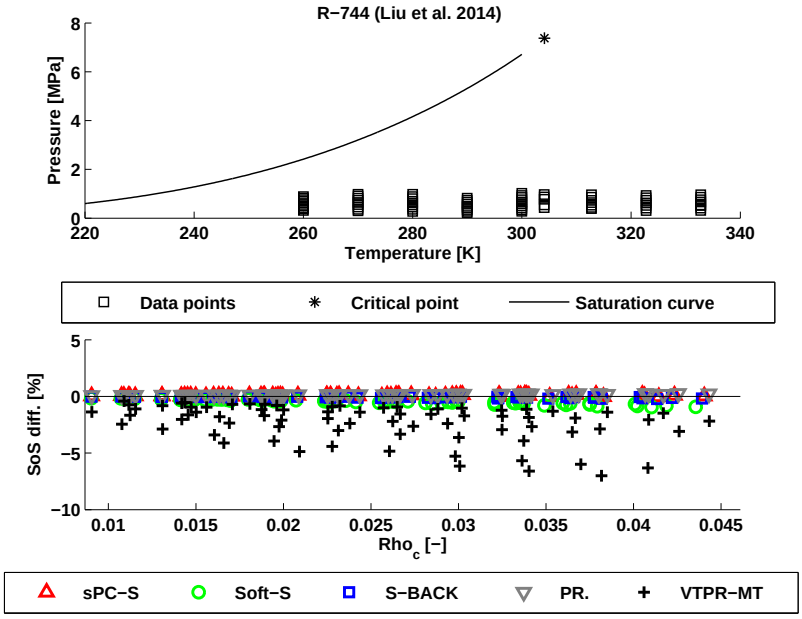

Figure 9.30: Speed of sound evaluation No17: R-744

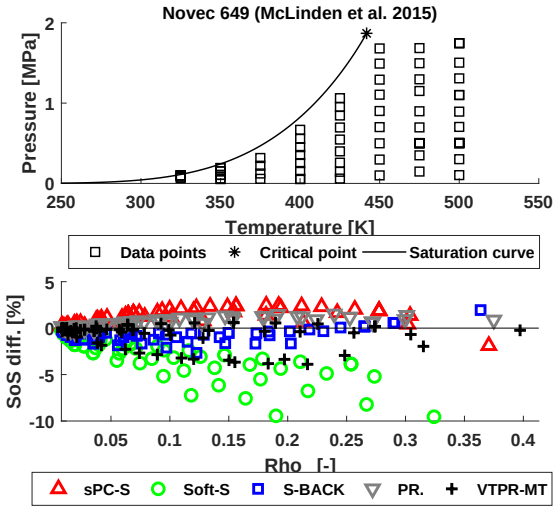

Figure 9.31: Speed of sound evaluation No18: Novec 649

9.2.2 Liquid phase

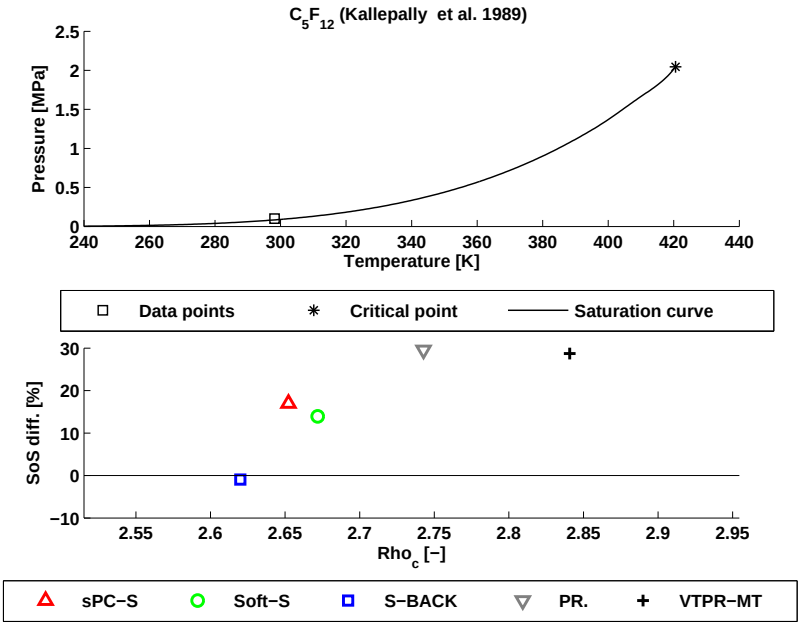

Figure 9.32: Speed of sound evaluation No19: C_5F_{12}

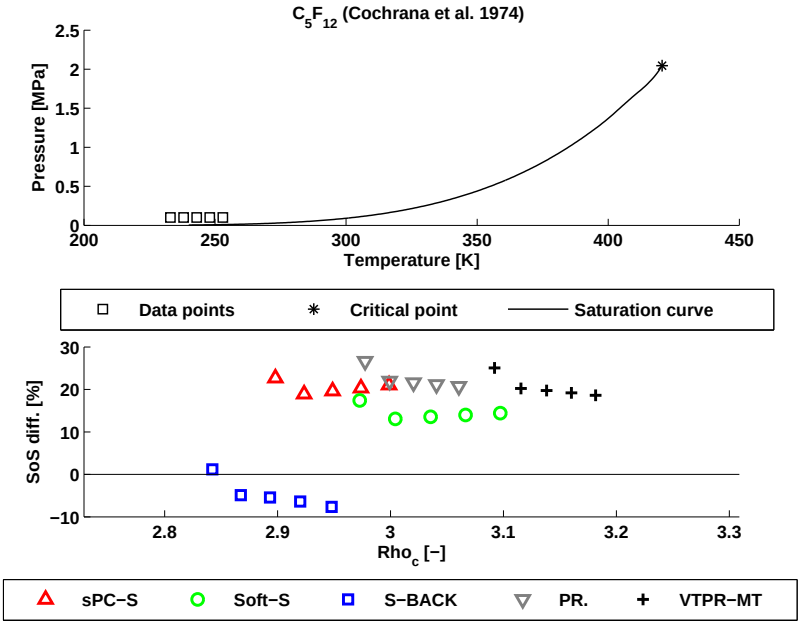

Figure 9.33: Speed of sound evaluation No20: C_5F_{12}

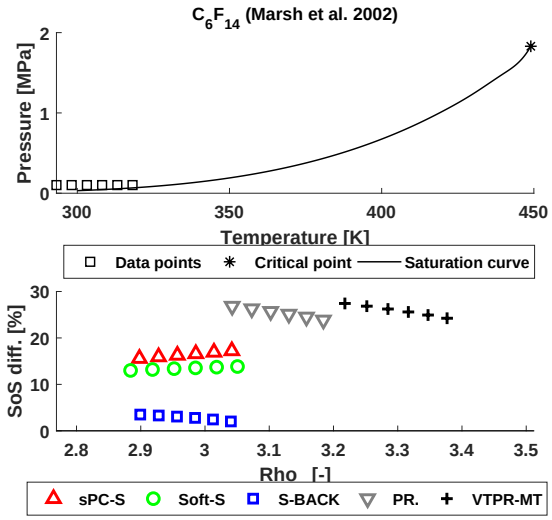

Figure 9.34: Speed of sound evaluation No21: C_6F_{14}

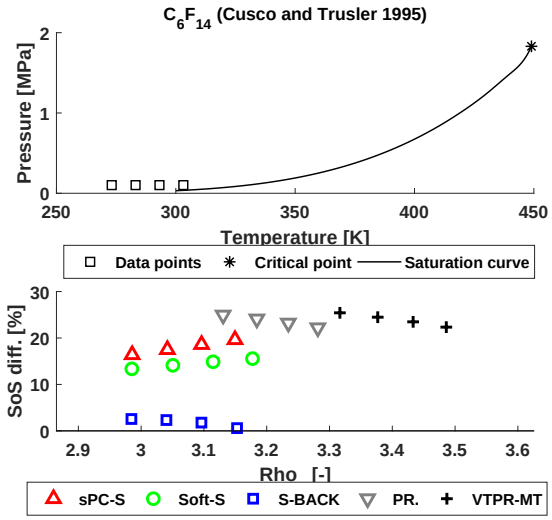

Figure 9.35: Speed of sound evaluation No22: C_6F_{14}

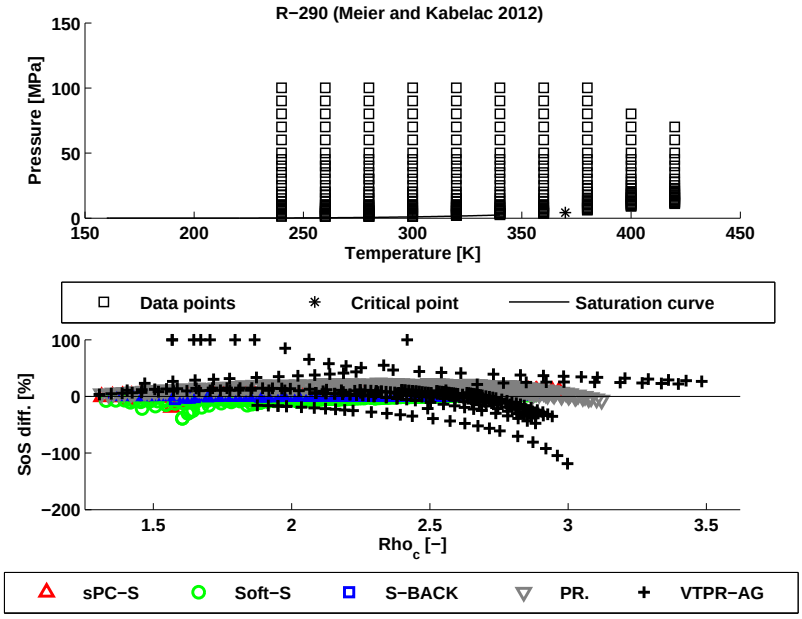

Figure 9.36: Speed of sound evaluation No23: R-290

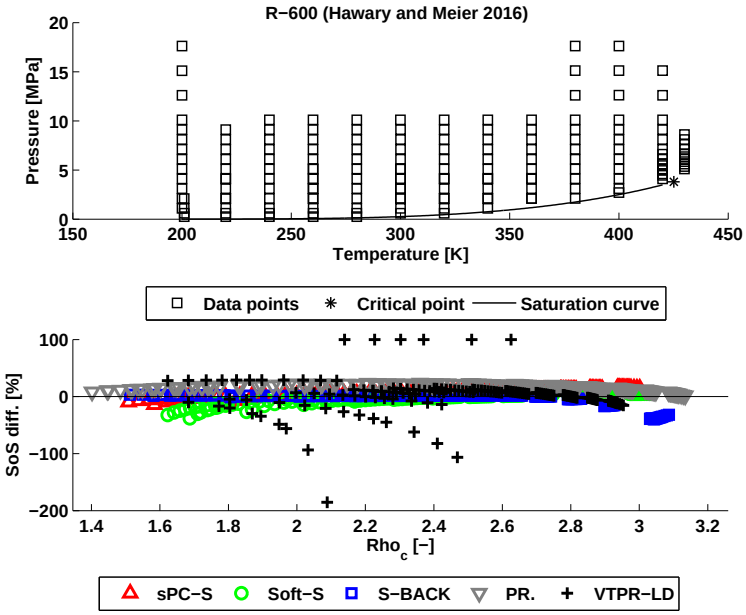

Figure 9.37: Speed of sound evaluation No24: R-600

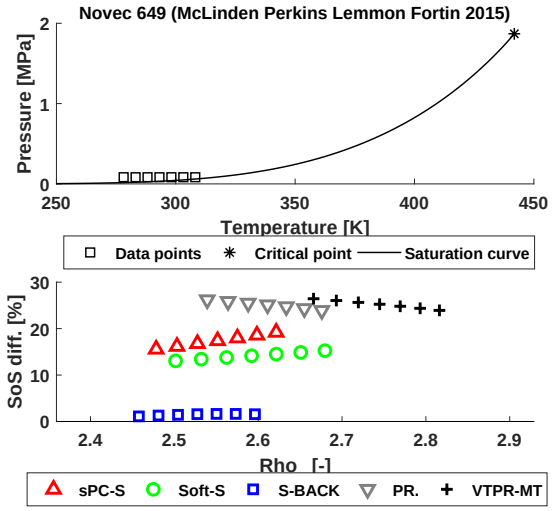

Figure 9.38: Speed of sound evaluation No25: Novec 649

9.3 Mixtures

The accuracy of the modes in predicting the phase composition is show in common two-phase diagrams. Note that the temperature and pressure were used as inputs to predict the vapour and liquid phase composition.

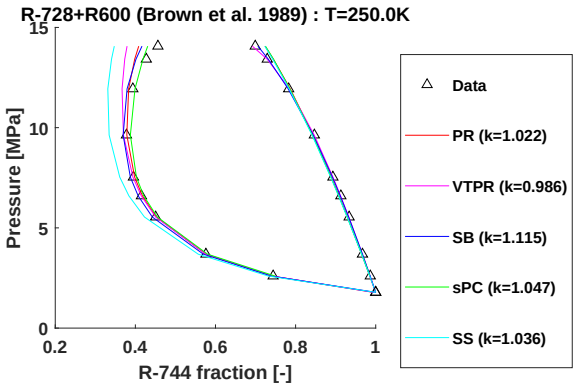

Figure 9.39: Mixtures evaluation No1

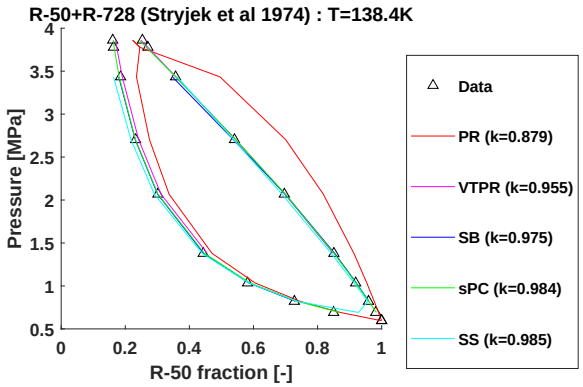

Figure 9.40: Mixtures evaluation No2

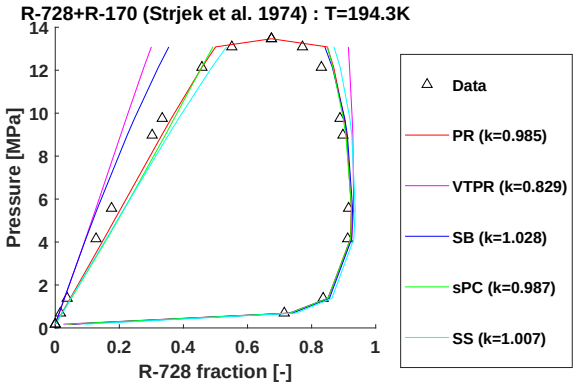

Figure 9.41: Mixtures evaluation No3

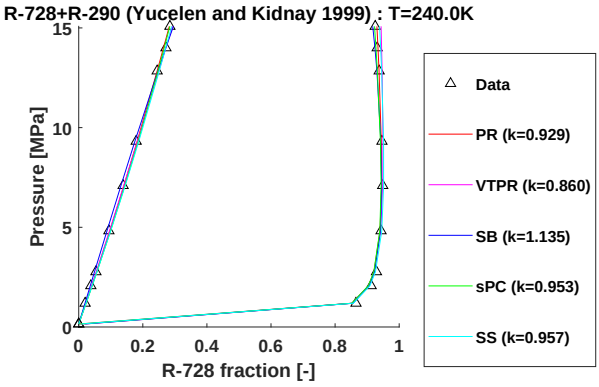

Figure 9.42: Mixtures evaluation No4

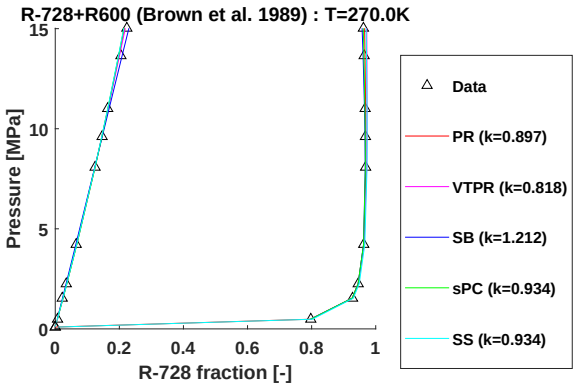

Figure 9.43: Mixtures evaluation No5

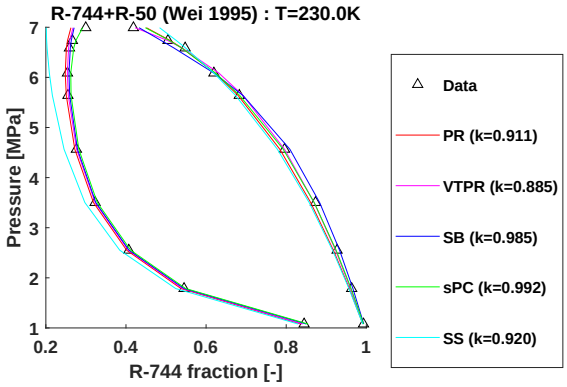

Figure 9.44: Mixtures evaluation No6

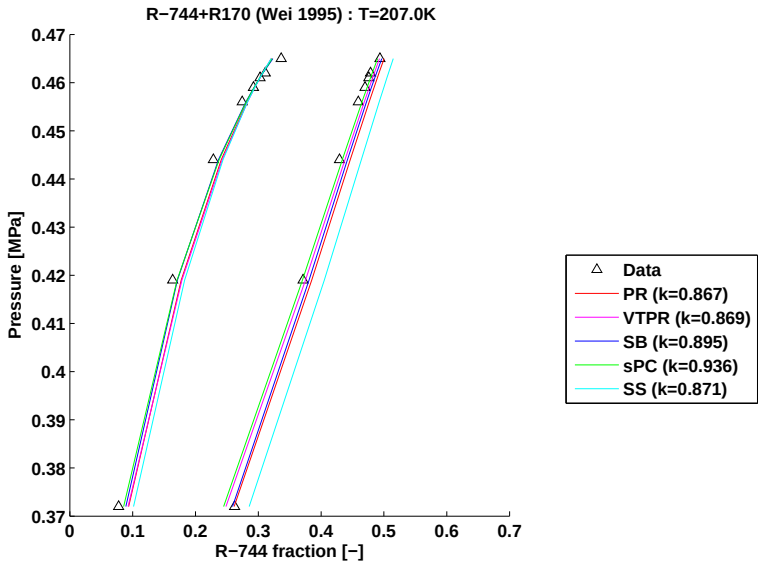

Figure 9.45: Mixtures evaluation No7

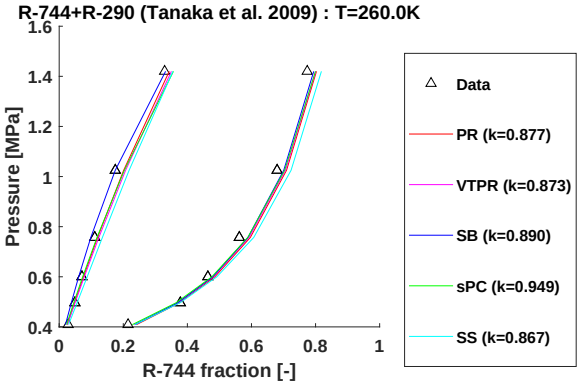

Figure 9.46: Mixtures evaluation No8

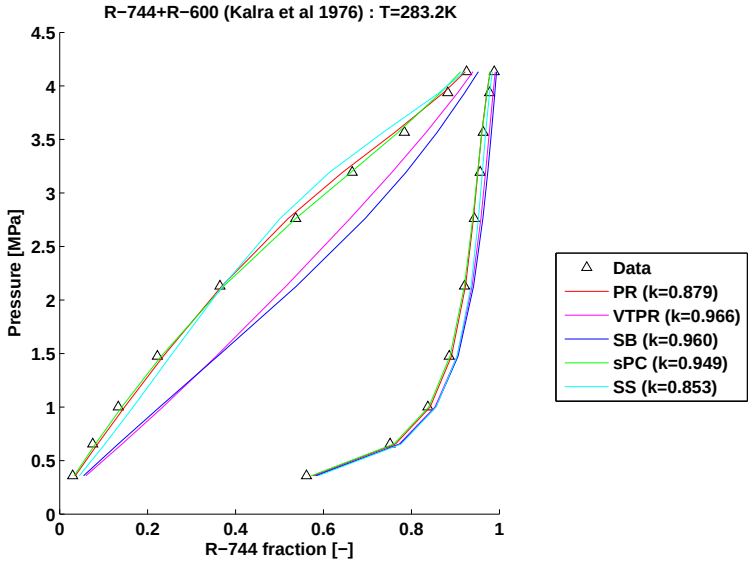

Figure 9.47: Mixtures evaluation No9

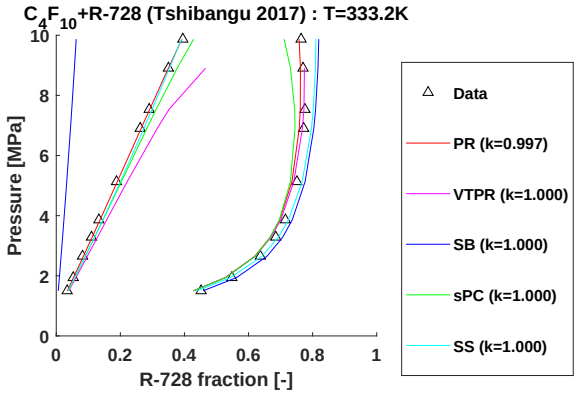

Figure 9.48: Mixtures evaluation No10

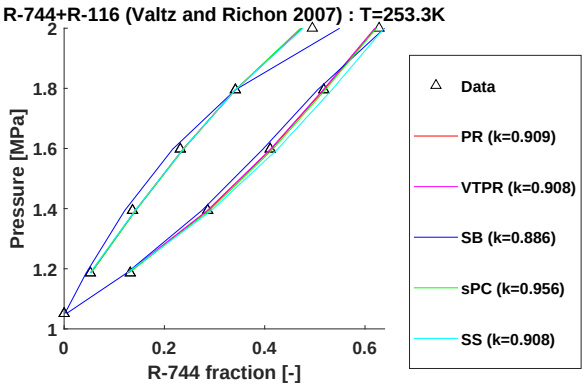

Figure 9.49: Mixtures evaluation No11

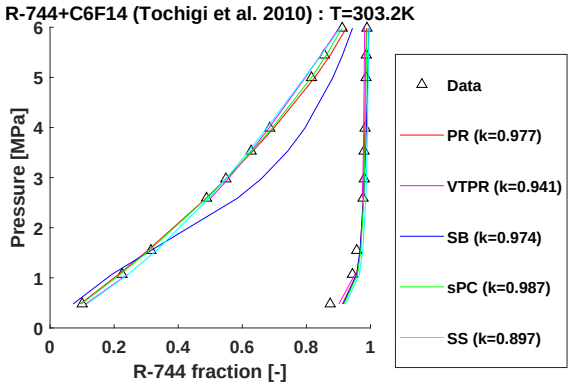

Figure 9.50: Mixtures evaluation No12

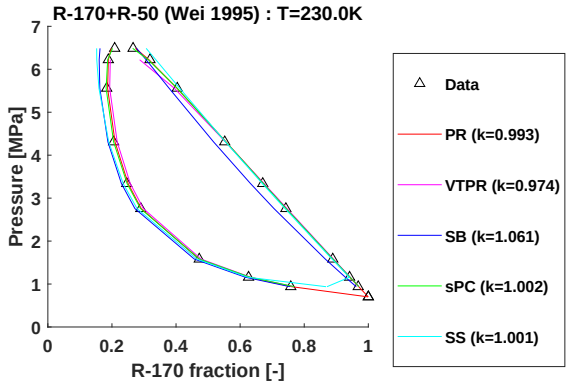

Figure 9.51: Mixtures evaluation No13

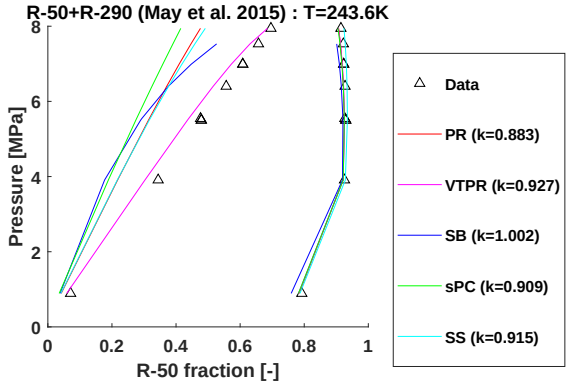

Figure 9.52: Mixtures evaluation No14

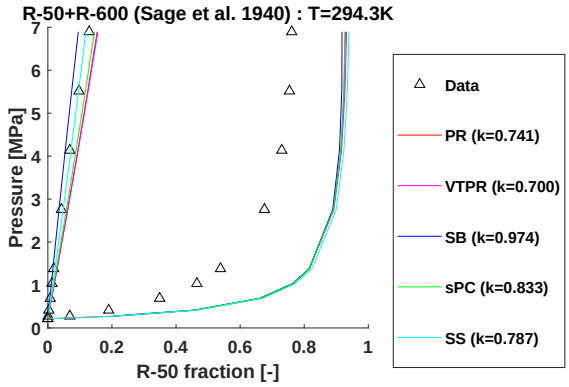

Figure 9.53: Mixtures evaluation No15

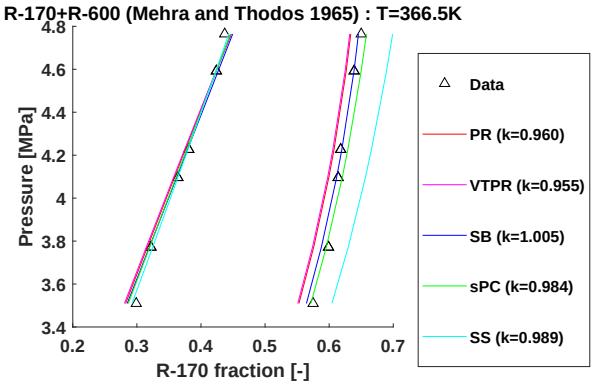

Figure 9.54: Mixtures evaluation No16

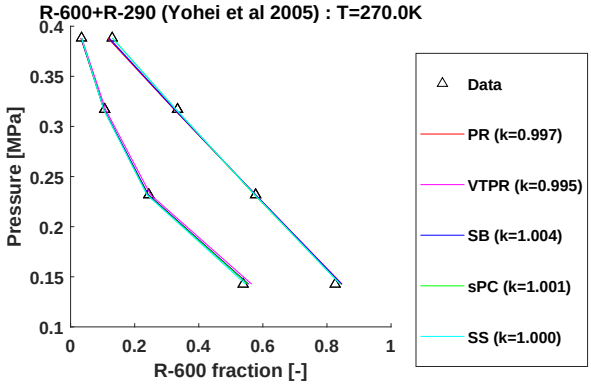

Figure 9.55: Mixtures evaluation No17

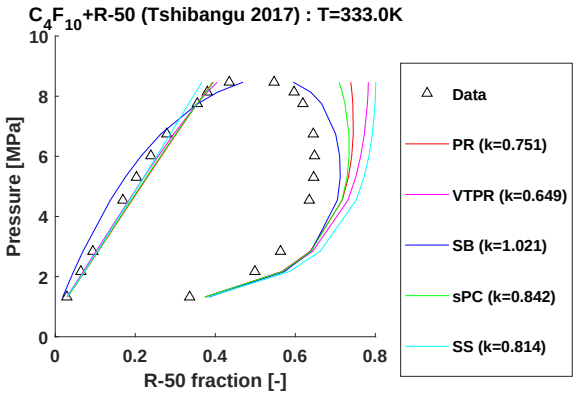

Figure 9.56: Mixtures evaluation No18

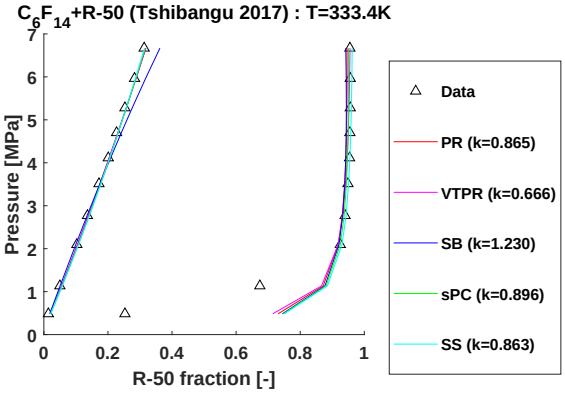

Figure 9.57: Mixtures evaluation No19

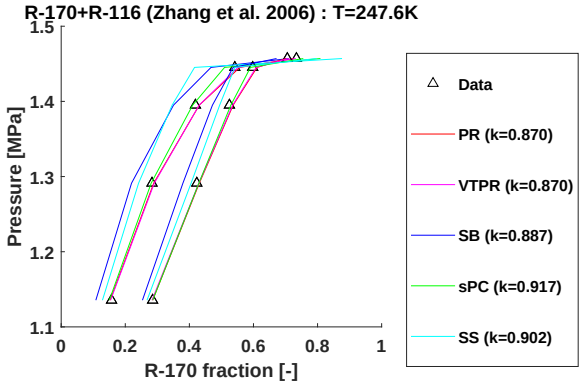

Figure 9.58: Mixtures evaluation No20

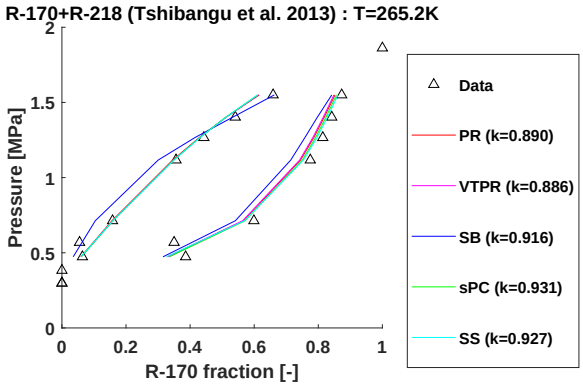

Figure 9.59: Mixtures evaluation No21

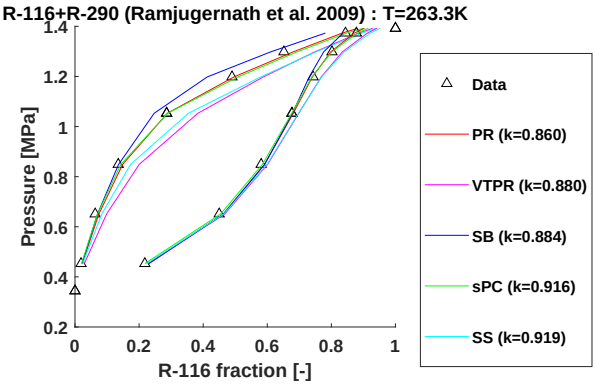

Figure 9.60: Mixtures evaluation No22

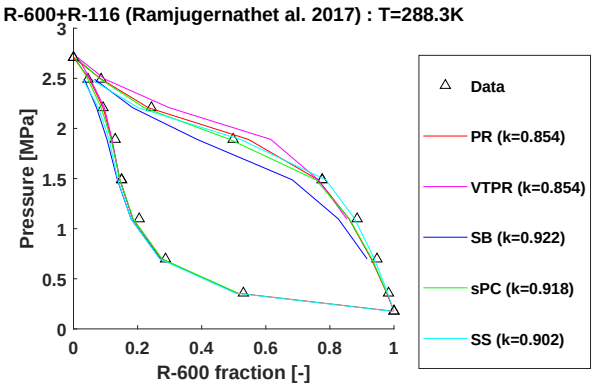

Figure 9.61: Mixtures evaluation No23

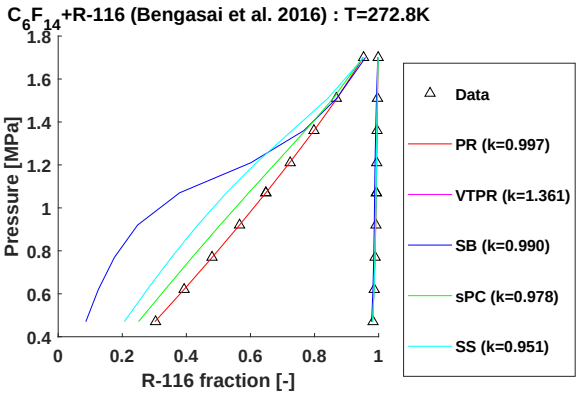

Figure 9.62: Mixtures evaluation No24